

**MODELING AND CONTROL OF
STAND-ALONE AC MICROGRIDS:
CENTRALIZED AND DISTRIBUTED STORAGE,
ENERGY MANAGEMENT AND DISTRIBUTED
PHOTOVOLTAIC AND WIND GENERATION**

PhD. dissertation prepared to
obtain the Doctor degree by

Andoni Urtasun Erburu

Supervisors

Luis Marroyo Palomo

Pablo Sanchis Gúrpide



Department of Electrical and Electronic Engineering

Pamplona, January 2015

ABSTRACT

The introduction of distributed renewable generators into the electrical grid is required for a sustainable system. In order to increase the penetration of renewable energies, microgrids are usually proposed as one of the most promising technologies. A microgrid is a combination of loads, distributed generators and storage elements which behaves as a single controllable unit for the grid operator. Furthermore, microgrids make it possible to improve the system reliability because they are capable of stand-alone operation in case of grid failure.

This thesis is focused on the development of AC microgrids under stand-alone operation. Its main objective is to design and implement overall control strategies which do not require the use of communication cables, thereby reducing costs and improving reliability. For this purpose, the following aspects are tackled:

- Energy management of an AC microgrid with diesel generator, centralized storage and distributed renewable generation
- Design of droop methods so that the current is shared among parallel-connected inverters
- Energy management of an AC microgrid with distributed storage and distributed renewable generation
- Control of the DC/DC stage in photovoltaic inverters with small input capacitors within a microgrid
- Sensorless MPPT control for small wind turbines within a microgrid

RESUMEN

El aumento de la penetración de energías renovables en la red eléctrica es necesario para el desarrollo de un sistema sostenible. Para hacerlo posible técnicamente, se ha planteado el uso de microrredes, definidas como una combinación de cargas, generadores distribuidos y elementos de almacenamiento controlados gracias a una estrategia global de gestión energética. Además, las microrredes aumentan la fiabilidad del sistema puesto que pueden funcionar en modo aislado en caso de fallo de red.

Esta tesis se centra en el desarrollo de microrredes AC en funcionamiento aislado. El objetivo principal es el diseño y la implementación de estrategias de gestión energéticas sin utilizar cables de comunicación entre los distintos elementos, lo que permite reducir los costes del sistema y aumentar su fiabilidad. Para ello, se abordan los siguientes aspectos:

- Gestión energética de una microrred AC con generador diesel, almacenamiento centralizado y generación renovable distribuida
- Diseño de técnicas de control “droop” para repartir la corriente entre inversores conectados en paralelo
- Gestión energética de una microrred AC con almacenamiento distribuido y generación renovable distribuida
- Control de la etapa DC/DC de inversores fotovoltaicos con pequeño condensador de entrada en el seno de una microrred
- Control de extracción de máxima potencia sin sensores mecánicos para sistemas minieólicos en el seno de una microrred

AGRADECIMIENTOS

Quería dedicar estas líneas a todas las personas que me han apoyado durante la realización de esta tesis, tanto a nivel técnico como a nivel personal.

A mis directores de tesis, Luis Marroyo y Pablo Sanchis, por darme la oportunidad de embarcarme en este proyecto, por la confianza que han depositado en mí y por su conocimiento y continuo apoyo.

A todos los miembros de Ingeper, gracias por estar siempre dispuestos a ayudarme y por esos buenos momentos que hemos pasado juntos. Espero conservar estas amistades tan valiosas, y ahora sí, empezar a organizar más Ingesalidas que antes.

A la empresa Ingeteam Power Technology por la colaboración en esta tesis. En especial a David Barricarte y Roberto González, por su confianza y dedicación.

To all the members of The Centre for Future Energy Networks, for their warm welcome and permanent support. In particular, to Dylan Dah-Chuan Lu, for giving me the opportunity to join their group, and for his advice and encouragement.

A mis amigos, por estar siempre a mi lado y ayudarme a desconectar por completo del trabajo cada fin de semana.

A mis padres Isabel y Pedro, y a mi hermana Andrea, por transmitirme con su ejemplo esa fuerza para seguir adelante en cualquier situación y por apoyarme en todas mis decisiones. Y también a Sara, por su cariño y apoyo y por atreverse a aventurarse conmigo por las antípodas.

CONTENTS

1	INTRODUCTION	1
1.1	Background and motivations / 2	
1.2	Microgrids / 4	
1.3	Objectives / 7	
1.4	References / 9	
2	AC MICROGRIDS WITH CENTRALIZED STORAGE	11
2.1	Introduction / 12	
2.2	System presentation and sizing / 15	
2.3	PV power limitation / 17	
2.3.1	Description / 17	
2.3.2	System modeling / 20	
2.3.3	Controller design / 22	
2.4	Proposed energy management strategy / 24	
2.4.1	Mode I: Normal operation / 24	
2.4.2	Mode II: PV power limitation / 25	
2.4.3	Mode III: Diesel generator / 25	
2.5	Simulation results / 26	
2.6	Experimental results / 30	
2.7	Conclusions / 34	
2.8	References / 35	
3	AC MICROGRID WITH DISTRIBUTED STORAGE	39
3.1	Introduction / 40	
3.1.1	Frequency and voltage regulation / 40	
3.1.2	Energy management / 42	
3.2	Power calculation / 45	
3.2.1	Product and low-pass filter / 45	
3.2.2	P-Q theory and digital sampling / 45	

3.3	Droop method for linear loads / 48
3.3.1	Droop method and RMS regulation / 48
3.3.2	Linear model of the power response for two inverters / 51
3.3.3	Small-signal model with stiff AC grid / 54
3.3.4	Small-signal model with load influence / 57
3.3.5	Simulation and experimental results / 59
3.3.6	Linear model of the power response for N inverters / 61
3.4	Issues about droop control / 64
3.4.1	Line impedance influence on reactive power sharing / 64
3.4.2	Inverter current limitation / 68
3.4.3	DC current control / 69
3.4.4	Overload voltage reduction / 71
3.5	Droop method for non-linear loads / 73
3.5.1	Harmonic distribution without control / 73
3.5.2	Harmonic compensation / 75
3.5.3	Simulation results / 77
3.6	Energy management during normal operation / 79
3.6.1	Slope changing method / 80
3.6.1.1	Description / 80
3.6.1.2	Influence of M_o and n on the power response / 82
3.6.1.3	Influence of n on the SOC response / 84
3.6.1.4	Simulation results / 87
3.6.2	Curve shifting method / 90
3.6.2.1	Description / 90
3.6.2.2	Influence of M_p and M_s on the power response / 91
3.6.2.3	Influence of M_p and M_s on the SOC response / 92
3.6.2.4	Simulation results / 93
3.6.2.5	SOC response for N batteries / 95
3.6.3	Experimental results / 96
3.7	Energy management during high/low SOC operation / 99
3.7.1	Proposed energy management strategy / 100
3.7.1.1	Description / 100
3.7.1.2	Battery inverter operation / 101
3.7.1.3	RES converter operation / 104
3.7.1.4	Non-critical loads operation / 107

3.7.2	Operating modes / 108	
3.7.2.1	Description / 108	
3.7.2.2	Mode I: Normal operation / 109	
3.7.2.3	Mode II: One battery charged / 110	
3.7.2.4	Mode III: PV power limitation / 110	
3.7.2.5	Mode IV: One battery discharged / 112	
3.7.2.6	Mode V: Load regulation / 113	
3.7.3	Small-signal modeling / 115	
3.7.3.1	Mode III: Identical battery system / 115	
3.7.3.2	Other modes: identical battery system / 121	
3.7.3.3	Different battery systems / 122	
3.7.4	Experimental results / 122	
3.8	Conclusions / 125	
3.8.1	Frequency and voltage regulation / 125	
3.8.2	Energy management / 125	
3.8.3	Summary for implementation of the whole system / 127	
3.9	References / 128	
4	CONTROL OF THE DC/DC STAGE IN PV INVERTERS WITH SMALL INPUT CAPACITORS	135
4.1	Introduction / 136	
4.2	PV array small-signal model / 140	
4.3	PV voltage control with boost converter / 144	
4.3.1	Inductor current control / 144	
4.3.2	Modeling for the voltage control / 146	
4.3.2.1	Traditional modeling / 146	
4.3.2.2	Small-signal modeling / 147	
4.3.3	Traditional control / 149	
4.3.4	Proposed control / 153	
4.3.4.1	Dynamic resistance estimation / 153	
4.3.4.2	Controller design / 153	
4.3.5	Experimental results / 156	
4.4	Dual PV voltage control with TIBuck converter / 159	
4.4.1	Dual MPPT with TIBuck converter / 159	
4.4.2	Small-signal modeling / 161	

4.4.3	Voltage regulation / 163	
4.4.3.1	Plant for the PV1 voltage regulation / 163	
4.4.3.2	Controller design for the PV1 voltage regulation / 165	
4.4.3.3	PV2 voltage regulation / 167	
4.4.4	Simulation results / 169	
4.4.5	Experimental results / 170	
4.5	PV power limitation / 174	
4.5.1	Proposed control strategy / 174	
4.5.1.1	MPPT operation / 174	
4.5.1.2	LPPT operation / 175	
4.5.1.3	MPPT and LPPT operation / 177	
4.5.2	Simulation results / 179	
4.5.2.1	Switch from MPPT to LPPT: P_{lpp}^* reduction / 180	
4.5.2.2	Switch from MPPT to LPPT: P_{mpp} increase / 181	
4.5.2.3	Switch from LPPT to MPPT: P_{lpp}^* increase / 182	
4.5.2.4	Switch from LPPT to MPPT: P_{mpp} reduction / 183	
4.6	Conclusions / 184	
4.7	References / 185	
5	SENSORLESS MPPT CONTROL OF SMALL WIND TURBINES: MODELING AND ROBUSTNESS ANALYSIS	191
5.1	Introduction / 192	
5.2	Modeling of the wind energy conversion system / 194	
5.2.1	Interaction between subsystems / 194	
5.2.2	PMSG with diode bridge / 196	
5.2.2.1	System description / 196	
5.2.2.2	Continuous conduction mode / 197	
5.2.2.3	Discontinuous conduction mode / 200	
5.2.2.4	Boundary between modes of conduction / 203	
5.2.2.5	Power curves / 204	
5.2.3	Experimental results / 205	
5.3	MPPT control / 207	
5.3.1	Integration of the wind turbine / 207	
5.3.2	Behavior of the whole system / 209	
5.3.3	Experimental results / 213	

5.4 Robustness analysis and lossless approach / 215	
5.4.1 Robustness analysis / 215	
5.4.1.1 Single parameter variation / 216	
5.4.1.2 Worst scenarios / 220	
5.4.1.3 Influence of the resistance / 222	
5.4.2 System modeling for the lossless approach / 222	
5.4.2.1 Continuous conduction mode / 222	
5.4.2.2 Discontinuous conduction mode / 223	
5.4.2.3 Boundary between modes of conduction / 224	
5.4.3 Simulation results / 225	
5.5 Conclusions / 226	
5.6 Appendices / 227	
5.6.1 Calculation of the current i_a for CCM / 227	
5.6.2 Calculation of the current i_a for DCM / 228	
5.7 References / 231	
6 CONCLUSIONS	233
6.1 Final conclusions / 234	
6.2 Contributions / 237	
6.3 Future work / 239	
6.3.1 Management of AC microgrids / 239	
6.3.2 Control of the photovoltaic system / 240	
6.3.3 Control of small wind turbines / 242	
NOMENCLATURE AND ACRONYMS	243

CHAPTER 1

INTRODUCTION

ABSTRACT

Although electricity generation is currently based on centralized power stations, the introduction of distributed renewable generators is favorable in terms of carbon emissions reduction, diversification of energy sources and efficiency increase due to decentralization. In order to increase the penetration of renewable energies, microgrids are usually proposed as one of the most promising technologies. A microgrid is a combination of loads, distributed generators and storage elements which behaves as a single controllable unit for the grid operator. Furthermore, microgrids make it possible to improve the system reliability because they are capable of stand-alone operation in case of grid failure.

This thesis is framed within the development of AC microgrids under stand-alone operation. Its main objective is to design and implement overall control strategies which do not require the use of communication cables, thereby reducing costs and improving reliability. While chapter 2 deals with the energy management of AC microgrids with centralized storage and diesel generator, chapter 3 addresses the energy management of AC microgrids with a number of distributed storage units. For its part, chapter 4 first tackles the PV voltage regulation and PV power limitation problem by using a DC/DC boost converter, and then presents the dual PV voltage regulation by using a DC/DC two-input buck converter. Then, chapter 5 deals with the MPPT operation of small wind turbines. Finally, the conclusions of the thesis are drawn in chapter 6.

1.1 BACKGROUND AND MOTIVATIONS

Electricity is certainly the most versatile form of energy, thanks to its excellent transformation capability, which facilitates its generation, transportation and utilization. This feature has made electricity become one of the main energetic vectors at present. Electrical energy has traditionally been generated by large thermal and nuclear power stations in a centralized manner, being then transported through long distances to the consumers. However, these primary energies bring along environmental problems related to air pollution and global warming, as well as economical dependence on the resource producers. For this reason, environmental organizations, governments and public opinion are driving the use of renewable energies for a sustainable energetic model.

In contrast to conventional generators, renewable energy sources are usually installed as Distributed Generators (DG). Distributed generators can be defined as power generators which are connected near the consumer centers and are not directly controlled by the grid operator [1.1]. The former makes it possible to improve the efficiency by reducing transportation losses. Furthermore, renewable energies are environment-friendly and widely spread, limiting the energy-dependence problem. These advantages are contributing to increase its worldwide installed power. The trend is especially noticeable in photovoltaic (PV) and wind energy, as it can be observed in Fig. 1.1 and Fig. 1.2 [1.2]. These figures show how PV and wind power world capacities have grown exponentially from 2004 to 2013, reaching an installed power of 139 GW and 318 GW at the end of 2013, respectively.

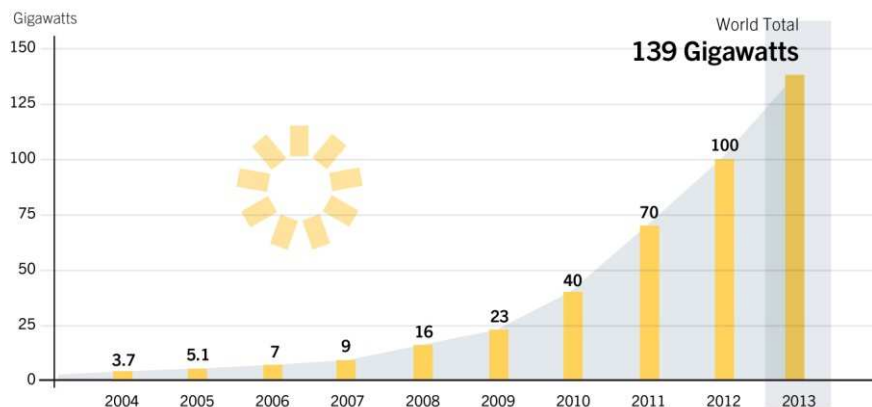


Figure 1.1. Solar PV total global capacity, 2004–2013 [1.2].

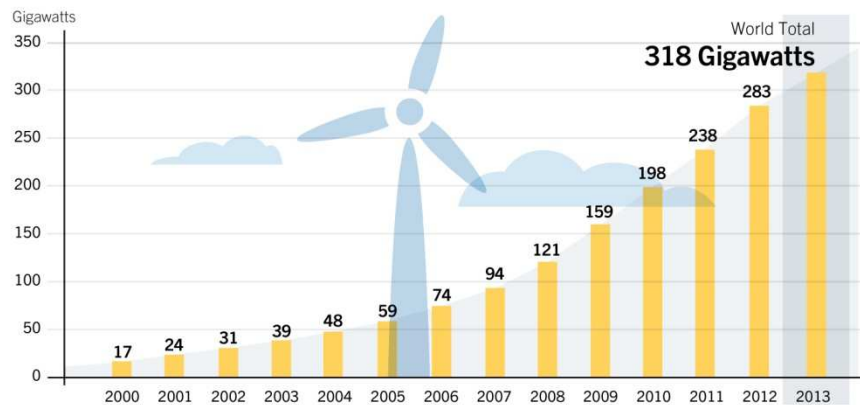


Figure 1.2. Wind power total world capacity, 2004–2013 [1.2].

However, renewable-energy DGs do not lack drawbacks. Traditionally, one of the main criticisms has been the high cost in relation to conventional generators. Nevertheless, this comparison is not currently equitable on account of the different stage of maturity. As a matter of fact, the cost of energy for renewable-energy sources has been continuously decreasing in the last years, and different stages of maturity can be found depending on the technology. For example, the cost of energy for conveniently located wind turbines has been estimated as 4 c\$/kWh, making it competitive against other energy sources [1.3]. Concerning photovoltaic energy, grid-connected installations are already profitable in some locations and are believed to become cost-effective in most countries in the near future.

Another issue of renewable energies has to do with its grid interaction. Due to the increasing renewable penetration, new regulations are demanding that the renewable generators participate in the grid support. Some requirement, such as low current THD or reactive power support, can be obtained thanks to the interfacing inverter, while others, such as low voltage ride-through, are more difficult to achieve and may require the use of additional hardware [1.4], [1.5]. On the other hand, since renewable-energy sources are usually connected by means of electronic inverters, no extra inertia is provided to the grid and, as a consequence, the system damping is reduced. In order to increase the damping and guarantee the success of conventional frequency regulation, renewable-source inverters can emulate a virtual inertia, but a storage unit or a power control is required [1.6].

Furthermore, the energy produced by a renewable generator cannot generally be controlled since it depends on the resource. High penetration of renewable energies decreases the ratio of dispatchable generators and adds at the same time an unpredicted component to the power profile, thus complicating the electrical grid regulation.

In order to cope with these issues and make a renewable energy-based grid possible, storage units or controllable generators have to be included close to the renewable distributed generators. Depending on the ratio between controllable and non-controllable elements, different levels of power regulation can be achieved in this system. This combination of elements together with loads is called microgrid, and its concept and characteristics are presented in next section.

1.2 MICROGRIDS

A microgrid is defined as a combination of loads, distributed generators (wind turbines, photovoltaic modules, fuel cells, micro-turbines...), and storage elements (batteries, hydrogen, supercapacitors, flywheels, storage tanks...) which are connected to the electrical grid at the Point of Common Coupling (PCC) [1.7]. Thanks to the energy management strategy implemented in the microgrid, it behaves as a single controllable unit for the grid operator. In this way, a high penetration of renewable energies becomes feasible and more cost-effective, with the consequent advantages in terms of carbon emissions reduction, diversification of energy sources and efficiency increase due to decentralization. Furthermore, microgrids make it possible to improve the system reliability because they are capable of stand-alone operation in case of grid failure.

Microgrids can be classified in three groups according to their configuration. The first one is the AC microgrid, in which all elements are connected to the AC bus, as traditionally carried out. This configuration originated from the intention of managing distributed generators and loads within a certain sector of the electrical grid. In this system, shown in Fig. 1.3, DC elements are connected to the AC bus through DC/AC inverters, and variable-frequency generators are connected by means of AC/DC/AC converters, while loads and fixed-frequency AC generators are directly attached to the bus. The AC bus can be connected or disconnected from the electrical grid through the point of common coupling. The main advantage of this topology is its versatility since most of the system elements are currently designed and prepared for AC grids.

The second configuration is the DC microgrid, in which all elements are connected to the DC bus, and the DC bus is in turn connected to the electrical grid by means of a DC/AC inverter. The main advantages of this topology in relation to the AC microgrid are a lower number of electronic converters and a simpler management within the DC section. In this system, shown in Fig. 1.4, DC elements generally require DC/DC converters, AC generators require AC/DC converters, some loads require DC/AC or DC/DC converters, and other loads and DC generators can be directly attached to the DC bus.

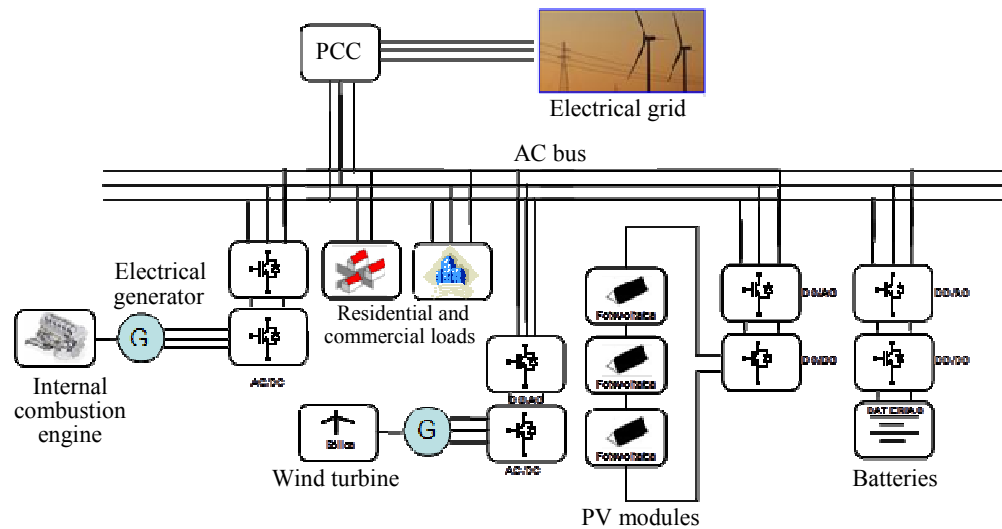


Figure 1.3. AC microgrid.

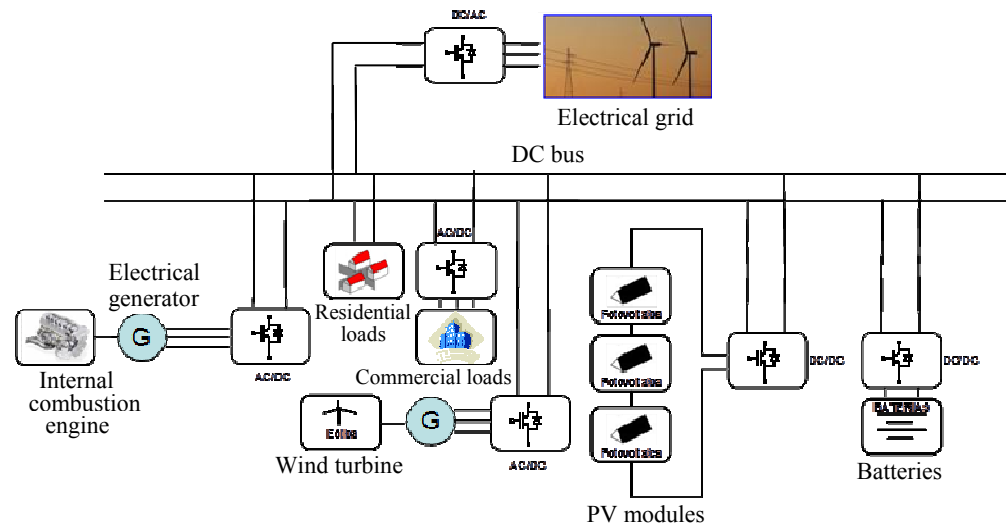


Figure 1.4. DC microgrid.

The third configuration is called hybrid microgrid because it has both DC and AC buses. This configuration possesses the advantages of DC microgrids and is more versatile. However, the presence of two buses makes the system and the control more complicated. In this system, shown in Fig. 1.5, each element can be connected to the AC or DC bus according to its nature. The AC and DC buses are attached by means of a DC/AC inverter and the AC bus can be connected or disconnected from the electrical grid.

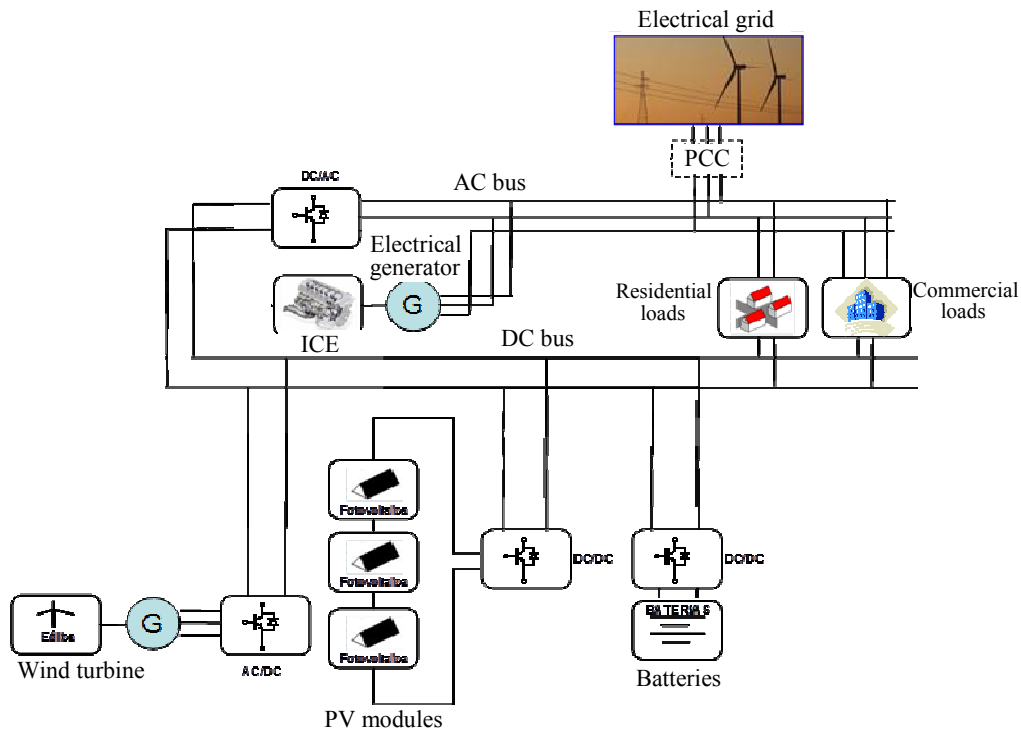


Figure 1.5. Hybrid microgrid.

Independently of the topology, the microgrid can operate either isolated or connected to the grid. In both cases, the control of the elements and the energy management is very important for a correct system operation. When the grid is present, the microgrid remains attached to it, exchanging real and/or reactive power. In this case, grid generation is obviously not needed, and the converters usually operate under current-control mode. Renewable-energy sources perform Maximum Power Point Tracking (MPPT), whereas storage units and controllable generators deliver or absorb a certain power according to the energy management strategy. The latter is usually implemented in a central supervisor, which sends the power reference to the different elements through low bandwidth communication. The type of strategy is different depending on the control objective; some examples include charging the storage units, optimizing the power exchanged with the grid in terms of peaks and fluctuations or maximizing the profit from selling energy to the grid [1.8]–[1.10].

In case of grid failure, microgrids are capable of stand-alone operation. There are several techniques to generate the grid voltage. One approach is to use a central or master-slave control where a supervisor sets in real time the operating point of each element [1.11]. The drawback of this approach is that it requires a fast communication

system between master and microgrid elements [1.12], [1.13]. Distributed control is another possible technique, which can be achieved with no communication thanks to droop methods [1.14]–[1.16]. Because the grid is not present in stand-alone operation, the energy management objective is to ensure the load supply. This is accomplished thanks to the storage units, which offset the difference between generation and consumption as long as their state-of-charge is within allowable limits. The energy management strategy can be implemented by means of a central supervisor and low bandwidth communication [1.17], or by using certain properties of the bus voltage as communication signals (DC voltage for DC microgrids or RMS voltage and frequency for AC microgrids) [1.18]–[1.20].

1.3 OBJECTIVES

This thesis is framed within the development of AC microgrids under stand-alone operation. The main objective is to design and implement overall control strategies which do not require the use of communication cables. Avoiding communication cables is favorable since it makes it possible to reduce the complexity of the system, thereby reducing costs. The reliability is also improved because one source of failure disappears. Furthermore, since all elements can operate independently, the failure of one of them does not affect the correct operation of the whole system.

The overall control strategy depends on the type of isolated AC microgrid and must be applied to every element of the system. Whereas renewable-energy generators and loads are generally distributed throughout the microgrid, diesel generators and storage units can be centralized or distributed. The centralized approach makes sense due to the current complexity of storage systems and also facilitates the control. The most frequently used system consists of distributed loads and PV generators together with centralized battery storage and diesel generator. The control of this system is addressed in chapter 2, in which an energy management strategy is proposed to ensure the correct operation of the system in every situation, improving system efficiency and optimizing the operating life of the battery and the diesel generator.

However, the installation of two or more energy-storage units is recommended for system redundancy. It may also be required when there is a consumption increase subsequent to installation [1.17]. For this reason, a system in which not only loads and PV generators are distributed, but also battery storage, is considered in chapter 3. The management of a number of distributed storage units becomes more problematic because, in real applications, their SOC does not evolve simultaneously. As a result, a new energy management strategy which also includes some additional controls is proposed in this chapter. Furthermore, in order to improve reliability, all battery inverters have to

be independent and control the same voltage. With this aim, droop methods are also analyzed in this chapter and new schemes are designed with the intention that real power, reactive power and harmonic currents are shared among the inverters regardless of the line impedance.

Since chapters 2 and 3 deal with the overall control strategy, more emphasis is put along these chapters on the storage system and energy management controls. Renewable generators are therefore considered as ideal elements, operating under MPPT or power limitation as dictated by the energy management strategy. On the contrary, chapters 4 and 5 focus on the renewable generators, taking into account the interfacing converters as well as the non-linear generator characteristics.

The aim of chapter 4 is to improve the control performance of the PV system within an AC microgrid. Whilst in MPPT operation the PV voltage is very close to the MPP voltage, the energy management strategy also requires a voltage control over the MPP voltage in order to reduce the PV power. Thus, a fast and stable regulation in the entire operating range is required for a proper tracking. However, the non-linear nature of the photovoltaic array can cause the regulation performance to change with the operating point. This effect is accentuated by the use of small polypropylene capacitors at the converter input, which are replacing the large electrolytic ones for the benefit of cost and reliability. As a result, the PV system control within a microgrid must be reassessed.

In low- and medium-power systems, a DC/DC boost converter is usually attached to the PV generator to step-up the PV voltage at the input of the inverter. In order to make the PV generator operate under either MPPT or power limitation, as dictated by the energy management strategy, chapter 4 proposes a control strategy for the DC/DC boost converter that makes it possible to operate in both modes. Another objective is to explain the variability of the PV voltage regulation when using this converter with cascaded feedback loops. It is also shown in this chapter that the control variability is caused by the non-linear characteristics of the PV arrays, and an adaptive control which achieves constant performance for the whole operating range is proposed. Finally, in PV systems with different conditions in terms of shades, orientation and/or technology, the use of more than one MPP trackers for different module groups is highly recommended in order to improve MPPT efficiency. For this reason, the control of two PV voltages at the same time by one DC/DC two-input buck converter followed by an inverter is also analyzed in chapter 4.

The objective of chapter 5 is to improve the MPPT control of small wind turbines within an AC microgrid. Since a robust and cost-effective system is desired, a very simple MPPT method is proposed. This method does not require any measurement from the mechanical system, and achieves maximum power for every wind speed by imposing the

relationship between the DC voltage and current under optimum operation. This method requires having knowledge of the system parameters, which can be difficult to obtain accurately in small wind energy conversion systems. For this reason, this chapter also evaluates the influence of the system parameters on the power captured by the MPPT control. Two negative but realistic scenarios of parameter variation, as well as the influence of neglecting the model losses are also considered.

Finally, chapter 6 includes the final conclusions of the thesis, the contributions which have been made so far, and some future research lines which will make it possible to give continuity to this work.

This thesis was carried out in collaboration with the company Ingeteam Power Technology and was supported in part by the Spanish Ministry of Economy and Competitiveness under Grants DPI2009-14713-C03-01, DPI2010-21671-C02-01 and DPI2013-42853-R, and in part by the Public University of Navarra through a doctoral scholarship.

1.4 REFERENCES

- [1.1] T. V. Van, A. Woyte, J. Soens, J. Driesen, R. Belmans, "Impacts of distributed generation on distribution system power quality", in *Electrical Power Quality and Utilization (EPQU)*, Cracow (Poland), 2003.
- [1.2] REN21 Renewable Energy Policy Network for the 21st Century, "Renewables global status report 2014".
- [1.3] S. Song, S. Kang, N. Hahm, "Implementation and control of grid connected ac-dc-ac power converter for variable speed wind energy conversion system," in *18th IEEE Applied Power Electronics Conference and Exposition (APEC)*, vol. 1, pp. 154–158, Miami Beach (USA), 2003.
- [1.4] C. Jauch, J. Matevosyan, T. Ackermann, "International comparison of requirements for connection of wind turbines to power systems," *Wind Energy*, vol. 8, no. 3, pp. 295-306, 2005.
- [1.5] Y. Yang, F. Blaabjerg, "Synchronization in single-phase grid-connected photovoltaic systems under grid faults," in *3rd IEEE International Symposium on Power Electronics for Distributed Generation Systems (PEDG)*, pp. 476–482, Aalborg (Denmark), 2012.
- [1.6] M. F. M. Arani, E. F. El-Saadany, "Implementing virtual inertia in DFIG-based wind power generation," *IEEE Transactions on Power Systems*, vol. 28, no. 2, pp. 1373–1384, 2013.
- [1.7] M. Reza, D. Sudarmadi, F. A. Viawan, W. L. Kling, L. Van Der Sluis, "Dynamic stability of power systems with power electronic interfaced DG", in *2006 IEEE Power Systems Conference and Exposition (PSCE)*, pp. 1423–1428, Atlanta (USA), 2006.

- [1.8] J. Pascual, P. Sanchis, and L. Marroyo, "Implementation and control of a residential electrothermal microgrid based on renewable energies, a hybrid storage system and demand side management," *Energies*, vol. 7, no. 1, pp. 210–237, 2014.
- [1.9] J. J. Barricarte, I. San Martín, P. Sanchis, L. Marroyo, "Energy management strategies for grid integration of microgrids based on renewable energy sources," in *10th International Conference on Sustainable Energy Technologies (SET)*, Istanbul (Turkey), 2011.
- [1.10] D. A. Aviles, F. Guinjoan, J. Barricarte, L. Marroyo, P. Sanchis, H. Valderrama, "Battery management fuzzy control for a grid-tied microgrid with renewable generation," in *38th Conference on IEEE Industrial Electronics Society (IECON)*, pp. 5607–5612, Montreal (Canada) 2012.
- [1.11] Y. Ito, Y. Zhongqing, H. Akagi, "DC microgrid based distribution power generation system," in *4th International Power Electronics and Motion Control Conference (IPEMC)*, vol. 3, pp. 1740–1745, Xi'an (China), 2004.
- [1.12] K. Techakittiroj, S. Patumtaewapibal, V. Wongpaibool, W. Threevithayanon, "Roadmap for implementation of DC system in future houses" in *13th International Conference on Harmonics and Quality of Power (ICHQP)*, pp. 1–5, Wollongong (Australia), 2008.
- [1.13] O. Haas, O. Ausburg, P. Palensky, "Communication with and within distributed energy resources," in *2006 IEEE International Conference on Industrial Informatics*, pp. 352–356, Singapore, 2006.
- [1.14] E. A. A. Coelho, P. C. Cortizo, P. F. D. Garcia, "Small-signal stability for parallel-connected inverters in stand-alone ac supply systems," *IEEE Transactions on Industry Applications*, vol. 38, pp. 533–542, 2002.
- [1.15] C. N. Rowe, T. J. Summers, R. E. Betz, D. J. Cornforth, T. G. Moore, "Arctan power-frequency droop for improved microgrid stability," *IEEE Transactions on Power Electronics*, vol. 28, no. 8, pp. 3747–3759, 2013.
- [1.16] A. Mohd, E. Ortjohann, D. Morton, O. Omari, "Review of control techniques for inverters parallel operation," *Electric Power Systems Research*, vol. 80, pp. 1477–1487, 2010.
- [1.17] T. Dragicevic, J. M. Guerrero, J. C. Vasquez, D. Skrlec, "Supervisory control of an adaptive-droop regulated dc microgrid with battery management capability," *IEEE Transactions on Power Electronics*, vol. 29, no. 2, pp. 695–706, 2014.
- [1.18] D. Wu, J. M. Guerrero, J. C. Vasquez, T. Dragicevic, F. Tang, "Coordinated power control strategy based on primary-frequency-signaling for islanded microgrids," in *2013 IEEE Energy Conversion Congress and Exposition (ECCE)*, pp. 1033–1038, Denver (USA), 2013.
- [1.19] A. Urtasun, P. Sanchis, D. Barricarte, L. Marroyo, "Energy management strategy for a battery-diesel stand-alone system with distributed PV generation based on grid frequency modulation," *Renewable Energy*, vol. 66, pp. 325–336, 2014.
- [1.20] E. Serban H. Serban, "A control strategy for a distributed power generation microgrid application with voltage- and current-controlled source converter," *IEEE Transactions on Power Electronics*, vol. 25, pp. 2981–2992, 2010.

CHAPTER 2

AC MICROGRIDS WITH CENTRALIZED STORAGE

ABSTRACT

This chapter presents the energy management of a hybrid PV-Battery-Diesel system used in islanded AC microgrids. This configuration is very attractive for stand-alone microgrids in terms of cost and reliability. In many cases, the battery and the diesel generator are centralized and generate the AC grid while the PV generators and loads are distributed and connected to the grid. However, in these cases, long communication cables are required in order to reduce the PV power when the battery is fully charged. This chapter proposes an energy management strategy which makes it possible to avoid the use of communication cables, rendering the system simpler, cheaper and more reliable. According to the strategy, when a power reduction is required, the battery inverter increases the grid frequency. This is detected by the PV inverters, which continuously reduce their power in order to prevent the battery from overcharge or over-current. The strategy also optimizes the efficiency and operating life of the diesel generator. Simulation and experimental validation is carried out for a system with 10 kW PV generation, a 5 kVA battery inverter, a 5 kVA diesel generator and a 5 kVA load.

2.1 INTRODUCTION

For remote locations with difficult access to the power grid, stand-alone systems are more cost-effective. In fact, these systems are widely established in hilly regions and remote villages where they are used for a wide range of applications such as rural electrification, auxiliary power units for emergency services or military applications, and manufacturing facilities using sensitive electronics [2.1], [2.2].

A diesel generator has been traditionally used in stand-alone systems since it greatly reduces the Loss of Load Probability (LOLP) and the initial investment. However, thanks to the PV cost reduction, the addition of photovoltaic generation to a pure diesel system is becoming favorable. The fact that the solar resource is free helps reduce the cost of energy and fuel consumption and avoid carbon dioxide emissions.

Given the similarities between this stand-alone system and the conventional electric grid, similar approaches could be envisaged for the energy management. Comprehensive reviews on load-frequency control for conventional grids, also including renewable-energy sources, can be found in [2.3] and [2.4]. Some conventional approaches include phase-shift methods [2.5], [2.6], and proportional-integral control [2.7]. Many authors show that photovoltaic systems can also contribute to the grid stability by providing primary frequency regulation [2.8]–[2.10]. In [2.11], an energy management is developed for a stand-alone system. The photovoltaic inverter follows load variations by means of a fuzzy control which requires irradiance and frequency deviation as inputs. Thanks to the control, frequency deviation is reduced at the expense of limiting the photovoltaic power. In all these cases, the regulation contributes to the energy management because the systems are based on synchronous generators and therefore have an associated inertia. However, energy management in non-inertial systems is considerably different from synchronous-generator-based systems.

A battery energy storage system can also be considered, leading to a hybrid PV-battery-diesel system. Adding a battery makes it possible to integrate a higher photovoltaic power and, at the same time, to reduce frequency deviations. In this case, the diesel generator is usually disconnected, which leads to a non-inertial system based on electronic converters. The hybrid solution is an extremely interesting option, since it achieves a tradeoff between cost and reliability [2.12]–[2.16]. The diesel generator duty cycle is reduced, resulting in an increased life and a lower maintenance [2.12], [2.17]. Furthermore, whenever the diesel generator is used, it can be forced to operate close to its nominal power and then with a high efficiency [2.17], [2.18]. Due to these advantages, photovoltaic generation with battery storage is being installed both in existing diesel installations and in new hybrid stand-alone systems [2.14], [2.15], [2.19].

The hybrid PV-battery-diesel system requires high-quality energy management for optimal operation. The diesel generator generally remains unconnected, whilst the PV arrays operate under MPPT and the battery offsets the difference between consumption and generation. As a result, the battery State of Charge (SOC) changes accordingly. Then, when the SOC is low, the diesel generator comes into operation. This prevents the battery from an over-discharge and increases the stored energy. On the contrary, when the battery is fully charged and generation is higher than consumption, the photovoltaic power have to be limited in order to protect the battery from overcharging [2.20], [2.21].

The type of energy management implemented depends on the system configuration. Two alternatives are generally used depending on the location of the photovoltaic generators, as shown in Fig. 2.1. In both of them, the diesel generator, loads and battery, through an inverter in that case, are connected to the common AC bus. However, in the first case, the PV arrays are connected to the battery through a DC/DC converter whereas in the second case, they are connected to the AC bus through an inverter.

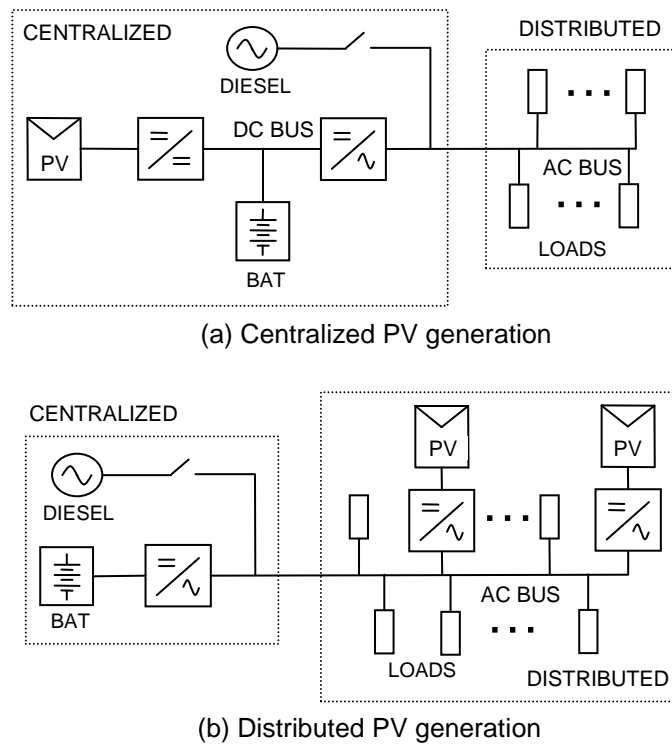


Figure 2.1. Stand-alone hybrid system: centralized/distributed generation.

Due to its simplicity, the first configuration (Fig. 2.1(a)) is advantageous in many situations. Since generation and storage are centralized, all the information passes through the control supervisor and a simple energy management strategy can therefore be implemented. When the battery is fully charged, the DC/DC converter can easily control the DC bus voltage with no need for communication cables [2.22]–[2.27]. However, this structure makes it necessary to install the PV generators close to the battery, which can be a limitation in applications where PV generation is distributed. In these cases, the second configuration becomes more attractive.

The second configuration (Fig. 2.1(b)) makes it possible to locate the PV arrays near the loads. It can be convenient in many applications such as rural electrification since the PV arrays can be placed on the house roof and connected directly to the mains [2.28]–[2.30]. In normal operation, the diesel generator is not connected. In this situation, the PV inverters operate as current-source inverters (CSI), delivering maximum power. The battery inverter operates as a voltage-source inverter (VSI), setting the grid frequency and voltage [2.31]. As a result, the battery inverter automatically supplies the required real and reactive power. However, the drawback of this system is that communication cables are required in order to reduce the PV power when the battery is fully charged, which makes the system more complex, more expensive and less reliable [2.32].

Well-known droop methods succeed in sharing the power among parallel VSIs without the need of communication cables [2.33], [2.34]. However, the PV power reduction in such a system with no communications has not yet been addressed. This chapter proposes an energy management strategy for the whole system. The strategy makes it possible to limit the distributed PV generation without the need for communication cables. When the battery is fully charged or the battery power exceeds its nominal value, the battery inverter transmits the information through the AC lines by means of a frequency increase. This message is detected by the PV inverters, which continuously reduce the power generated in order to regulate the battery voltage or power, preventing an overcharge or over-current. In doing so, the battery charge is optimized and its life increased. Besides, the battery is protected from over-current, making it possible to install a PV peak power higher than the battery inverter rated power, which is often required by the system sizing. This strategy also optimizes the diesel generator operation since it is only connected when there is a low SOC and operates at a high power, thereby increasing its efficiency and expected life.

2.2 SYSTEM PRESENTATION AND SIZING

The hybrid stand-alone system is shown in Fig. 2.2, where v_{bat} and i_{bat} are the battery voltage and current, v_{grid} the grid voltage, i_{inv} the battery inverter current, v_{diesel} and i_{diesel} the diesel voltage and current, i_{gen} the total PV inverter current, i_{load} the total load current, P_{bat} and Q_{bat} the real and reactive power absorbed by the battery inverter, P_{diesel} and Q_{diesel} the real and reactive power supplied by the diesel generator, P_{load} and Q_{load} the real and reactive power demanded by the loads, and P_{pv} the power generated by the PV arrays. The PV inverters do not provide reactive power and power losses are neglected for the analysis. The supervisor is located in the battery inverter and directly measures v_{bat} , i_{bat} , v_{grid} , i_{inv} , v_{diesel} and i_{diesel} . From these variables, the difference between the load and PV currents can be obtained as

$$i_{load} - i_{gen} = i_{diesel} - i_{inv}. \quad (2.1)$$

However, due to the system configuration and the lack of communication cables, it is not possible to distinguish between i_{load} and i_{gen} . The SOC of the battery is also determined by means of

$$SOC = SOC_i + \frac{\int i_{bat} \cdot \eta_{bat} dt}{C_{Ah}}, \quad (2.2)$$

where SOC_i is the initial SOC and η_{bat} is the battery efficiency.

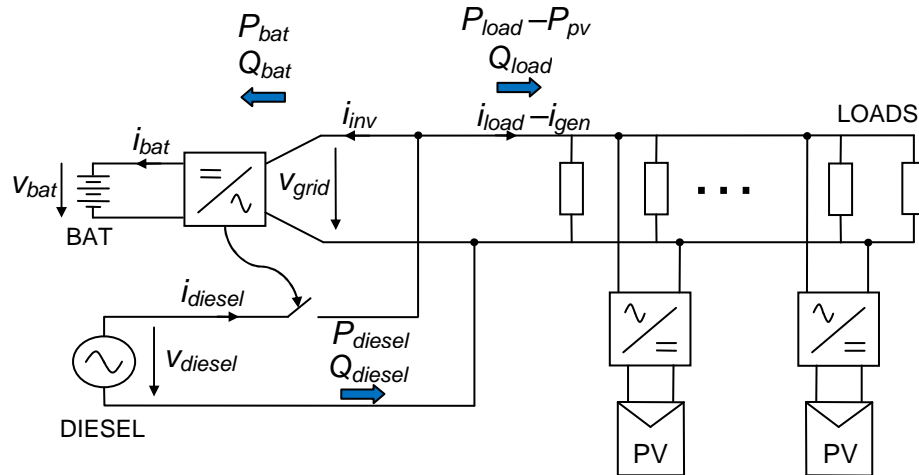


Figure 2.2. Voltages, currents and powers known by the supervisor.

The rated values of the system with distributed PV generation are shown in Fig. 2.3, where C_{Ah} is the battery rated capacity, $S_{bat,nom}$ is the battery inverter rated power, $S_{diesel,nom}$ is the diesel generator rated power, $S_{load,nom}$ is the load rated power, and $S_{pv,nom}$ is the total PV inverter rated power.

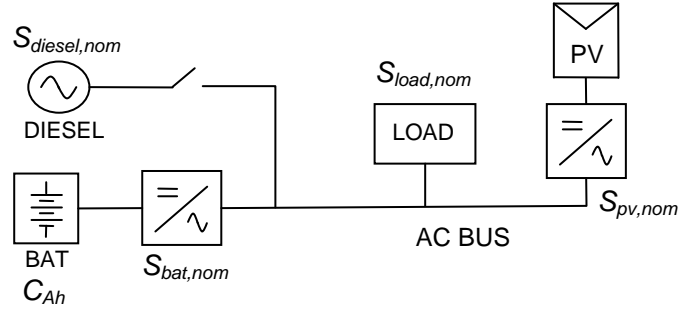


Figure 2.3. Sizing of the distributed PV generation system.

For a certain application, $S_{load,nom}$ is given. The battery should at least be able to feed the loads even in the worst case scenario, i.e. with maximum consumption and no generation. It is thus advisable that $S_{bat,nom} \geq S_{load,nom}$.

The PV power sizing strongly depends on the generation and consumption power profiles and therefore on the application and system location. In many cases, the most cost-effective PV power is higher than the load rated power. In principle, this would make it necessary to increase the battery inverter power over $S_{pv,nom}$ in order to provide system overcurrent protection whenever generation is high and there is no load. However, these systems always require a reduction in the PV power in order to protect the battery from overcharging when it is fully charged. This power limitation can also be used to reduce the size of the battery inverter with regard to the PV inverters, that is $S_{bat,nom} < S_{pv,nom}$. Then, the power absorbed by the battery inverter can reach $S_{pv,nom}$ during a short transient until the PV power has been reduced. This condition restricts the minimum size of the battery inverter. In this work, it is assumed that the battery inverter can withstand twice its rated power for a very short transient (about one second) and thus it must be guaranteed that $S_{bat,nom} \geq S_{pv,nom}/2$. In short, the two restrictions for the battery inverter are $S_{bat,nom} \geq S_{pv,nom}/2$ and $S_{bat,nom} \geq S_{load,nom}$.

Regarding the diesel generator, it should be sized so that $S_{diesel,nom} \geq S_{load,nom}$. This guarantees that, when the SOC is low and there is no PV generation, the diesel can completely meet the load demand [2.12].

The system rated values used throughout this chapter for the simulation and experimental results, in accordance with the aforementioned sizing, are shown in Table 2.1.

$S_{load,nom}$	5000 VA
$S_{bat,nom}$	5000 VA
$S_{diesel,nom}$	5000 VA
$S_{pv,nom1}$	5000 W
$S_{pv,nom2}$	5000 W
C_{Ah} (10 h)	240 Ah
$V_{bat,nom}$	120 V

Table 2.1. Sizing of the distributed PV generation system.

2.3 PV POWER LIMITATION

2.3.1 Description

There are two situations in which it is necessary to limit the photovoltaic power. The first one is related to the battery overcharge. When the battery is charged and cannot absorb more power, its voltage will exceed the maximum voltage, $v_{bat,max}$. The PV power must then be reduced in order to limit the battery voltage to $v_{bat,max}$. The value of the voltage $v_{bat,max}$ depends on the battery type and the charging method. For lead-acid batteries, Three-Stage Charging is the most suitable charging algorithm, whereby $v_{bat,max}$ is the absorption voltage $V_{bat,abs}$ during both normal operation and absorption charging, and the float voltage $V_{bat,fl}$ during float charging [2.35], [2.36]. For lithium-ion batteries, $v_{bat,max}$ is the overcharge voltage [2.37].

The second situation is related to over-current protection. When the current or the power absorbed is too high, the battery current i_{bat} will exceed the maximum current $i_{bat,max}$. In this situation, the current must be limited to $i_{bat,max}$, which is also achieved thanks to the PV power reduction. The value of $i_{bat,max}$ depends on two restrictions. It must first be guaranteed that the battery inverter RMS current does not exceed its nominal value or, in other words, that the inverter apparent power does not exceed $S_{bat,nom}$. This can occur even for a low battery power if the battery inverter is feeding high reactive loads. In order to avoid this, $i_{bat,max}$ is set to $i_{bat,Smax}$, which is calculated as follows

$$i_{bat,Smax} = \frac{S_{bat,nom} \cdot \cos \varphi}{v_{bat,m}}, \quad (2.3)$$

where φ is the angle between v_{grid} and i_{inv} , and $v_{bat,m}$ is the measured battery voltage.

Secondly, it is also necessary to protect the battery from currents over its maximum allowable current, $i_{bat,max}$. According to this, $i_{bat,max}$ would be selected as the minimum value between $i_{bat,lmax}$ and $i_{bat,smax}$. However, in order to make the analysis clearer, the $i_{bat,smax}$ is considered to be more restrictive hereafter, making it possible not to account for $i_{bat,lmax}$.

This chapter proposes a technique for reducing the PV power without the need for communication cables. Since the frequency is the same at all the points of the grid, this variable can be used to transmit the information through the AC lines. When a PV power limitation is required, the battery inverter increases the frequency. Then, the PV inverters detect the frequency increase and reduce their generated power in order to set the voltage to $v_{bat,max}$ or the current to $i_{bat,max}$.

The grid frequency is $f = f_0 + \Delta f$, where f_0 is the nominal frequency (typically 50/60 Hz) and Δf is the deviation from the nominal value. Figure 2.4 shows how the frequency deviation Δf is obtained. Both frequency deviations Δf_v and Δf_i , defined in the figure, are calculated to meet the voltage and current limitations, respectively. On the one hand, the difference between the measured battery voltage, $v_{bat,m}$, and the reference battery voltage $v_{bat,max}$ is entered in the controller C_v , which calculates Δf_v , limited from 0 to Δf_{max} . On the other hand, from the difference between the measured battery current, $i_{bat,m}$, and the reference battery current $i_{bat,max}$, the controller C_i determines Δf_i , also limited from 0 to Δf_{max} . Then, the highest value Δf is selected as the most restrictive and the battery inverter imposes the frequency $f_0 + \Delta f$.

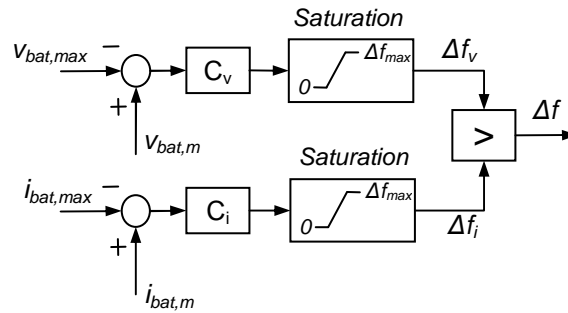


Figure 2.4. Calculation of Δf .

The battery inverter imposes a constant RMS value V_0 and a frequency $f = f_0 + \Delta f$. Thus, v_{grid} can be expressed as

$$v_{grid} = \sqrt{2}V_0 \cdot \sin(2\pi(f_0 + \Delta f) \cdot t). \quad (2.4)$$

Each PV inverter measures the frequency and obtains the measured frequency deviation Δf_m . The frequency measurement does not involve an additional cost since it is already included in PV inverters for grid synchronization and islanding detection. The microprocessor makes this measurement by detecting the period between two zero crossings of the grid voltage. The frequency is then highly filtered in order to avoid noise, transients and external interferences. If Δf_m is higher than a minimum safe value Δf_{min} , then the PV inverter stores the MPP power, to be called $P_{mpp,fr}$, and continuously reduces the power generated up to a frequency deviation Δf_{max} , where the power is zero. Since the value of $P_{mpp,fr}$ is taken instead of $S_{pv,nom}$, the PV power starts to be reduced just when $\Delta f_m > \Delta f_{min}$, resulting in a faster control. The frequency sensing and filtering H_f and the relationship between the frequency deviation and the reference PV power P_{pv}^* are shown in Fig. 2.5.

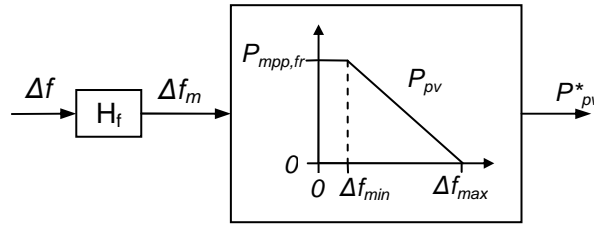


Figure 2.5. Calculation of PV power reference P_{pv}^* .

In order to carry out the PV power regulation, the first stage of the PV inverter, which is a DC/DC boost converter, is controlled as shown in Fig. 2.6. When Δf_m gets higher than Δf_{min} , the MPPT algorithm is cancelled and the PV voltage reference v_{pv}^* is frozen to its last value, $v_{mpp,fr}$. The PV voltage is then regulated by means of a PI controller [2.38]. On the other hand, the power reference P_{pv}^* is divided by the measured PV voltage $v_{pv,m}$. Then, the lowest value is selected as the current reference i_L^* for the inner current control. In so doing, when $\Delta f_m > \Delta f_{min}$, the power regulation is active and $v_{pv} > v_{mpp}$. However, there are situations in which the power reference can no longer be delivered, for example after an irradiance drop. In these cases, the PV voltage decreases and the control switches to voltage regulation, which prevents a PV voltage drop in the system. This is achieved thanks to the saturation with anti windup to I_{max} , where it is important to select a low value for I_0 in order to limit the PV voltage drop. The voltage control is maintained until Δf_m gets lower than Δf_{min} and the MPPT is then performed. More details about this technique are shown in chapter 4 and [2.39].

Normally, v_{bat} is lower than $v_{bat,max}$ and i_{bat} is lower than $i_{bat,max}$. As a result, Δf_v and Δf_i remain saturated to zero, the grid frequency is f_0 and the PV generators operate under MPPT (see Fig. 2.4 and Fig. 2.5). Then, when the battery is charged and its voltage

exceeds $v_{bat,max}$, the controller C_v increases Δf_v and the battery inverter increases the grid frequency. When $\Delta f_v > \Delta f_{min}$, the PV inverter reduces the power generated and regulates the battery voltage. Similarly, when the apparent power of the battery inverter is higher than its nominal value, $i_{bat} > i_{bat,max}$, the controller C_i increases the frequency and the PV generation is reduced, limiting the battery inverter current.

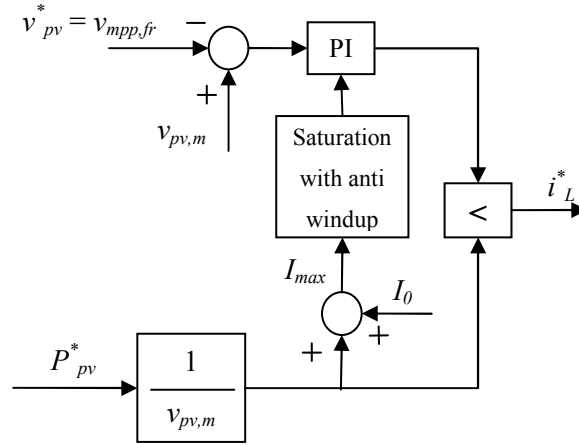


Figure 2.6. PV power regulation in the PV boost converter.

2.3.2 System modeling

The speed and stability of the battery voltage and current controls depend on the system and controller features. In order to correctly calculate the controller parameters, a model of the system is carried out in this section. The loops for the battery voltage and current regulations are shown in Fig. 2.7 and Fig. 2.8, respectively. The different blocks are presented below.

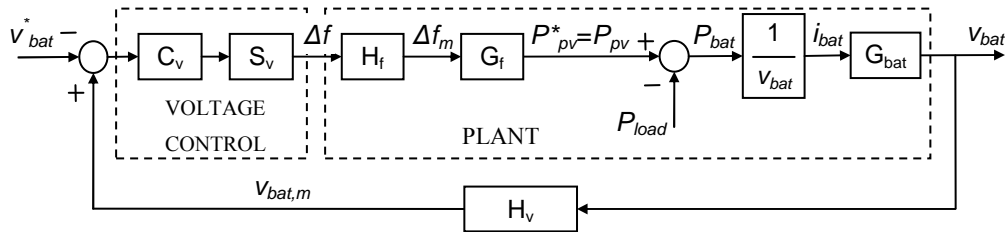


Figure 2.7. Battery voltage control loop.

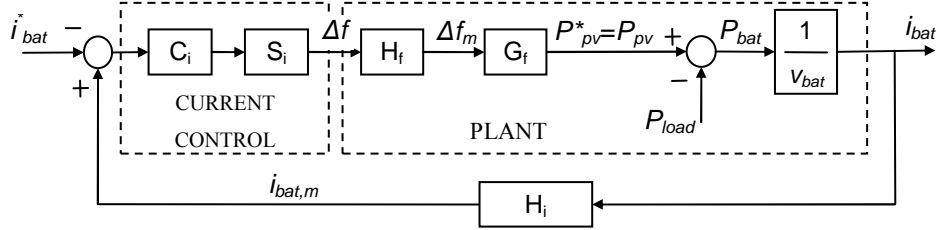


Figure 2.8. Battery current control loop.

The sensing transfer functions for the battery voltage v_{bat} , the battery current i_{bat} and frequency f , H_v , H_i and H_f , respectively, can be considered as a first order:

$$H_v(s) = \frac{1}{\tau_v \cdot s + 1} \quad (2.5)$$

$$H_i(s) = \frac{1}{\tau_i \cdot s + 1} \quad (2.6)$$

$$H_f(s) = \frac{1}{\tau_f \cdot s + 1}, \quad (2.7)$$

where τ_v , τ_i and τ_f are the time constants of the battery voltage, battery current and grid frequency sensing, respectively.

The controllers C_v and C_i are Proportional-Integral (PI) regulators with parameters K_{pv} , T_{nv} , K_{pi} , T_{ni} . Their transfer functions are

$$C_v(s) = K_{pv} \frac{T_{nv} \cdot s + 1}{T_{nv} \cdot s} \quad (2.8)$$

$$C_i(s) = K_{pi} \frac{T_{ni} \cdot s + 1}{T_{ni} \cdot s}. \quad (2.9)$$

Since the controllers used for the implementation are digital, a digital sampler S_v and S_i must be added to the model. Being T_s the sample time, they can be approximated as [2.40]

$$S_v(s) = S_i(s) = \frac{1}{1.5 \cdot T_s \cdot s + 1}. \quad (2.10)$$

The relationship between the frequency deviation Δf and the reference PV power P_{pv}^* for $\Delta f > \Delta f_{min}$ is expressed as (see Fig. 2.5)

$$P_{pv}^* = \frac{\Delta f_{\max} - \Delta f}{\Delta f_{\max} - \Delta f_{\min}} \cdot P_{mpp,fr}. \quad (2.11)$$

By means of (2.11) and small-signal modeling (small-signal variables are marked with a circumflex), the frequency deviation to power reference transfer function G_f becomes

$$G_f = \frac{\hat{P}_{pv}^*(s)}{\hat{\Delta f}(s)} = -\frac{P_{mpp,fr}}{\Delta f_{\max} - \Delta f_{\min}}. \quad (2.12)$$

The PV power regulation is carried out by means of the technique developed in [2.39] and presented in Fig. 2.6. This technique achieves high dynamics for the power regulation, being therefore possible to assume that $P_{pv} = P_{pv}^*$ for the outer loop.

Neglecting power losses, battery power P_{bat} and current i_{bat} can be obtained as

$$P_{bat} = P_{pv} - P_{load} \quad (2.13)$$

$$i_{bat} = \frac{P_{bat}}{v_{bat}}. \quad (2.14)$$

Finally, considering the small-signal analysis of the lead-acid battery Thevenin equivalent circuit model, the battery current to voltage transfer function G_{bat} can be obtained as [2.25]

$$G_{bat}(s) = \frac{\hat{v}_{bat}(s)}{\hat{i}_{bat}(s)} = \frac{(R_S + R_C) + R_S \cdot R_C C_{bat} \cdot s}{1 + R_C C_{bat} \cdot s}, \quad (2.15)$$

where R_S is the internal resistance and R_C and C_{bat} represent the first order dynamics of the battery. These parameters can be considered constant for modeling purposes since the SOC slightly changes within the operating range of the voltage regulation.

2.3.3 Controller design

The controller parameters are obtained by means of the aforementioned modeling, which is summarized in Fig. 2.7 and Fig. 2.8. In our system, the parameters are $\tau_f = 1$ s, $T_s = 100$ ms, $\Delta f_{\min} = 0.2$ Hz, $\Delta f_{\max} = 1$ Hz, $R_S = 50$ m Ω , $R_C = 12$ m Ω , $C_{bat} = 1.5$ F, $v_{bat,max} = 147$ V. Voltage and current sensing transfer functions can be neglected since $1/\tau_v = 1/\tau_i = 13500$ rad/s, which is much higher than the cutoff frequency. For both voltage and current loops, $P_{mpp,fr}$ is first taken as $S_{pv,nom}/2 = 5$ kW for the controller parameter calculation. However, $P_{mpp,fr}$ largely depends on the irradiance and can vary up to $S_{pv,nom} = 10$ kW in this case (see Table 2.1). Thus, a robustness analysis is carried out for other values of $P_{mpp,fr}$.

For the voltage control loop, the operating battery voltage is very close to $v_{bat,max}$ and thus it can be considered that $v_{bat} = v_{bat,max}$. The values of K_{pv} and T_{nv} are calculated for a cutoff frequency $f_{cv} = 0.2$ Hz and a phase margin $PM_v = 60^\circ$. However, when a variable takes a value different than that initially considered in the model, the cutoff frequency and phase margin are not equal to 0.2 Hz and 60° . For this reason, the cutoff frequency f_{cv} and the phase margin PM_v have been obtained for different values of $P_{mpp,fr}$, from 1 to 10 kW, and are represented in Fig. 2.9. It can be observed that the regulation is always stable with a minimum $PM_v = 54.4^\circ$ for $P_{mpp,fr} = 10$ kW. The figure also shows that the regulation becomes slower for low values of $P_{mpp,fr}$, which does not represent a problem since the over-voltage is less important for low $P_{mpp,fr}$.

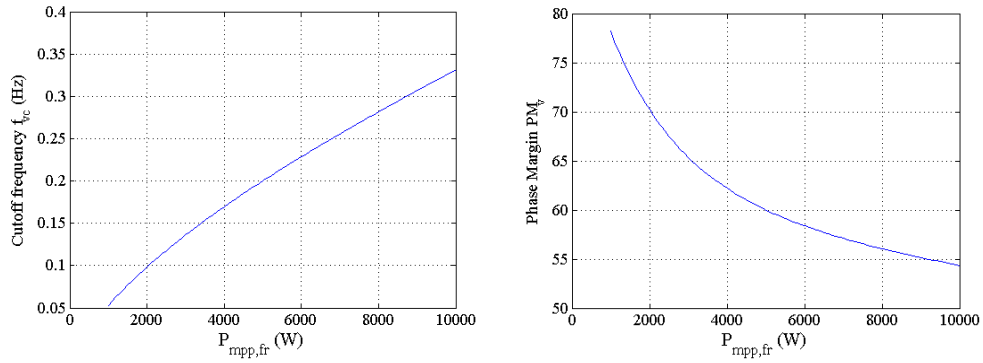


Figure 2.9. Cutoff frequency and phase margin of the voltage control for different values of $P_{mpp,fr}$.

For the current control, the operating battery voltage is around nominal voltage and thus it can be considered that $v_{bat} = v_{bat,nom}$. Current control parameters K_{pi} and T_{ni} are obtained for a cutoff frequency $f_{ci} = 0.3$ Hz and a phase margin $PM_i = 60^\circ$. Similarly to the voltage control loop, the cutoff frequency f_{ci} and phase margin PM_i are depicted in Fig. 2.10 as a function of $P_{mpp,fr}$. The regulation is also stable in this case, with a minimum $PM_v = 53.6^\circ$ for $P_{mpp,fr} = 10$ kW. The cutoff frequency increases for high $P_{mpp,fr}$, which protects the battery converter from dangerous over-currents.

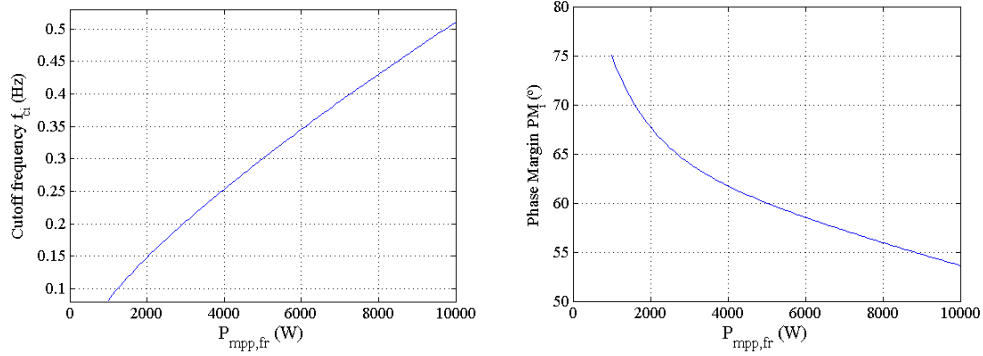


Figure 2.10. Cutoff frequency and phase margin of the current control for different values of $P_{mpp,fr}$.

2.4 PROPOSED ENERGY MANAGEMENT STRATEGY

The proposed energy management strategy consists of three modes of operation. The behavior of each element of the system in each mode of operation as well as the conditions required to switch from one mode to another are represented in Fig. 2.11.

Mode of operation	Battery inverter	PV inverters	Diesel
Mode I: Normal operation	Voltage source $\Delta f < \Delta f_{min}$	MPPT	Off
Mode II: PV power limitation	Voltage source $\Delta f > \Delta f_{min}$	Power limitation	Off
Mode III: Diesel generator	Current source $P_{bat} = \min(P_{available}, S_{bat,nom})$	MPPT	On $f \approx f_0$

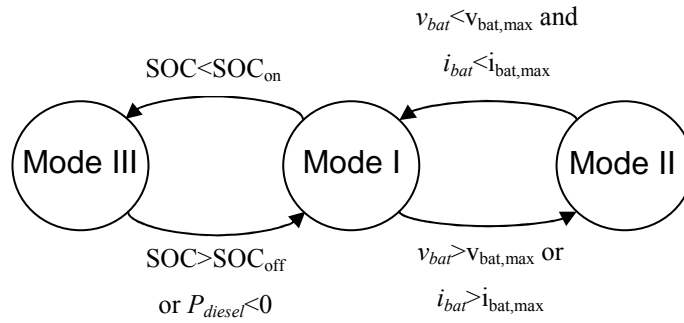


Figure 2.11. Mode of operation and change conditions.

2.4.1 Mode I: Normal operation

In mode I, the diesel generator is not connected, the PV inverters operate under MPPT and the battery inverter creates the grid. As a result, the battery absorbs or supplies the difference between generation and consumption and its SOC varies according to (2.2). The power balance becomes

$$P_{bat} = P_{pv} - P_{load} \quad (2.16)$$

$$Q_{bat} = -Q_{load} \quad (2.17)$$

In this mode, the frequency deviation Δf is zero or lower than Δf_{min} . When due to a high battery voltage or current, the regulation increases Δf to more than Δf_{min} (see Fig. 2.4 and Fig. 2.5), then the PV inverters reduce their power and the system switches to mode II. On the other hand, if the SOC falls below SOC_{on} , then the diesel generator is turned on and, after a synchronization period, the system switches to mode III.

2.4.2 Mode II: PV power limitation

In mode II, the diesel generator is not connected and the battery inverter creates the grid. The grid frequency deviation is higher than Δf_{min} and, as a result, the PV power is lower than its maximum power. The power balance is the same as for mode I. Thanks to the voltage or current control, the frequency and PV power are regulated in order to keep a constant voltage or current, equal to its reference (see Fig. 2.7 and Fig. 2.8). When the system is not able to maintain that reference, for example due to a decrease in irradiance, the regulation reduces the frequency below Δf_{min} and the system switches to mode I.

2.4.3 Mode III: Diesel generator

In mode III, the diesel generator is connected and creates the grid whereas the battery inverter operates as a current source inverter (CSI) in phase with the grid voltage. The frequency generated by the diesel generator does not need to be just equal to f_0 but must be lower than $f_0 + \Delta f_{min}$. Thus, the PV inverters operate under MPPT. The power balance is as follows:

$$P_{diesel} = P_{bat} + P_{load} - P_{pv} \quad (2.18)$$

$$Q_{diesel} = Q_{load} \quad (2.19)$$

In this mode, the battery power is a degree of freedom. In order to optimize the system operation, the battery inverter demands a power $P_{available}$, defined as the power available in the diesel generator once the PV arrays and the loads have been considered:

$$P_{available} = \sqrt{S_{diesel,nom}^2 - Q_{load}^2} + P_{pv} - P_{load} . \quad (2.20)$$

Since in this mode the battery demands $P_{available}$, it can be observed from (2.18)–(2.20) that the diesel generator operates at nominal current ($S_{diesel} = S_{diesel,nom}$). However, if $P_{available} > S_{bat,nom}$, the battery cannot absorb $P_{available}$ and demands $P_{bat} = S_{bat,nom}$. Under these circumstances, it is not possible to operate the diesel generator at its nominal current ($S_{diesel} < S_{diesel,nom}$). Then, by means of (2.18), the power balance becomes

$$P_{diesel} = S_{bat,nom} + P_{load} - P_{pv} . \quad (2.21)$$

The system will continue in mode III with $P_{bat} = \min(P_{available}, S_{bat,nom})$ until the SOC exceeds SOC_{off} , the point at which the diesel generator is disconnected and the system switches to mode I. As a result, its efficiency is maximized and its connection time is reduced, increasing its life expectancy.

However, during mode III, if the PV generation increases and the load decreases, the diesel generator could absorb power. From (2.21), $P_{diesel} < 0$ could occur for

$$P_{pv} - P_{load} > S_{bat,nom} . \quad (2.22)$$

In this situation, in order to prevent the diesel generator from absorbing power and accelerating, it is disconnected and the system therefore switches to mode I. Right away, the battery inverter absorbs a power higher than $S_{bat,nom}$ (see (2.16) and (2.22)). As a result, the battery current regulation makes the battery inverter increase the frequency and the system switches to mode II.

2.5 SIMULATION RESULTS

The proposed energy management strategy was first validated by simulation. Using the PSIM software, an accurate model was developed for all the elements of the system with distributed PV generation. The system is illustrated in Fig. 2.3, including two PV generators with their inverters. The rated power of the elements is shown in Table 2.1.

The goal of the first simulation was to validate the system operation in mode I and mode II as well as the transition from one mode to another. In these modes, the diesel generator is not connected. The results are shown in Fig. 2.12. The represented variables are $v_{bat}^* = V_{bat,abs} = 147 \text{ V}$ and $v_{bat,m}$ (graph 1); $S_{bat,nom} = 5 \text{ kVA}$ and S_{bat} (graph 2); Δf_i , Δf_v (note that $\Delta f = \max(\Delta f_v, \Delta f_i)$ was imposed by the battery inverter) and the frequency

deviation measured by the PV inverters Δf_m (graph 3); P_{bat} , P_{load} , $P_{pv} = P_{pv1} + P_{pv2}$ and $P_{mpp} = P_{mpp1} + P_{mpp2}$ (graph 4); Q_{bat} , Q_{load} and the reactive power delivered by the PV inverters $Q_{pv} = Q_{pv1} + Q_{pv2}$ (graph 5).

At the start, the nominal load is connected, consuming $P_{load} = 4$ kW and $Q_{load} = 3$ kVar, and the PV generators operate under MPPT, with $P_{pv} = P_{mpp} = 3$ kW. Since $v_{bat,m} < v_{bat}^*$ and $S_{bat} < S_{bat,nom}$, the frequency deviation Δf is saturated at 0 (see Fig. 2.4) and the system remains in mode I. Then, the irradiance increases and so does P_{mpp} . Initially, the MPPT algorithms maximize the PV power. However, when $v_{bat,m}$ exceeds v_{bat}^* , controller C_v increases Δf_v , and when S_{bat} exceeds $S_{bat,nom}$, controller C_i increases Δf_i . As a result, the battery inverter selects the highest Δf value and increases the frequency. When the frequency filtered by PV inverter Δf_m becomes higher than $\Delta f_{min} = 0.2$ Hz, then the PV power is limited following the curve shown in Fig. 2.5 and the system switches to mode II. Thanks to the battery current control (see Fig. 2.8), S_{bat} is regulated to its nominal power 5 kVA, with $P_{bat} = 4$ kW and $Q_{bat} = -3$ kVar. The transient over-current has a duration of 1.2 seconds, which does not affect the components. Then, the irradiance and thus P_{mpp} decrease. At the start, the PV power remains at $P_{pv} = 8$ kW. However, when P_{mpp} falls below 8 kW, this power cannot be delivered. The PV voltage is then controlled to the last MPP voltage $v_{mpp,fr}$ in order to avoid a voltage drop (see Fig. 2.6). In this case, the PV power is close to the MPP power since the MPP voltage had not changed significantly during the power limitation. As a result of the irradiance drop, S_{bat} falls below $S_{bat,nom}$ and controller C_i reduces Δf . When Δf_m falls below 0.2 Hz, the PV arrays change to MPPT and the system switches to mode I. Then, at second 7.8, the whole load is instantly disconnected. At this moment, the battery power changes from $P_{bat} = 2$ kW to $P_{bat} = 6$ kW, $Q_{bat} = 3$ kVar to $Q_{bat} = 0$ and $S_{bat} = 3.6$ kVA to $S_{bat} = 6$ kVA and the battery voltage changes from 146 V to 148 V. Since there is no reactive power, the voltage condition is now more restrictive and Δf_v increases to above Δf_i . When Δf_m increases to more than $\Delta f_{min} = 0.2$ Hz, the system switches to mode II and the PV power is reduced in such a way that the battery voltage is regulated to the absorption voltage. Finally, at second 12.5, the irradiance decreases and the PV voltage is initially controlled. Then, the frequency is reduced, the PV arrays change to MPPT and the system switches to mode I.

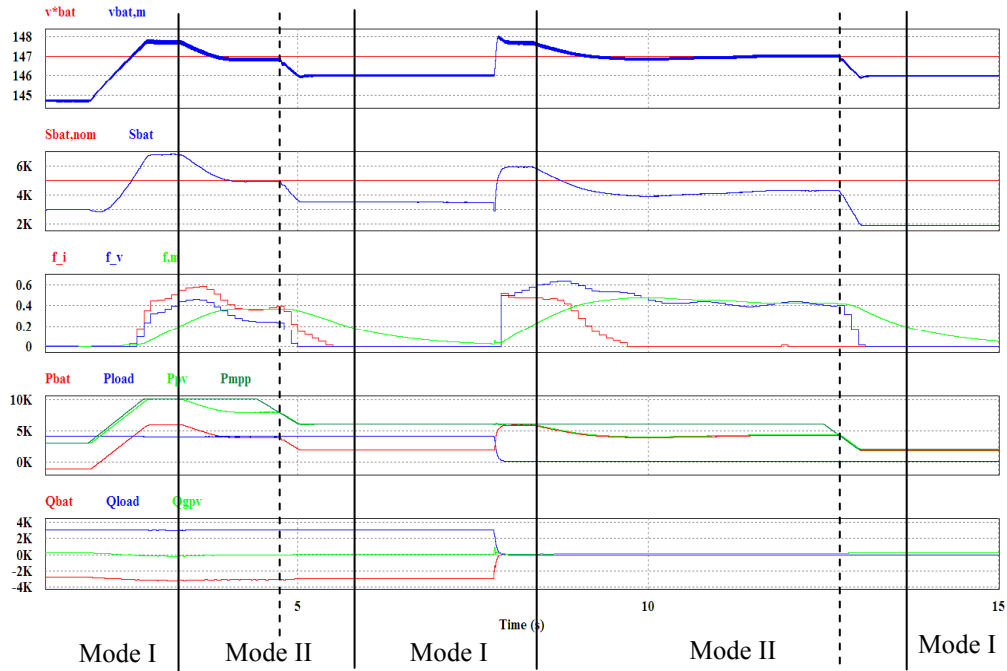


Figure 2.12. Simulation results.

The second simulation was to validate the system operation in mode III as well as the connection and disconnection of the diesel generator. The results are plotted in Fig. 2.13 for real powers P_{bat} , P_{load} , P_{pv} and P_{diesel} (graph 1), reactive powers Q_{bat} , Q_{load} , Q_{pv} and Q_{diesel} (graph 2), $S_{bat,nom} = S_{diesel,nom} = 5$ kVA, S_{bat} and S_{diesel} (graph 3).

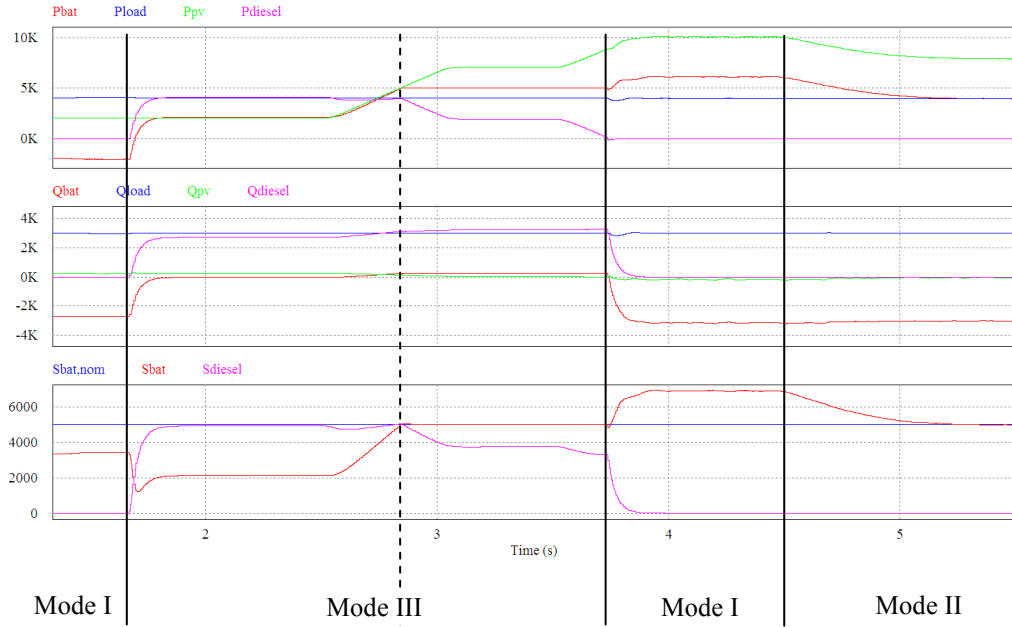


Figure 2.13. Simulation results.

The system is initially in mode I. The nominal load is connected and consumes $P_{load} = 4$ kW and $Q_{load} = 3$ kVAr while the PV inverters function under MPPT with $P_{pv} = 2$ kW. The diesel generator is not connected and the battery inverter therefore provides the difference between generation and consumption, that is $P_{bat} = -2$ kW and $Q_{bat} = -3$ kVAr. After some time in this mode, the battery SOC falls below SOC_{on} . As a result, the diesel generator is turned on, the battery inverter voltage is synchronized and then, at about second 1.7, the diesel generator is connected, switching to mode III. From that moment onwards, the battery inverter functions as a current source demanding power $P_{available}$ (see (2.20)), which causes the diesel generator to operate at nominal power $S_{diesel} = S_{diesel,nom} = 5$ kVA, with $P_{diesel} = 4$ kW and $Q_{diesel} = 3$ kVAr. Then, at second 2.5, the irradiance increases, as does the PV power generation up to $P_{pv} = 7$ kW. During this PV power increase, at first S_{diesel} remains equal to $S_{diesel,nom}$ thanks to a higher P_{bat} demand. However, when S_{bat} reaches $S_{bat,nom}$ at second 2.8, the battery inverter is unable to absorb more power. As a result, P_{diesel} and S_{diesel} decrease until the irradiance stops rising at second 3, leading to $P_{diesel} = 2$ kW and $S_{diesel} = 3.7$ kVA. Then, at second 3.5, the irradiance increases again and so does the PV power generation up to $P_{pv} = 10$ kW. At the beginning, since the battery inverter cannot demand more power, P_{diesel} continues decreasing. At second 3.7, P_{diesel} is very low and, in order to prevent the diesel generator from absorbing power, it is disconnected. The system therefore switches to mode I: the battery inverter controls the grid voltage and the PV inverters remains under MPPT. Consequently, at the

end of the irradiance increase, the battery inverter is overcharged, with $P_{bat} = 6$ kW and $S_{bat} = 6.8$ kVA. This fact causes controller C_i to increase the frequency and, at second 4.5, Δf_m becomes higher than $\Delta f_{min} = 0.2$ Hz, making the system switch to mode II. As a result, the PV power is continuously reduced and S_{bat} is controlled to $S_{bat,nom}$.

2.6 EXPERIMENTAL RESULTS

The proposed energy management strategy was experimentally validated for the system represented in Fig. 2.3 (for two PV generators with their corresponding inverters). The elements used for the experimental setup are shown in Fig. 2.14, and their rated power is indicated in Table 2.1. The PV emulators (only one is shown) reproduce the behavior of two 5 kW PV arrays and make it possible to change the irradiance as required. The battery and PV inverters are commercial inverters whose configuration has been modified in order to implement the proposed strategy. The battery inverter was programmed to increase the grid frequency according to the strategy developed in section 2.3 and also to manage the diesel generator connection and operation following the strategy presented in section 2.4. The PV inverters were programmed to reduce the power generated as a function of the grid frequency according to Fig. 2.5. The load bank made it possible to select the desired power and power factor. The experimental values were taken from the battery and PV inverter microprocessors. The irradiance variations represent quick cloud passages and account for the size of the PV generator. The irradiance variation was not simultaneous for both PV generators, thus modeling their different locations.

In the first test, the PV power limitation for over-current protection was verified. The test conditions were similar to those of the first part of the first simulation (see section 2.5, switch from mode I to mode II and back to mode I). The experimental results were taken from the microprocessor and are shown in Fig. 2.15. Variables $S_{bat,nom} = 5$ kVA and S_{bat} are represented in the first graph; grid frequency f_{bat} and grid frequency filtered by the PV inverter, f_{pv1} and f_{pv2} , in the second graph; and P_{bat} , P_{pv1} and P_{pv2} , in the third graph. At the start, the system is operating in mode I with the PV inverters under MPPT. However, after an irradiance increase, the battery inverter absorbs an over-current. As a result, the battery inverter increases the grid frequency, which leads to a PV power reduction when $f_{pv1} = f_{pv2} > 50.2$ Hz. This makes it possible to control the battery apparent power to its rated value. Then, due to a fall in irradiance, it is not possible to maintain $S_{bat,nom}$. Thus, according to the control of Fig. 2.4, the frequency falls below 50.2 Hz, the system switches to mode I and the PV inverters once again operate under MPPT. With this test, it can be observed that the current control is fast enough to protect

the battery inverter. Indeed, after a quick irradiance increase, the transient over-current lasts for about one second, which does not pose an overheating hazard for the inverter.



Figure 2.14. PV emulator, battery bank, load bank and diesel generator used for the experimental setup.

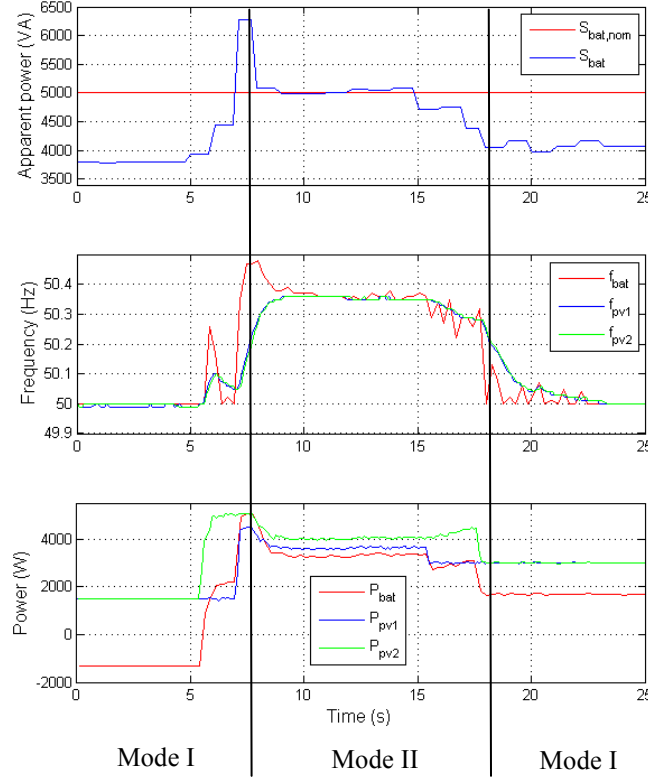


Figure 2.15. Experimental results for the over-current protection.

In the second test, the battery voltage control was verified. The test conditions were similar to those of the second part of the first simulation (see section 2.5, switch from mode I to mode II and back to mode I). The experimental results are shown in Fig. 2.16. The first graph shows $v_{bat}^* = 147$ V and v_{bat} whilst the other graphs represent the same variables as for the previous test. At the start, the system is operating in mode I and the PV arrays are delivering the MPP power. Then, a load with $P_{load} = 4.3$ kW and $Q_{load} = 3.4$ kVAR is disconnected. As a result, the battery absorbs a higher current and its voltage increases over absorption voltage v_{bat}^* . According to the control of Fig. 2.4, the battery inverter increases the frequency. This leads to a PV power reduction, making it possible to control the battery voltage to its reference value. Some seconds later there is an irradiance drop, the battery voltage and therefore the frequency decrease, the system switches to mode I and the PV inverters change to MPPT. In this test, a load with $S_{load} = 5.5$ kVA, which is even higher than $S_{bat,nom}$, was instantly disconnected. For such a critical situation, it is shown how the voltage control performs correctly, preventing the battery from overcharging.

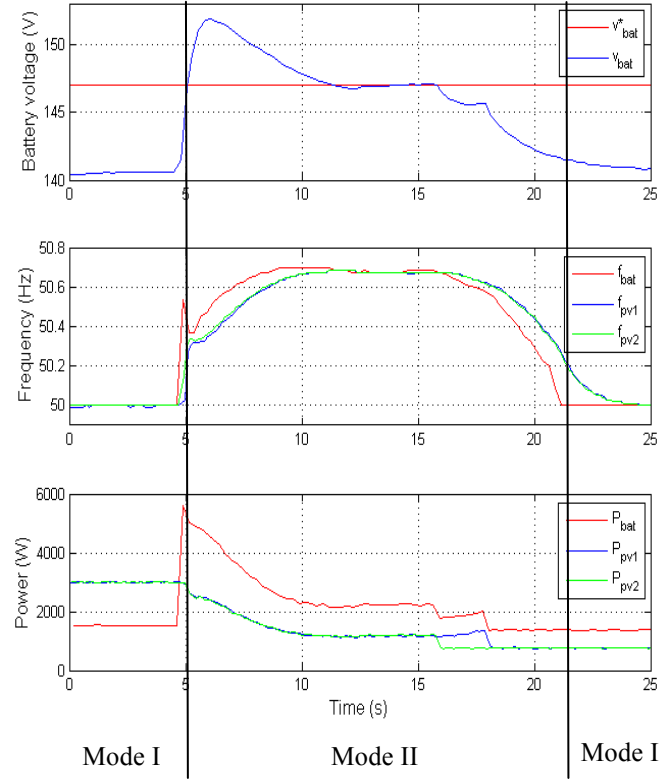


Figure 2.16. Experimental results for the overcharge protection.

In the third test, the diesel generator management was verified. The test conditions were similar to those of the second simulation (see section 2.5). The experimental results are shown in Fig. 2.17. Powers P_{bat} , P_{pv1} , P_{pv2} and P_{diesel} are shown in the first graph, and the apparent powers $S_{bat,nom} = S_{diesel,nom}$, S_{bat} and S_{diesel} are plotted in the second graph. Initially, the system is operating in mode I. Since consumption is higher than generation, the battery SOC is decreasing. When the battery SOC falls below SOC_{on} , the diesel generator is connected and the system switches to mode III. Then, the battery inverter demands $P_{available}$ (see (2.20)), which makes the diesel generator operate at its rated power $S_{diesel} = 5$ kVA. Some seconds later, the irradiance increases. As a result, $P_{available}$ becomes too high and the battery inverter demands its rated power, leading to a reduction in the diesel apparent power. Then, the irradiance increases again. Since the battery inverter is unable to absorb more power, the diesel generator power becomes negative and is disconnected, leading to mode I. This mode is not shown in the figure because it is very short. The diesel disconnection leads to an over-current in the battery inverter, which therefore increases the frequency and the system switches to mode II. This results in a PV power reduction and a limitation of the battery inverter current.

With this test, it can be observed that the diesel generator management strategy makes it operate at its rated power for as long as possible and protects it from absorbing power. This optimizes the diesel generator efficiency and duty cycle.

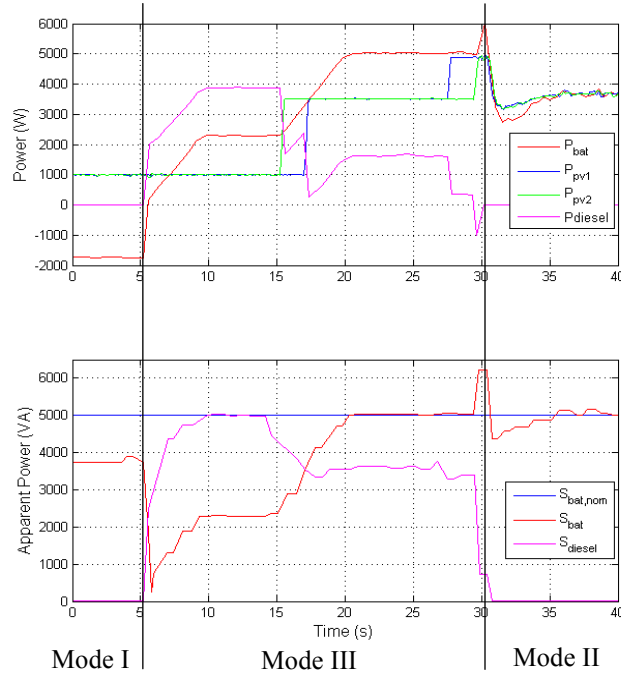


Figure 2.17. Experimental results for the diesel generator management.

2.7 CONCLUSIONS

This chapter develops an energy management strategy for a stand-alone system in which the battery and the diesel generator are centralized and generate the grid whilst the loads and the PV generators are distributed and connected to the grid.

During normal operation, the diesel generator is not connected and the battery absorbs the difference between generation and consumption. Whenever the battery is fully charged or its power exceeds its nominal value, the PV power has to be limited. In order to transmit this information, the battery inverter increases the frequency, which is detected by the PV generators. As a result, the PV power is continuously reduced in order to control the battery voltage or battery current to the maximum value. The use of frequency means that communication cables are unnecessary, making the system simpler, cheaper and more reliable. The control is fast and stable enough for any situation, preventing the battery from overcharge and over-current, improving its

expected life and making it possible to install a PV power higher than the battery inverter rated power. On the other hand, when the battery SOC is low, the diesel generator is connected. Here, the strategy makes the diesel generator operate at its rated power as far as possible, optimizing its efficiency and expected life.

Furthermore, this energy management strategy makes it possible to supply the loads in case of battery failure. Whilst the strategy is based on the battery inverter, the battery is also the most vulnerable element. If the battery is broken down, the diesel generator is connected and generates the grid whereas the PV inverters operate under MPPT. In this mode, if the PV power becomes higher than the load power, the diesel generator absorbs power. As a result, the grid frequency increases and the PV power is reduced, which ensures a correct system operation.

Simulation and experimental results were obtained for a system with a 10 kW PV generation, a 5 kVA battery inverter, a 5 kVA diesel generator and a 5 kVA load, validating the energy management strategy for the most critical situations.

2.8 REFERENCES

- [2.1] D. P. Kaundinya, P. Balachandra, N. H. Ravindranath, "Grid-connected versus stand-alone energy systems for decentralized power—A review of literature," *Renewable and Sustainable Energy Reviews*, vol. 13, pp. 2041–2050, 2009.
- [2.2] K. Bandara, T. Sweet, J. Ekanayake, "Photovoltaic applications for off-grid electrification using novel multi-level technology with energy storage," *Renewable Energy*, vol. 37, pp. 82–88, 2012.
- [2.3] S. K. Pandey, S. R. Mohanty, N. Kishor, "A literature survey on load-frequency control for conventional and distribution generation power systems," *Renewable and Sustainable Energy Reviews*, vol. 25, pp. 318–334, 2013.
- [2.4] H. Shayeghi, H. A. Shayanfar, A. Jalili, "Load frequency control strategies: A state-of-the-art survey for the researcher," *Energy Conversion and Management*, vol. 50, pp. 334–353, 2009.
- [2.5] I. Ngamroo, Y. Mitani, K. Tsuji, "Application of SMES coordinated with solid-state phase shifter to load frequency control," *IEEE Transactions on Applied Superconductivity*, vol. 9, no. 2, pp. 322–325, 1999.
- [2.6] I. Ngamroo, Y. Mitani, K. Tsuji, "Robust load frequency control by solid-state phase shifter based on H_∞ control design," in *IEEE Power Engineering Society 1999 Winter Meeting*, pp. 725–730, New York (USA), 1999.
- [2.7] M. Aldeen, J. F. Marsh, "Decentralized proportional-plus-integral control design method for interconnected power systems," *Proceedings of Institute of Electrical Engineering*, vol. 138, no. 4, pp. 263–274, 1991.

- [2.8] H. Xin, Y. Liu, Z. Wang, D. Gan, T. Yang, "A new frequency regulation strategy for photovoltaic systems without energy storage," *IEEE Transactions on Sustainable Energy*, vol. 4, no. 4, pp. 985–993, 2013.
- [2.9] A. Hoke, D. Maksimovic, "Active power control of photovoltaic power systems," in *1st IEEE Conference on Technologies for Sustainability (SusTech)*, pp. 70–77, Portland (USA), 2013.
- [2.10] L. D. Watson, J. W. Kimball, "Frequency regulation of a microgrid using solar power," in *26th IEEE Applied Power Electronics Conference and Exposition (APEC)*, pp. 321–326, Fort Worth (USA), 2011.
- [2.11] M. Datta, T. Senjyu, A. Yona, T. Funabashi, C. Kim, "A frequency-control approach by photovoltaic generator in a PV-diesel hybrid power system," *IEEE Transactions on Energy Conversion*, vol. 26, no. 2, pp. 559–571, 2011.
- [2.12] R. Langella, G. Margiotta, D. Proto, A. Testa, "Hybrid PV-diesel stand-alone system sizing for remote microgrids," in *2012 IEEE Energy Conference and Exhibition (ENERGYCON)*, pp. 475–482, Florence (Italy), 2012.
- [2.13] P. Bajpai, V. Dash, "Hybrid renewable energy systems for power generation in stand-alone applications: A review," *Renewable and Sustainable Energy*, vol. 16, pp. 2926–2939, 2012.
- [2.14] E. S. Hrayshat, "Techno-economic analysis of autonomous hybrid photovoltaic-diesel-battery system," *Energy for Sustainable Development*, vol. 13, pp. 143–150, 2009.
- [2.15] S. Rehman, L.M. Al-Hadhrami, "Study of a solar PV-diesel-battery hybrid power system for remotely located population near Rafha, Saudi Arabia," *Energy*, vol. 35, pp. 4986–4995, 2010.
- [2.16] J. K. Kaldellis, "An integrated model for performance simulation of hybrid wind-diesel systems," *Renewable Energy*, vol. 32, pp. 1544–1564, 2007.
- [2.17] A. A. Setiawan, Y. Zhao, C. V. Nayar, "Design, economic analysis and environmental considerations of mini-grid hybrid power system with reverse osmosis desalination plant for remote areas," *Renewable Energy*, vol. 34, pp. 374–383, 2009.
- [2.18] J. H. Jeon, J. Y. Kim, S. K. Kim, J. M. Kim, "Unified compensation control of a hybrid storage system for enhancing power quality and operation efficiency in a diesel and wind-turbine based stand-alone microgrid," in *3rd IEEE Symposium on Power Electronics for Distributed Generation Systems (PEDG)*, pp. 264–270, Aalborg (Denmark), 2012.
- [2.19] L. A. S. Ribeiro, O. R. Saavedra, S. L. Lima, J. G. Matos, G. Bonan, "Making isolated renewable energy systems more reliable," *Renewable Energy*, vol. 45, pp. 221–231, 2012.
- [2.20] H. Ghoddami, M. B. Delghavi, A. Yazdani, "An integrated wind-photovoltaic-battery system with reduced power-electronic interface and fast control for grid-tied and off-grid applications," *Renewable Energy*, vol. 45, pp. 128–137, 2012.
- [2.21] A. K. Daud, M. S. Ismail, "Design of isolated hybrid systems minimizing costs and pollutant emissions," *Renewable Energy*, vol. 44, pp. 215–224, 2012.

- [2.22] F. Valenciaga, P. F. Puleston, "Supervisor control for a stand-alone hybrid generation system using wind and photovoltaic energy," *IEEE Transactions on Energy Conversion*, vol. 20, no. 2, pp. 398–405, 2005.
- [2.23] Z. Liao, X. Ruan, "A novel power management control strategy for stand-alone photovoltaic power system," in *IEEE 6th Power Electronics and Motion Conference (IPEMC)*, pp. 445–449, Wuhan (China), 2009.
- [2.24] D. B. Cândido, L. Michels, H. L. Hey, "Integrated control of a stand-alone photovoltaic system based on decentralized DC-DC converters," in *2010 IEEE Symposium on Industrial Electronics (ISIE)*, pp. 213–218, Bari (Italy), 2010.
- [2.25] S. G. Tesfahunegn, P. J. S. Vie, O. Ulleberg, T. M. Undeland, "A simplified battery charge controller for safety and increased utilization in stand-alone PV applications," in *2011 Conference on Clean Electric Power (ICCEP)*, pp. 137–144, Ischia (Italy), 2011.
- [2.26] B. S. Manju, R. Ramaprabha, B. L. Mathur, "Modelling and control of standalone solar photovoltaic charging system," in *2011 Conference on Emerging Trends in Electrical and Computer Technology (ICETECT)*, pp. 78–81, Tamil Nadu (India), 2011.
- [2.27] N. Eghtedarpour, E. Farjah, "Control strategy for distributed integration of photovoltaic and energy storage systems in DC micro-grids," *Renewable Energy*, vol. 45, pp. 96–110, 2012.
- [2.28] S. Jiang, W. Wang, H. Jin, D. Xu, "Power management strategy for microgrid with energy storage system," in *37th Annual Conference on IEEE Industrial Electronics Society (IECON)*, pp. 1524–1529, Melbourne (Australia), 2011.
- [2.29] K. O. Oureilidis, C. S. Demoulias, "Microgrid wireless energy management with energy storage system," in *47th Universities Power Engineering Conference (UPEC)*, pp. 1–6, London (UK), 2012.
- [2.30] A. Tuladhar, "Power management of an off-grid PV inverter system with generators and battery banks," in *2011 IEEE Power & Energy Society General Meeting*, pp. 1–5, San Diego (USA), 2011.
- [2.31] J. M. Guerrero, J. C. Vasquez, J. Matas, L. G. Vicuña, M. Castilla, "Hierarchical control of droop-controlled ac and dc microgrids—A general approach toward standardization," *IEEE Transactions on Industrial Electronics*, vol. 58, no. 1, pp. 158–172, 2011.
- [2.32] S. Kuszmaul, S. Gonzalez, A. Ellis, E. Serban, "Commanding inverters to establish coordinated μ grid functionality at Sandia National Laboratories," in *34th IEEE Photovoltaic Specialists Conference (PVSC)*, pp. 1513–1518, Philadelphia (USA), 2009.
- [2.33] A. Mohd, E. Ortjohann, D. Morton, O. Omari, "Review of control techniques for inverters parallel operation," *Electric Power Systems Research*, vol. 80, no. 12, pp. 1477–1487, 2010.
- [2.34] S. Sanchez, M. Molinas, M. Degano, P. Zanchetta, "Stability evaluation of a DC micro-grid and future interconnection to an AC system," *Renewable Energy*, vol. 62, pp. 649–656, 2014.

- [2.35] S. Armstrong, M. E. Glavin, W. G. Hurley, "Comparison of battery charging algorithms for stand alone photovoltaic systems," in *IEEE Power Electronics Specialists Conference (PESC)*, pp. 1469–1475, Rhodes (Greece), 2008.
- [2.36] B. J. Huang, P. C. Hsu, M. S. Wu, P. Y. Ho, "System dynamic model and charging control of lead-acid battery for stand-alone solar PV system," *Solar Energy*, vol. 84, pp. 822–830, 2010.
- [2.37] X. Li, J. Li, L. Xu, M. Ouyang, X. Han, L. Lu, C. Lin, "Online management of lithium-ion battery based on time-triggered controller area network for fuel-cell hybrid vehicle applications," *Journal of Power Sources*, vol. 195, pp. 3338–3343, 2010.
- [2.38] A. Urtasun, P. Sanchis, L. Marroyo, "Adaptive voltage control of the dc/dc boost stage in PV converters with small input capacitor," *IEEE Transactions on Power Electronics*, vol. 28, no. 11, pp. 5038–5048, 2013.
- [2.39] A. Urtasun, P. Sanchis, L. Marroyo, "Limiting the power generated by a photovoltaic system," in *10th Multi-Conference on Systems, Signals & Devices (SSD)*, pp. 1–6, Hammamet (Tunisia), 2013.
- [2.40] K. Jalili, S. Bernet, "Design of LCL filters of active-front-end two-level voltage-source converters," *IEEE Transactions on Industrial Electronics*, vol. 56, no. 5, pp. 1674–1689, 2009.

CHAPTER 3

AC MICROGRIDS WITH DISTRIBUTED STORAGE

ABSTRACT

This chapter presents the frequency and voltage regulation together with the energy management of an islanded ac microgrid with distributed energy storage and power generation. The use of the frequency as a communication signal prevents the need for communication cables, rendering the system more cost-effective and reliable.

For the frequency and voltage regulation, the droop method is employed. This chapter first proposes a simple linear model which makes it possible to discern the different dynamic properties and to readily design the control parameters. The effect of not considering the load is also evaluated. Regarding the AC voltage regulation, an interesting approach is to control the RMS voltage instead of its instantaneous value. This chapter also proposes a harmonic compensation to cope with the problems of the RMS control, making it possible to reduce the voltage THD and equally share the current harmonics among the inverters.

The energy management is then presented. When the battery SOC's are within limits, the proposed SOC-based droop control makes it possible to maintain the same SOC level for all batteries and, at the same time, optimize the power response performance. On the other hand, when the batteries are fully charged/discharged, the strategy modifies the conventional droop method so that the power becomes unbalanced, allowing for the regulation of one or more battery voltages or currents, as required. When needed, the frequency is also modified in order to reduce the generation, regulate the non-critical loads or make an emergency stop.

Simulation and experimental validation is provided throughout the chapter.

3.1 INTRODUCTION

3.1.1 Frequency and voltage regulation

As discussed in chapter 1, distributed energy storage and generation present attractive features for islanded AC microgrids [3.1]–[3.4]. A frequently adopted and sustainable solution includes photovoltaic (PV) and wind generation with battery energy storage [3.5]–[3.8]. This configuration is shown in Fig. 3.1, where the wind turbines are connected to the AC grid through AC/AC converters whilst the batteries and PV generators are connected using DC/AC inverters [3.9], [3.10].

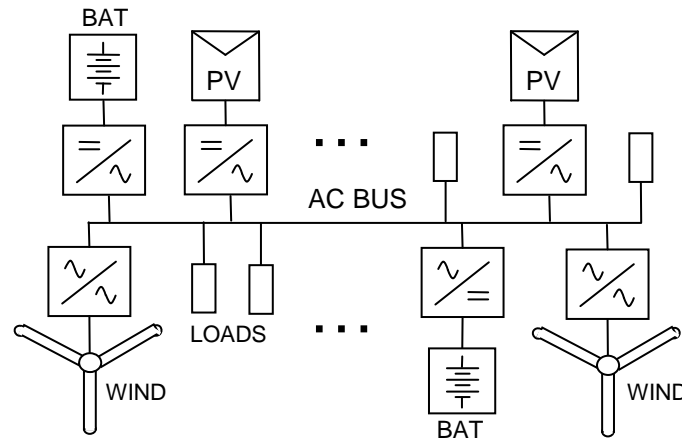


Figure 3.1. Stand-alone hybrid system with distributed energy storage and generation.

There are several techniques to implement the frequency and voltage regulation in this system [3.11]. On one hand, there is a central control or master-slave approach where a supervisor sets in real time the operating point of each element [3.12]. The drawback of this approach is that it requires a fast communication system between master and microgrid elements [3.13], [3.14]. Distributed control is another possible technique. In this case, the battery inverters operate as Voltage Source Inverters (VSI) using droop methods and regulate the grid frequency and voltage. This makes the inverters independent and avoids the need for communication between them, thereby reducing costs and improving reliability [3.15]–[3.17]. For their part, the photovoltaic/wind converters harvest the solar/wind energy and operate as Current Source Inverters (CSI) injecting power into the grid [3.18], [3.19].

For inverter-based microgrids with distributed control, frequency and voltage regulation are based on droop methods because only local measurements are required.

In the conventional droop control, each inverter measures its real and reactive powers, and then a frequency and voltage droop is applied following the real power–frequency (P – f) and reactive power–voltage (Q – V) droops. As a result, the power is equally shared among the inverters.

Small-signal analysis is generally used for modeling the voltage and frequency regulation in droop-based microgrids. Even though the control can be decoupled into P – f and Q – V droops for purely inductive output impedances, the real and reactive power responses are actually coupled. For this reason, their modeling is jointly carried out in the literature [3.15], [3.20]–[3.24]. However, this modeling is complicated and hides the different dynamic properties of the real and reactive power responses. In section 3.3, an approximate model where the real and reactive power dynamics are clearly distinguished is proposed. The approximation makes it possible to derive a linear model, thereby simplifying the analysis and preventing the small-signal modeling. The error of the proposed model is shown to be small by comparison with an accurate small-signal model.

In the previous models, the load effect is not considered. However, the load can also have an effect on the stability. While some authors take the load into account for the system modeling [3.15], [3.20], [3.21], others consider the stiff AC grid approximation [3.22]–[3.24]. The error of not considering the load is also evaluated in section 3.3 for a low-voltage AC grid by means of the linear and small-signal models. It is shown that the load can be neglected in this case, which validates the accuracy of the proposed model.

With regard to the AC grid voltage regulation, an interesting approach consists of regulating the RMS voltage instead of the instantaneous voltage [3.25], [3.26]. Since the voltage regulation is designed in DC, a simple PI controller can provide accurate voltage tracking [3.25]. In addition, the inner current loop can be avoided [3.26], [3.27]. Although a current protection must be added, the system implementation becomes much simpler. What is more, since no instantaneous voltage measurement is required by the control, low Total Harmonic Distortion (THD) is provided when feeding linear loads [3.25], [3.27]. However, this approach also has drawbacks. Due to the RMS controller, transients for load connections are longer [3.25], [3.26]. Besides, when feeding non-linear loads, the voltage THD increases and current harmonics are not equally shared by the inverters [3.25].

In this chapter, section 3.5 proposes to solve the problems of the RMS voltage control for single-phase parallel-connected inverters when feeding non-linear loads. It will be shown how the implementation of a harmonic compensation reduces the voltage THD while, at the same time, makes it possible to equally share the current harmonics among the different inverters.

3.1.2 Energy management

Although conventional droop methods achieve power sharing, they are unable to perform energy management by themselves. For this reason, local droop control is usually extended by a global control through low bandwidth communication [3.19], [3.28]. In order to avoid completely any kind of communication cables, a new energy management approach is proposed in this chapter.

The system presented in Fig.3.1 requires high-quality energy management for optimal operation. In normal operation, the Renewable Energy Sources (RES) operate under Maximum Power Point Tracking (MPPT) and the batteries offset the difference between consumption and generation. In this situation, the battery inverters operate as Voltage Source Inverters (VSI) controlling the grid frequency and voltage while the photovoltaic/wind converters harvest the solar/wind energy and operate as Current Source Inverters (CSI) injecting power into the grid. In this operating mode, the State-of-Charge (SOC) of the Energy Storage Systems (ESS) changes according to the difference between consumption and generation.

Although it is desirable that all battery SOC's evolve at the same time, the droop method is unable to achieve this objective by itself. When using conventional droop methods, the P - f curve slope is normally set according to the inverter rated power, in order to share the real powers in proportion to their ratings [3.29], [3.30]. Although the ratios between the battery capacity and the inverter rated power (C/S_{bat}) should ideally be the same for all battery inverters to ensure that all battery SOC's change simultaneously, in real applications this is not so. The initial C/S_{bat} ratio will never be exactly the same for all battery inverters due to manufacturing variation or inadequate system sizing. Moreover, the battery aging will lead to a capacity reduction which will be more pronounced in some battery banks than in others. The initial SOC can also vary considerably from one battery to another. These situations cause the batteries to operate with different SOC's leading to less than optimal operation.

In [3.31], a fuzzy control is used for the storage energy control of electric-double-layer capacitors in dc microgrids. The fuzzy control changes the dc voltage reference to balance the stored energy. However, this method is not based on local measurements since the fuzzy control input requires information about the energy stored in other electric-double-layer capacitors.

In order to maintain the same SOC for all energy storage units without the use of communication circuits, the P - f curve (V_{dc} - I_{dc} curve for DC microgrids) must be changed as a function of the SOC of each storage unit. Some authors have proposed changing the slope of this curve [3.19], [3.20], [3.23], [3.32], [3.33]. In [3.32], it can be observed how the SOC of two batteries in an AC microgrid tends to reach the same value after a

different initial SOC. However, the authors fail to analyze what occurs after that initial transient when each battery inverter has a different C/S_{bat} ratio. Furthermore, changing the P - f curve slope has an effect on the stability and dynamic performance of the power response [3.21], [3.25], [3.34], [3.35]. This fact prevents the optimization of the power response and results in operating point-dependent damping and dynamics.

In this chapter, section 3.6 proposes a new SOC-based droop control for islanded AC microgrids with distributed energy storage whereby the P - f curve is shifted either upwards or downwards in line with the battery SOC. As a result, the battery with a higher SOC will either deliver more power or absorb less power until all the batteries reach the same SOC, with no need for communication cables. Thanks to this curve shifting, the time constant for the battery SOC convergence can be set independently of the power response dynamics, unlike the slope changing method. The P - f curve slope is kept constant, making it possible to optimize the power response performance and achieve constant damping and dynamics. Furthermore, this method limits the SOC imbalance as required for batteries with different C/S_{bat} ratios, without affecting the system stability.

The control discussed so far in this section corresponds to the energy management during normal operation, i.e. while the battery SOC's are within limits. However, when the batteries are fully charged and generation is higher than consumption, the RES power has to be limited in order to protect the batteries from overcharging [3.36]. Similarly, if the charging current exceeds its maximum value, then the RES power also has to be reduced in order to provide over-current protection. On the contrary, when the batteries are fully discharged and consumption is higher than generation or if the discharging current exceeds its maximum value, the loads have to be disconnected or the system has to be shutdown in order to prevent serious damage to the batteries.

Some authors have implemented this energy management strategy for islanded AC microgrids with only one battery bank. The most complicated part of the control consists in regulating the battery overcharge voltage or the maximum charging current yet with no communication cables between the distributed inverters. Whilst in some works a central supervisor is required for the energy management [3.37], [3.38], other authors completely avoid the communication system by using the grid frequency as a communication signal [3.18], [3.39], [3.40]. In [3.40], an integral term is added to the conventional droop method in order to increase or decrease the frequency. The frequency is used by the RES and the battery to switch from voltage control mode to power control mode and vice versa, making it possible to control the battery power when required in order to regulate the SOC. In [3.18] and [3.39], the battery inverter always operates as VSC and the RES as CSC. When the battery is fully charged or the battery current exceeds its maximum value, then the battery inverter increases the

frequency as dictated by the PI controller output. This message is detected by the RES inverters, which continuously reduce the power generated in order to regulate the battery voltage or current, preventing an overcharge or over-current.

An energy management strategy with multiple battery banks has been vaguely analyzed in the literature [3.20]. However, the installation of two or more energy-storage units is recommended for system redundancy [3.31]. It may also be required when there is a consumption increase subsequent to installation [3.20]. The management of a number of batteries becomes more problematic because, in real applications, their SOC does not evolve simultaneously. As a result, the energy management strategy must also include some additional controls. Specifically, the voltage of the most charged battery must first be controlled, followed by the voltage of the other batteries and finally the voltage of all batteries, all this in an inverter-based system with extremely variable generation and consumption. In [3.20], a supervisory control for the management of multiple batteries is proposed. Whenever the battery voltages reach their maximum values, the battery inverters switch to CSC operation whilst the RES inverters switch to VSC and generate the DC grid, providing the required power to supply the batteries and the loads. The control also alternates the charging of the various batteries. However, this energy management is possible thanks to the central supervisor. Furthermore, battery over-current protection is not implemented.

In this chapter, section 3.7 proposes an energy management strategy for a multiple-battery system during high and low SOC operation with no need for communication cables between inverters or with a central supervisor. Whenever the batteries are fully charged or are absorbing too much current, then the grid frequency is increased. This is measured by the RES inverters, which reduce their power in order to control the battery voltages or currents. Furthermore, the control coordinates the various batteries. If some batteries have not reached their maximum voltage or current, then the surplus power is transferred from the charged batteries to the non-charged batteries without limiting the RES power, making the most of the solar/wind energy. This chapter also addresses protection during battery discharging. As in the case of battery charging, when the batteries are either fully discharged or delivering too much current, the grid frequency is decreased. The power is first transferred from some batteries to the others. However, if all the batteries have reached the minimum voltage or maximum discharging current, then the frequency reduction is detected by the non-critical loads, which are either regulated or disconnected. If this is not possible, then the system is shutdown in order to prevent irreversible damage to the batteries.

3.2 POWER CALCULATION

3.2.1 Product and low-pass filter

Since the real and reactive powers are required as inputs for the droop control, an accurate and fast calculation is desirable. Real and reactive powers can be obtained from the grid voltage and the inverter current by means of different methods. The simplest one is presented here and is named the Product and Low-Pass Filter (P&LPF) [3.41], [3.42]. The grid voltage and inverter current can be expressed as

$$v(t) = \sqrt{2}V \cdot \sin(\omega t) \quad (3.1)$$

$$i(t) = I_{dc} + \sqrt{2}I_1 \cdot \sin(\omega t - \varphi_1) + \sqrt{2}I_3 \cdot \sin(3\omega t - \varphi_3) + \sqrt{2}I_5 \cdot \sin(5\omega t - \varphi_5) + \dots, \quad (3.2)$$

where ω is the fundamental angular frequency, V is the RMS grid voltage, I_{dc} is the DC current, $I_1, I_3, I_5 \dots$ are the RMS harmonic currents, and $\varphi_1, \varphi_3, \varphi_5 \dots$ are the angles between the grid voltage and the harmonic currents. It is assumed that the inverters are feeding typical non-linear loads, and the voltage harmonics are neglected for simplifying derivation. The DC current can be due to a non-linear load such a half-wave rectifier or can represent a low-frequency transient.

The instantaneous power can be obtained as the product of grid voltage and inverter current as follows:

$$p(t) = v(t) \cdot i(t) = V \cdot I_1 \cdot \cos \varphi_1 + \sqrt{2}V \cdot I_{dc} \cdot \sin \omega t - V \cdot I_1 \cdot \cos(2\omega t - \varphi_1) + V \cdot I_3 \cdot \cos(2\omega t - \varphi_3) - V \cdot I_3 \cdot \cos(4\omega t - \varphi_3) + V \cdot I_5 \cdot \cos(4\omega t - \varphi_5) + \dots \quad (3.3)$$

The real power is defined as the average value of (3.3). It can be observed that the instantaneous power has many harmonic components, which should be filtered in order to work out the real power. The main harmonic is generally due to the fundamental current, with amplitude $V \cdot I_1$ and at twice the grid frequency. In order to filter this harmonic, the cutoff frequency of the low-pass filter should be much lower than 2ω , which is usually below 10 rad/s (1.59 Hz), slowing down the dynamic performance.

3.2.2 P-Q theory and digital sampling

To enhance dynamic performance, a power calculation based on p-q theory is used [3.42]–[3.44]. According to the p-q theory, the real and reactive powers can be obtained as

$$p_{\alpha\beta}(t) = 1/2 \cdot (v_\alpha \cdot i_\alpha + v_\beta \cdot i_\beta) \quad (3.4)$$

$$q_{\alpha\beta}(t) = 1/2 \cdot (v_{\beta} \cdot i_{\alpha} - v_{\alpha} \cdot i_{\beta}), \quad (3.5)$$

where $v_{\alpha}=v(t)$, $i_{\alpha}=i(t)$, and the voltage v_{β} and current i_{β} are obtained by introducing a phase delay of $\pi/2$ to v_{α} and i_{α} by using a circular buffer.

In this work, a digital microprocessor is used. It is then much simpler to delay the voltage and current a certain time $T_d=2\pi/4\omega_0$, where ω_0 is the nominal frequency (for 50 Hz, $T_d=5$ ms), preventing the use of extra hardware. As a result, the v_{α} and i_{α} expressions change because the fundamental component and harmonics 5, 9, 13... are delayed $\pi/2$ but harmonics 3, 7, 11... are delayed $3\pi/2$. The voltage v_{β} and current i_{β} can then be expressed as

$$v_{\beta} = \sqrt{2}V \cdot \sin\left(\omega t - \frac{\pi}{2}\right) \quad (3.6)$$

$$i_{\beta} = I_{dc} + \sqrt{2}I_1 \cdot \sin\left(\omega t - \varphi_1 - \frac{\pi}{2}\right) + \sqrt{2}I_3 \cdot \sin\left(3\omega t - \varphi_3 - \frac{3\pi}{2}\right) + \sqrt{2}I_5 \cdot \sin\left(5\omega t - \varphi_5 - \frac{\pi}{2}\right) + \dots \quad (3.7)$$

Using the expression for $p_{\alpha\beta}(t)$ and $q_{\alpha\beta}(t)$ presented in (3.4) and (3.5), and considering (3.1), (3.2), (3.6) and (3.7), one obtains

$$p_{\alpha\beta}(t) = V \cdot I_1 \cdot \cos \varphi_1 + V \cdot I_{dc} \cdot \sin(\omega t - \pi/4) + \\ -V \cdot I_3 \cdot \cos(4\omega t - \varphi_3) + V \cdot I_5 \cdot \cos(4\omega t - \varphi_5) + \dots \quad (3.8)$$

$$q_{\alpha\beta}(t) = V \cdot I_1 \cdot \sin \varphi_1 - V \cdot I_{dc} \cdot \cos(\omega t - \pi/4) - V \cdot I_5 \cdot \sin(4\omega t - \varphi_5) + \dots \quad (3.9)$$

The real and reactive powers are defined as the average value of (3.8) and (3.9), respectively. By comparing these expressions to (3.3), it can be observed that the most problematic harmonic, at a frequency of 2ω , has disappeared, and the harmonic due to the DC current has been reduced. As a result, the cutoff frequency of the low-pass filter can be higher than with the previous method, specifically about 60 rad/s (9.55 Hz). This makes it possible to improve the droop method dynamic performance.

Expressions (3.6)–(3.9) are obtained for $\omega=\omega_0$. However, the frequency varies around its nominal value during operation due to the droop method. Because a fixed delay time T_d is used for v_{β} and i_{β} , the actual phase delay will be around $\pi/2$ or $3\pi/2$ when $\omega \neq \omega_0$. Although it is not shown here for space reasons, the harmonics at ω , 2ω , 4ω ... slightly change in relation to (3.8) and (3.9) and the average value of $p_{\alpha\beta}(t)$ is still equal to the real power P . However, the average value of $q_{\alpha\beta}(t)$ does change and is not equal to the reactive power Q anymore but to

$$Q_{\alpha\beta,av} = V \cdot I_1 \cdot \sin \varphi_1 \cdot \cos\left(\pi/2 \cdot (1 - \omega/\omega_0)\right). \quad (3.10)$$

This expression shows that, with this method, the calculated reactive power will be always lower than its actual value when $\omega \neq \omega_0$. However, since the frequency variation range must be between $\pm 2\%$ according to IEEE standards, the reactive power error is lower than 0.05%, which can be totally neglected.

This method was validated and compared to the previous method by means of simulation results, shown in Fig. 3.2. At the beginning, the inverter is supplying both a linear and non-linear loads, with $P_{load}=3500$ W and $Q_{load}=1300$ VAR in total. Then, at second 1.5, other linear and non-linear loads, with $P_{load}=1700$ W and $Q_{load}=600$ VAR in total, are connected. As a result of the power increase, the grid frequency changes from 49.63 Hz to 49.53 Hz. The high value of the current harmonics can be observed in the first graph. The second graph represents the method presented in section 3.2.1, both the instantaneous power $p(t)$ given by (3.3) and the real power P obtained after applying a LPF with cutoff frequency of 10 rad/s. The large value of the power harmonic at 2ω as well as the slow response of the calculation can be observed. In the third and fourth graphs, the method presented in this section is shown. It can be noted that the harmonics of $P_{\alpha\beta}$ and $Q_{\alpha\beta}$ have both lower amplitude and higher frequency, as predicted by (3.8) and (3.9). As a result, the real power P and reactive power Q are accurately obtained after applying a LPF with cutoff frequency of 40 rad/s.

Thanks to its superior dynamic performance, the power calculation explained in this section, including the p-q theory, the fixed time delay and the low-pass filter, will be used from now on in this work.

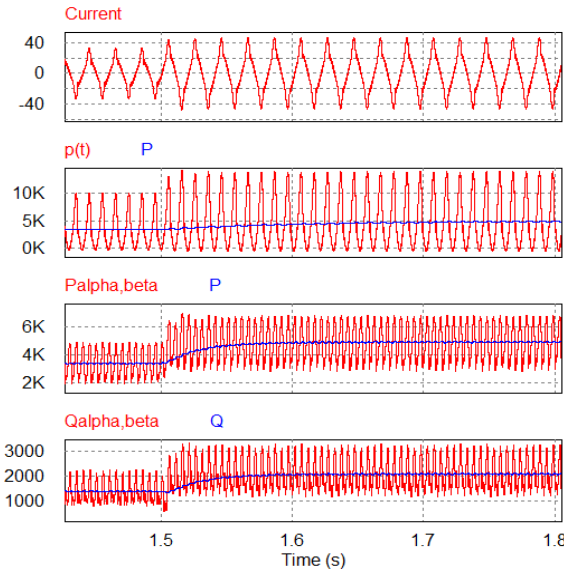


Figure 3.2. Power calculation for product plus LPF (method 1) and for p-q theory and digital sampling plus LPF (method 2).

3.3 DROOP METHOD FOR LINEAR LOADS

3.3.1 Droop method and RMS voltage regulation

Fig. 3.3 represents an islanded microgrid with N single-phase Voltage Source Inverters (VSIs) connected in parallel. Thanks to the droop method, the VSIs jointly control the grid voltage and frequency. The power sources $S1$ to S_N are modeled as voltage sources, implying that their power response is much quicker than the droop method dynamics. As a result, the droop method modeling presented in this section is valid for an energy storage system such as a battery or a supercapacitor, or a renewable energy source such as a photovoltaic generator, in which their dynamic response is very quick [3.45]–[3.47]. To be coherent with the energy management presented at the end of this chapter, batteries will be chosen as the power source.

The inverters are connected to the AC bus through an inductive filter L_{fi} . In order to generalize, they can have different rated powers $S_{bat,i}$, and also different per-unit output impedances. Linear loads and Current Source Inverters (CSIs) are also connected to the AC bus, absorbing (or delivering when negative) a net real power P_T and a net reactive power Q_T . The instantaneous values of voltages and currents are defined in the figure.

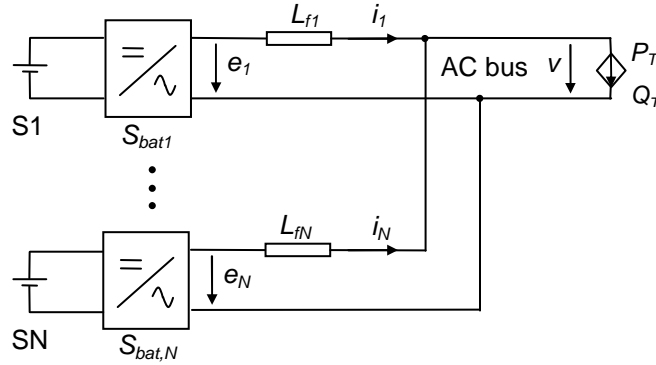


Figure 3.3. Voltage source inverters connected in parallel.

Fig. 3.4 shows the block diagram of the droop method and RMS voltage regulation. For every inverter, the droop method obtains the frequency and RMS grid voltage reference, f and V^* , respectively, as a function of the real and reactive powers, P and Q . By means of a PI controller and the RMS measured voltage V_m , the RMS output voltage E is obtained. Since the RMS output voltage and frequency are known, the instantaneous voltage e can finally be obtained and modulated.

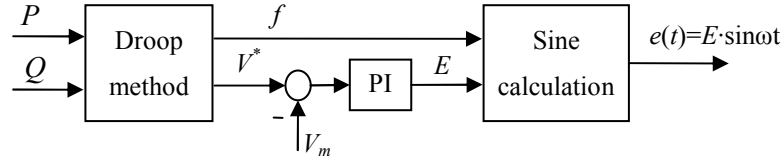


Figure 3.4. Block diagram of the droop method and RMS voltage regulation.

Fig. 3.5 shows the equivalent circuit of N inverters connected to a common AC bus through their output impedances. These output impedances Z_i can be resistive or inductive depending on both the type of grid and the control. Its real part is the output resistance R_i and its imaginary part is the output reactance X_i . The real and reactive powers injected into the bus by every unit can be expressed as follows [3.48]:

$$P_i = \frac{V \cdot E_i}{Z_i^2} \cdot X_i \cdot \sin \delta_i + \frac{V}{Z_i^2} \cdot R_i \cdot (E_i \cdot \cos \delta_i - V), \quad i = 1, \dots, N \quad (3.11)$$

$$Q_i = -\frac{V \cdot E_i}{Z_i^2} \cdot R_i \cdot \sin \delta_i + \frac{V}{Z_i^2} \cdot X_i \cdot (E_i \cdot \cos \delta_i - V), \quad i = 1, \dots, N, \quad (3.12)$$

where δ_i is the power angle (angle between e_i and v).

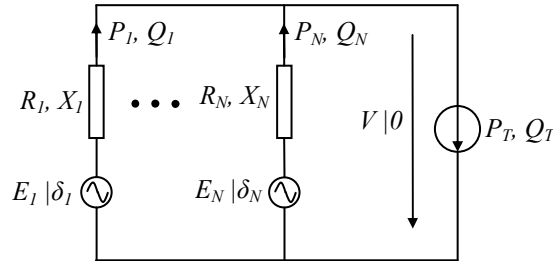


Figure 3.5. Equivalent circuit of N inverters connected to an AC bus.

An important aspect of the RMS regulation is that the filter inductance also becomes part of the output impedance for the droop method. Given the high value of this filter impedance (the per-unit value is typically about 10%), it is possible to consider the output impedance as inductive, regardless of the line impedance. Thanks to this assumption, and from (3.11) and (3.12), the real power P_i and reactive power Q_i provided by each inverter can be expressed as

$$P_i = \frac{V \cdot E_i}{X_i} \cdot \sin \delta_i, \quad i = 1, \dots, N \quad (3.13)$$

$$Q_i = \frac{V}{X_i} (E_i \cdot \cos \delta_i - V), \quad i = 1, \dots, N. \quad (3.14)$$

In practical applications, the power angle δ is small. Thus, (3.13) and (3.14) can be rewritten as

$$P_i \approx \frac{V \cdot E_i}{X_i} \cdot \delta_i, \quad i = 1, \dots, N \quad (3.15)$$

$$Q_i \approx \frac{V}{X_i} (E_i - V), \quad i = 1, \dots, N. \quad (3.16)$$

As a consequence, the inverter real power can be controlled by the power angle δ and the reactive power by the output voltage E . Based on these relationships, the conventional droop method imposes the following control to every inverter:

$$f_i = f_0 - m_{p_i} \cdot P_i, \quad i = 1, \dots, N \quad (3.17)$$

$$V_i^* = V_0 - m_{Q_i} \cdot Q_i, \quad i = 1, \dots, N, \quad (3.18)$$

where f_0 is the non-load frequency, m_{p_i} is the droop coefficient of the real power, V_0 is the non-load RMS grid voltage, and m_{Q_i} is the droop coefficient of the reactive power.

The P - f and Q - V slopes are normally set according to the inverter rated power in order to share the real powers in proportion to their ratings. Taking into account that in steady-state every inverter operates with the same frequency and voltage reference, this condition leads to

$$m_{p_i} = \frac{M_p}{S_{bat,i}}, \quad i = 1, \dots, N \quad (3.19)$$

$$m_{Q_i} = \frac{M_q}{S_{bat,i}}, \quad i = 1, \dots, N, \quad (3.20)$$

where M_p is the droop coefficient of the per-unit real power and M_q is the droop coefficient of the per-unit reactive power. Unlike m_p and m_q , M_p and M_q have the same value for every inverter and represent the frequency and voltage maximum deviations.

The two inverters and the system parameters used throughout this section are presented in Table 3.1.

Inverter 1 rated power S_{bat1}	6000 VA
Inverter 1 output inductance L_1	3 mH
Inverter 1 droop coefficient m_{P1}	0.05 Hz/kW
Inverter 1 droop coefficient m_{Q1}	3.33 V/kVAr
Inverter 2 rated power S_{bat2}	3000 VA
Inverter 2 output inductance L_2	4 mH
Inverter 2 droop coefficient m_{P2}	0.1 Hz/kW
Inverter 2 droop coefficient m_{Q2}	6.67 V/kVAr
Common droop coefficient M_p	0.3 Hz
Common droop coefficient M_q	20 V
Non-load frequency f_0	50 Hz
Non-load voltage V_0	230 V
Time constant of the real power filter τ_P	25 ms
Time constant of the reactive power filter τ_Q	50 ms
Time constant of the RMS voltage filter τ_V	40 ms

Table 3.1. System parameters.

3.3.2 Linear model for two inverters

An approximate linear model is derived in this section for two inverters. For this purpose, the following assumptions are considered:

- The output impedance is purely inductive.
- The power angle is very small. As a consequence of these two assumptions, (3.15) and (3.16) can be used.
- The voltage variation is very small with regard to the rated value. As a result, from (3.15) and (3.16), one obtains

$$P_i \approx \frac{V_0 \cdot E_0}{X_i} \cdot \delta_i, \quad i = 1, 2 \quad (3.21)$$

$$Q_i \approx \frac{V_0}{X_i} \cdot (E_i - V), \quad i = 1, 2, \quad (3.22)$$

where $E_0 = V_0$ is the non-load rms output voltage.

- The load powers P_T and Q_T are independent of the grid voltage.

By means of these assumptions, P and Q linearly depend on δ and $E - V$, respectively. As a result, the system becomes linear, making it possible to apply linear modeling techniques. Moreover, since P does not depend on the voltage and Q does not depend on

the power angle, these approximations decouple the real and reactive power responses, which can therefore be separately analyzed.

The real power response is first presented. Equation (3.21) applied to two inverters becomes

$$P_1 = \frac{V_0 \cdot E_0}{X_1} \cdot \delta_1, \quad P_2 = \frac{V_0 \cdot E_0}{X_2} \cdot \delta_2. \quad (3.23)$$

From its definition, the power angles can be worked out as

$$\delta_1 = (\theta_{1i} + I \cdot f_1) - \theta_v, \quad \delta_2 = (\theta_{2i} + I \cdot f_2) - \theta_v, \quad (3.24)$$

where θ_v is the angle position of v , θ_{1i} is the initial angle position of e_1 , θ_{2i} is the initial angle position of e_2 , and $I=2\pi/s$ is the Laplace integrator.

The power balance at the point of common coupling is

$$P_1 + P_2 = P_T. \quad (3.25)$$

From (3.23)–(3.25), expressions for the system plant can be determined as

$$P_1 = \frac{X_2}{X_1 + X_2} \cdot P_T + \frac{V_0 E_0}{X_1 + X_2} \cdot \theta_i + \frac{V_0 E_0}{X_1 + X_2} I \cdot (f_1 - f_2) \quad (3.26)$$

$$P_2 = \frac{X_1}{X_1 + X_2} \cdot P_T - \frac{V_0 E_0}{X_1 + X_2} \cdot \theta_i - \frac{V_0 E_0}{X_1 + X_2} I \cdot (f_1 - f_2), \quad (3.27)$$

where $\theta_i = \theta_{1i} - \theta_{2i}$.

The droop method changes f_1 and f_2 in order to equally share the power P_T . From (3.17), the transfer functions of the frequency droops can be modeled as

$$f_1 = f_0 - m_{p1} \cdot H_P \cdot P_1, \quad f_2 = f_0 - m_{p2} \cdot H_P \cdot P_2, \quad (3.28)$$

where H_P is a low-pass band filter which represents the measurement of the real power. The real and reactive power measurement was presented in section 3.2.

Introducing (3.28) into (3.26) and (3.27), expressions for the closed-loop powers can be determined as

$$P_1 = \frac{V_0 E_0 \cdot m_{p2} \cdot I \cdot H_P + X_2}{den_p} \cdot P_T + \frac{V_0 E_0}{den_p} \cdot \theta_i \quad (3.29)$$

$$P_2 = \frac{V_0 E_0 \cdot m_{p1} \cdot I \cdot H_P + X_1}{den_p} \cdot P_T - \frac{V_0 E_0}{den_p} \cdot \theta_i \quad (3.30)$$

$$den_p = V_0 E_0 \cdot (m_{p1} + m_{p2}) \cdot I \cdot H_P + X_1 + X_2. \quad (3.31)$$

The closed-loop stability and power transient are determined by the transfer function poles, i.e. the roots of den_p . Hence, for given certain system parameters, the choice of M_p is important for the design of the power response [see (3.19)]. The parameter M_p must be chosen as a trade-off between fast dynamics and high stability margin. In this case, $M_p=0.3$ Hz is selected, which yields to a crossover frequency $f_{cp}=3.2$ Hz and a phase margin $PM_p=63^\circ$. As a result, the operating frequency will vary between $f_0-M_p=49.7$ Hz and $f_0+M_p=50.3$ Hz, which is within the admissible variation range.

After obtaining the real power response for two inverters, the reactive power and voltage responses are determined below. Equation (3.22) applied to two inverters becomes

$$Q_1 = \frac{V_0}{X_1} \cdot (E_1 - V), \quad Q_2 = \frac{V_0}{X_2} \cdot (E_2 - V). \quad (3.32)$$

The power balance at the point of common coupling is

$$Q_1 + Q_2 = Q_T. \quad (3.33)$$

From (3.32) and (3.33), expressions for the system plant can be determined as

$$Q_1 = \frac{X_2}{X_1 + X_2} \cdot Q_T + \frac{V_0}{X_1 + X_2} \cdot (E_1 - E_2) \quad (3.34)$$

$$Q_2 = \frac{X_1}{X_1 + X_2} \cdot Q_T - \frac{V_0}{X_1 + X_2} \cdot (E_1 - E_2) \quad (3.35)$$

$$V = \frac{X_2}{X_1 + X_2} \cdot E_1 + \frac{X_1}{X_1 + X_2} \cdot E_2 - \frac{X_1 // X_2}{V_0} \cdot Q_T. \quad (3.36)$$

The droop method changes V_1^* and V_2^* in order to equally share the power Q_T . To follow those voltage references, the voltage regulation changes E_1 and E_2 . From (3.18) and Fig. 3.4, the transfer functions of the voltage droops together with the voltage regulation can be modeled as

$$E_1 - E_{1i} = C_V (V_1^* - H_V \cdot V) = C_V (V_0 - m_{Q1} \cdot H_Q \cdot Q_1 - H_V \cdot V) \quad (3.37)$$

$$E_2 - E_{2i} = C_V (V_2^* - H_V \cdot V) = C_V (V_0 - m_{Q2} \cdot H_Q \cdot Q_2 - H_V \cdot V), \quad (3.38)$$

where E_{1i} and E_{2i} are the initial controller outputs, H_Q is a low-pass band filter which models the measurement of the reactive power, H_V is a low-pass band filter which models the measurement of the RMS grid voltage, and C_V represents the PI voltage controller.

Introducing (3.37) and (3.38) into (3.34)–(3.36), expressions for the closed-loop powers and voltage can be determined as

$$Q_1 = \frac{V_0 \cdot m_{Q2} \cdot C_V \cdot H_Q + X_2}{den_Q} \cdot Q_T + \frac{V_0}{den_Q} \cdot (E_{1i} - E_{2i}) \quad (3.39)$$

$$Q_2 = \frac{V_0 \cdot m_{Q1} \cdot C_V \cdot H_Q + X_1}{den_Q} \cdot Q_T - \frac{V_0}{den_Q} \cdot (E_{1i} - E_{2i}) \quad (3.40)$$

$$V = \frac{C_V}{den_V} \cdot V_0 + \frac{X_2 / (X_1 + X_2)}{den_V} \cdot E_{1i} - \frac{X_2 \cdot m_{Q1} \cdot C_V \cdot H_Q / (X_1 + X_2) + (X_1 / X_2) / V_0}{den_V} \cdot Q_1 + \quad (3.41)$$

$$+ \frac{X_1 / (X_1 + X_2)}{den_V} \cdot E_{2i} - \frac{X_1 \cdot m_{Q2} \cdot C_V \cdot H_Q / (X_1 + X_2) + (X_1 / X_2) / V_0}{den_V} \cdot Q_2$$

$$den_Q = V_0 \cdot (m_{Q1} + m_{Q2}) \cdot C_V \cdot H_Q + X_1 + X_2 \quad (3.42)$$

$$den_V = C_V \cdot H_V + 1. \quad (3.43)$$

As it can be observed, two different expressions, den_Q and den_V , determine the transfer function poles in this case. The reactive power response depends on den_Q , while the voltage response mainly depends on den_V , but also on den_Q through Q_1 and Q_2 . Since C_V appears in both den_Q and den_V , its design is important for both responses, while M_q only appears in den_Q and its design is important for the reactive power response [see (3.20)]. Using (3.43), the PI controller is designed to obtain a voltage response with a crossover frequency $f_{cV}=1$ Hz and a phase margin $PM_V=80^\circ$. The low f_{cV} value prevents dangerous load transients, for example when operating with motors or transformers, while the high PM_V value avoids voltage overshoots.

Then, the parameter M_q is chosen as 20 V, which from (3.42) yields to a reactive power crossover frequency $f_{cQ}=1$ Hz and a phase margin $PM_Q=76^\circ$. The high M_q value makes the voltage vary between $V_0-M_q=210$ V and $V_0+M_q=250$ V, which is within the admissible variation range. It also helps reduce the inaccuracy of reactive power control due to line impedance, as it will be shown later [3.49]. A higher M_q value would further improve the steady-state and transient responses but would bring the voltage variation range beyond limits.

3.3.3 Small-signal model with stiff AC grid

The model developed in this section makes the following assumptions:

- The output impedance is purely inductive. As a result, (3.13) and (3.14) can be used.
- The load powers P_T and Q_T are independent of the grid voltage.

This model is thus more accurate than the previous one. From (3.13) and (3.14), both powers P and Q depend on δ , E and V through non-linear expressions. As a consequence, the real and reactive power responses are coupled and a small-signal analysis is required, which makes the analysis much more complicated. It must be noted that $P_T=0$ and $Q_T=0$ for the small-signal given that the stiff AC grid approximation is considered.

Applying small-signal analysis to two inverters, (3.13) and (3.14) become

$$\hat{P}_1 = \frac{VE_1}{X_1} \cos \delta_1 \cdot \hat{\delta}_1 + \frac{V}{X_1} \sin \delta_1 \cdot \hat{E}_1 + \frac{E_1}{X_1} \sin \delta_1 \cdot \hat{V} \quad (3.44)$$

$$\hat{Q}_1 = -\frac{VE_1}{X_1} \sin \delta_1 \cdot \hat{\delta}_1 + \frac{V}{X_1} \cos \delta_1 \cdot \hat{E}_1 - \frac{2V - E_1 \cos \delta_1}{X_1} \cdot \hat{V} \quad (3.45)$$

$$\hat{P}_2 = \frac{VE_2}{X_2} \cos \delta_2 \cdot \hat{\delta}_2 + \frac{V}{X_2} \sin \delta_2 \cdot \hat{E}_2 + \frac{E_2}{X_2} \sin \delta_2 \cdot \hat{V} \quad (3.46)$$

$$\hat{Q}_2 = -\frac{VE_2}{X_2} \sin \delta_2 \cdot \hat{\delta}_2 + \frac{V}{X_2} \cos \delta_2 \cdot \hat{E}_2 - \frac{2V - E_2 \cos \delta_2}{X_2} \cdot \hat{V}, \quad (3.47)$$

where the small-signal variables are marked with a circumflex and the operating point is defined by

$$V = V_0 - M_q \cdot \frac{Q_T}{S_{bat1} + S_{bat2}} \quad (3.48)$$

$$E_1 \sin \delta_1 = \frac{X_1}{V} \frac{S_{bat1} \cdot P_T}{S_{bat1} + S_{bat2}}, \quad E_1 \cos \delta_1 = V + \frac{X_1}{V} \frac{S_{bat1} \cdot Q_T}{S_{bat1} + S_{bat2}} \quad (3.49)$$

$$E_2 \sin \delta_2 = \frac{X_2}{V} \frac{S_{bat2} \cdot P_T}{S_{bat1} + S_{bat2}}, \quad E_2 \cos \delta_2 = V + \frac{X_2}{V} \frac{S_{bat2} \cdot Q_T}{S_{bat1} + S_{bat2}}. \quad (3.50)$$

From the linearized expressions for (3.24), (3.25) and (3.33), and by means of (3.44)–(3.47), expression for the system plant are obtained as

$$\begin{bmatrix} \hat{P}_1 & \hat{Q}_1 & \hat{P}_2 & \hat{Q}_2 & \hat{V} \end{bmatrix}^T = A \cdot \begin{bmatrix} I \cdot \hat{f}_1 & I \cdot \hat{f}_2 & \hat{E}_1 & \hat{E}_2 \end{bmatrix}^T, \quad (3.51)$$

where A is 5x4 matrix whose coefficients are not shown for space reasons.

The droop control expressions for f_1 , f_2 , E_1 and E_2 were given in (3.28), (3.37) and (3.38). By introducing the corresponding linearized expressions into (3.51), the system eigenvalues can be determined.

Fig. 3.6 shows a comparison between the small-signal and the linear models. The poles obtained from the linear model are plotted as points, and their location agrees with the frequency domain design carried out in section 3.3.2. In particular, it can be observed

that the real power response is quicker and less damped than the reactive power and voltage responses. On the other hand, the poles obtained from the small-signal model are plotted as x-marks for different operation points, with $Q_T=0$ and P_T varying from $S_{bat1}+S_{bat2}=9$ kW to $-(S_{bat1}+S_{bat2})=-9$ kW. For the operation point $P_T=0$, $Q_T=0$, both models totally coincide, while it can be observed that the influence of P_T variations is very small, making the linear model valid for the whole real power range.

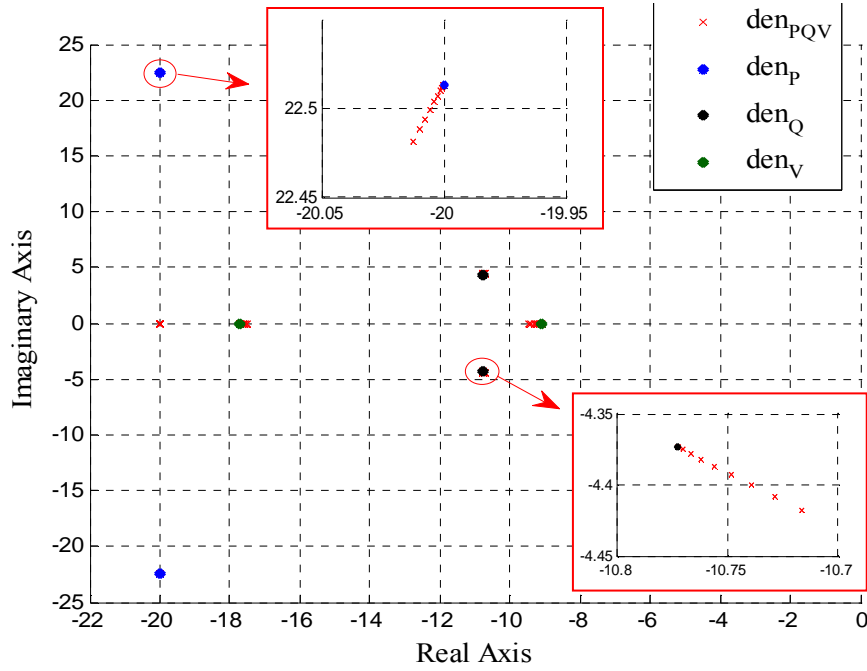


Figure 3.6. System poles for the linear model (den_P , den_Q , den_V) and for the small-signal model (den_{PQV} with $Q_T=0$, P_T varying from -9 to 9 kW).

Fig. 3.7 shows the same plot for different small-signal operating points, with $P_T=S_{bat1}+S_{bat2}=9$ kW and Q_T varying from -5 kVar to 5 kVar. It can be observed that, although the effect of Q_T variation is higher than the one of P_T variation, its influence is also small. In particular, the effect on the real and reactive power responses is negligible while the voltage response becomes slightly faster for high reactive power consumption.

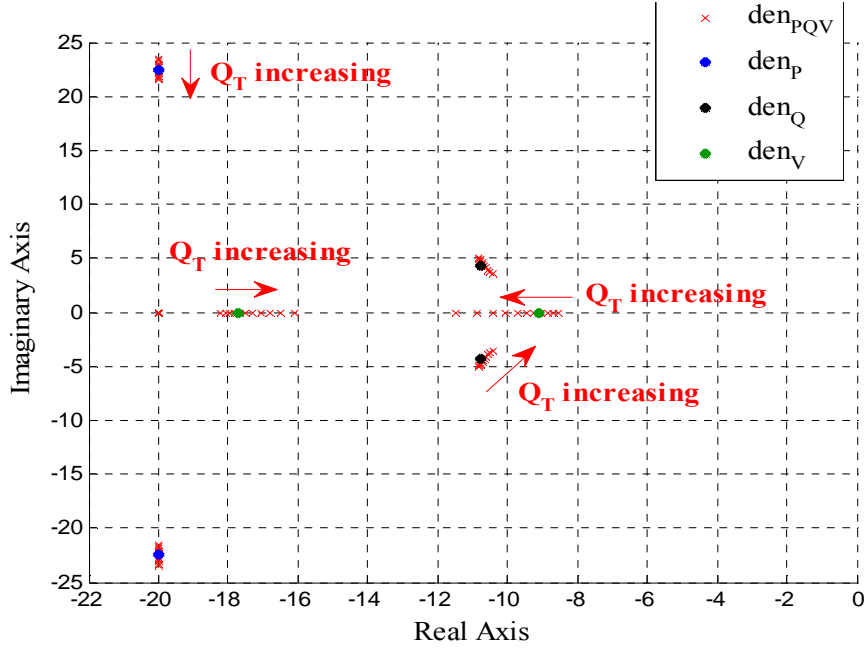


Figure 3.7. System poles for the linear model ($\text{den}_P, \text{den}_Q, \text{den}_V$) and for the small-signal model (den_{PQV} with $P_T=9$ kW, Q_T varying from -5 to 5 kVar).

3.3.4 Small-signal model with load influence

A similar model to the one obtained in section 3.3.3 but considering the load influence is derived here. It is assumed that the output impedance is purely inductive, making it possible to use (3.13) and (3.14) and their linearized expressions (3.44)–(3.47) for the operation points given by (3.48)–(3.50). Because the load is also considered, this model is more accurate than the two previous ones.

Three types of loads/sources are considered, namely an impedance-like load/source, whose power is dependent on V^2 , a current source, whose power is proportional to the voltage, and a power source, which does not depend on the voltage. On account of these loads, the small-signal net powers can be expressed as

$$\hat{P}_T = I_d \cdot \hat{v}, \quad \hat{Q}_T = I_q \cdot \hat{v}, \quad (3.52)$$

where I_d and I_q are the small-signal current coefficients.

From (3.24), (3.25) and (3.33) linearized by considering (3.52), and by means of (3.44)–(3.47), expression for the system plant are obtained as

$$\begin{bmatrix} \hat{P}_1 & \hat{Q}_1 & \hat{P}_2 & \hat{Q}_2 & \hat{V} \end{bmatrix}^T = B \cdot \begin{bmatrix} I \cdot \hat{f}_1 & I \cdot \hat{f}_2 & \hat{E}_1 & \hat{E}_2 \end{bmatrix}^T, \quad (3.53)$$

where B is 5×4 matrix whose coefficients are not given for space reasons.

By introducing the linearized droop control expressions obtained from (3.28), (3.37) and (3.38) into (3.53), the system eigenvalues can be determined.

Fig. 3.8 shows a comparison among the three different models. The poles obtained from the linear model, and from the stiff ac grid small-signal model with $P_T=8$ kW and $Q_T=5$ kVar, are plotted as points. The poles obtained from the model developed in this section are plotted as x-marks for different operation points, with $P_T=8$ kW, $Q_T=5$ kVar, $S_{load}=8$ kVA, and Φ_{load} varying from -50° to 50° , where S_{load} and Φ_{load} represent an impedance load and the rest of the net power is made by power sources. It can be observed that the load effect on the real and reactive power responses is negligible while the voltage response becomes slightly slower for high Φ_{load} values. When compared with the linear model, the most accurate model also obtains similar results, especially for the real and reactive power responses.

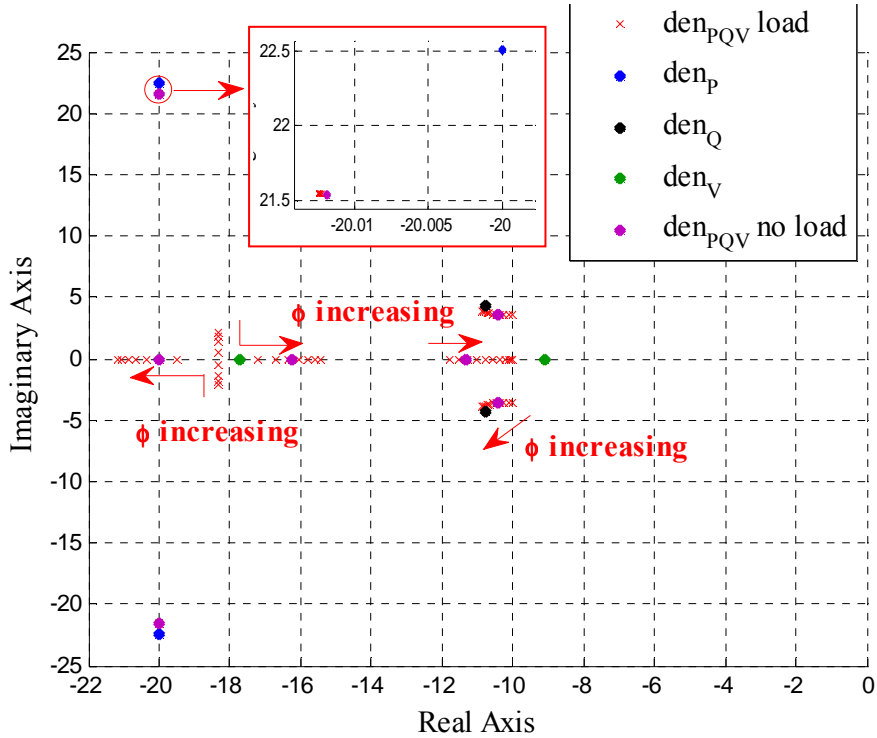


Figure 3.8. System poles for the linear model (den_p , den_Q , den_V), for the stiff ac grid small-signal model (den_{pQV} no load with $P_T=8$ kW, $Q_T=5$ kVar), and for the load-influence small-signal model (den_{pQV} load with $P_T=8$ kW, $Q_T=5$ kVar, $S_{load}=8$ kVA, Φ_{load} varying from -50° to 50°).

3.3.5 Simulation and experimental results

The system presented in Fig. 3.3, including 2 VSIs and some impedance loads, was modeled using the software PSIM. The droop method and voltage regulation shown in Fig. 3.4 were used for the control. The system parameters were presented in Table 3.1.

The simulation results are represented in Fig. 3.9, showing the per-unit real powers (first graph), per-unit reactive power (second graph), reference voltages V_{ref1} and V_{ref2} , measured voltage V , and output voltages E_1 and E_2 (third graph). At the beginning, only inverter 1 is operating and an RL load with rated values $P_{load}=4$ kW and $Q_{load}=2.5$ kVar is being supplied. The voltage response can be clearly observed during the startup from second 0.05. The rise time and the lack of overshoot agree with the crossover frequency $f_{cV}=1$ Hz and $PM_V=80^\circ$ obtained in section III. Then, just after second 1, inverter 2 is connected. The real power, reactive power and voltage responses can be observed in the figure. Again, the obtained crossover frequencies $f_{cV}=1$ Hz, $f_{cQ}=1$ Hz, and $f_{cP}=3.2$ Hz, and phase margins $PM_V=80^\circ$, $PM_Q=76^\circ$, and $PM_P=63^\circ$, agree with the corresponding responses. Furthermore, the powers are equally shared between the inverters. Finally, at second 1.6, an identical RL load is connected. In this case, the powers are also perfectly distributed at steady-state.

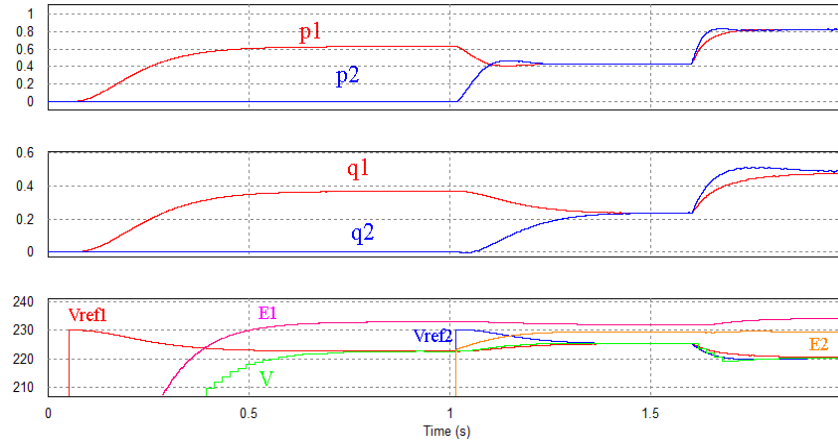


Figure 3.9. Simulation results for the droop method.

The same system was tested in the laboratory. In this case, the system parameters are also those presented in Table 3.1, with the exception that both inverters have the same features, corresponding to inverter 1.

The experimental results are shown in Fig. 3.10, where i_1 , i_2 and i_1-i_2 are represented in green, purple and red, respectively. The transient responses for the second inverter and load connections are augmented in Fig. 3.11. At the beginning, only inverter 1 is

operating and a linear load with $S_{load}=3300$ VA is connected. Then, when inverter 2 is connected, the current is well distributed thanks to the droop method. The currents are completely established after about 0.5 seconds, which is fast enough for this application. Finally, when an identical linear load is connected, the powers remain also perfectly distributed after a short transient.

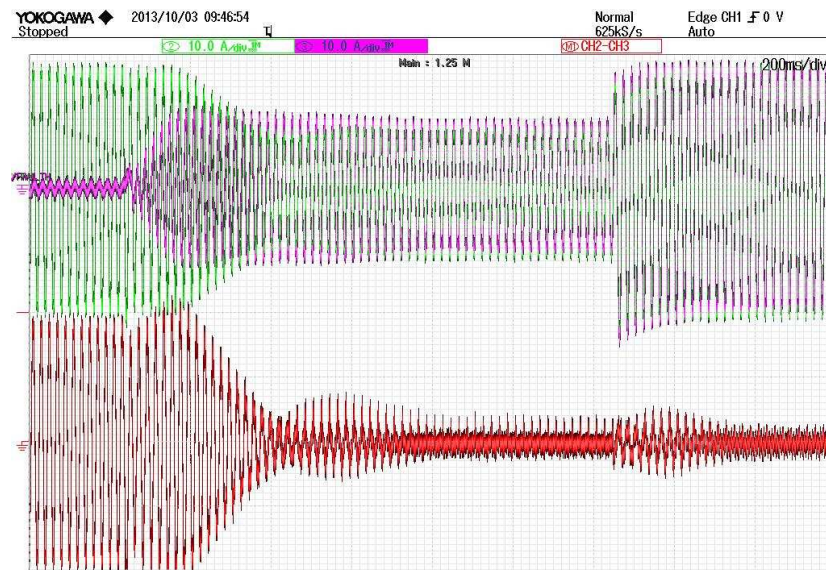


Figure 3.10. Experimental results for the droop method.

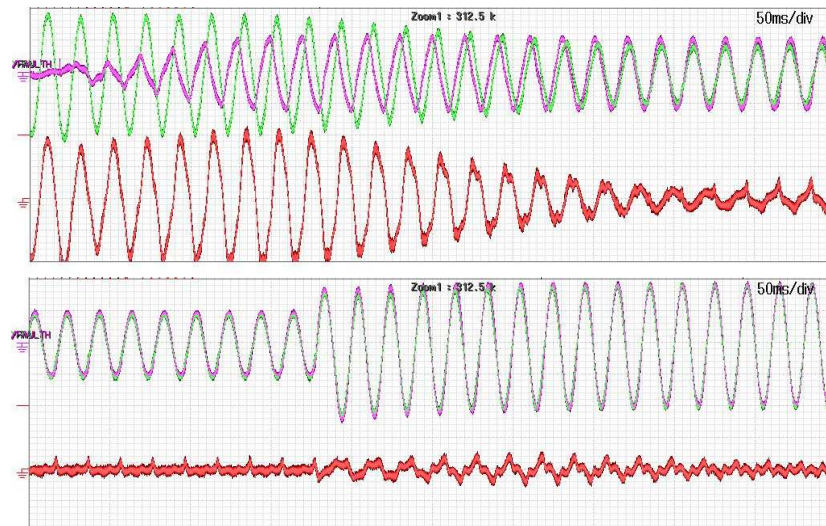


Figure 3.11. Detail of the transients for the droop method.

3.3.6 Linear model for N inverters

After validating the proposed linear model, this model is generalized for an arbitrary number of N inverters. The power response modeling, developed in section 3.3.2 for two inverters, will be derived in this section for N inverters. The purpose is to obtain the transfer function poles in order to predict the transient response. The expression for the characteristic equation is thus determined, which makes it possible to disregard the independent terms, such as net power P_T , net reactive power Q_T , initial angle θ_i , and initial controller output E_i .

After the derivations, some examples will be provided for 4 inverters. In these examples, the parameters presented in Table 3.1 are used together with two other battery inverters. Battery inverter 3 has a rated power $S_{bat3}=5000$ VA and an output inductance $L_3=3$ mH while battery inverter 4 has a rated power $S_{bat4}=4000$ VA, an output inductance $L_4=4$ mH. The droop coefficients $M_p=0.3$ Hz and $M_q=20$ V as well as the voltage controller C_V remain unchanged in relation to the two-inverter analysis.

In this case, the real and reactive power responses are also decoupled. For this reason, the analysis can be independently carried out, and the real power response is first presented. Rewriting (3.23)–(3.25) for N battery inverters leads to

$$P_i = \frac{V_0 E_0}{X_i} \cdot \delta_i, \quad \delta_i = I \cdot f_i - \theta_v, \quad i = 1, \dots, N \quad (3.54)$$

$$\sum_{j=1}^N P_j = 0. \quad (3.55)$$

From (3.54), one can obtain simplified equations for the system plant as

$$P_1 \cdot X_1 - P_i \cdot X_i = V_0 E_0 \cdot I \cdot (f_1 - f_i), \quad i = 2, \dots, N. \quad (3.56)$$

The conventional droop method changes the frequencies in order to share the power. Considering that the real power measurement (transfer function H_p) is the same for every inverter, the control is expressed as follows:

$$f_i = f_0 - m_{pi} \cdot H_p \cdot P_i, \quad i = 1, \dots, N. \quad (3.57)$$

From (3.56) and (3.57), every power can be expressed as a function of P_1 , i.e.

$$P_i = \frac{X_1 + V_0 E_0 \cdot m_{p1} \cdot I \cdot H_p}{X_i + V_0 E_0 \cdot m_{pi} \cdot I \cdot H_p} \cdot P_1, \quad i = 2, \dots, N. \quad (3.58)$$

By introducing (3.58) into (3.55) and operating, it is possible to obtain the characteristic equation as

$$den_p = \sum_{j=1}^N \frac{1}{X_j + V_0 E_0 \cdot m_{pj} \cdot I \cdot H_p} . \quad (3.59)$$

The roots of this expression correspond to the closed-loop transfer function poles for the real power response. Some examples are provided in Table 3.2 for different inverter configurations, where the different inverters were presented in this section. It can be seen that the system has $N-1$ pairs of conjugate poles. Furthermore, the poles for configurations with different inverters are between the extreme poles for configurations with equal inverters.

Configuration	Poles
N times Inv1	N-1 times $-20.0 \pm 17.5j$ ($\xi=0.75$)
N times Inv2	N-1 times $-20.0 \pm 25.7j$ ($\xi=0.62$)
N times Inv3	N-1 times $-20.0 \pm 21.1j$ ($\xi=0.69$)
N times Inv4	N-1 times $-20.0 \pm 19.8j$ ($\xi=0.71$)
Inv1, Inv2	$-20.0 \pm 22.5j$ ($\xi=0.66$)
Inv1, Inv2, Inv3, Inv4	$-20.0 \pm 24.5j$ ($\xi=0.63$) $-20.0 \pm 20.5j$ ($\xi=0.70$) $-20.0 \pm 18.5j$ ($\xi=0.73$)

Table 3.2. Closed-loop poles for the real power response.

After obtaining the real power response for two inverters, the reactive power response is determined below. Rewriting (3.32) and (3.33) for N inverters gives

$$Q_i = \frac{V_0}{X_i} \cdot (E_i - V), \quad i = 1, \dots, N \quad (3.60)$$

$$\sum_{j=1}^N Q_j = 0 . \quad (3.61)$$

From (3.60), simplified expressions for the system plant can be obtained as

$$Q_1 \cdot X_1 - Q_i \cdot X_i = V_0 \cdot (E_1 - E_i), \quad i = 2, \dots, N . \quad (3.62)$$

It is assumed that the reactive power measurement (H_Q), RMS voltage measurement (H_V) and voltage controller (C_V) are the same for every inverter. Then, using the

expression for the voltage control (3.37), the control for N inverters is expressed as follows:

$$E_i = C_v \cdot (V_0 - m_{Q_i} \cdot H_Q \cdot Q_i - H_v \cdot V), \quad i = 1, \dots, N. \quad (3.63)$$

From (3.62) and (3.63), every reactive power can be expressed as a function of Q_1 , i.e.

$$Q_i = \frac{X_1 + V_0 \cdot m_{Q_1} \cdot C_v \cdot H_Q}{X_i + V_0 \cdot m_{Q_i} \cdot C_v \cdot H_Q} \cdot Q_1, \quad i = 2, \dots, N. \quad (3.64)$$

By introducing (3.64) into (3.61) and operating, it is possible to obtain the characteristic equation as

$$\text{den}_Q = \sum_{j=1}^N \frac{1}{X_j + V_0 \cdot m_{Q_j} \cdot C_v \cdot H_Q}. \quad (3.65)$$

The closed-loop transfer function poles for the reactive power response can be determined from the roots of (3.65). Combining different configurations of the four inverters presented in this section, different poles are obtained, as shown in Table 3.3. As in the case of the real power, it can be seen that the system has N-1 pairs of poles and that the poles for configurations with different inverters are between the extreme poles for configurations with equal inverters.

Configuration	Poles
N times Inv1	N-1 times -7.91, -13.3 ($\xi=1$)
N times Inv2	N-1 times -10.9 \pm 6.23j ($\xi=0.87$)
N times Inv3	N-1 times -10.7 \pm 3.35j ($\xi=0.96$)
N times Inv4	N-1 times -10.7 \pm 2.07j ($\xi=0.98$)
Inv1, Inv2	-10.8 \pm 4.37j ($\xi=0.93$)
Inv1, Inv2, Inv3, Inv4	-10.9 \pm 5.62j ($\xi=0.89$) -10.7 \pm 2.75j ($\xi=0.97$) -9.10, -12.2 ($\xi=1$)

Table 3.3. Closed-loop poles for the reactive power response.

Finally, the voltage response is obtained. Introducing (3.63) into (3.60) yields to:

$$V = -\frac{X_i + V_0 \cdot m_{Q_i} \cdot C_V \cdot H_Q}{V_0 \cdot den_V} \cdot Q_i, \quad i = 1, \dots, N \quad (3.66)$$

$$den_V = C_V \cdot H_V + 1. \quad (3.67)$$

It can be observed that the voltage response depends on den_V , which has the same expression as for the two-inverter case [see (3.43)], but also on den_Q through Q_i expression. As a result, the voltage controller design is independent of the number of inverters and can be carried out as shown in section 3.3.2 for the two-inverter case.

3.4 ISSUES ABOUT DROOP METHOD

3.4.1 Line impedance influence on reactive power sharing

In this section, the inaccuracy of the reactive power control due to the line impedance is evaluated. In contrast, the real power control is not affected by the line impedance since the steady-state frequency is the same at all points of the grid [3.49], [3.50].

Once the droop method has been applied, the equivalent circuit of Fig. 3.5 can be substituted by the one presented in Fig. 3.12. The differences between these two equivalent circuits are the voltage sources and impedances. In Fig. 3.5, the voltage source $E_i|\delta_i$ represents the inverter output voltage before the filter impedance while here the voltage source $V_i|\theta_i$ represents the voltage after the filter impedance, which is controlled by means of the droop method and the voltage regulation. As a result, the impedance $R_i + X_i \cdot j$ shown in Fig. 3.5 includes the filter and line impedances while here the impedance $R_{li} + X_{li} \cdot j$ only includes the line impedance.

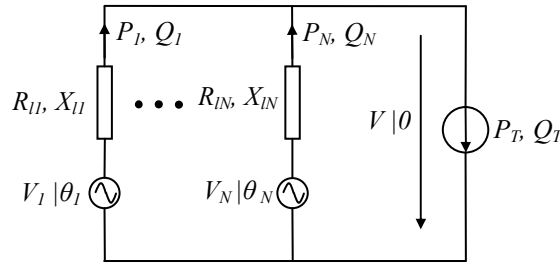


Figure 3.12. Equivalent circuit of N droop-controlled inverters connected to an AC bus through line impedances.

In the system of Fig. 3.5, the real and reactive powers injected into the bus by every inverter were determined as (3.11) and (3.12). These expressions can be readily adapted

for the system of Fig. 3.12. Assuming that the voltage variation is very small with regard to the rated value and the power angle is very small, the following expressions are obtained from (3.11) and (3.12):

$$P_i = \frac{V_0^2}{Z_{li}^2} \cdot X_{li} \cdot \theta_i + \frac{V_0}{Z_{li}^2} \cdot R_{li} \cdot (V_i - V), \quad i = 1, \dots, N \quad (3.68)$$

$$Q_i = -\frac{V_0^2}{Z_{li}^2} \cdot R_{li} \cdot \theta_i + \frac{V_0}{Z_{li}^2} \cdot X_{li} \cdot (V_i - V), \quad i = 1, \dots, N. \quad (3.69)$$

As it can be observed, the real and reactive powers now linearly depend on θ_i , V_i and V . From (3.68) and (3.69), power angle θ_i and output voltage V_i can then be worked out as a linear function of P_i , Q_i and V :

$$\theta_i = \frac{X_{li}}{V_0^2} \cdot P_i - \frac{R_{li}}{V_0^2} \cdot Q_i, \quad i = 1, \dots, N \quad (3.70)$$

$$V_i = V + \frac{R_{li}}{V_0} \cdot P_i + \frac{X_{li}}{V_0} \cdot Q_i, \quad i = 1, \dots, N. \quad (3.71)$$

Equation (3.71) shows that the real power causes a voltage drop when it flows through a resistance while the reactive power causes a voltage drop when it flows through an inductance.

Due to the droop method and the voltage regulation, the voltage droop curve (3.18) can be expressed at steady-state as

$$V_i = V_0 - m_{Qi} \cdot Q_i, \quad i = 1, \dots, N. \quad (3.72)$$

By means of (3.71) and (3.72), an expression for the grid voltage can be obtained for every inverter as

$$V = V_0 - m_{Qi} \cdot Q_i - \frac{X_{li}}{V_0} \cdot Q_i - \frac{R_{li}}{V_0} \cdot P_i, \quad i = 1, \dots, N. \quad (3.73)$$

It can be observed that, concerning the voltage droop, the droop method behaves like a constant voltage source with an output inductance. As a result, (3.73) can be modified and expressed as

$$V = V_0 - \frac{X_{di} + X_{li}}{V_0} \cdot Q_i - \frac{R_{li}}{V_0} \cdot P_i, \quad i = 1, \dots, N \quad (3.74)$$

$$X_{di} = m_{Qi} \cdot V_0 = \frac{M_q}{S_{bat,i}} \cdot V_0, \quad i = 1, \dots, N, \quad (3.75)$$

where X_{di} is the equivalent droop reactance.

Taken these considerations into account, the equivalent circuit of Fig. 3.12 can be substituted by the equivalent circuit presented in Fig. 3.13, where the circuit is now only valid for the voltage drop but not for the phase calculation. Because the droop reactances have the same per-unit value, the reactive power will be equally distributed if the line impedances are low in relation with the droop reactances. For this reason, a high droop coefficient M_q is desirable for the power sharing. However, since a too high value would cause an excessive voltage deviation in steady-state, a trade-off must be reached.

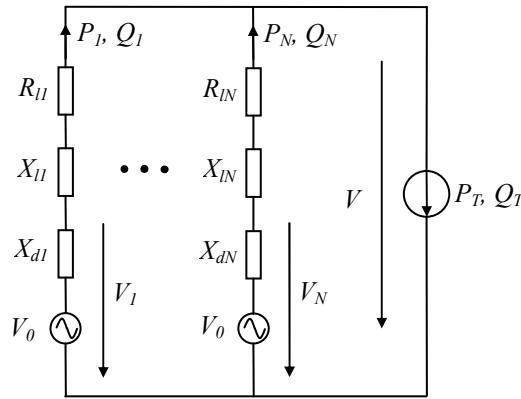


Figure 3.13. Equivalent circuit of N droop-controlled inverters connected to an AC bus through line impedances, valid for the RMS voltage calculation.

By means of the equivalent circuit of Fig. 3.13, the expressions for the reactive power distribution are derived below. Considering that the real power is perfectly distributed because it is not affected by the line, (3.74) becomes

$$V = V_0 - \frac{X_{di} + X_{li}}{V_0} \cdot Q_i - \frac{R_{li}}{V_0} \cdot \frac{S_{bat,i}}{S_{bat,tot}} \cdot P_T, \quad i = 1, \dots, N \quad (3.76)$$

where $S_{bat,tot}$ is the rated power of all inverters.

By equalizing (3.76) for $i=1$ and $i \neq 1$, every reactive power can be expressed as a function of Q_1 and P_T , i.e.

$$Q_i = \frac{X_{d1} + X_{l1}}{X_{di} + X_{li}} \cdot Q_1 + \frac{R_{l1} \cdot S_{bat1} - R_{li} \cdot S_{bat,i}}{(X_{di} + X_{li}) \cdot S_{bat,tot}} \cdot P_T, \quad i = 2, \dots, N. \quad (3.77)$$

Introducing (3.77) into (3.61) and operating makes it possible to obtain the expression for Q_1 as a function of Q_T and P_T . Proceeding similarly for the other inverters, a general expression for Q_i is determined as

$$Q_i = \frac{1}{\sum_{j=1}^N \frac{1}{X_{dj} + X_{lj}}} \cdot \left[Q_T + \sum_{\substack{j=1 \\ j \neq i}}^N \frac{R_{lj} \cdot S_{bat,j} - R_{li} \cdot S_{bat,i}}{(X_{dj} + X_{lj}) \cdot S_{bat,tot}} \cdot P_T \right], \quad i=1, \dots, N. \quad (3.78)$$

As an example, (3.78) particularized for two inverters becomes

$$Q_1 = \frac{X_{d2} + X_{l2}}{X_{d1} + X_{l1} + X_{d2} + X_{l2}} \cdot Q_T + \frac{R_{l2} \cdot S_{bat2} - R_{l1} \cdot S_{bat1}}{(X_{d1} + X_{l1} + X_{d2} + X_{l2}) \cdot S_{bat,tot}} \cdot P_T \quad (3.79)$$

$$Q_2 = \frac{X_{d1} + X_{l1}}{X_{d1} + X_{l1} + X_{d2} + X_{l2}} \cdot Q_T + \frac{R_{l1} \cdot S_{bat1} - R_{l2} \cdot S_{bat2}}{(X_{d1} + X_{l1} + X_{d2} + X_{l2}) \cdot S_{bat,tot}} \cdot P_T. \quad (3.80)$$

In order to better understand how the reactive power is distributed in a real case, an example is provided for two inverters connected in parallel in a low-voltage grid with long lines. The inverters are the ones previously presented in Table 3.1, and the line cables are selected from recent regulations [3.51]. The line for inverter 1 is chosen with a cross-sectional area of 6 mm², which leads to a resistance of 3.56 Ω/km and a reactance of 2.06 Ω/km, and the line for inverter 2 is selected with a cross-sectional area of 2.5 mm², which leads to a resistance of 8.57 Ω/km and a reactance of 4.93 Ω/km, both at a 60°C copper operation temperature [3.52]. It is worth noting that the cable lengths correspond to the distance before both inverters are connected in parallel because the line after this point can be considered as part of the load and does not therefore cause power inaccuracy.

Fig. 3.14 shows the per-unit reactive power provided by each inverter with a cable length equal to 100 m for inverter 1 and a cable length varying from 0 to 200 m for inverter 2. The first graph is obtained for a situation with more consumption than generation, with $P_T=7$ kW and $Q_T=5$ kVAr, while the second graph is determined for higher generation, with $P_T=-7$ kW and $Q_T=5$ kVAr. Although $S_T=8.6$ kVA is lower than the rated power $S_{bat,tot}=9$ kVA, one inverter is overloaded in many situations, specifically when $q_i > 0.63$. It can be observed that the line influence is very important in this system and that the real power also has a high effect in low-voltage grids due to the ratio $R/X > 1$. As a conclusion, in a low-voltage system with very long lines, the inverters should be placed at a similar distance from the loads. If this is not possible, a more complicated reactive power droop method should be applied [3.50], [3.53]–[3.55].

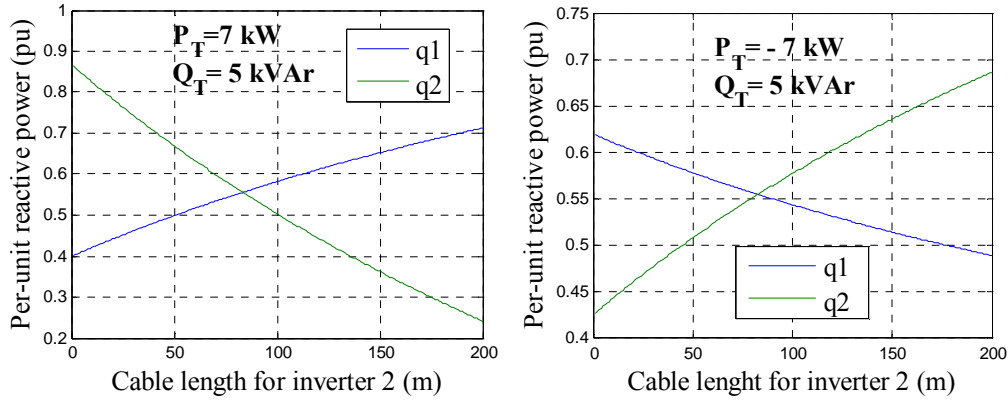


Figure 3.14. Reactive power inaccuracy due to line impedance in a low-voltage grid with long lines, cable length for inverter 1 is 100 m.

3.4.2 Inverter current limitation

The RMS voltage regulation controls the RMS grid voltage V by changing directly the RMS inverter output voltage E (see Fig. 3.4). Since there is no inner current loop, the inverter current is not controlled. For this reason, a hardware current limitation is carried out as a means of protection against severe overloads or short-circuits. Even with this current protection, the implementation and design of the RMS voltage regulation is much simpler than the instantaneous voltage regulation.

Fig. 3.15 shows the circuit used for the current protection, where T1–T4 are the switching signals for the inverter IGBTs, and T1v–T4v are the switching signals coming from the PWM modulation. If the inverter current is within limits ($\pm 35 \text{ A}$ peak value in the example), T1–T4=T1v–T4v and the commutations are not modified. However, when the inverter current reaches the limit current, the switching signals T1–T4 are set to zero, regardless of the PWM modulation. Since all the IGBTs are open, only the inverter diodes must be taken into account. Thus, when the inverter current is higher than zero, the output voltage is equal to minus the DC bus voltage, and when it is lower than zero, the output voltage is equal to the DC bus voltage. As a result, the peak current value is limited to the desired value.

Fig. 3.16 shows simulation results with inverter current limitation. The inverter current is represented in first graph and the grid voltage is plotted in the second graph. At the beginning, the inverter is able to supply the load and the voltage is correctly generated. Then, when another load is connected, the inverter current exceeds its limit value and the current protection activates. As a result, the peak current is limited to $\pm 35 \text{ A}$, and the grid voltage drops. That load is then disconnected and, after a period, a

short-circuit is applied. It can be observed that the current protection achieves its objective and the current always stays within limits, even though the grid voltage drops to zero. In this situation, the inverter can remain connected for some cycles waiting for the short-circuit to cease, after which it should be disconnected.

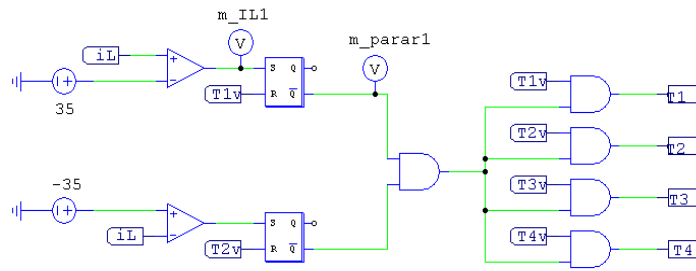


Figure 3.15. Circuit used for the inverter current limitation.

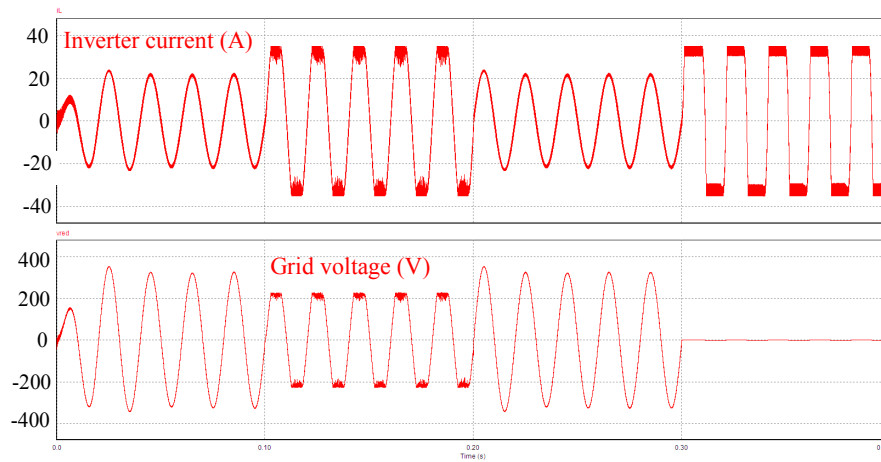


Figure 3.16. Overload and short-circuit simulation results with inverter current limitation.

This current limitation scheme generates many harmonics. However, this is not an issue because this protection is intended to extreme situations, in which the equipment safety is much more important than the power quality.

3.4.3 DC current control

Thanks to the presented droop method, all inverters equally share their per-unit real and reactive powers. This control only acts on the fundamental current and does not account for the DC voltage and current.

Fig. 3.17 shows the DC equivalent circuit of N inverters connected in parallel. Voltage $E_{dc,i}$ represents the DC voltage generated by the inverter, $I_{dc,i}$ is the inverter DC current, V_{dc} is the DC grid voltage, R_i includes the filter inductor equivalent resistance and the line resistance, R_L is the load resistance and $I_{dc,T}$ represents the DC current absorbed by non-linear loads.

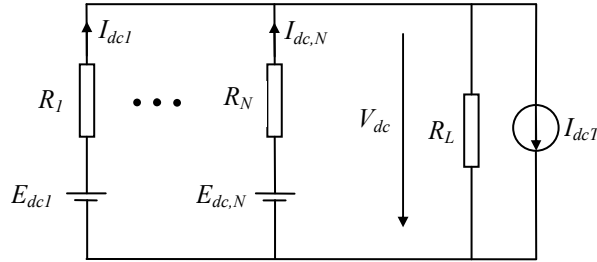


Figure 3.17. DC equivalent circuit of N inverters connected to a common bus.

In systems with short lines, the value of R_i tends to be very small. As a consequence, if the inverters have no control on the DC voltage or if they try to set their output DC voltage to zero, very small differences between DC generated voltages $E_{dc,i}$ will result in large DC circulating currents. On the other hand, in systems with longer lines, the different cable sizes and distances to the point of common coupling leads to different per-unit equivalent resistances r_i . As a result, the DC current will not be equally shared among the inverters.

In order to solve these problems, the implementation of a virtual capacitor has been proposed [3.56]. The authors claim that the DC circulating currents are completely eliminated. However, in a real case, the DC load voltage is considerably increased due to offsets in the current sensors. Instead, a DC voltage droop, very similar to the RMS voltage droop employed for the reactive power regulation, can be used [3.57]. With this method, the DC voltage reference is obtained as

$$V_{dc,i}^* = -R_{dc,i} \cdot I_{dc,i}, \quad i = 1, \dots, N. \quad (3.81)$$

where $R_{dc,i}$ is the droop resistance. In order to share the DC current in proportion to the inverter ratings, this resistance is set to

$$R_{dc,i} = \frac{V_0^2}{S_{bat,i}} \cdot r_{dc}, \quad i = 1, \dots, N. \quad (3.82)$$

where r_{dc} is the per-unit droop resistance, which has the same value for every inverter.

Then, the DC voltage is regulated by means of a PI controller C_{Vdc} . The DC voltage generated by each inverter can be expressed as

$$E_{dc,i} = C_{Vdc} \cdot (V_{dc,i}^* - V_{dc,i}), \quad i = 1, \dots, N. \quad (3.83)$$

At steady-state, thanks to the DC voltage regulation, (3.81) becomes

$$V_{dc,i} = -R_{dc,i} \cdot I_{dc,i}, \quad i = 1, \dots, N. \quad (3.84)$$

As a result, the equivalent circuit of Fig. 3.17 can be substituted by the equivalent circuit of Fig. 3.18 after the DC droop method has been applied. Because the droop resistances have the same per-unit value, the DC current will be equally distributed if the line resistances are low in relation with the droop resistances. For this reason, a high droop resistance r_{dc} is desirable for the DC current sharing. However, a too high value could bring the DC current response unstable and would cause an excessive DC grid voltage. As consequence, similarly to the reactive power droop design, a trade-off must be reached.

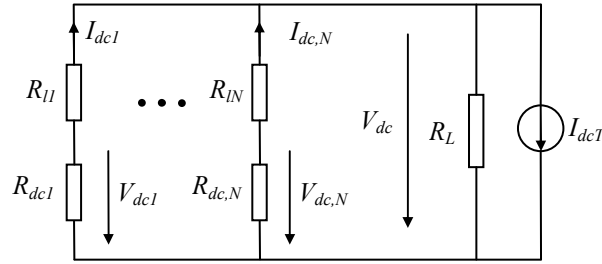


Figure 3.18. DC equivalent circuit of N droop-controlled inverters connected to a common bus.

Although it is not shown here for space reasons, the equivalent circuit of Fig. 3.18 makes it possible to derive the expressions for the DC current distribution following the procedure used in section 3.4.1 for the reactive power distribution.

3.4.4 Overload voltage reduction

Overload occurs when the load demand is very high and the generation is low. As a result, the current delivered by the inverters exceed their rated values. In this situation, the inverters cannot operate continuously, and they must stop to prevent from overheating. In order to make it possible that the system continues in operation, a modification of the voltage droop is presented in this section.

The RMS voltage–reactive power droop is represented by (3.18) and (3.20). By means of this voltage droop, the voltage is reduced as the provided reactive power increases. With the intention of augmenting this effect, the curve slope is enlarged as the provided real power increases. In doing so, the grid voltage and consequently the load absorbed current will further decrease for linear loads. This is only carried out when the real power is positive (when it is negative, the renewable energy should be reduced), and when the reactive power is positive, i.e. for inductive loads. The modified voltage droop is thus expressed as

$$V_i^* = V_0 - M_q \cdot q_i, \quad \text{if } p_i < 0 \text{ or } q_i < 0, \quad i = 1, \dots, N. \quad (3.85)$$

$$V_i^* = V_0 - \frac{M_q}{1 - a \cdot p_i} \cdot q_i, \quad \text{if } p_i > 0 \text{ and } q_i > 0, \quad i = 1, \dots, N, \quad (3.86)$$

where p_i and q_i are the per-unit real and reactive power provided by each inverter, and $a < 1$ is the overload coefficient.

The overload RMS voltage–reactive power droop for constant real power is shown in Fig. 3.19 for $M_q = 20$ V and $a = 3/4$. According to regulations, the voltage has to be between $V_{max} = 1.1 \cdot V_0 = 253$ V and $V_{min} = 0.85 \cdot V_0 = 195.5$ V, which allows for a voltage reduction below the limit of the non-modified voltage droop $V = V_0 - M_q = 210$ V.

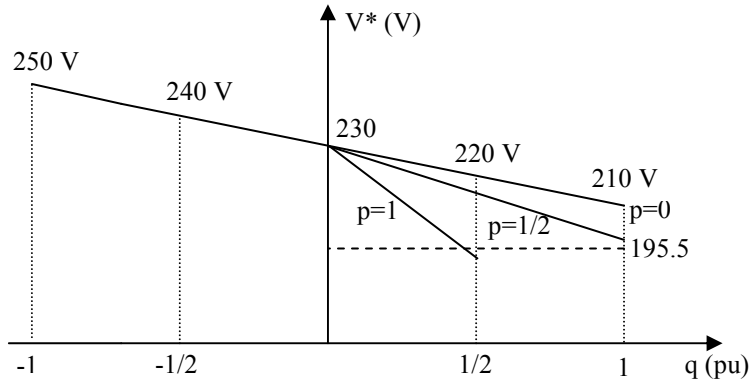


Figure 3.19. Overload RMS voltage–reactive power droop.

Fig. 3.20 shows the RMS voltage versus reactive power curves for constant apparent power, where $s_i = S/S_{bat,i}$ represents the per-unit apparent power. It can be observed that when the apparent power is small, the curve is very similar to the original one, thus having little impact on the loads. However, when the apparent power is higher, the voltage is further reduced, making it possible to supply linear loads with a high rated

power. As it can be observed in the figure, when the inverters are providing their rated apparent power ($s=1$), the lowest voltage will be close to $V=200\text{ V} > V_{min}=195\text{ V}$.

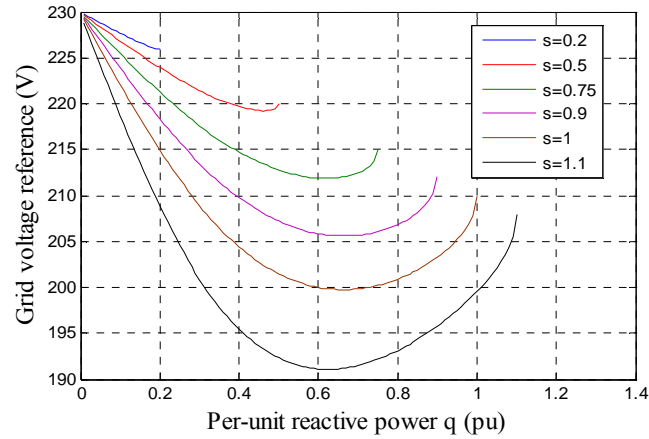


Figure 3.20. RMS voltage versus per-unit reactive power curves for constant apparent power.

This method makes it possible to supply large loads at the expense of reducing the power below the load rated power. This power reduction also occurs when the inverters are not overloaded. However, the method is advantageous with some load profiles, for example with loads which alternate between high and low power demand. Apart from this, it is worth noting that the voltage can drop below the minimum permitted value for long lines and that it does not work with systems mainly based on constant power loads.

3.5 DROOP METHOD FOR NON-LINEAR LOADS

3.5.1 Harmonic distribution without control

The droop method presented so far makes it possible to equally share the per-unit real and reactive powers and the DC current among the various inverters. The control only acts on the fundamental and DC current. However, when feeding non-linear loads, the lack of control on the harmonic currents will cause poor sharing of these harmonics and a high voltage THD, as it is shown in this section. In the following section, a harmonic compensation will be presented to show how the control performance can be improved for non-linear loads.

The system represented in Fig. 3.3 is valid for non-linear loads if one considers that the total current i_T is composed by the fundamental component $i_{T,fund}$ and the harmonic

components $i_{T,harm}$. The harmonic components are $i_{T,m}$, where m is odd for typical non-linear loads:

$$i_T = i_{T,fund} + i_{T,harm} = i_{T,fund} + i_{T,3} + i_{T,5} + i_{T,7} + \dots \quad (3.87)$$

Similarly, the current supplied by the battery inverters i_i can be split into:

$$i_i = i_{i,fund} + i_{i,harm} = i_{i,fund} + i_{i,3} + i_{i,5} + i_{i,7} + \dots, \quad i = 1, \dots, N. \quad (3.88)$$

Grid voltage v and output voltage e_i can also be split into their fundamental and harmonic components:

$$v = v_{fund} + v_{harm} = v_{fund} + v_3 + v_5 + v_7 + \dots \quad (3.89)$$

$$e_i = e_{i,fund} + e_{i,harm} = e_{i,fund} + e_{i,3} + e_{i,5} + e_{i,7} + \dots, \quad i = 1, \dots, N. \quad (3.90)$$

Making use of the control presented in section 3.3, the output voltage e_i only has the fundamental component, i.e. $e_i = e_{i,fund}$ and $e_{i,harm} = 0$. Then, the equivalent circuit for the harmonic distribution is as shown in Fig. 3.21.

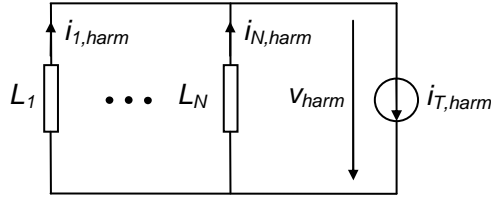


Figure 3.21. Equivalent circuit for the harmonic distribution.

From Fig. 3.21, harmonic currents can be obtained for each different harmonic m as

$$i_{1,m} + \dots + i_{N,m} = i_{T,m}, \quad m = 3, 5, 7, \dots \quad (3.91)$$

$$v_m = -L_i \frac{di_{i,m}}{dt}, \quad m = 3, 5, 7, \dots, \quad i = 1, \dots, N. \quad (3.92)$$

For the N inverters, introducing (3.92) in (3.91) yields to

$$v_m = -(L_1 // \dots // L_N) \cdot \frac{di_{T,m}}{dt}. \quad (3.93)$$

This equation shows that harmonics in the grid voltage are proportional to the equivalent parallel impedance. Since these inductances are considerable, the harmonic voltage is significant. Moreover, due to the inductor behavior, high frequency harmonics are magnified.

The harmonic current sharing among the inverters can be determined from (3.92) and (3.93) as

$$i_{i,m} = \frac{L_1 // \dots // L_N}{L_i} \cdot i_{T,m}, \quad m = 3, 5, 7, \dots, \quad i = 1, \dots, N. \quad (3.94)$$

This equation shows that the per-unit harmonic currents are equally distributed only if all inverters have the same per-unit output impedance. However, this is not often the case and, as a result, the harmonic currents are not equally shared among the inverters.

3.5.2 Harmonic compensation

Obviously, there will always be a harmonic voltage drop in the output inductance because of the harmonic current through it. In order to avoid that this voltage drop is reflected in the grid voltage, the inverter must generate a harmonic compensation in its output voltage e_i . As a solution, we propose that each inverter generates the following harmonic voltage:

$$e_{i,m} = L_{vi} \cdot \frac{di_{i,m}}{dt}, \quad m = 3, 5, 7, \dots, \quad i = 1, \dots, N, \quad (3.95)$$

where L_{vi} is the virtual inductance of the inverter i and $L_{vi} < L_i$.

In so doing, and defining the harmonic inductance as $L_{harm,i} = L_i - L_{vi}$, the harmonic components of the grid voltage become

$$v_m = e_{i,m} - L_i \cdot \frac{di_{i,m}}{dt} = -L_{harm,i} \cdot \frac{di_{i,m}}{dt}, \quad m = 3, 5, 7, \dots, \quad i = 1, \dots, N. \quad (3.96)$$

Considering all inverters, the grid voltage harmonics and the harmonic current distribution is now as follows:

$$v_m = -\left(L_{harm,1} // \dots // L_{harm,N}\right) \cdot \frac{di_{T,m}}{dt}, \quad m = 3, 5, 7, \dots \quad (3.97)$$

$$i_{i,m} = \frac{L_{harm,1} // \dots // L_{harm,N}}{L_{harm,i}} \cdot i_{T,m}, \quad m = 3, 5, 7, \dots, \quad i = 1, \dots, N. \quad (3.98)$$

From (3.98), it can be observed that the per-unit harmonic current is now equally distributed only if all inverters have the same per-unit harmonic inductance. In other words, if

$$L_{harm,i} \cdot S_{bat,i} = k, \quad i = 1, \dots, N. \quad (3.99)$$

where k is a constant.

3.5.3 Simulation results

The proposed technique has been validated by simulation. For this purpose, the system has been modeled in the software PSIM. Two single-phase inverters have been parallelized and generate the grid. A full diode bridge rectifier feeding a RC load has been connected to the grid together with a linear inductive load. The features of the inverters are shown in Table 3.4 and those of the loads are shown in Table 3.5. Accounting for the rated powers, inverter 1 should supply 66.6% of the current harmonics and inverter 2 33.3%.

	Inverter 1	Inverter 2
Rated power S_{nom}	6000 VA	3000 VA
Output inductance L	3 mH	4 mH
Virtual inductance L_v	2.2 mH	2.4 mH
Harmonic inductance L_{harm}	0.8 mH	1.6 mH
Parameter k	4.8 VA·H	4.8 VA·H

Table 3.4. Inverter features.

Linear load active power	1800 W
Linear load reactive power	750 VAr
Resistance at the output of the diode bridge	70 Ω
Capacitance at the output of the diode bridge	1 mF
Non-linear load active power	1500 W

Table 3.5. Load features.

In the first simulation, the droop method and the voltage regulation are applied but there is no harmonic compensation, as in section 3.5.1. Instantaneous currents and powers as well as current and grid voltage harmonics in steady-state are represented in Fig. 3.23. At the beginning, inverter 1 is supplying the whole load. Then, inverter 2 is connected. Thanks to the droop method, the fundamental current is well shared because $P_1=2 \cdot P_2$ and $Q_1=2 \cdot Q_2$. However, as it was expected from (3.94), $i_{1,m}=57\% \cdot i_{T,m}$ and $i_{2,m}=43\% \cdot i_{T,m}$, which represents a poor harmonic current distribution. In addition, high harmonics are introduced to the grid voltage, as predicted by (3.93).

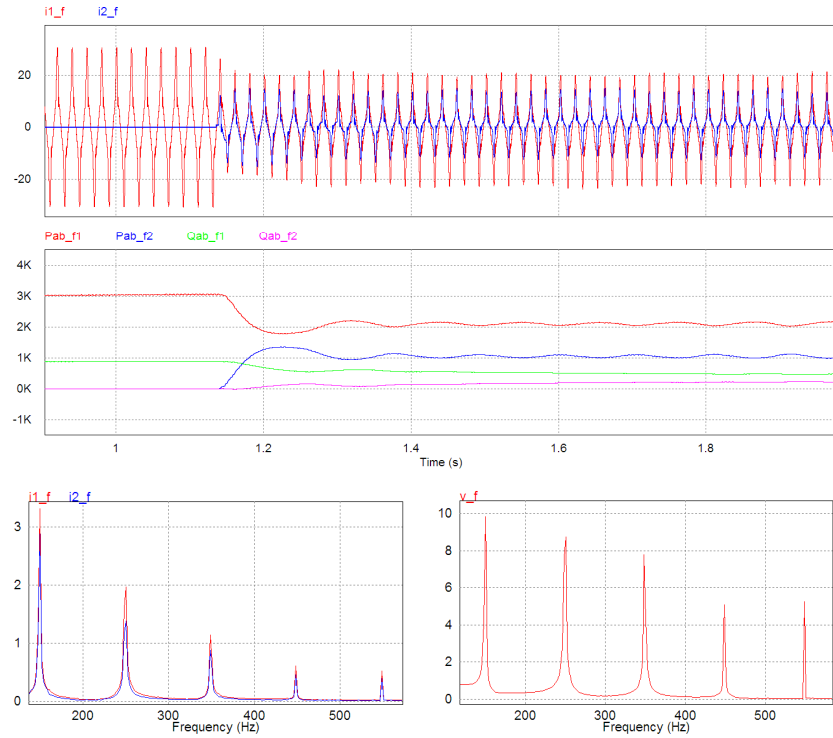


Figure 3.23. Simulation results without harmonic compensation.

The second simulation is the same as the first one but applying the harmonic compensation for $m=3, 5, 7$ and 9 , as in section 3.5.2. The results are shown in Fig. 3.24. It can be observed that harmonic currents are now equally shared among the inverter since $i_{1,m}=2 \cdot i_{2,m}$. In addition, grid voltage harmonics for $m=3, 5, 7$ and 9 are considerably reduced.

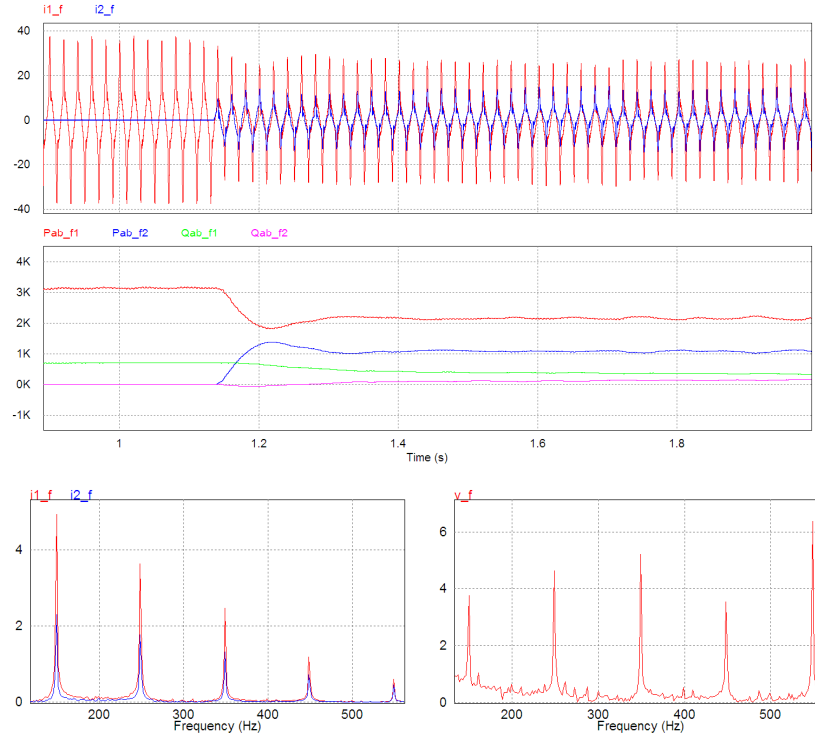


Figure 3.24. Simulation results with harmonic compensation.

3.6 ENERGY MANAGEMENT DURING NORMAL OPERATION

Thanks to the employed droop method, the real power, reactive power, DC current and harmonic currents are equally shared among the different battery inverters. Although the ratios between the battery capacity and the inverter rated power (C/S_{bat}) should ideally be the same for all battery inverters to ensure that all battery state-of-charges (SOC) change simultaneously, in real applications this is not so. The initial C/S_{bat} ratio will never be exactly the same for all battery inverters due to manufacturing variation or inadequate system sizing. Moreover, the battery aging will lead to a capacity reduction which will be more pronounced in some battery banks than in others. The initial SOC can also vary considerably from one battery to another. These situations cause the batteries to operate with different SOC's leading to less than optimal operation. For this reason, SOC management is required, which is presented in this section for normal operation, i.e. when the battery voltage and current are within rated values.

Section 3.6.1 analyzes the existing SOC-based droop method which modifies the $P-f$ curve slope as a function of the SOC, hereinafter to be called the slope changing method.

The power and SOC responses are first studied and then simulation results for a real power profile are presented. Section 3.6.2 analyzes the proposed SOC-based droop control, to be called the curve shifting method. Following a similar study to the slope changing method, both techniques are compared. Then, in section 3.6.3, the experimental results for the proposed method are shown.

The two inverters and the system parameters used throughout this section are presented in Table 3.6.

Nominal RMS amplitude E_0	230 V
Nominal RMS amplitude V_0	230 V
Battery 1 nominal capacity C_1	48 kWh
Battery 2 nominal capacity C_2	24 kWh
Inverter 1 rated power S_{bat1}	6000 VA
Inverter 2 rated power S_{bat2}	3000 VA
Inverter 1 output inductance L_1	3 mH
Inverter 2 output inductance L_2	4 mH
Time constant of the power filter τ_P	20 ms
Power sample time T_S	5 ms

Table 3.6. System parameters.

3.6.1 Slope changing method

3.6.1.1 Description

For the purpose of balancing the battery SOC's without the use of communications, the $P-f$ curve must be changed as a function of each battery's SOC. From (3.17), two parameters can be used for this purpose, namely f_0 and M_p . The slope changing method, described in [3.32], proposes modifying the $P-f$ curve slope M_p . The curve proposed in [3.32] is chosen for the comparison because it represents a more general approach. This curve is expressed as follows:

$$f_i = f_0 - M_p \cdot p_i = f_0 - \frac{M_0}{SOC_i^n} \cdot p_i, \quad p_i > 0, \quad i = 1, \dots, N \quad (3.102)$$

$$f_i = f_0 - M_p \cdot p_i = f_0 - M_0 \cdot SOC_i^n \cdot p_i, \quad p_i < 0, \quad i = 1, \dots, N, \quad (3.103)$$

where M_0 is the droop coefficient for $SOC_i=1$, and n is the SOC exponent ($n>0$). Low n values cause slope M_p to vary slightly and, as a result, M_p always remains similar to M_0 .

On the contrary, high n values cause slope M_p to change significantly for low SOC_s and, as a result, M_p reaches higher values than M_0 for $p>0$ and lower values than M_0 for $p<0$.

As an example, the $P-f$ curve is shown in Fig. 3.25 for $f_0=50$ Hz, $M_0=0.1$ Hz, $n=1$ and two batteries ($SOC_1=1$ and $SOC_2=0.5$). It can be observed that for battery inverter 1, $M_p = M_0 = 0.1$ Hz when it is supplying or absorbing power because $SOC_1=1$. However, for battery inverter 2, $M_p=0.2$ Hz $> M_0$ when it is discharging and $M_p=0.05$ Hz $< M_0$ when it is charging. Two steady-state operating points for two frequencies (49.94 and 50.04 Hz) are also shown in the figure. When the load demand is higher than generation ($P_T>0$), both batteries discharge. It can be seen how inverter 1 supplies more per-unit power than inverter 2, thus helping balance the SOC_s. On the other hand, when the generation is higher than the load demand ($P_T<0$), both batteries charge. In this case, inverter 2 absorbs more per-unit power than inverter 1, which also helps balance the SOC_s.

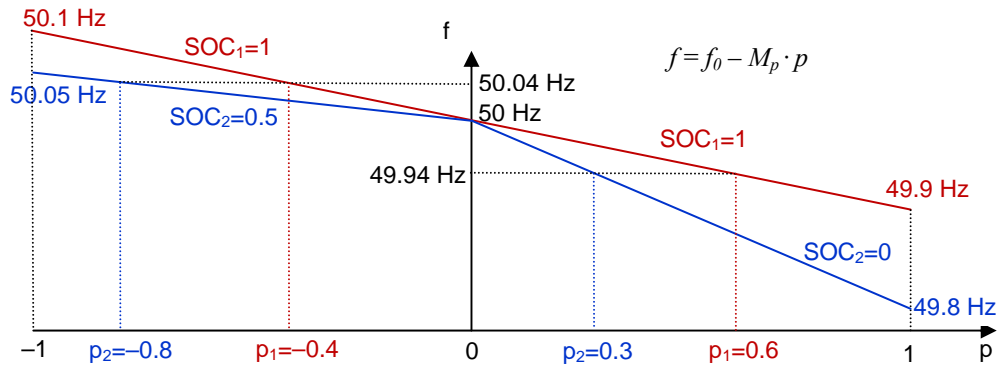


Figure 3.25. $P-f$ curve for the slope changing method.

The steady-state operating point can be easily obtained if it is considered that $f_1=f_2$ after the power transient. Equations (3.25) and (3.102) serve to obtain, for $P_T>0$,

$$\frac{p_1}{p_2} = \left(\frac{SOC_1}{SOC_2} \right)^n, \quad p_1, p_2 > 0 \quad (3.104)$$

$$P_1 = \frac{S_{bat1} \cdot SOC_1^n}{S_{bat1} \cdot SOC_1^n + S_{bat2} \cdot SOC_2^n} \cdot P_T, \quad P_T > 0 \quad (3.105)$$

$$P_2 = \frac{S_{bat2} \cdot SOC_2^n}{S_{bat1} \cdot SOC_1^n + S_{bat2} \cdot SOC_2^n} \cdot P_T, \quad P_T > 0. \quad (3.106)$$

Equation (3.104) shows that, using this method, the real power ratio depends on the ratio between the SOC_s. The parameter n increases ($n>1$) or lowers ($n<1$) the power ratio for the same SOC ratio.

Depending on the inverter powers and the battery SOC, the grid frequency will have different values. The frequency will be lower than f_0 when the battery is delivering power and it will be higher than f_0 when the battery is absorbing power. The minimum frequency f_{min} is given for $SOC = SOC_{min}$ and $p=1$, whereas the maximum frequency f_{max} is found for $SOC = SOC_{max}$ and $p=-1$. The SOC is saturated to $SOC_{min}=0.1$ to prevent M_p from rising to a very large value. Using (3.102) and (3.103), the limit frequency values are then determined as

$$f_{min} = f_0 - \frac{M_0}{0.1^n}, \quad f_{max} = f_0 + M_0. \quad (3.107)$$

The slope changing method has two degrees of freedom for the design: M_0 and n . Careful consideration should be given to the selection of these parameters since they affect the frequency deviation, the power response performance and the SOC responsiveness. With regard to the frequency deviation, f_{min} can reach very low values, as shown in (3.107). However, this problem has already been solved in the literature by means of a secondary control which restores the frequency to its nominal value [3.32].

3.6.1.2 Influence of M_0 and n on the power response

By using the model developed in section 3.3.2 and taking into account the system parameters presented in Table 3.6, the root locus diagram for the parameter M_p is obtained, as shown in Fig. 3.26. For this root locus, the sampling and measurement of the real power is considered by means of H_p transfer function, which is defined as

$$H_p = \frac{1}{1 + \tau_p s} \cdot \frac{1}{1 + 1.5 \cdot T_s \cdot s}. \quad (3.108)$$

Although the system has three poles, only the two dominant ones are shown in Fig. 3.26. It can be observed that the system has first order dynamics for low M_p values. Increasing M_p makes the system less damped. Finally, from a certain M_p value, the system becomes unstable. In this case, a good solution for parameter M_p is 0.3 Hz, which has been chosen as a trade-off between fast dynamics and a high stability margin.

As shown in Fig. 3.26, droop method dynamics are highly dependent on the droop coefficient M_p . The slope changing method is based on modifying this coefficient in order to balance the SOC. Consequently, this method results in variable power response performance. The slope variation range must then be restricted in order to prevent the system from a slow power response (low M_p) or instability (high M_p). According to (3.102) and (3.103), the maximum M_p (charging side) and minimum M_p (discharging side) can be found for $SOC = SOC_{min}=0.1$ as

$$M_{p\max} = \frac{M_0}{0.1^n}, \quad M_{p\min} = 0.1^n \cdot M_0. \quad (3.109)$$

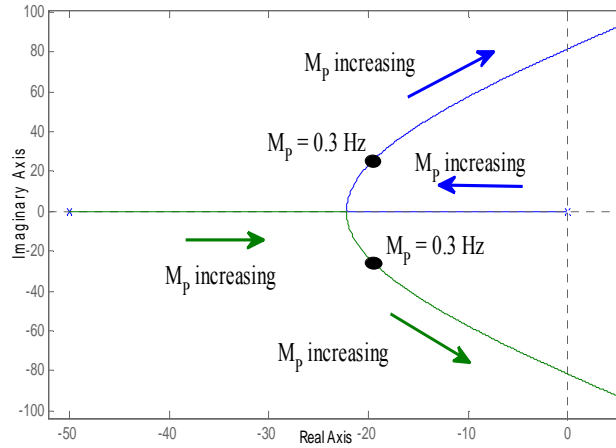


Figure 3.26. Root locus diagram for the parameter M_p .

A high M_p value leads to a faster response and reduces the damping factor. That means that $M_{p\max}$ has to be limited in order to guarantee a certain stability margin. Here, the minimum damping factor ξ_{\min} has been taken as 0.2, which determines the maximum slope $M_{p\max}$. The constraint $\xi \geq 0.2$ is very important since it is related to the system stability. Due to this constraint, one degree of freedom is already used and the slope changing method has now only one design parameter, namely parameter n .

Table 3.7 shows the power response parameters for different n values for the system presented in Table 3.6. $M_{p\max}$ is set at 1 Hz due to the stability constraint. This value can be determined from the root locus of Fig. 3.26 for $\xi = 0.2$. The remaining parameters depend on n . For a certain n value, M_0 and $M_{p\min}$ can be obtained from (3.109). Parameter τ_{\min} is the power response time constant of the slowest operating point and is obtained from the root locus of Fig. 3.26 for $M_p = M_{p\min}$. As can be observed in Table 3.7, the power response becomes very slow for high n values. The power distribution accuracy is another problem related to low M_p values. In fact, errors in the frequency generated by the converter lead to important errors in the power distribution when M_p is very low. This power error, referred to as $\Delta P_{\max_ \Delta f_{er}}$, is defined for the worst case, i.e. $SOC_1 = SOC_2 = SOC_{\min}$, and its expression for a total frequency error $\Delta f_{error} = f_{error1} + f_{error2}$ can be obtained by means of (3.25) and (3.103) as

$$\Delta P_{\max_ \Delta f_{er}} = \frac{2 \cdot S_{bat1} \cdot S_{bat2}}{S_{bat1} + S_{bat2}} \cdot \frac{\Delta f_{error}}{M_{p\min}}. \quad (3.110)$$

n	M_{Pmax}	M_0	M_{Pmin}	ξ_{min}	τ_{min}	$\Delta P_{max_ \Delta f_{er}}$
0.5	1 Hz	0.32 Hz	0.1 Hz	0.2	0.10 s	400 W
0.8	1 Hz	0.16 Hz	0.025 Hz	0.2	0.50 s	1592 W
1	1 Hz	0.1 Hz	0.01 Hz	0.2	1.30 s	4000 W
1.2	1 Hz	0.063 Hz	0.004 Hz	0.2	3.28 s	10000 W
1.5	1 Hz	0.032 Hz	0.001 Hz	0.2	13.2 s	40000 W

Table 3.7. Power response parameters for different n values.

In Table 3.7, $\Delta P_{max_ \Delta f_{er}}$ is calculated for a frequency error $\Delta f_{error} = 0.01$ Hz. As shown, it reaches very large values. The table also shows the strong influence of parameter n . For $n > 1$, the power response becomes very slow and the power errors become very important for the worst operating conditions (with low SOC and charging the batteries). From the point of view of the power response, it is therefore preferable to set low n values. In so doing, slope M_p will not vary too much and its value will always be close to the optimum one.

3.6.1.3 Influence of n on the SOC response

In order to analyze the influence of parameter n on the SOC, a simple modeling for the SOC response is first developed for a two-battery system. This will make it possible to determine the time constant for the SOC balancing as well as the SOC imbalance for different C/S_{bat} ratios. Only the battery discharging situation will be shown here. The analysis for battery charging is similar and leads to the same conclusions.

The battery SOC can be calculated as

$$SOC = SOC_i - \frac{1}{C_{Ah}} \cdot \int i_{bat} \cdot dt, \quad (3.111)$$

where SOC_i is the initial SOC, C_{Ah} is the battery capacity in Ah, and i_{bat} is the battery current (delivered). For a better SOC estimation, an enhanced coulomb counting method is used here [3.58]. Furthermore, in order to prevent long-term errors, the SOC is reset to 100% when the lead-acid battery operates at float voltage during a certain time, which is given by the manufacturer. This situation is frequent in stand-alone systems with no dispatchable units since the renewable generators must be oversized in order to reduce the loss of load probability [3.59].

Disregarding conversion losses and considering the battery voltage to be constant, (3.111) applied to the two batteries becomes

$$SOC_1 = SOC_{i1} - \frac{1}{C_1} \cdot \int P_1 \cdot dt \quad (3.112)$$

$$SOC_2 = SOC_{i2} - \frac{1}{C_2} \cdot \int P_2 \cdot dt, \quad (3.113)$$

where C_1 and C_2 are the battery capacity in Wh.

Perturbing (3.112) and (3.113) and applying Laplace transform gives (small-signal variables are marked with a circumflex)

$$\hat{SOC}_1 = -\frac{\hat{P}_1}{C_1 \cdot s}, \quad \hat{SOC}_2 = -\frac{\hat{P}_2}{C_2 \cdot s}. \quad (3.114)$$

As the power response is much faster than the SOC response, it can be considered that the powers have reached their steady-state values and equations (3.104)–(3.106) are valid. The condition $f_1=f_2$ is thus also true, and by means of (3.102) it results in

$$P_1 \cdot SOC_2^n \cdot S_{bat2} = P_2 \cdot SOC_1^n \cdot S_{bat1}. \quad (3.115)$$

Perturbing (3.115) leads to

$$\begin{aligned} n \cdot SOC_2^{n-1} \cdot P_1 \cdot S_{bat2} \cdot \hat{SOC}_2 + SOC_2^n \cdot S_{bat2} \cdot \hat{P}_1 = \\ = n \cdot SOC_1^{n-1} \cdot P_2 \cdot S_{bat1} \cdot \hat{SOC}_1 + SOC_1^n \cdot S_{bat1} \cdot \hat{P}_2. \end{aligned} \quad (3.116)$$

Then, introducing in this equation \hat{SOC}_1 and \hat{SOC}_2 expressions shown in (3.114), P_1 and P_2 expressions shown in (3.105) and (3.106), and small-signal P_2 expression obtained from (3.25), the characteristic equation den_{SOC} for the SOC response is obtained as

$$\begin{aligned} den_{SOC} = n \cdot P_T \cdot S_{bat1} \cdot S_{bat2} \left(\frac{SOC_1^n \cdot SOC_2^{n-1}}{C_2} + \frac{SOC_1^{n-1} \cdot SOC_2^n}{C_1} \right) + \\ + (S_{bat1} \cdot SOC_1^n + S_{bat2} \cdot SOC_2^n) \cdot s \end{aligned} \quad (3.117)$$

The closed-loop transient response is determined by the roots of den_{SOC} . Since it is a first order equation with positive coefficients, the SOC response is always stable. The small-signal time constant $\tau_{SOC,sl}$ associated with the pole can be easily obtained from (3.117) as

$$\tau_{SOC,sl} = \frac{C_1 \cdot C_2 \cdot (S_{bat1} \cdot SOC_1^n + S_{bat2} \cdot SOC_2^n)^2}{n \cdot P_T \cdot S_{bat1} \cdot S_{bat2} (C_1 \cdot SOC_1^n \cdot SOC_2^{n-1} + C_2 \cdot SOC_1^{n-1} \cdot SOC_2^n)}. \quad (3.118)$$

From (3.118), it can be stated that $\tau_{SOC,sl}$ depends both on some constant system parameters (battery capacities, inverter rated powers and parameter n) and on some

variables (the SOC_s and the net power P_T). As a result, $\tau_{SOC,sl}$ varies during operation due to SOC and P_T variations. It is clear from (3.118) that the SOC response is faster for high values of net power P_T . The time constant $\tau_{SOC,sl}$ is represented in Fig. 3.27 as a function of SOC₁ for different n values. In this figure, SOC₂=0.5, $P_T=4500$ W, and the system parameters are the ones presented in Table 3.6. It can be observed that the response is faster for low SOC values and for high n values. In order to achieve a rapid SOC convergence, it is thus preferred to select a high value for parameter n , which contrasts with the low n value preferred in terms of power response.

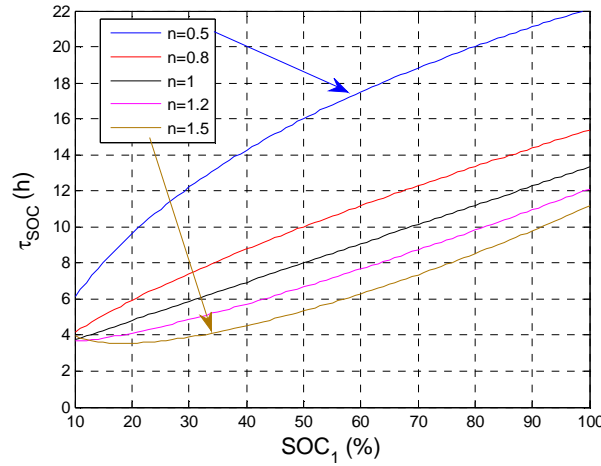


Figure 3.27. Time constant $\tau_{SOC,sl}$ as a function of SOC₁ for different n values.

The time constant $\tau_{SOC,sl}$ determines the transient response for a two-battery system with different initial SOC_s. If the C_1/S_{bat1} and C_2/S_{bat2} ratios are equal, then variations in the net power do not contribute to SOC imbalance and both SOC_s remain equal after the initial transient. However, in real applications, the C_1/S_{bat1} and C_2/S_{bat2} ratios differ and it is not possible to keep both SOC_s equal. This fact can be understood when considering a situation where $SOC_1=SOC_2$ and $C_1/S_{bat1} \neq C_2/S_{bat2}$. In this case, since $SOC_1=SOC_2$, the control will cause $p_1=p_2$, as shown in (3.104). However, since $C_1/S_{bat1} \neq C_2/S_{bat2}$, $p_1=p_2$ will lead to an unequal SOC variation. This makes it necessary to analyze how net power variations contribute to SOC imbalance for different C/S_{bat} ratios and how this can be limited.

Proceeding as indicated above, the expression for the small-signal difference $\hat{SOC}_1 - \hat{SOC}_2$ can be determined as a function of the small signal net power. After an initial situation with $SOC_{i1} \neq SOC_{i2}$, both SOC_s will be similar thanks to the control. Thus, in order to obtain a clearer expression, it is considered that $SOC_1=SOC_2=SOC$. Using (3.25), (3.105), (3.106), (3.114) and (3.116) gives

$$\hat{SOC}_1 - \hat{SOC}_2 = \frac{S_{rat1} + S_{rat2}}{C_1 + C_2} \left(\frac{C_1}{S_{rat1}} - \frac{C_2}{S_{rat2}} \right) \cdot SOC \frac{\hat{P}_T}{n \cdot P_T (\tau_{SOC,sl} \cdot s + 1)}. \quad (3.119)$$

From (3.119), it is obvious that when the C_1/S_{bat1} and C_2/S_{bat2} ratios are equal, net power variations do not contribute to SOC imbalance. Equations (3.118) and (3.119) show that P_T variations are best rejected for low SOC values, low C/S_{bat} differences, high n values, and high P_T . The influence of the C/S_{bat} ratio and parameter n can be observed in Fig. 3.28, which shows the bode diagram of small-signal SOC imbalance in front of the net power. The plot is carried out for the system presented in Table 3.6 and for an operating point with $SOC_1 = SOC_2 = 0.5$ and $P_T = 4500$ W. The curves are obtained for three different n values ($n=0.5$, $n=1$ and $n=1.5$) and assuming that battery 2 has a reduced capacity due to aging. More specifically, two families of curves are shown, one for $C_2=18$ kWh (25% of capacity loss) and another for $C_2=12$ kWh (50% of capacity loss). It can be observed in the figure that, for both cases, the SOC imbalance caused by the net power is lower for high n values, which makes high n values preferable to limit the SOC imbalance. Furthermore, it is worth mentioning that these curves are only valid for a certain operating point due to the small-signal modeling. Thus, net power variation rejection will worsen for operating points with higher SOC values and lower P_T values.

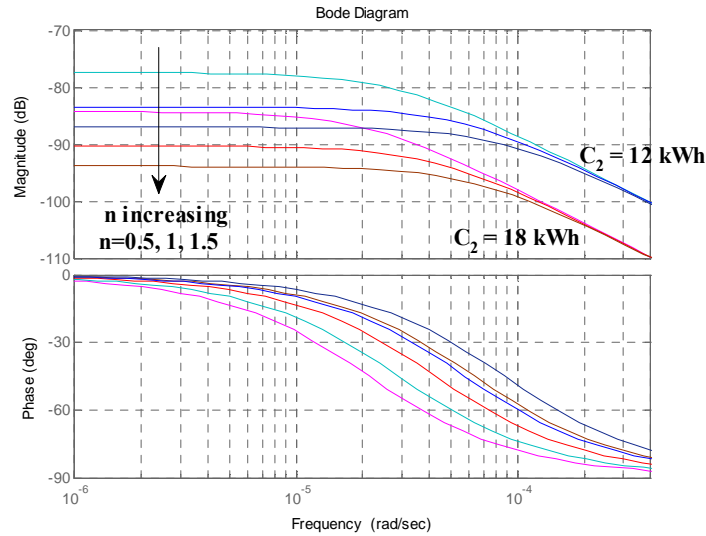


Figure 3.28. Bode diagram of the SOC imbalance in front of the net power.

3.6.1.4 Simulation results

After analyzing the slope changing method in detail, it is then possible to select the two method parameters, namely M_0 and n . However, as shown in Table 3.7, M_0 is defined

after selecting n due to the stability constraint for the power response. As a result, our actual degree of freedom is parameter n .

As shown previously, the slope changing method does not decouple the power and SOC responses since changes in parameter n have an effect on both. With regard to the real power, its response is optimized for a certain M_P slope. It is then desirable to set a low n value in order to make the M_P slope slightly variable. Setting a high n value causes a slow power response as well as power errors for some operating points. On the other hand, the SOC response is optimized for high n values. This makes the response quicker and avoids high SOC imbalance in real systems. Therefore, it is impossible to simultaneously optimize the power and SOC responses, and parameter n needs to be chosen as a trade-off between both responses. Based on the previous analysis, parameter $n=1$ is selected for our system, resulting in $M_0=0.1$ Hz.

A one-year simulation is carried out for the system presented in Table 3.6 but with $C_2=18$ kWh (25% of capacity loss due to aging). The simulation is conducted with Simulink based on the model previously developed, using (3.105), (3.106), (3.112) and (3.113) for $P_T>0$, and the equivalent equations for $P_T<0$. When a battery is fully charged (SOC=1) and $P_T<0$, the generation is limited so that the battery does not absorb more power. The power profile P_T is shown in Fig. 3.29 with values calculated every fifteen minutes and corresponding to measured data for consumption and generation from 1st February 2009 to 31th January 2010. The load profile was taken from two houses located in Pamplona, Spain, occupied by nine people in all. The PV and wind generation profiles were adapted from irradiance, cell temperature and wind speed data taken from the Public University of Navarra, in Pamplona, Spain, for a 10 kWp PV generator and a 5 kWp wind turbine. The generation and battery sizing for the stand-alone system is carried out based on [3.59].

Fig. 3.30 shows the simulation results for the system described with different initial SOC, $SOC_{i1}=80\%$ and $SOC_{i2}=30\%$. The transient SOC response is plotted in the first graph. It can be observed that, thanks to the control, both SOC tend to adopt the same value. Moreover, it can be clearly seen that the small-signal dynamics are highly variable, with a quicker response for high P_T values, as predicted by (3.118). The second graph represents the entire one-year simulation, showing the SOC imbalance to be moderate. After the initial transient, the net power causes the SOC difference to change because $C_1/S_{bat1}=8$ h \neq $C_2/S_{bat2}=6$ h, as predicted by (3.119). The SOC_1-SOC_2 difference during the one-year period, disregarding the initial transient, reaches a peak value of -11.1% , an RMS value of 2.48% and an average value of -0.65% .

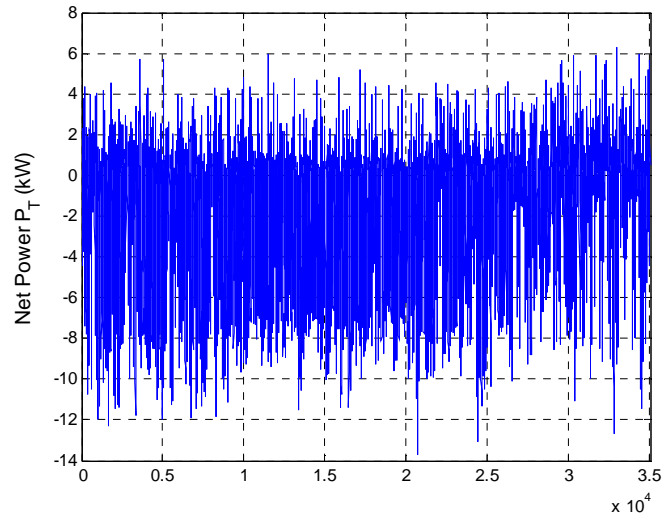


Figure 3.29. One year net power profile P_T .

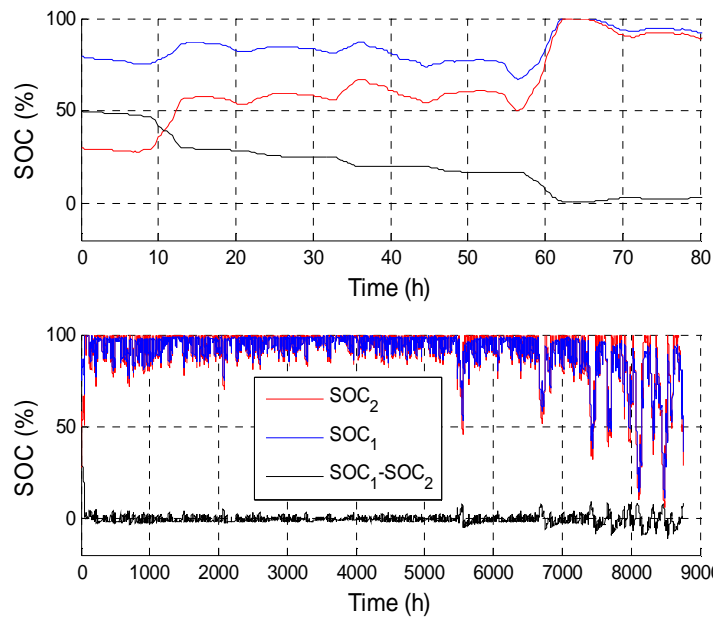


Figure 3.30. SOC evolution for a stand-alone system for the slope changing method.

3.6.2 Curve shifting method

3.6.2.1 Description

As presented above, the slope changing method changes parameter M_p in (3.17) [see also (3.19)] in order to balance the SOC. As a result, the power response is highly dependent on the operating point, leading to slow dynamics and power errors when operating with low SOC. In contrast, the curve shifting method proposed now in this section modifies parameter f_0 . This method shifts the $P-f$ curve either upwards or downwards depending on the battery SOC. The $P-f$ curve is expressed as follows:

$$f_i = f_0 - M_p \cdot p_i + M_s \cdot (SOC_i - SOC_{i0}), \quad i = 1, \dots, N, \quad (3.120)$$

where M_s is the SOC coefficient and is the same for all inverters. Term SOC_{i0} makes it possible to define the desired SOC distribution between the batteries. In this case, the control objective is $SOC_1 = SOC_2$ and, for this purpose, $SOC_{10} = SOC_{20} = SOC_0$ is imposed. However, in some situations, an unequal SOC distribution can be desired, which can be readily achieved by setting different values for SOC_{10} and SOC_{20} . In doing so, the control objective will become $SOC_1 = SOC_2 + SOC_{10} - SOC_{20}$. Furthermore, both the power and SOC dynamic responses will not be altered given that the term $M_s \cdot SOC_0$ is constant during operation.

The $P-f$ curve is shown in Fig. 3.31 for $f_0 = 50$ Hz, $M_p = 0.3$ Hz, $M_s = 0.3$ Hz, $SOC_0 = 0.8$ and two batteries ($SOC_1 = 1$ and $SOC_2 = 0.5$). It can be observed that the curve for battery inverter 1 is shifted upwards in relation to the curve for battery inverter 2, although slope M_p is constant. Two operating points are plotted in the figure, for $P_T > 0$ and $P_T < 0$. In both cases, p_1 is higher than p_2 , making it possible to balance the SOC.

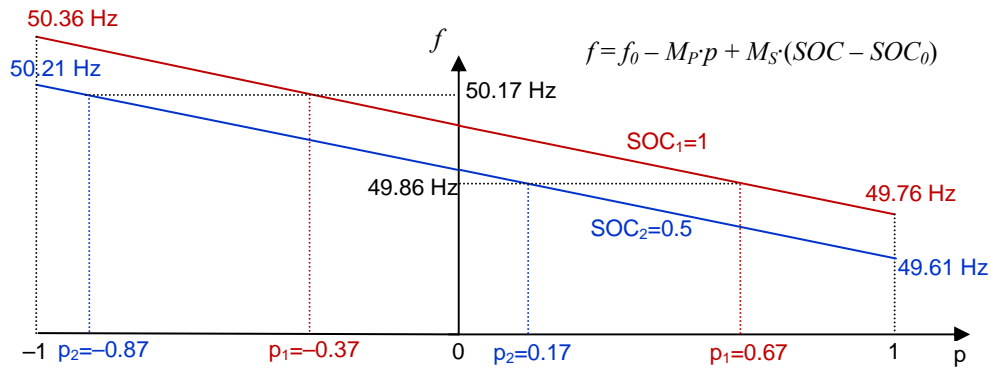


Figure 3.31. $P-f$ curve for the curve shifting method.

The steady-state power distribution can be determined by taking into account that $f_1=f_2$ after the power transient. Equations (3.25) and (3.120) give

$$p_1 - p_2 = \frac{M_s}{M_p} \cdot (SOC_1 - SOC_2) \quad (3.121)$$

$$P_1 = \frac{S_{bat1}}{S_{bat1} + S_{bat2}} \cdot P_T + \frac{S_{bat1} \cdot S_{bat2}}{S_{bat1} + S_{bat2}} \cdot \frac{M_s}{M_p} \cdot (SOC_1 - SOC_2) \quad (3.122)$$

$$P_2 = \frac{S_{bat2}}{S_{bat1} + S_{bat2}} \cdot P_T - \frac{S_{bat1} \cdot S_{bat2}}{S_{bat1} + S_{bat2}} \cdot \frac{M_s}{M_p} \cdot (SOC_1 - SOC_2). \quad (3.123)$$

From equation (3.121), it can be observed that the real power difference is proportional to the SOC difference, where quotient M_s/M_p is the proportionality constant.

With this method, the grid frequency also varies in operation as a function of the inverter power and the battery SOC. The frequency reaches its minimum f_{min} value for $SOC=SOC_{min}=0.1$ and $p=1$, and its maximum value f_{max} for $SOC=SOC_{max}=1$ and $p=-1$.

$$f_{min} = f_0 - M_p - M_s \cdot (SOC_0 - 0.1) \quad (3.124)$$

$$f_{max} = f_0 + M_p + M_s \cdot (1 - SOC_0). \quad (3.125)$$

The proposed curve shifting method has two degrees of freedom for the design: M_p and M_s . The selection of these parameters is important since they exert a great influence on the frequency deviation, the power response performance and the SOC response performance. Thus, the power and SOC responses will be theoretically analyzed in this section in order to make a correct choice. With regard to the frequency deviation, the frequency variation obtained is low for a stand-alone system, except for very high M_p and M_s values. For example, with the parameters chosen for Fig. 3.31, $f_{min}=49.49$ Hz and $f_{max}=50.36$ Hz, which are allowable.

3.6.2.2 Influence of M_p and M_s on the power response

The model developed in section 3.3.2 is now used to determine the power response for the curve shifting method. The system plant was modeled by (3.26) and (3.27). For the control modeling, H_p is added to (3.120) in order to account for the measurement and power sampling [see (3.108)], and the SOC's are considered as constant. The control then becomes

$$f_1 = f_0 - m_{p1} \cdot H_p \cdot P_1 + M_s \cdot (SOC_1 - SOC_0) \quad (3.126)$$

$$f_2 = f_0 - m_{p2} \cdot H_p \cdot P_2 + M_s \cdot (SOC_2 - SOC_0). \quad (3.127)$$

Inserting these equations into (3.26) and (3.27) leads to the closed-loop power expressions

$$P_1 = \frac{VE \cdot I \cdot m_{p2} \cdot H_p + X_2}{den_p} P_T + \frac{VE}{den_p} \theta_i + \frac{VE \cdot I \cdot M_s}{den_p} (SOC_1 - SOC_2) \quad (3.128)$$

$$P_2 = \frac{VE \cdot I \cdot m_{p1} \cdot H_p + X_1}{den_p} P_T - \frac{VE}{den_p} \theta_i - \frac{VE \cdot I \cdot M_s}{den_p} (SOC_1 - SOC_2), \quad (3.129)$$

where den_p was defined in (3.31).

It can be observed from (3.128) and (3.129) that the characteristic equation is the same as for the conventional droop method. As a result, the power response poles are also the same, as was expected since the M_p slope is not changed by the curve shifting method. Since parameter M_s does not appear in the expression of den_p , it does not affect the power response. The power response for this method has therefore the one analyzed in section 3.6.1.2 by means of the M_p root locus diagram shown in Fig. 3.26.

3.6.2.3 Influence of M_p and M_s on the SOC response

Similarly to section 3.6.1.3, the time constant for the SOC response, and the SOC imbalance for different ratios C/S_{bat} is now obtained for a two-battery system. The model for an N-battery system is shown in section 3.6.2.5. In this case, a small-signal analysis is not necessary since linear modeling is possible.

Applying Laplace transform to (3.112) and (3.113) gives

$$SOC_1 = SOC_{i1} - \frac{P_1}{C_1 \cdot s}, \quad SOC_2 = SOC_{i2} - \frac{P_2}{C_2 \cdot s}. \quad (3.130)$$

Taking into account power and SOC dynamics, it can be considered that the power steady-state has been reached and equations (3.121)–(3.123) are valid. By means of (3.25), (3.121) and (3.130), the expression for the SOC difference is obtained as

$$SOC_1 - SOC_2 = \frac{M_p}{M_s} \frac{1}{C_1 + C_2} \left(\frac{C_1}{S_{bat1}} - \frac{C_2}{S_{bat2}} \right) \cdot \frac{P_T}{\tau_{SOC,sh} \cdot s + 1} + \frac{\tau_{SOC,sh} \cdot s}{\tau_{SOC,sh} \cdot s + 1} (SOC_{i1} - SOC_{i2}) \quad (3.131)$$

$$\tau_{SOC,sh} = \frac{M_p}{M_s} \cdot \frac{1/S_{bat1} + 1/S_{bat2}}{1/C_1 + 1/C_2}. \quad (3.132)$$

As shown in (3.131) and (3.132), the transfer function has only one pole, which has an associated time constant $\tau_{SOC,sh}$. This parameter $\tau_{SOC,sh}$ depends on the battery capacities, the inverter rated powers, and parameters M_p and M_s ; however, unlike the slope changing method, it does not vary in operation. In addition, its constant value can

be set as desired by means of parameter M_S once parameter M_p has been selected for optimizing the power response. Increasing M_S and thus the M_S/M_p ratio makes the response faster. As an example, for the system presented in Table 1, $M_p=0.3$ Hz and $M_S=0.3$ Hz, $\tau_{SOC,sh}=8$ hours is obtained.

Once again from (3.131), it is possible to determine the influence of net power on the SOC imbalance for different C/S_{bat} ratios, as performed in section 3.6.1.3. It should be noted that net power P_T is best rejected for low C/S_{bat} ratio difference and a high M_S/M_p ratio. The bode diagram for the SOC imbalance in front of the net power is shown in Fig. 3.32, conducted for the system presented in Table 3.6. The curves are obtained for $M_p=0.3$ Hz, three different M_S values ($M_S=0.1$ Hz, $M_S=0.3$ Hz and $M_S=0.5$ Hz) and assuming that battery 2 has lost part of its capacity due to aging. More specifically, two families of curves are shown, one for $C_2=18$ kWh (25% of capacity loss) and another for $C_2=12$ kWh (50% of capacity loss). Unlike the slope changing method, the linear modeling means that these curves are valid for every operating point. From the figure, it can be concluded that the SOC imbalance caused by the net power can be reduced by means of high M_S values. Thus, since M_S exerts no influence on the power response, it is possible to increase this parameter in order to limit the SOC imbalance.

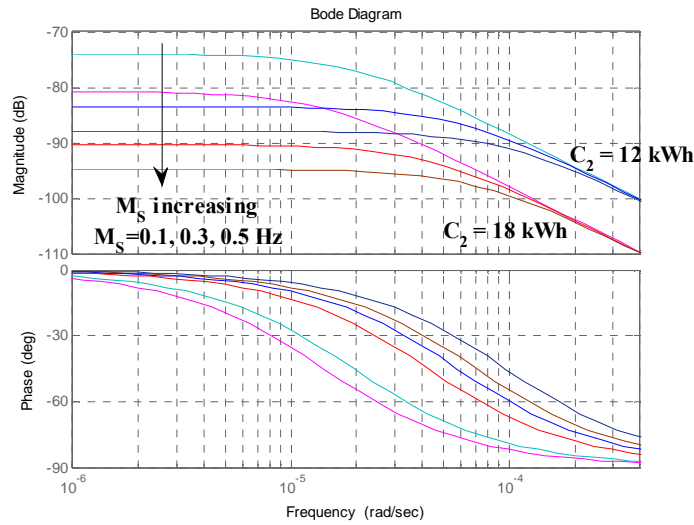


Figure 3.32. Bode diagram of the SOC imbalance in front of the net power.

3.6.2.4 Simulation results

In order to simulate the system, the curve shifting method parameters are first selected. The method has two design degrees of freedom, namely the power droop coefficient M_p and the SOC coefficient M_S .

As it was shown above, only the droop coefficient M_p has an influence on the power transient. This parameter can thus be selected in order to optimize the power response, as was done in section 3.6.1.2. With regard to the SOC response, high values of the M_S/M_p ratio reduce the transient time constant and prevents from high SOC imbalance in real systems. As a result, once parameter M_p has been set for the power response, parameter M_S can be selected in order to limit the SOC imbalance. Hence, the power and SOC responses can be independently designed by means of the proposed control. Based on the theoretical analysis, the parameter values selected are $M_p=0.3$ Hz and $M_S=0.3$ Hz for our system.

One-year simulation is also carried out here for the system presented in Table 3.6 but with $C_2=18$ kWh (25% of capacity loss due to aging). Similarly to the previous case (see section 3.6.1.4), the system represented by (3.112), (3.113), (3.122) and (3.123) is modeled in Simulink. The simulation is carried out for the same stand-alone system with the same net power profile (see Fig. 3.29).

The results are shown in Fig. 3.33 considering $SOC_{i1}=80\%$ and $SOC_{i2}=30\%$. The first graph plots the transient SOC response. Thanks to the control, both SOC's tend to reach the same value after a different initial status. Comparing this figure to Fig. 3.30, it can be observed that the SOC response is much faster for the curve shifting method. Furthermore, it has constant dynamics, which are determined by $\tau_{SOC,sh} = 6.6$ hours from (3.132). In the second graph, the entire one-year simulation is represented, showing a low SOC imbalance. After the initial transient, the net power causes the SOC difference to change because $C_1/S_{bat1}=8$ h \neq $C_2/S_{bat2}=6$ h, as predicted by (3.131). The SOC_1-SOC_2 difference during the one-year period, disregarding the initial transient, reaches a peak value of -9.9% , an RMS value of 1.35% and an average value of -0.02% . These values are lower than those for the slope changing method and can still be further reduced if desired by increasing M_S yet without interacting with the power response dynamics.

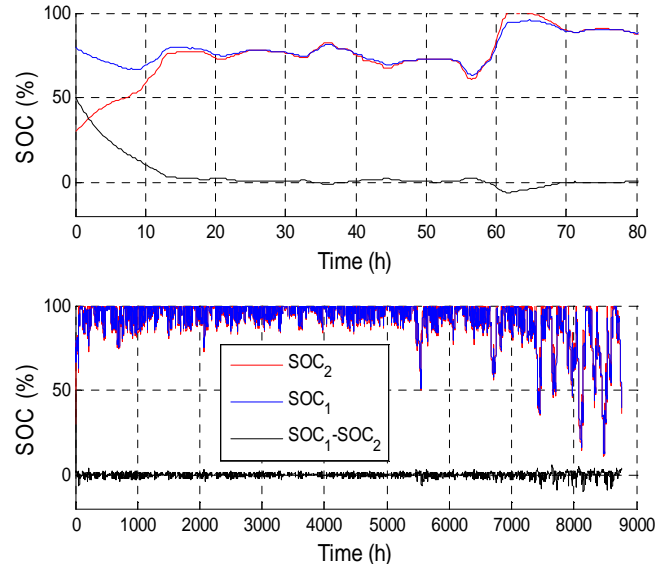


Figure 3.33. SOC evolution for a stand-alone system for the curve shifting method.

3.6.2.5 SOC response for N batteries

After validating the proposed control for a two-battery system, it is now generalized for an N-battery system. The power response for an N-battery system was developed in section 3.3.6.1. The SOC response modeling was developed in section 3.6.2.3 for two batteries and will be derived in this section for N inverters. The purpose is to obtain the transfer function poles in order to predict the transient response. The expression for the characteristic equation is thus determined, which makes it possible to disregard the independent terms.

Rewriting (3.120) and (3.130) for N battery inverters leads to

$$f_i = f_0 - M_p \cdot P_i / S_{bat,i} + M_s \cdot (SOC_i - SOC_0), \quad i = 1, \dots, N \quad (3.133)$$

$$SOC_i = -\frac{P_i}{C_i \cdot s}, \quad i = 1, \dots, N. \quad (3.134)$$

From these equations and considering that $f_i = f_1$ (for $i=2, \dots, N$), every power can be expressed as a function of P_1 , that is

$$P_i = \frac{\frac{M_p}{M_s} \cdot \frac{1}{S_{bat1}} s + \frac{1}{C_1}}{\frac{M_p}{M_s} \cdot \frac{1}{S_{bat,i}} s + \frac{1}{C_i}} \cdot P_1, \quad i = 2, \dots, N. \quad (3.134)$$

Introducing (3.134) into (3.55) and operating makes it possible to obtain the characteristic equation as

$$den_{SOC} = \sum_{j=1}^N \frac{1}{\frac{M_p}{M_s} \cdot \frac{1}{S_{bat,j}} \cdot s + \frac{1}{C_j}}. \quad (3.135)$$

From this expression, the closed-loop transfer function poles for the SOC response can be obtained. One example is provided for 4 inverters, where the parameters presented in Table 3.6 are used together with two other battery inverters. Note that it is considered that $C_2=18$ kWh due to aging. Moreover, battery inverter 3 has a rated power $S_{bat3}=5000$ VA and a battery capacity $C_3=25$ kWh while battery inverter 4 has a rated power $S_{bat4}=4000$ VA, and a battery capacity $C_4=40$ kWh. Table 3.8 shows the time constants associated with the poles for $M_s=M_p=0.3$ Hz. It can be seen that the system has $(N-1)$ real poles. In addition, the poles for configurations with different inverters are between the poles for configurations with equal inverters.

Configuration	Time constants
N times Inv1	N-1 times $\tau = 8$ h
N times Inv2	N-1 times $\tau = 6$ h
N times Inv3	N-1 times $\tau = 5$ h
N times Inv4	N-1 times $\tau = 10$ h
Inv1, Inv2	$\tau = 6.6$ h
Inv1, Inv2, Inv3, Inv4	$\tau = 5.4$ h, 6.6 h, 9.2 h

Table 3.8. Closed-loop time constants for the SOC response.

3.6.3 Experimental results

The proposed SOC-based droop method is now validated by experimental tests. Two batteries with their inverters are connected in parallel and create the ac grid. Their features are shown in Table 3.6. The battery inverter models are Ingecon Hybrid AC Link 3TL and Ingecon Hybrid AC Link 6TL. Their configuration has been modified in order to implement the proposed droop method. The used $P-f$ curve is (3.120) for $f_0=50$ Hz, $M_p=0.3$ Hz, $M_s=0.3$ Hz, $SOC_0=0.8$, as selected in section 3.6.2.4 and shown in Fig. 3.31. This curve is programmed in the inverter microprocessors. Each inverter measures its output power and then changes the output voltage frequency accordingly. The battery banks are made by series connection of vented lead-acid batteries, model 6 PVS 660. During the experiments, battery 1 has a greater charge than battery 2, with $SOC_1=0.8$ and $SOC_2=0.4$. A load bank and a PV emulator with its inverter is connected to the grid. They make it possible to change the real and reactive power as desired and thus to set the desired

operating point. Precision power analyzer WT1800 served to obtain the data, recording powers and frequencies every 50 ms. The battery inverters, battery banks, PV emulator and load bank are shown in Fig. 3.34.

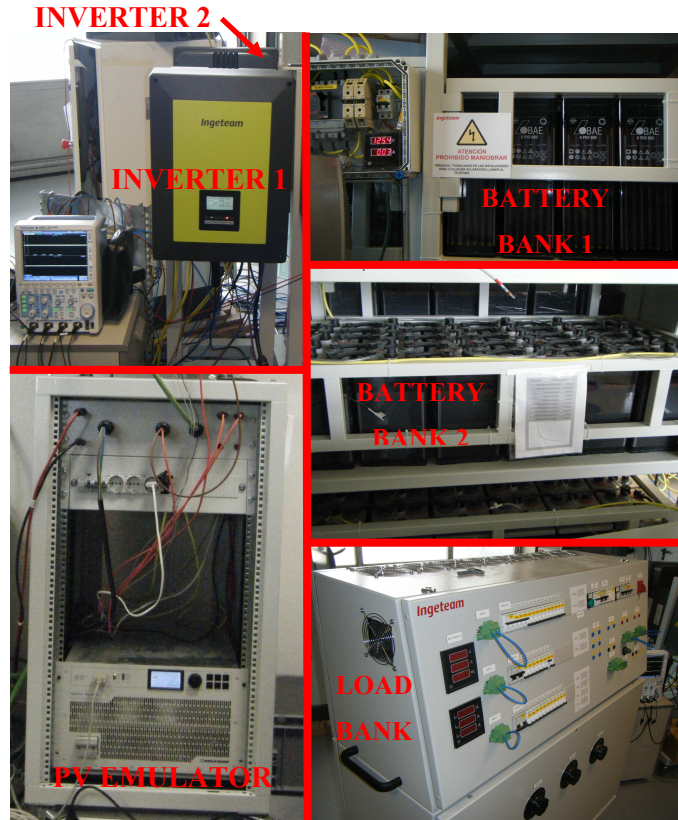


Figure 3.34. PV emulator, battery and load banks used for the experimental setup.

The first test was conducted for the battery inverters in discharging mode. The per-unit real powers and the filtered grid frequency are shown in Fig. 3.35. At the start, inverter 1 is operating alone, supplying a 4 kW load. As a result, $P_1 = 4$ kW, $p_1 = 0.67$, $P_2 = 0$, and $p_2 = 0$. Then, at second 2, inverter 2 is connected and helps supply the load. The power distribution can now be obtained by means of (3.122) and (3.123) as $P_1 = 3.47$ kW, $p_1 = 0.58$, $P_2 = 0.53$ kW, and $p_2 = 0.18$. Then, a 2.7 kW load is added to the AC bus. The net power becomes $P_T = 6.7$ kW and the power distribution becomes $P_1 = 5.27$ kW, $p_1 = 0.88$, $P_2 = 1.43$ kW, and $p_2 = 0.48$. Finally, at second 7.5, the 2.7 kW load is disconnected, and the system returns to the previous operating point. The figure shows how p_1 is always higher than p_2 thanks to the control. Since $SOC_1 = 0.8$ and $SOC_2 = 0.4$, this helps balance the SOC. With regard to the grid frequency, this changes in

line with net power variations according to (3.120). The figure shows that this frequency variation is moderate and totally acceptable for a stand-alone system.

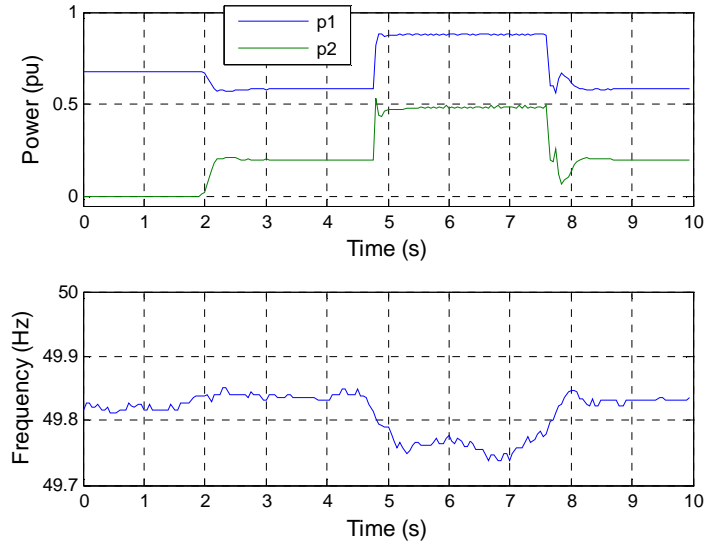


Figure 3.35. Experimental results for two battery inverters in discharging mode.

The second test was carried out for the battery inverters in charging mode. Fig. 3.36 shows the per-unit powers and the filtered grid frequency. Throughout the entire experiment, the PV inverter operates under MPPT and supplies 6 kW to the AC grid. Inverter 1 is initially connected with no load and, consequently, $P_1 = -6$ kW, $p_1 = -1$, $P_2 = 0$, and $p_2 = 0$. After a while, inverter 2 is connected, resulting in a different power distribution with $P_1 = -3.2$ kW, $p_1 = -0.53$, $P_2 = -2.8$ kW, and $p_2 = -0.93$. Then, at about second 5.5, a 2.7 kW load is connected, leading to a net power $P_T = -3.3$ kW. The power distribution becomes $P_1 = -1.4$ kW, $p_1 = -0.23$, $P_2 = -1.9$ kW, and $p_2 = -0.63$. The figure shows that, when both inverters are connected, p_1 is always higher than p_2 . Thus, battery 2 is charged with more per-unit power, which helps balance the SOC. The grid frequency, also shown in Fig. 3.36, follows net power variations and its variation range is between allowable limits for a stand-alone system. It is also worth noting that, for the curve shifting method, the power response is slightly affected by the operating point. In effect, focusing on the power transients in Fig. 3.35 and Fig. 3.36, it can be noted that the rising time is similar in all cases.

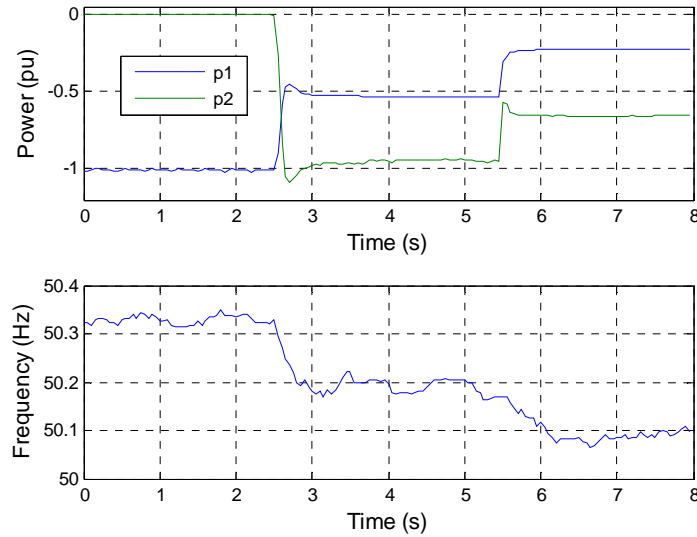


Figure 3.36. Experimental results for two battery inverters in charging mode.

3.7 ENERGY MANAGEMENT DURING HIGH/LOW SOC OPERATION

This section proposes an energy management strategy for a multiple-battery system during high/low SOC operation, in which the battery voltage or current have to be controlled to the rated values. As previously, the energy management strategy does not use communication cables between inverters or with a central supervisor. Although the strategy proposed here is also defined for normal operation, it uses the conventional droop method in this mode. Therefore, the strategy proposed in section 3.6 during normal operation is compatible and complements the strategy presented in this section during high/low SOC operation.

The proposed strategy operates in the following way. Whenever the batteries are fully charged or absorbing too much current, then the grid frequency is increased. This is measured by the Renewable Energy Source (RES) inverters, which reduce their power in order to control the battery voltages or currents. Furthermore, the control coordinates the various batteries. If some batteries have not reached their maximum voltage or current, then the surplus power is transferred from the charged batteries to the non-charged ones without limiting the RES power, making the most of the solar/wind energy. This section also addresses protection during battery discharging. As in the case of battery charging, when the batteries are either fully discharged or are delivering too much current, the grid frequency is decreased. The power is first transferred from some batteries to the others. However, if all the batteries have reached the minimum voltage

or maximum discharging current, then the frequency reduction is detected by the less critical loads, which are either regulated or disconnected. If this is not possible, then the system is shutdown in order to prevent irreversible damage to the batteries.

This section is organized as follows. Section 3.7.1 presents the proposed energy management strategy by describing the different converter operation. Section 3.7.2 defines the operating modes resulting from the converter operation, and provides some simulation results. In section 3.7.3, small-signal modeling is presented in order to analyze the system stability and dynamic performance. Finally, experimental results are provided in section 3.7.4 to verify the proposed strategy.

3.7.1 Proposed energy management strategy

3.7.1.1 Description

Fig. 3.37 represents the same stand-alone system shown in Fig. 3.1, but now with N battery inverters, M PV inverters, and a number of loads are connected to the common AC bus. The battery inverters are connected in parallel through the output impedance, formed by the filter inductance and the line impedance. However, since the line impedance is much smaller than the filter impedance, the output impedance can be approximated as the filter inductance, L_i . The battery inverter rated powers $S_{bat,i}$, battery capacities C_i , battery real powers P_i , battery reactive powers Q_i , net real power P_T , net reactive power Q_T , PV inverter rated powers $S_{pv,i}$, and instantaneous value of voltages and currents e_i and i_i , are also defined in the figure.

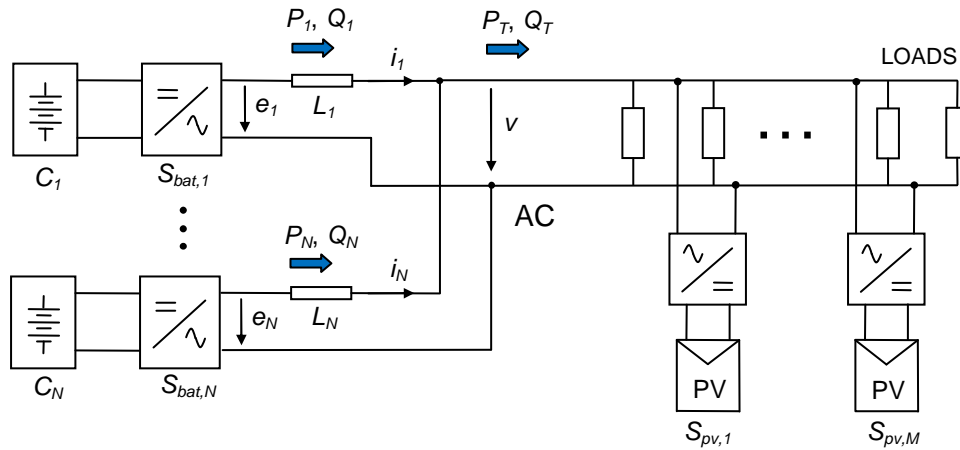


Figure 3.37. Battery inverters, PV inverters and loads connected in parallel.

In this system, the battery inverters always operate as Voltage Source Inverters (VSIs) using droop methods, and generate the grid. For their part, the RES converters operate as Current Source Inverters (CSIs), injecting either the maximum available power or a power below the MPP into the grid. The operation of the battery inverters, RES converters and non-critical loads is presented below.

3.7.1.2 Battery inverter operation

As seen before, the droop method is an advantageous grid generation technique for multiple VSIs, making it possible to share the real and reactive powers in proportion to the inverter ratings with no need for communication. This section addresses energy management and therefore the real power. For this reason, the reactive power droop method is not analyzed here, however a number of droop methods can be consulted in [3.60], [3.61]. For the sake of clarity, the real power analysis is carried out for two battery inverters, however this can be readily generalized for N inverters. As it was explained in previous sections, the conventional droop characteristic is expressed as follows:

$$f = f_0 - M_p \cdot p, \quad (3.136)$$

where f is the inverter frequency, f_0 is the nominal frequency, M_p is the droop coefficient, and $p=P/S_{bat}$ is the per-unit real power.

In steady-state operation, the inverter frequency is the same for all inverters. Hence, from (3.136), and setting the same values f_0 and M_p for all inverters, the following is obtained:

$$f_1 = f_2 \Rightarrow p_1 = p_2. \quad (3.137)$$

Here, (3.136) is used during normal operation and, as a result, the power is shared among the inverters. However, in some situations equal power sharing is not desirable. The proposed strategy then modifies (3.136) as follows:

$$f = f_0 - M_p \cdot p + \delta f, \quad (3.138)$$

where δf is the shifting frequency and will be changed by the control.

In steady-state operation, from (3.138), the condition $f_1=f_2$ leads to

$$f_1 - f_2 \Rightarrow p_1 - p_2 = \frac{\delta f_1 - \delta f_2}{M_p}. \quad (3.139)$$

This equation shows that adding the term δf results in an unequal power distribution. From (3.139), if δf_2 and the load are maintained constant, increasing δf_1 results in

increasing p_1 and reducing p_2 whilst reducing δf_1 results in decreasing p_1 and increasing p_2 . Taking this into account, if battery 1 reaches its minimum voltage or its maximum discharging current, battery inverter 1 will reduce δf_1 and its power will decrease, preventing over-discharge. On the other hand, if battery 1 becomes fully charged or absorbs an excessive current, then the battery inverter will increase δf_1 and its power will increase. Since the power in charging mode is negative, this will result in a battery current and voltage reduction, preventing overcharge.

This fact can be observed in Fig. 3.38, where three different $P - f$ curves are shown. The parameters are $f_0 = 50$ Hz, $M_p = 0.3$ Hz for all curves. The curve for inverter 2 is not modified ($\delta f_2 = 0$) while two modified curves are plotted for inverter 1 ($\delta f_1 = -0.1$ Hz and $\delta f_1 = 0.1$ Hz). Two operating points are plotted in the figure, for $P_T > 0$ and for $P_T < 0$. In discharging mode ($P_T > 0$), battery 1 has reduced the shifting frequency to $\delta f_1 = -0.1$ Hz. As a result, inverter 1 delivers less power than inverter 2. On the other hand, in charging mode ($P_T < 0$), battery 1 has increased the shifting frequency to $\delta f_1 = 0.1$ Hz. Thus, inverter 1 absorbs less power than inverter 2.

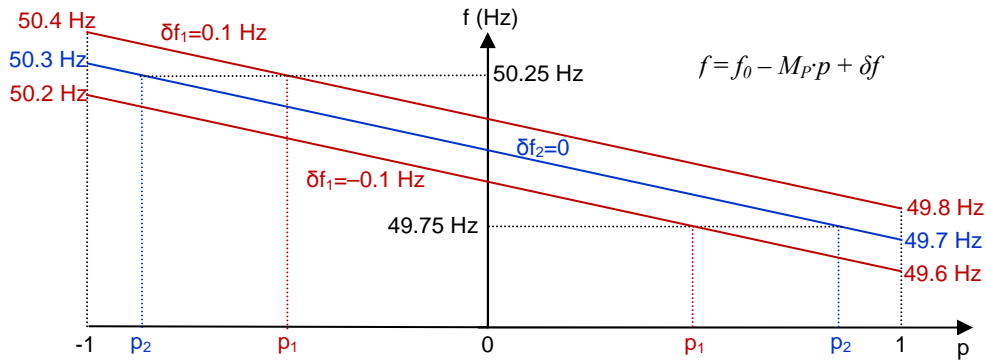


Figure 3.38. Proposed $P - f$ curve.

Although parameters f_0 and M_p are the same for all battery inverters in order to share the per-unit power in normal operation, parameter δf varies as a function of the operating point and is calculated for each battery inverter as

$$\delta f = \delta f_c - \delta f_d. \quad (3.140)$$

where δf_c ($\delta f_c \geq 0$) is the charge shifting frequency and δf_d ($\delta f_d \geq 0$) is the discharge shifting frequency.

The calculation of δf_c and δf_d is shown in Fig. 3.39. During charging mode, $\delta f_d = 0$, and $\delta f_c \geq 0$. On the one hand, the difference between the measured battery voltage, $v_{bat,m}$, and the maximum battery voltage, $v_{bat,max}$, is entered in controller $C_{c,v}$, which calculates $\delta f_{c,v}$, limited from 0 to $\delta f_{c,max}$. On the other hand, from the difference between the measured

battery current, $i_{bat,m}$ (negative for charging mode), and the maximum battery charging current, $i_{bat,c,max}$, controller $C_{c,i}$ determines $\delta f_{c,i}$, also limited from 0 to $\delta f_{c,max}$. Then, the highest value δf_c is selected since it is more restrictive. During discharging mode, $\delta f_c = 0$, and $\delta f_d \geq 0$. In this case, the calculations are similar to the charging mode, but the references are the minimum battery voltage, $v_{bat,min}$, and the maximum battery discharging current, $i_{bat,d,max}$. The outputs in this case are $\delta f_{d,v}$, and $\delta f_{d,i}$, the limit value is $\delta f_{d,max}$, and the highest value δf_d is selected as the most restrictive.

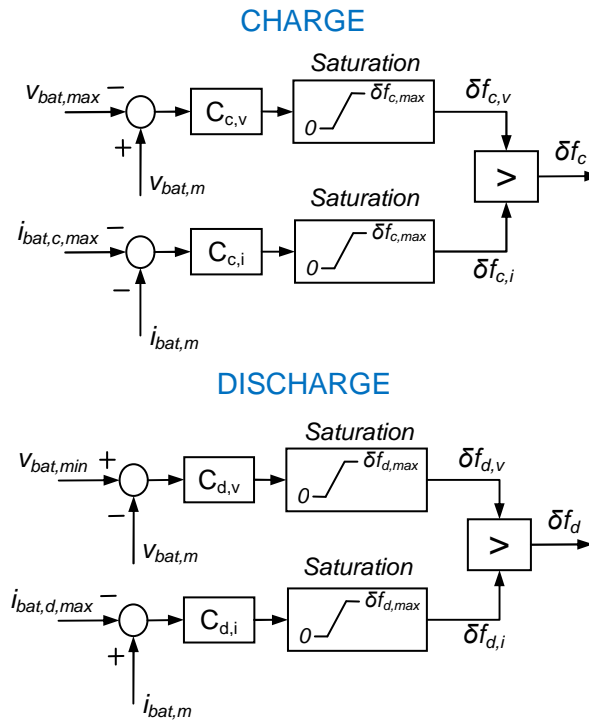


Figure 3.39. Calculation of δf_c and δf_d .

Normally, the battery currents and voltages are within limits, that is $v_{bat,min} < v_{bat} < v_{bat,max}$ and $-i_{bat,c,max} < i_{bat} < i_{bat,d,max}$. As a result, the controller outputs are saturated to zero, $\delta f_c = 0$, $\delta f_d = 0$, $\delta f = 0$, and expressions (3.136) and (3.137) are valid, leading to an equal power distribution. When a battery is fully charged and its voltage exceeds $v_{bat,max}$ ($v_{bat} > v_{bat,max}$), or its charging current exceeds $i_{bat,c,max}$ ($i_{bat} < -i_{bat,c,max}$), then δf is increased, making it possible to reduce the power absorbed by that battery. On the other hand, when the battery is fully discharged and its voltage drops below $v_{bat,min}$ ($v_{bat} < v_{bat,min}$), or its discharging current exceeds $i_{bat,d,max}$ ($i_{bat} > i_{bat,d,max}$), then δf is decreased, resulting in a reduction in the power delivered by that battery.

If there is no variation in generation and consumption, in other words, net power P_T is constant, then the reduction in the power absorbed (delivered) by one battery leads to an increase in the power absorbed (delivered) by the other battery. As a result, the control presented will be stable if the entire storage system is able to support the net power. However, if all batteries are fully charged or they are absorbing too much current, then all batteries will increase the frequency together. An RES power reduction is then required, which is presented in section 3.7.1.3. On the other hand, if all batteries have reached the minimum voltage or maximum discharging current, all of them will decrease the frequency together. In this case, the non-critical loads should be regulated, as presented in section 3.7.1.4.

3.7.1.3 RES converter operation

The RES converters operate under current-control mode, injecting power into the grid. They usually perform MPPT and can reduce the power depending on the grid frequency deviation. The grid frequency deviation Δf is defined as

$$\Delta f = f - f_0 . \quad (3.141)$$

Each RES converter measures the frequency and obtains the measured frequency deviation Δf_m . The frequency measurement does not involve an additional cost since this is already included in the RES inverters for grid synchronization and islanding detection. The frequency obtained by the phase locked loop (PPL) is then filtered in order to avoid noise, transients and external interferences. A high value is preferred for the filter time constant, τ_f , to prevent transient frequency oscillations from reducing the RES power when it is not required. However, a very high value would decrease the control stability margin, and a trade-off must be balanced. If the measured frequency deviation Δf_m is higher than a minimum value Δf_{min} , then the RES converter stores the MPP power, to be called $P_{mpp,fr}$, and continuously reduces the power generated up to frequency deviation Δf_{max} , where the power is zero. The value of Δf_{min} should be higher than M_p in order to prevent interaction with the battery inverter droop and limiting the power when not required. Since the value of $P_{mpp,fr}$ is taken instead of the rated power S_{pv} , the RES power starts to be reduced just when $\Delta f_m > \Delta f_{min}$, resulting in a faster control. The frequency sensing and filtering H_f , and the relationship between the frequency deviation and the reference RES power P_{RES}^* are shown in Fig. 3.40.

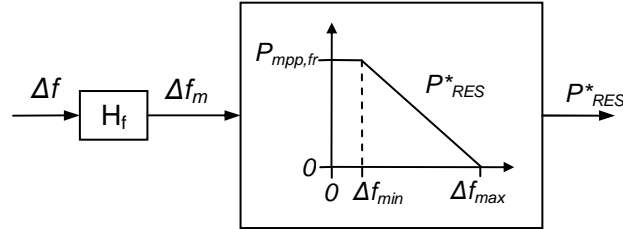


Figure 3.40. Calculation of RES power reference P^*_{RES} .

The implementation of the RES power regulation is described here for a photovoltaic system as well as for a wind-energy conversion system. The PV generator and two-stage PV inverter are shown in Fig. 3.41(a), while the small wind turbine, the permanent magnet synchronous generator (PMSG) and the AC/DC stage of the wind-energy AC/AC converter are shown in Fig. 3.41(b). In order to carry out the PV power reduction, the first stage of the PV inverter, which is a DC/DC boost converter, is controlled as shown in Fig. 3.42. When Δf_m exceeds Δf_{min} , then the MPPT algorithm is cancelled and the PV voltage reference is frozen to its last value, $v_{mpp,fr}$. The PV voltage is regulated by means of a PI controller [3.10]. On the other hand, power reference P^*_{pv} is divided by the measured PV voltage $v_{pv,m}$. Then, the lowest value is selected as the current reference for the inner current control. In so doing, when $\Delta f_m > \Delta f_{min}$, the power regulation is active, with $v_{pv} > v_{mpp}$. However, there are situations in which the power reference can no longer be delivered, for example after an irradiance drop. In these cases, the PV voltage decreases and the control switches to voltage regulation, which prevents a PV voltage drop in the system. The voltage control is maintained until Δf_m decreases to below Δf_{min} and then the MPPT is performed. More details about this technique are shown in chapter 4 and in [3.62].

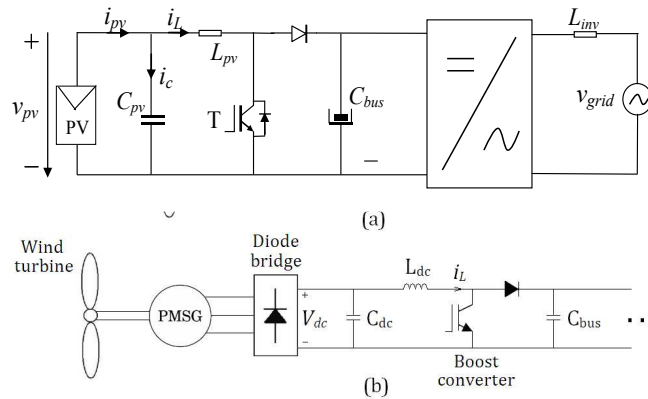


Figure 3.41. Renewable-energy-source systems: (a) Single-phase two-stage PV inverter and (b) AC/DC stage of the wind energy converter.

method, occurring not only during power limitation but also during MPPT, some modifications of certain inverter functionalities are required. Although an in-depth analysis is out of the scope of this work, a brief discussion about grid synchronization and islanding detection is carried out here.

During operation, the voltage frequency evolves according to (3.137), where δf is obtained as shown in Fig. 3.39. Because the term δf is related to the battery energy management, its variation is slow with regard to the term $M_p \cdot p$. For this reason, the frequency variation caused by the proposed method implies the same synchronization requirement as for the conventional droop method. For the conventional droop method, the frequency variation can be very fast in the event of load connections/disconnections, and high-performance phase locked loop (PLL) methods are required [3.64]–[3.66]. In any case, errors in the frequency estimation during load transients occur. This will cause reactive power injection by the RES inverter, which will be compensated by the battery inverters.

In stand-alone systems in which security risks could arise, islanding detection can be an important issue. Concerning islanding detection methods, it is well-known that, in grid-connected inverters, frequency shift methods are generally preferred over voltage shift or impedance measurement methods. This is mainly due to both its lower grid perturbation and its success in islanding detection [3.67], [3.68]. Frequency shift methods could also be applied to stand-alone systems, provided that the frequency limits are expanded beyond $f_0 \pm \Delta f_{max}$. A higher run-on time could also be allowed in comparison with grid-connected systems. The main drawback is that frequency shift methods could also perturb the grid generation in droop-based stand-alone microgrids. Consequently, further investigation is required in this field concerning either modifications on conventional frequency shift methods or using other methods that could be more suitable for this type of systems.

3.7.1.4 Non-critical loads operation

If the system has non-critical loads which can be regulated, their power can be controlled as a function of the grid frequency. Similarly to the RES inverters (see Fig. 3.40), a $P-f$ curve can also be programmed so that the consumed power is reduced when the frequency is low. The frequency deviation limits can be set independently of the RES regulation but, in this case, they will be considered as the opposite of the RES regulation limits, that is $-\Delta f_{min}$ and $-\Delta f_{max}$. Typical programmable loads include thermal loads such as water heaters, refrigerators and air conditioning units [3.69], [3.70].

If load regulation is not feasible or all non-critical loads have already been disconnected, then the system should be shutdown whenever the frequency is very low

in order to prevent irreversible damage to the batteries. The value of the shutdown frequency deviation is defined as $-\Delta f_{stop}$. If load regulation is feasible, then the shutdown frequency deviation should be $\Delta f_{stop} > \Delta f_{min}$ so that the system does not shutdown when the load regulation is active. However, if the loads do not allow for regulation, it should just be $\Delta f_{stop} > M_p$ in order to prevent interaction with the battery inverter droop.

3.7.2 Operating modes

3.7.2.1 Description

Depending on the values of δf and Δf , there are five operating modes. These operating modes are defined in Table 3.9, and the transitions from one mode to another are shown in Fig. 3.44 and explained below for two batteries. Fig. 3.45 shows the frequency deviation for the different operating modes.

Mode I applies during normal operation, when the battery voltages and currents are within limits. In Mode II, one battery is fully charged while, in Mode III, both batteries are fully charged and a PV power limitation is required. On the other hand, in Mode IV, one battery is discharged while, in Mode V, both batteries are fully discharged and a load regulation is required.

Operating mode	Frequencies Δf , δf_1 , and δf_2	Battery voltages and currents V_{bat1} , V_{bat2} , i_{bat1} , and i_{bat2}	PV inverters	Non-critical loads
Mode I: Normal operation	$\delta f = 0$ for both batteries $-\Delta f_{min} < -M_p < \Delta f$ $\Delta f < M_p < \Delta f_{min}$	V_{bat} within limits for both batteries i_{bat} within limits for both batteries	MPPT	As required
Mode II: One battery charged	$\delta f > 0$ for one battery $\delta f = 0$ for the other $-\Delta f_{min} < -M_p < \Delta f$ $\Delta f < M_p < \Delta f_{min}$	$V_{bat} = V_{bat,max}$ or $i_{bat} = -i_{bat,c,max}$ for one battery V_{bat} and i_{bat} within limits for the other	MPPT	As required
Mode III: PV power limitation	$\delta f > 0$ for both batteries $\Delta f_{min} < \Delta f < \Delta f_{max}$	$V_{bat} = V_{bat,max}$ or $i_{bat} = -i_{bat,c,max}$ for one battery $V_{bat} = V_{bat,max}$ or $i_{bat} = -i_{bat,c,max}$ for the other	Power limitation	As required
Mode IV: One battery discharged	$\delta f < 0$ for one battery $\delta f = 0$ for the other $-\Delta f_{min} < -M_p < \Delta f$ $\Delta f < M_p < \Delta f_{min}$	$V_{bat} = V_{bat,min}$ or $i_{bat} = i_{bat,d,max}$ for one battery V_{bat} and i_{bat} within limits for the other	MPPT	As required
Mode V: Load regulation	$\delta f < 0$ for both batteries $-\Delta f_{max} < \Delta f < -\Delta f_{min}$	$V_{bat} = V_{bat,min}$ or $i_{bat} = i_{bat,d,max}$ for one battery $V_{bat} = V_{bat,min}$ or $i_{bat} = i_{bat,d,max}$ for the other	MPPT	Load regulation

Table 3.9. Operating modes.

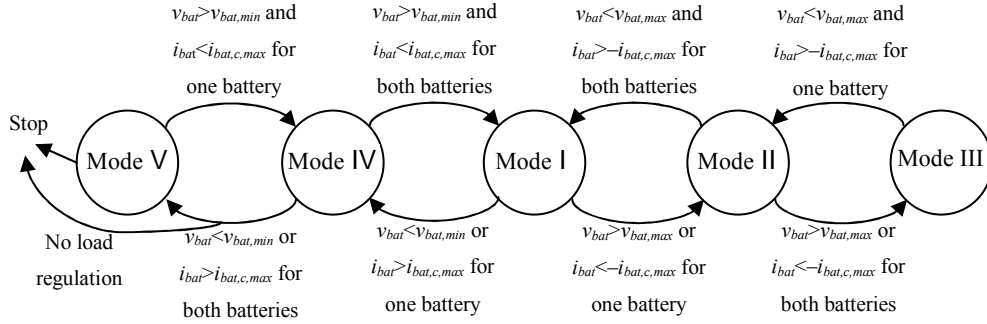


Figure 3.44. Transitions between operating modes.

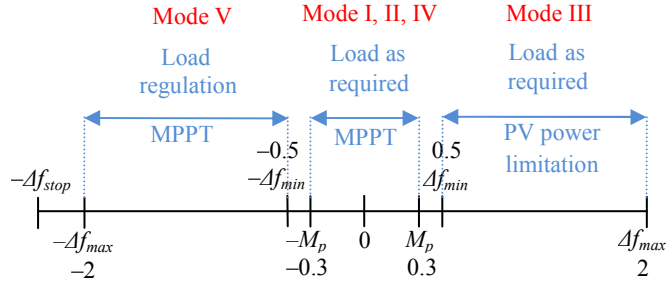


Figure 3.45. Frequency deviation (Hz) and operating modes.

3.7.2.2 Mode I: Normal operation

In Mode I, the battery voltages and currents are within limits and, as a result, from Fig. 3.39, $\delta f = 0$ for both batteries. By means of (3.136) and (3.137), the per-unit power is the same for both batteries, which either absorb or supply the difference between generation and consumption, and their SOC's vary accordingly. Since $\delta f = 0$, from (3.136), the frequency deviation Δf is between $\pm M_p$. Since it was imposed that $\Delta f_{min} > M_p$, the PV inverters operate under MPPT and the loads are not regulated (see Fig. 3.40).

When the voltage for one battery exceeds $v_{bat,max}$ ($v_{bat} > v_{bat,max}$), or the charging current exceeds $i_{bat,c,max}$ ($i_{bat} < -i_{bat,c,max}$), then the control increases δf , the power absorbed by that battery is reduced and the system switches to Mode II.

On the contrary, if the voltage for one battery decreases to below $v_{bat,min}$ ($v_{bat} < v_{bat,min}$), or the discharging current exceeds $i_{bat,d,max}$ ($i_{bat} > i_{bat,d,max}$), then the control decreases δf , the power delivered by that battery is reduced and the system switches to Mode IV.

3.7.2.3 Mode II: One battery charged

In Mode II, one battery voltage or current is controlled to its maximum value, $v_{bat} = v_{bat,max}$ or $i_{bat} = -i_{bat,c,max}$, while the other battery voltage and current are within limits. Due to the control, $\delta f = 0$ for the second battery, and $\delta f > 0$ for the first one. As a result, from (3.139), the second battery is absorbing a higher power than the first battery. Also in this case, since $\delta f = 0$ for one battery inverter, the frequency deviation Δf is between $\pm M_p$ and the net power is not modified.

In this mode, one battery has its voltage and current within limits, and with $\delta f = 0$. If the voltage or current of this battery also exceeds its maximum value, then the net power cannot be absorbed by the whole storage system. In this situation, the power cannot be reorganized between the batteries, as it is carried out in this mode. According to the control, both batteries increase δf . At first, this has no effect on the net power. However, when the grid frequency deviation becomes higher than Δf_{min} , then the PV power starts to be limited and the system switches to Mode III.

On the other hand, in this Mode II, there is a battery whose voltage or current is being regulated to its maximum value. When this voltage or current decreases, the battery inverter reduces δf and the system switches to Mode I.

3.7.2.4 Mode III: PV power limitation

In Mode III, the voltage or current of all batteries is regulated to its maximum value, $v_{bat} = v_{bat,max}$ or $i_{bat} = -i_{bat,c,max}$. The control sets $\delta f > 0$ for both batteries, leading to a frequency deviation $\Delta f > \Delta f_{min}$. As a result, the PV power is reduced according to Fig. 3.40. This operating point requires a certain net power, which is obtained thanks to the frequency imposed by the control.

In this mode, if the net power increases (for example due to an irradiance drop), and the system is not able to maintain the voltage or current reference for one battery, then the regulation reduces the frequency deviation to below Δf_{min} and the system switches to Mode II.

A number of simulations were carried out in order to validate the strategy in different modes of operation. An accurate model of the system shown in Fig. 3.37, comprising two PV inverters, two battery inverters and a number of resistive loads, was developed using the PSIM software. The features of the system are shown in Table 3.10. The first simulation addresses the voltage regulation during the transition from Mode I – Mode II – Mode III – Mode I. This is shown in Fig. 3.46 and represents the voltage of battery 1 divided by two, the voltage of battery 2, the maximum voltage for both batteries

(Fig. 3.46(a)), the total PV power, the battery powers (Fig. 3.46(b)), the frequency imposed by the battery inverters and the frequency measured by the PV inverters (Fig. 3.46(c)). During the simulation, the MPP power is always 6 kW, and a number of resistive loads are disconnected and connected.

PV inverter 1 rated power $S_{pv,1}$	5 kVA
PV inverter 2 rated power $S_{pv,2}$	5 kVA
Battery inverter 1 rated power $S_{bat,1}$	6 kVA
Battery inverter 1 output inductance L_1	3 mH
Battery 1 rated capacity C_1	48 kWh
Battery 1 rated voltage $V_{bat,nom1}$	240 V
Battery 1 absorption voltage $V_{bat,abs1}$	284 V
Battery inverter 2 rated power $S_{bat,2}$	3 kVA
Battery inverter 2 output inductance L_2	4 mH
Battery 2 rated capacity C_2	18 kWh
Battery 2 rated voltage $V_{bat,nom2}$	120 V
Battery 2 absorption voltage $V_{bat,abs2}$	142 V
RMS amplitude of the inverter output voltage E	230 V
RMS amplitude of the ac bus voltage V	230 V
Droop coefficient M_p	0.3 Hz
Time constant of the real power filter τ_p	10.6 ms
Time constant of the grid frequency filter τ_f	1 s
Minimum frequency deviation Δf_{min}	0.5 Hz
Maximum frequency deviation Δf_{max}	2 Hz

Table 3.10. System features.

At the start, the load consumes 4 kW and the net power is therefore $P_T = -2$ kW. Given the fact that the battery voltages are lower than the absorption values, $\delta f = 0$ for both batteries (see Fig. 3.39), the system is in Mode I, the per-unit power is the same for both batteries ($P_1 = 2 \cdot P_2$) and the grid frequency is below $f_0 + \Delta f_{min} = 50.5$ Hz.

Then, at second 5, a 2.7 kW load is disconnected, leading to a net power $P_T = -4.7$ kW. The battery 2 voltage exceeds its maximum value and thus, $\delta f_2 > 0$. According to (3.139), the absorbed power then passes from battery 2 to battery 1 so that the battery 2 voltage is controlled, making the system operate in Mode II. Since $\delta f_1 = 0$, the frequency is also lower than $f_0 + \Delta f_{min}$ in this case, and the PV power requires no limitation.

Then, at second 12, a 1.3 kW load is disconnected, resulting in a net power $P_T = -6$ kW. The voltages of both batteries exceed their absorption values, meaning that the storage system cannot absorb this power and the PV power has to be reduced.

Thanks to the control, δf_1 , δf_2 and the grid frequency increase. Then, when the frequency measured by the PV inverters exceeds $f_0 + \Delta f_{min} = 50.5$ Hz, the PV power is limited so that both battery voltages are regulated. The system is thus operating in Mode III, with $P_{pv} = 4.5$ kW and $f = 50.87$ Hz.

Finally, at second 20, a 4 kW load is connected, leading to a net power $P_T = -0.5$ kW. As a result, both battery voltages decrease to below their maximum values, and δf_1 and δf_2 decrease to reach $\delta f_1 = \delta f_2 = 0$. The grid frequency also decreases, the PV inverters perform MPPT and the system switches to Mode I.

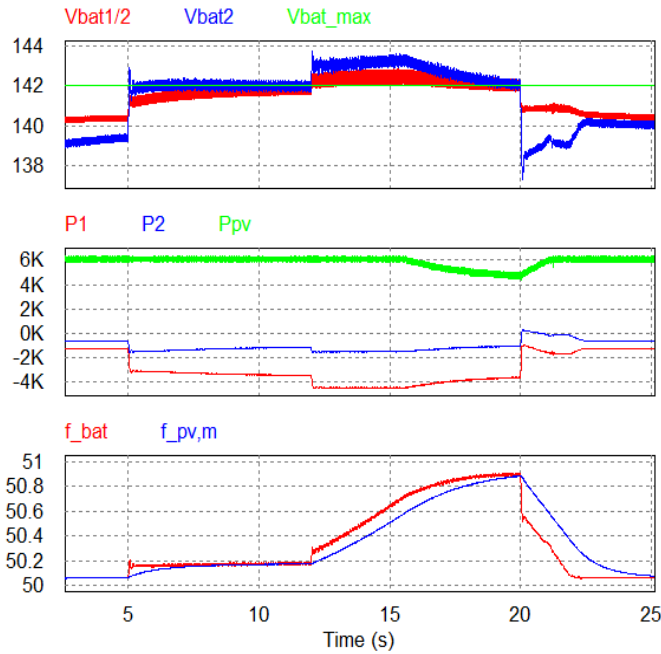


Figure 3.46. Voltage regulation during the transition Mode I – Mode II – Mode III – Mode I.

3.7.2.5 Mode IV: One battery discharged

In this mode, one battery voltage or current is controlled to its reference value, $v_{bat} = v_{bat,min}$ or $i_{bat} = i_{bat,d,max}$, and the other battery voltage and current are within limits. The control imposes $\delta f < 0$ for the first battery and $\delta f = 0$ for the second one. From (3.139), the first battery is therefore supplying less power than the second one. Since $\delta f = 0$ for one battery inverter, the frequency deviation Δf is between $\pm M_p$ and the net power is not modified.

In this mode, one battery has its voltage and current within limits, and with $\delta f = 0$. When, for this battery, the voltage drops to below $v_{bat,min}$ or the discharging current exceeds $i_{bat,d,max}$, the net power cannot be delivered by the whole storage system. In this case, the power cannot be reorganized between the batteries, as was the case for this mode. According to the control, both batteries reduce δf . At first, this has no effect on the net power. However, when the grid frequency deviation becomes lower than $-\Delta f_{min}$, the load power starts to be regulated and the system switches to Mode V. If the system does not allow for non-critical load regulation, then the frequency will continue to decrease until $\Delta f < -\Delta f_{stop}$, where the system shuts down in order to prevent irreversible damage to the batteries.

On the other hand, in this Mode IV, there is a battery whose voltage or current is being regulated to its reference value, $v_{bat} = v_{bat,min}$ or $i_{bat} = i_{bat,d,max}$. When this voltage increases or this current decreases, the battery inverter raises δf and the system changes to Mode I.

3.7.2.6 Mode V: Load regulation

In Mode V, the voltage or current of all batteries is regulated to its reference value, $v_{bat} = v_{bat,min}$ or $i_{bat} = i_{bat,d,max}$. Due to the control, $\delta f < 0$ for both batteries, which results in a frequency deviation $\Delta f < -\Delta f_{min}$. As a result, the load power is regulated, making it possible to impose the required net power so that the voltage or current is maintained to its reference value.

In this mode, if the net power to be supplied decreases (for example due to an increase in irradiance), then the regulation increases the frequency deviation to over $-\Delta f_{min}$, and the system switches to Mode IV.

On the other hand, if all non-critical loads have already been disconnected and the storage system cannot supply the required net power, then $v_{bat} < v_{bat,min}$ or $i_{bat} > i_{bat,d,max}$ for both batteries, and the control continues to decrease δf until $\Delta f < -\Delta f_{stop}$, where the system is shutdown in order to prevent irreversible damage to the batteries.

Another simulation was carried out for the system presented above in Fig. 3.37 and Table 3.10. It addresses current regulation during the transition from Mode I – Mode IV – Mode V – Mode I. The simulation results are plotted in Fig. 3.47 and show the battery currents, the maximum discharging current for both batteries (Fig. 3.47(a)), the load power, the battery powers (Fig. 3.47(b)), the frequency imposed by the battery inverters and the frequency measured by the controllable load (Fig. 3.47(c)). It is assumed that, due to adverse conditions, both batteries are very hot. In order to protect the batteries, their maximum current is reduced to $i_{bat,d,max1} = 20$ A and $i_{bat,d,max2} = 10$ A. During the

simulation, the PV power is always 0, and a number of resistive loads are disconnected and connected, including a 2.7 kW controllable load.

At the beginning, a 3 kW load is connected to the grid. Since the battery currents are under their maximum values, $\delta f = 0$ for both batteries (see Fig. 3.39), and the system is in Mode I. As a result, the per-unit power is the same for both batteries ($P_1 = 2 \cdot P_2$) and the grid frequency is higher than $f_0 - \Delta f_{min} = 49.5$ Hz.

Then, at second 5, a 2 kW load is connected. The battery 2 current becomes higher than the maximum value, which leads to $\delta f_2 < 0$. The delivered power then passes from battery 2 to battery 1 so that the battery 2 current is controlled, making the system operate at Mode IV. Since $\delta f_1 = 0$, the frequency is also higher than $f_0 - \Delta f_{min}$ in this case, and the load does not require regulation.

Next, at second 10, a 1.4 kW load is connected. At that moment, the currents of both batteries exceed their maximum values, meaning that the storage system cannot deliver the power required and the load needs to be reduced. Thanks to the control, δf_1 , δf_2 and the grid frequency decrease. When the frequency measured by the controllable load drops to below $f_0 - \Delta f_{min} = 49.5$ Hz, the load power is regulated in such a way that both battery currents are controlled. The system is then operating in Mode V, with $P_{load} = 5.8$ kW, $P_{load,cont} = 2.1$ kW and $f = 49.15$ Hz.

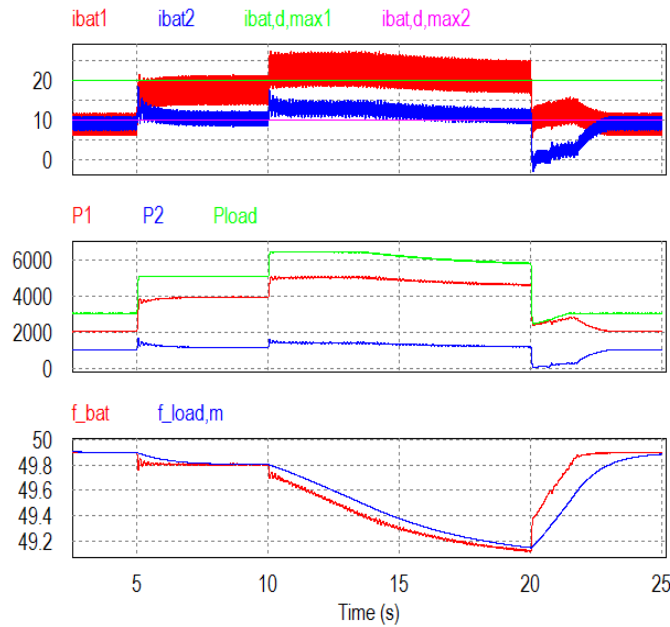


Figure 3.47. Current regulation during the transition Mode I – Mode IV – Mode V – Mode I.

Finally, a 3.4 kW load is disconnected at second 20. This causes the battery currents to drop to below their maximum values, and δf_1 and δf_2 increase to reach $\delta f_1 = \delta f_2 = 0$. The grid frequency also increases, the controllable load consumes more power and the system switches to Mode I.

3.7.3 Small-signal modeling

Small-signal modeling is developed in this section in order to design the controllers so that a certain stability margin and dynamic response is obtained for the system. In section 3.7.3.1, the small-signal modeling is applied to a system operating in Mode III. Furthermore, it is assumed that there are two batteries and two battery inverters with identical characteristics. The small-signal modeling for other modes is explained in section 3.7.3.2. Then, the modeling for different battery systems is developed in section 3.7.3.3. Although the modeling for more than two batteries is not shown here, it can be readily obtained from the two-battery model.

3.7.3.1 Mode III: Identical battery system

When both battery systems are identical, the power response can be decoupled into the power distribution response and the net power regulation, as it will be shown in this section. The power distribution is related to the difference between the power supplied by both batteries, $P_1 - P_2$, and will be called difference (D) response. The net power regulation is related to PV and load power regulation, i.e. to the sum of the battery powers, $P_1 + P_2$, and will be called sum (S) response.

The power delivered by a battery inverter to the AC bus can be expressed as [3.48]

$$P = \frac{V \cdot E}{X} \cdot \sin \delta, \quad (3.142)$$

where E is the RMS amplitude of the inverter output voltage, δ is the power angle, V is the RMS amplitude of the AC bus voltage and X is the output reactance.

In practical applications, δ is very low. Furthermore, the influence of small variations in E and V on the real power can be disregarded. Applying these approximations and the small-signal analysis to (3.142), the following is obtained:

$$\hat{P} = \frac{V_0 \cdot E_0}{X} \cdot \hat{\delta}, \quad (3.143)$$

where $V_0 = E_0$ is the rated voltage.

With regard to the difference response, the battery power difference can be readily calculated using (3.143) as

$$\hat{P}_1 - \hat{P}_2 = \frac{V_0 \cdot E_0}{X} \cdot (\hat{\delta}_1 - \hat{\delta}_2). \quad (3.144)$$

The difference between the power angles only changes if the frequencies imposed by the battery inverters, f_1 and f_2 , are different. By means of the relationship between the power angle and the frequency, and (3.144), the following applies:

$$\hat{P}_1 - \hat{P}_2 = D_{PL} \cdot (\hat{f}_1 - \hat{f}_2) \quad (3.145)$$

$$D_{PL} = \frac{V_0 \cdot E_0}{X} \cdot \frac{2\pi}{s}. \quad (3.146)$$

Equation (3.145) shows that the power distribution can be controlled by changing the frequency difference between the battery inverters, as performed for the conventional droop method.

Concerning the sum response, the sum of P_1 and P_2 can be easily obtained from the power balance as

$$\hat{P}_1 + \hat{P}_2 = \hat{P}_T = \hat{P}_{load} - \hat{P}_{RES}, \quad (3.147)$$

where P_{RES} is the total renewable-energy-source power, and P_{load} is the total load power.

The total load can include linear loads and constant power loads (CPLs). While the real power of the CPLs does not depend on the grid voltage, the real power of the linear loads increases as the voltage augments. However, this has a small effect on the power response in this case since the load impedance is always much higher than the inverter output impedance [3.24], [3.71]. Furthermore, the influence on the real power is much smaller than on the reactive power due to the lower sensitivity to voltage variations [3.72]. The power P_{load} is also independent of the frequency in Mode III and will not therefore be considered for the analysis.

The photovoltaic and wind-energy systems can be considered as constant power sources (CPSs) since their power depends on the resource during MPPT operation and on the power reference during power limitation [3.73]. As a result, the real power of the RES is independent of the grid voltage. However, the power P_{RES} does depend on the frequency according to Fig. 3.40, which leads to the following expression:

$$P_{RES} = \frac{\Delta f_{max} - \Delta f_m}{\Delta f_{max} - \Delta f_{min}} \cdot P_{mpp,tot}, \quad (3.148)$$

where $P_{mpp,tot}$ is the total stored MPP power.

Applying small-signal analysis to (3.148) and taking account of the first-order filter H_f shown in Fig. 3.40, gives

$$\hat{P}_{RES} = -\frac{P_{mpp,tot}}{\Delta f_{max} - \Delta f_{min}} \cdot H_f \cdot \Delta \hat{f}. \quad (3.149)$$

It can be considered that the grid frequency deviation Δf is the average between the frequency deviations imposed by both inverters. As a result, from (3.147) and (3.149)

$$\hat{P}_1 + \hat{P}_2 = S_{RES} (\hat{f}_1 + \hat{f}_2) \quad (3.150)$$

$$S_{RES} = \frac{1}{2} \cdot \frac{P_{mpp,tot}}{\Delta f_{max} - \Delta f_{min}} \cdot H_f. \quad (3.151)$$

Equation (3.150) shows that the net power can be regulated by changing the sum of battery inverters frequencies, in effect thanks to the PV power regulation shown in Fig. 3.40.

Equations (3.145) and (3.150) represent the power response of the system to frequency variations. Once the system plant has been obtained, the control model can now be developed. The frequency of the battery inverters is imposed as dictated by (3.138), where the first part of the equation represents the conventional droop method and the term δf is added according to Fig. 3.39. Since the analysis is based on Mode III, $\delta f_d = 0$ and $\delta f = \delta f_c$. It is also assumed that the battery voltages are being regulated, which leads to $\delta f = \delta f_{c,v}$ (see Fig. 3.39). The modeling of the current regulation is not shown in this section because it is similar and simpler than the modeling of the voltage regulation. Taking these considerations into account, (3.138) and Fig. 3.39, the following is obtained:

$$f = f_0 - \frac{M_P}{S_{bat}} \cdot H_P \cdot P + C_{c,v} \cdot S_v \cdot (v_{bat} - v_{bat,max}), \quad (3.152)$$

where H_P models the measurement and sampling of the power, and S_v models the sampling of the battery voltage.

Applying small-signal analysis to (3.152) gives

$$\hat{f} = -\frac{M_P}{S_{bat}} \cdot H_P \cdot \hat{P} + C_{c,v} \cdot S_v \cdot \hat{v}_{bat}. \quad (3.153)$$

Considering the small-signal analysis of the Thevenin lead-acid battery equivalent circuit model, the battery power to voltage transfer function G_{bat} can be obtained as [3.74]

$$\frac{\hat{v}_{bat}}{\hat{P}_{bat}} = -\frac{C_{bat} R_C R_S \cdot s + R_C + R_S}{C_{bat} R_C (V_{bat} + R_S I_{bat}) s + V_{bat} + (R_C + R_S) I_{bat}}, \quad (3.154)$$

where p_{bat} is the power delivered by the battery, V_{bat} and I_{bat} are the battery voltage and current (DC operating points), R_S is the internal resistance and R_C and C_{bat} represent the first order dynamics of the battery. Parameters R_S , R_C and C_{bat} can be considered constant for modeling purposes since the SOC changes but slightly within the operating range of the voltage regulation.

Due to the DC bus capacitor voltage regulation, the power delivered by the battery inverter, P , is delayed in relation to p_{bat} . A first order filter, named B, will be used to model this delay. In this case, it also can be considered that $(R_C + R_S) \cdot I_{bat} \ll V_{bat}$. Based on these two considerations, (3.154) leads to the following:

$$\hat{v}_{bat} = -\frac{1}{V_{bat}} \cdot \frac{C_{bat} R_C R_S \cdot s + R_C + R_S}{C_{bat} R_C s + 1} \cdot B \cdot \hat{P} = -G_{bat} \cdot B \cdot \hat{P}. \quad (3.155)$$

From (3.153) and (3.155), the frequency reference can be obtained as a function of P

$$\hat{f} = -(D_{CON} + S_{BAT}) \cdot \hat{P} \quad (3.156)$$

$$D_{CON} = \frac{M_P}{S_{bat}} \cdot H_P \quad (3.157)$$

$$S_{BAT} = C_{c,v} \cdot S_v \cdot G_{bat} \cdot B. \quad (3.158)$$

Equation (3.156) shows how the control of each battery inverter changes its frequency when its delivered power varies. By means of (3.145), and (3.156) applied to both inverters, the characteristic equation for the power distribution, den_D , can be obtained as

$$den_D = 1 + D_{PL} (D_{CON} + S_{BAT}). \quad (3.159)$$

The conventional droop control, represented by D_{CON} , was initially designed to have an effect on the power distribution [3.21], whilst the voltage regulation, represented by S_{BAT} , was initially designed to have an effect on the net power [3.39]. However, as (3.159) shows, both terms are important for the power distribution response. To evaluate the influence of each term more precisely, the root locus diagrams of den_D for different values of M_P and K_P are shown in Fig. 3.48, where K_P is the proportional parameter of PI controller $C_{c,v}$. The analysis is carried out for the system presented in Table 3.10 but assuming that the features of battery inverter 2 are those of battery inverter 1, in other words identical battery systems. As can be observed in Fig. 3.48, the characteristic equation den_D has four important roots. Poles λ_1 and λ_2 , the two poles closest to the origin, are the dominant ones. The rapidity of the power distribution response is therefore determined by them. The appearance of these slow poles is due to the battery voltage regulation (term δf or transfer function S_{BAT}), since they are not present for the

conventional droop control [3.21]. On the other hand, poles λ_3 and λ_4 , the two poles farthest away from the origin, represent the stability margin of the power distribution response. Although these poles are also influenced by the voltage regulation, their appearance is due to the conventional droop method (term $M_p \bar{p}$ or transfer function D_{CON}). As can be observed in Fig. 3.48(a), increasing M_p moves poles λ_3 and λ_4 closer to the imaginary axis, making the system less damped, whilst at the same time reduces the real part of λ_1 and λ_2 , slowing down the response. On the other hand, as shown in Fig. 3.48(b), increasing K_p has the same effect on λ_3 and λ_4 , making the response less damped, but increases the real part of λ_1 and λ_2 , speeding up the response.

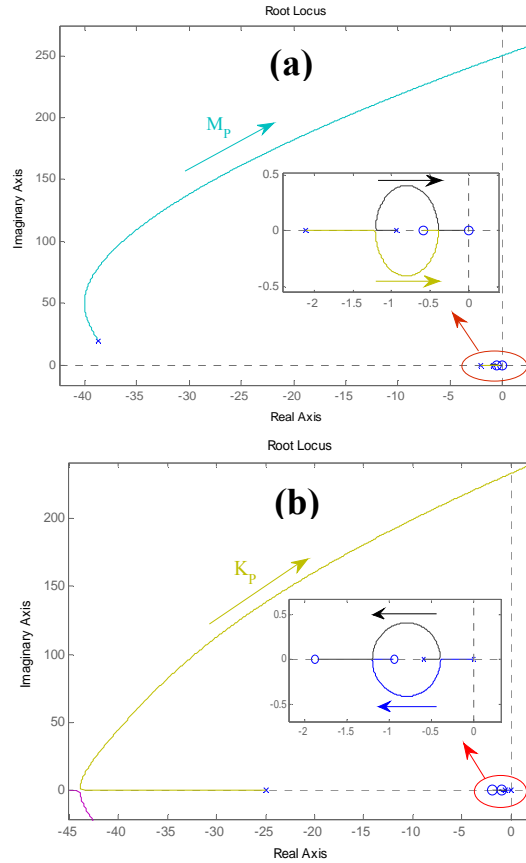


Figure 3.48. Root locus diagrams for den_D : (a) M_p increasing ($K_p = 0.07$) and (b) K_p increasing ($M_p = 0.3$ Hz).

By means of (3.150), and (3.156) applied to both inverters, the characteristic equation for the net power, den_s , can be obtained as

$$den_s = 1 + S_{RES} (D_{CON} + S_{BAT}). \quad (3.160)$$

This expression shows that, also in this case, both terms D_{CON} (due to $M_p \Delta p$) and S_{BAT} (due to δf) are important for the net power response. The influence of each term on dens is also evaluated here by means of the root locus analysis. The root locus diagrams of dens for different values of M_p and K_p are shown in Fig. 3.49 for the system above. As can be observed in the figures, dens has three important roots. Poles λ_1 and λ_2 are the ones closest to the origin, and their appearance is due to the battery voltage regulation (term δf or transfer function S_{BAT}). On the other hand, pole λ_3 is the one farthest away from the origin and its appearance is due to the conventional droop method (term $M_p \Delta p$ or transfer function D_{CON}), since it does not exist when the droop control is not present [3.39]. As shown in Fig. 3.49(a), increasing M_p moves λ_1 and λ_2 closer to the real axis, making the response more damped. The response also becomes slower if M_p is high enough. On the other hand, as also shown in Fig. 3.49(b), increasing K_p slightly changes the damping of λ_1 and λ_2 (from a certain value of K_p), and has little effect on the pole λ_3 . Furthermore, if K_p is high enough, the real pole λ_3 , which is more affected by M_p , becomes dominant.

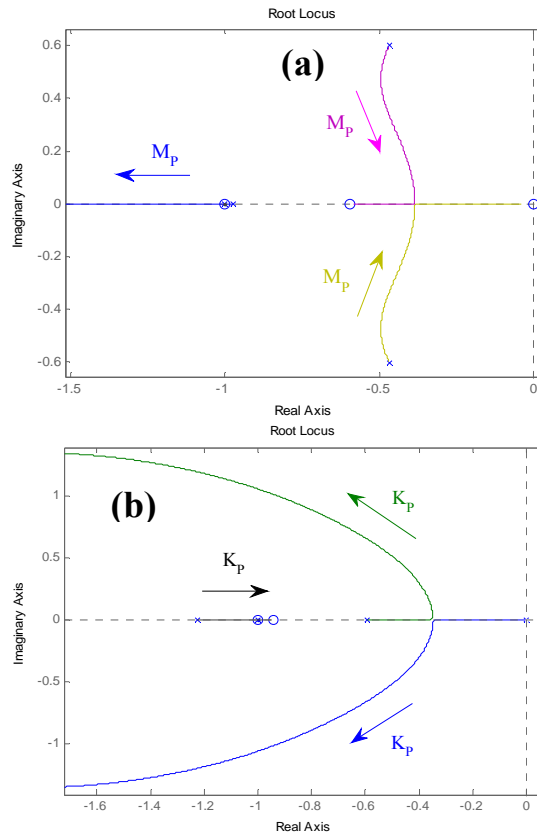


Figure 3.49. Root locus diagrams for dens : (a) M_p increasing ($K_p = 0.07$) and (b) K_p increasing ($M_p = 0.3$ Hz).

Although the demonstration is not shown here, the characteristic equations den_D and den_S are exactly the same for an n identical battery system if a slight modification is made: the 2 in A_{RES} expression [see (3.151)] must be changed by N . As a result, the analysis carried out in this section is also applicable to an n identical battery system.

3.7.3.2 Other modes: Identical battery system

The system modeling when operating in Modes I, II, IV and V can be obtained from the analysis developed in section 3.7.3.1 for Mode III. In this section, the differences in relation to Mode III are highlighted for the other operating modes.

When the system is operating in Mode V, (3.159) and (3.160) apply for the power distribution and net power responses, respectively. However, the total controllable load power must be considered in S_{RES} instead of the total MPP power $P_{mpp,tot}$ [see (3.151)], controller $C_{d,v}$ must be considered in S_{BAT} instead of $C_{c,v}$ (see (3.158)), and the battery model parameters must be given for a low SOC level (see (3.155)).

When the system is operating in Mode II or IV, the net power is not modified because the RES or load power is not changed by the control. As a result, the net power response does not apply in these modes. With regard to the power distribution response, (3.159) must be modified. In these modes, only one battery is varying the term δf while, in the other, the controller outputs are inactive due to saturation $\delta f = 0$ (see Fig. 3.39). As a result, (3.156) is only valid for one battery inverter, and in the other $S_{BAT} = 0$. On account of this, the characteristic equation for the power distribution now becomes

$$den_D = 1 + D_{PL} (D_{CON} + S_{BAT} / 2) . \quad (3.161)$$

Furthermore, controller $C_{c,v}$ and a high-SOC battery model must be used in Mode II while controller $C_{d,v}$ and a low-SOC battery model must be used in Mode IV. Equation (3.161) can be analyzed by means of the root locus diagram for den_D of Fig. 3.48, considering K_P is equal to half the K_P value used in Mode III. As a result, the power distribution response for Mode II and IV is more damped and slower than for Mode III.

Finally, when the system is operating in Mode I, both battery voltage controllers are inactive because their outputs are saturated to $\delta f = 0$ (see Fig. 3.39). As a result, only the conventional droop method applies, which leads to

$$den_D = 1 + D_{PL} \cdot D_{CON} . \quad (3.162)$$

In this case, poles λ_1 and λ_2 of Fig. 3.48 do not appear and the power distribution response therefore becomes much quicker and more damped, as can be observed in Fig. 3.48 for $K_P = 0$ and in [3.21].

3.7.3.3 Different battery system

If the two battery systems are not identical, even if they have the same per-unit characteristics, then the power response cannot be decoupled. For Mode III, proceeding similarly to section 3.7.3.1, the characteristic equation for the power response, den_{DS} , is expressed as

$$den_{DS} = 1 + 1/2 \cdot D_{PL} (S_{RES1} + S_{RES2}) (D_{CON1} + S_{BAT1}) (D_{CON2} + S_{BAT2}) + 1/2 \cdot (D_{PL} + S_{RES1}) (D_{CON1} + S_{BAT1}) + 1/2 \cdot (D_{PL} + S_{RES2}) (D_{CON2} + S_{BAT2}) \quad (3.163)$$

$$D_{PL1} = D_{PL2} = D_{PL} = 2 \cdot \frac{V \cdot E}{X_1 + X_2} \cdot \frac{2\pi}{s} \quad (3.164)$$

$$S_{RES1} = \frac{X_2}{X_1 + X_2} \cdot \frac{P_{mpp,tot}}{\Delta f_{max} - \Delta f_{min}} \cdot H_f, \quad S_{RES2} = \frac{X_1}{X_1 + X_2} \cdot \frac{P_{mpp,tot}}{\Delta f_{max} - \Delta f_{min}} \cdot H_f \quad (3.165)$$

$$D_{CON1} = \frac{M_P}{S_{bat,1}} \cdot H_P, \quad D_{CON2} = \frac{M_P}{S_{bat,2}} \cdot H_P \quad (3.166)$$

$$S_{BAT1} = C_{c,v1} \cdot S_{v1} \cdot G_{bat1} \cdot B_1, \quad S_{BAT2} = C_{c,v2} \cdot S_{v2} \cdot G_{bat2} \cdot B_2. \quad (3.167)$$

The different control parameters of each battery inverter can be designed according to section 3.7.3.1, assuming that all the inverters operating are identical. Equations (3.163)–(3.167) then make it possible to verify the real dynamic response. In effect, in doing so, it can be verified that the dynamic response for the different battery system remains similar to the one for the identical battery system (design system).

3.7.4 Experimental results

The proposed frequency-based energy management strategy was validated by experimental tests. Two batteries with their inverters were connected in parallel and generated the AC grid. A load bank and two PV emulators with their inverters were connected to the grid. The battery and PV inverters are commercial ones, with a modified configuration, in order to implement the proposed strategy. More precisely, the proposed droop method presented by (3.138), where δf is obtained from (3.140) and Fig. 3.39, was programmed in the battery inverters whilst the PV power regulation, represented by Fig. 3.40 and Fig. 3.42, was programmed in the PV inverters. The system features were shown in Table 3.10 (section 3.7.2.4). As it can be observed, the two battery systems have different characteristics. Precision power analyzer WT1800 served to obtain the data, recording voltages, currents, powers and frequencies every 50 ms.

The first test was conducted to validate the battery voltage regulation during the transition from Mode I – Mode II – Mode III, similarly to the simulation presented in

Fig. 3.46. The experimental results are shown in Fig. 3.50 and represent the battery 1 voltage divided by two, the battery 2 voltage, the maximum voltage for both batteries (Fig. 3.50(a)), the battery powers, the load power, the total PV power (Fig. 3.50(b)), and the grid frequency (Fig. 3.50(c)). At the start, both battery voltages are lower than their maximum values. As a result, the battery inverters share the power in proportion to their ratings ($P_1=2 \cdot P_2$), the frequency is close to 50 Hz and the system is operating in Mode I. Then, at about second 8, a 2.6 kW load is disconnected. The battery 2 voltage exceeds its maximum value but, thanks to the control, the absorbed power switches from battery 2 to battery 1 so that the battery 2 voltage is controlled, making the system operate in Mode II. The grid frequency increases in this mode but remains lower than $f_0 + \Delta f_{min} = 50.5$ Hz because the PV power does not need to be limited. Then, at about second 25, a 1.3 kW load is also disconnected, making the voltage of both batteries exceed their maximum value. As a result, the grid frequency is increased by the control. Then, when the frequency measured by the PV inverters becomes higher than 50.5 Hz, the PV power is reduced so that both battery voltages are regulated, making the system operate in Mode III. The figure shows how the proposed strategy is successful in controlling the absorption voltage of one or two batteries as required while at the same time making the most of the solar energy, yet with no need for communication cables.

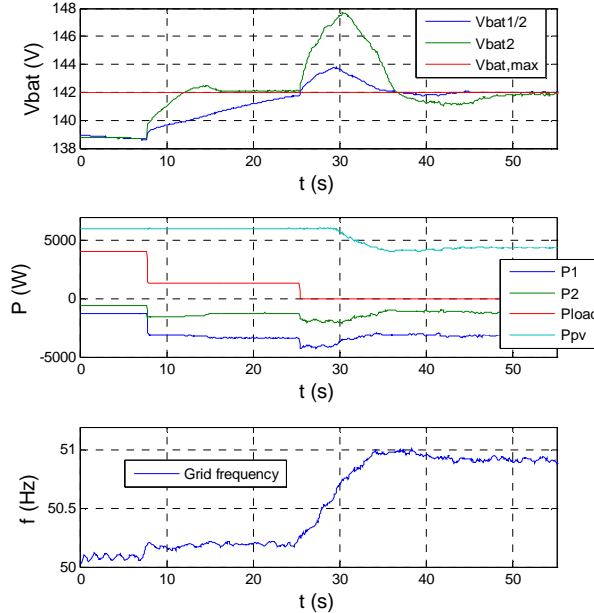


Figure 3.50. Voltage regulation during the transition Mode I – Mode II – Mode III.

The second test validated the battery current regulation during the transition from Mode I – Mode IV – Stop, in a similar way to the simulation presented in Fig. 3.47. The

experimental results, shown in Fig. 3.51, represent the battery currents, the maximum discharging current for both batteries (Fig. 3.51(a)), the load power, the battery powers (Fig. 3.51(b)), and the grid frequency (Fig. 3.51(c)). It is assumed that, due to adverse conditions, both batteries are very hot. In order to protect them, their maximum current is reduced to $i_{bat,d,max1} = 20$ A and $i_{bat,d,max2} = 10$ A. During the test, the PV power is always 0, and there are no controllable loads. At the beginning, both battery currents are below their maximum values. Hence, the system operates in Mode I, the load power is shared by the inverters and the frequency is close to 50 Hz. At about second 3, a 2 kW load is connected. The battery 2 current then becomes higher than 10 A and, as a result, the control makes battery inverter 1 deliver more power so that the battery 2 current is regulated, making the system operate in Mode II. Then, at about second 5, a 1.3 kW load is also connected, making each battery current exceed its maximum value. As a result, the grid frequency is reduced by the control. Since there are no controllable loads in this test, the frequency continues decreasing until it reaches the value $f_0 - \Delta f_{stop} = 49.4$ Hz, when the system stops in order to protect the batteries. The figure shows how the proposed strategy manages to either control the current of one battery or to stop the system as required with no need for communication cables. Furthermore, the value of Δf_{stop} can be configured in order to control the overload time, depending on the system thermal properties.

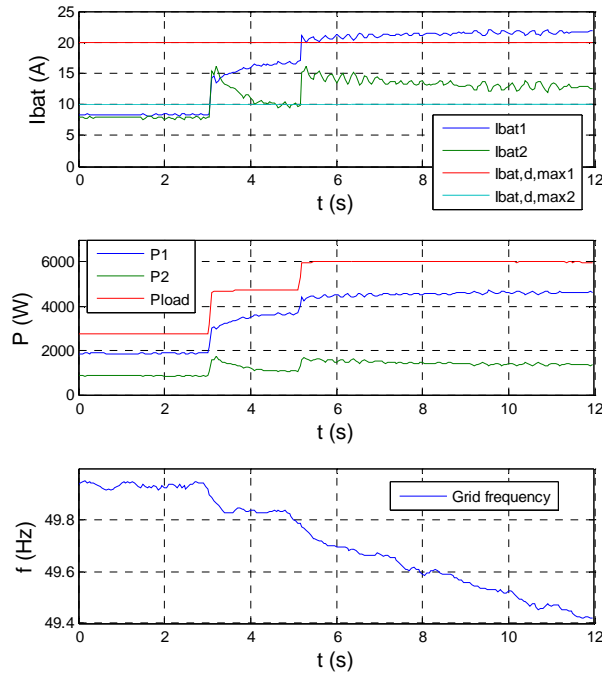


Figure 3.51. Current regulation during the transition Mode I – Mode IV – Stop.

3.8 CONCLUSIONS

3.8.1 Frequency and voltage regulation

In the first part of this chapter, three different models for droop-based microgrids were presented and compared. Two of the models use small-signal analysis and do not decouple the real and reactive power responses. As a result, these models are more accurate but also much more complicated, making it difficult to discern the different dynamic properties of the real and reactive power responses. Thanks to these models, it was shown for a particular case that the operation point and the load type have small effect on the system eigenvalues. The third model is a linear model which does not consider the load effect. Although it is an approximate model, its accuracy was validated by comparison with the small-signal models. This model is much simpler and decouples the real and reactive power responses. As a result, the control parameters such as the droop coefficients and the voltage controller parameters can be readily designed. Simulation results validate the models and the control design.

The droop control method with RMS voltage regulation used in this part of the chapter is suitable for parallel-connected inverters. However, the analysis also shows that this technique has significant drawbacks when feeding non-linear loads. It is therefore proposed a harmonic compensation in order to improve its performance. For the harmonic currents, the control emulates a virtual inductance in such a way that the output inductance is reduced and its per-unit value is equalized for every inverter. As a result, the proposed technique succeeds in equally distribute the inverter currents while at the same time reducing the grid voltage THD. The improvements of the proposed control were validated by simulations results.

3.8.2 Energy management

Next in the chapter, a new SOC-based droop control method which achieves energy management for different battery inverters in stand-alone ac supply systems with distributed energy storage was proposed. The proposed technique shifts the $P-f$ curve either upwards or downwards in line with the battery SOC and, as a result, the stored energy becomes balanced with no need for communications between the inverters. Thanks to the proposed SOC-based droop control, power and SOC responses are decoupled, making it possible to optimize both responses by means of the two $P-f$ curve parameters. The power response can be optimized by means of power droop coefficient M_p , in the same way as for the conventional droop method. With regard to the SOC

response, it is possible to improve the transient and reduce the SOC imbalance by increasing SOC coefficient M_S .

The proposed method was compared to the existing slope changing method, which modifies the $P - f$ curve slope as a function of the battery SOC. In contrast to the method proposed in this work, the power and SOC response are not decoupled in the slope changing method, and the design parameter, n , must be chosen as a trade-off between both responses. Furthermore, the power response is highly dependent on the operating point, leading to slow dynamics and power errors when operating with low SOC.

A one-year simulation was conducted for both techniques using a real power profile. The results show adequate energy management for both techniques, however the proposed method achieves better performance for both the transient response and the SOC imbalance. The experimental results for the proposed control validate the theoretical analysis for different operating points, showing how the battery with a higher SOC delivers more power or absorbs less power than the battery with a lower SOC, which helps balance the SOC.

These techniques correspond to the energy management during normal operation, i.e. while the battery SOC are within limits. The subsequent part of this chapter is focused on the high/low SOC operation, in which the battery voltage and current have to be controlled to the rated values. Also in this case, the energy management is carried out with no need for communication cables between the inverters or to a central supervisor, using frequency as a communication signal, resulting in a more reliable and cost-effective system. During normal operation, the power is shared among the various battery inverters thanks to the conventional droop method. Then, when some batteries are fully charged or are absorbing too much current, the frequency is increased. As a result, the power is first transferred from some of the batteries to the others. However, if all batteries have reached the maximum voltage or current, then the renewable-energy sources detect the high frequency and reduce their power in order to adjust the battery voltages or currents. Similarly, when the batteries are either fully discharged or delivering excessive current, then the frequency is decreased. This makes it possible to regulate the voltage/current of one or more batteries as required. Then, if all batteries reach their minimum voltage or maximum discharging current, the less critical loads are regulated. If this is not possible, then the system stops in order to prevent serious damage to the batteries.

Small-signal modeling for the whole system was finally carried out. This modeling makes it possible to evaluate the new control in relation to the conventional droop method, as well as to design the main control parameters even for uncertain systems, and validate the power response dynamics and stability for a given system.

The proposed strategy is validated by means of simulation and experimental tests for a system with two battery inverters, two PV inverters and a number of loads. The results show how the regulation of battery voltages or currents, the PV power reduction and the non-critical loads control are correctly performed. As a result, the energy management is successfully carried out for the most critical situations with no use of communication cables.

3.8.3 Summary for implementation of the whole system

In order to implement the proposed techniques in a real system, a summary of the different controls is provided in this section. The general scheme of the system was presented in Fig. 3.37. It is worth noting that each inverter only has information about local variables and the control is thus based on them.

The implementation for the battery inverter is shown in Fig. 3.52. The real and reactive powers are obtained from the grid voltage and inverter current as described in section 3.2.2. For the reactive power management, the conventional droop method is used, defined by (3.18), where the droop coefficient is obtained from (3.20). This control determines the RMS voltage reference V^* , which is in turn regulated by a PI controller, as shown in the figure. On the other hand, the conventional droop method for real power, defined by (3.17) and (3.19), is modified in order to realize the battery energy management. The regulation of the battery voltages and currents is carried out thanks to (3.138), where δf is obtained from (3.140) and Fig. 3.39. This makes it possible to balance the SOC during high/low SOC operation. Equation (3.138) can be combined with (3.120) to balance the SOC also during normal operation. The combination of both methods represents the overall energy management strategy and can be expressed as

$$f = f_0 - M_p \cdot p + M_s \cdot (SOC - SOC_0) + \delta f. \quad (3.168)$$

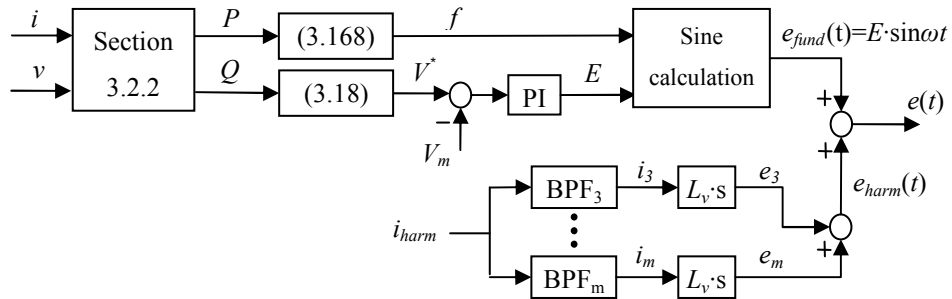


Figure 3.52. Implementation for the battery inverter.

Since the RMS output voltage E and the frequency are now known, the instantaneous voltage e can finally be obtained and modulated, as shown in Fig. 3.52. In this control there is no inner current loop, and the hardware current limitation presented in section 3.4.2 is also implemented as a means of protection.

The regulation summarized so far deals with the fundamental components. However, some additional controls must be added in the presence of non-linear loads. In this case, the inverter current harmonics are obtained by means of a BPF, and a harmonic voltage compensation is calculated as shown in (3.95). The harmonic voltage is then added to the fundamental voltage, as shown in Fig. 3.52. Finally, if the loads also demand DC current, a DC voltage droop is also applied, represented by (3.81)–(3.83).

With regard to the PV and wind converters, they operate under MPPT as long as the frequency deviation is below Δf_{min} . When frequency exceeds this value, the renewable power is reduced following the curve shown in Fig. 3.40. The power limitation is carried out by controlling the DC/DC boost stage of the PV and wind converter, as shown in Fig. 3.42 for photovoltaic generators and in Fig. 3.43 for small wind turbines.

3.9 REFERENCES

- [3.1] D. P. Kaundinya, P. Balachandra, N. H. Ravindranath, "Grid-connected versus stand-alone energy systems for decentralized power—A review of literature," *Renewable and Sustainable Energy Reviews*, vol. 13, pp. 2041–2050, 2009.
- [3.2] K. Bandara, T. Sweet, J. Ekanayake, "Photovoltaic applications for off-grid electrification using novel multi-level technology with energy storage," *Renewable Energy*, vol. 37, pp. 82–88, 2012.
- [3.3] L. Wang, X. Q. Guo, H. R. Gu, W. T. Wu, J. M. Guerrero, "Precise modeling based on dynamic phasors for droop-controlled parallel-connected inverters," in *2012 IEEE Symposium on Industrial Electronics (ISIE)*, pp. 475–480, Hangzhou (China), 2012.
- [3.4] M. C. Chandorkar, D. M. Divan, R. Adapa, "Control of parallel connected inverters in standalone ac supply systems," *IEEE Transactions on Industry Applications*, vol. 29, no. 1, pp. 136–143, 1993.
- [3.5] H. Ghoddami, M. B. Delghavi, A. Yazdani, "An integrated wind-photovoltaic-battery system with reduced power-electronic interface and fast control for grid-tied and off-grid applications," *Renewable Energy*, vol. 45, pp. 128–137, 2012.
- [3.6] F. Valenciaga, P. F. Puleston, "Supervisor control for a stand-alone hybrid generation system using wind and photovoltaic energy," *IEEE Transactions on Energy Conversion*, vol. 20, no. 2, pp. 398–405, 2005.
- [3.7] K. Strunz, E. Abbasi, D. N. Huu, "DC microgrid for wind and solar power integration," *IEEE Journal of Emerging and Selected Topics in Power Electronics*, vol. 2, no. 1, pp. 115–126, 2014.

- [3.8] Y. Chen, A. Q. Huang, X. Yu, "A high step-up three-port dc-dc converter for stand-alone PV/battery power systems," *IEEE Transactions on Power Electronics*, vol. 28, no. 11, pp. 5049–5062, 2013.
- [3.9] A. Urtasun, P. Sanchis, I. San Martín, J. López, L. Marroyo, "Modeling of small wind turbines based on PMSG with diode bridge for sensorless maximum power tracking," *Renewable energy*, vol. 55, pp. 138–149, 2013.
- [3.10] A. Urtasun, P. Sanchis, L. Marroyo, "Adaptive voltage control of the dc/dc boost stage in PV converters with small input capacitor," *IEEE Transactions on Power Electronics*, vol. 28, no. 11, pp. 5038–5048, 2013.
- [3.11] O. Gehrke, S. Ropenus, P. Venne, "Distributed energy resources and control: a power system point of view," http://www.risoe.dk/rispubl/reports/ris-r-1608_248-257.pdf, 2007.
- [3.12] Y. Ito, Y. Zhongqing, H. Akagi, "DC microgrid based distribution power generation system," in *4th Power Electronics and Motion Control Conference (IPEMC)*, vol. 3, pp. 1740–1745, Xi'an (China), 2004.
- [3.13] K. Techakittiroj, S. Patumtaewapibal, V. Wongpaibool, W. Threevithayanon, "Roadmap for implementation of dc system in future houses" in *13th International Conference on Harmonics and Quality of Power (ICHQP)*, pp. 1–5, Wollongong (Australia), 2008.
- [3.14] O. Haas, O. Ausburg, P. Palensky, "Communication with and within distributed energy resources," in *2006 IEEE Conference on Industrial Informatics*, pp. 352–356, Singapore, 2006.
- [3.15] E. A. A. Coelho, P. C. Cortizo, P. F. D. Garcia, "Small-signal stability for parallel-connected inverters in stand-alone ac supply systems," *IEEE Transactions on Industry Applications*, vol. 38, pp. 533–542, 2002.
- [3.16] C. N. Rowe, T. J. Summers, R. E. Betz, D. J. Cornforth, T. G. Moore, "Arctan power-frequency droop for improved microgrid stability," *IEEE Transactions on Power Electronics*, vol. 28, no. 8, pp. 3747–3759, 2013.
- [3.17] A. Mohd, E. Ortjohann, D. Morton, O. Omari, "Review of control techniques for inverters parallel operation," *Electric Power Systems Research*, vol. 80, pp. 1477–1487, 2010.
- [3.18] E. Serban H. Serban, "A control strategy for a distributed power generation microgrid application with voltage- and current-controlled source converter," *IEEE Transactions on Power Electronics*, vol. 25, pp. 2981–2992, 2010.
- [3.19] J. M. Guerrero, J. C. Vasquez, J. Matas, L. G. de Vicuña, M. Castilla, "Hierarchical control of droop-controlled ac and dc microgrids- A general approach toward standarization," *IEEE Transactions on Industrial Electronics*, vol. 58, pp. 158–172, 2011.
- [3.20] E. Barklund, N. Pogaku, M. Prodanovic, C. Hernandez-Aramburu, T. C. Green, "Energy management in autonomous microgrid using stability-constrained droop control of inverters," *IEEE Transactions on Power Electronics*, vol. 23, pp. 2346–2352, 2008.
- [3.21] N. Pogaku, M. Prodanovic, T. C. Green, "Inverter-based microgrids: small-signal modelling and testing," in *3rd IET Conference on Power Electronics, Machines and Drives (PEMD)*, pp. 499–504, Dublin (Ireland), 2006.

- [3.22] J. M. Guerrero, J. C. Vasquez, J. Matas, M. Castilla, L. G. de Vicuña, "Control strategy for flexible microgrid based on parallel line-interactive UPS systems," *IEEE Transactions on Industrial Electronics*, vol. 56, no. 3, pp. 726–736, 2009.
- [3.23] E. A. A. Coelho, P. C. Cortizo, P. F. D. Garcia, "Small signal stability for single phase inverter connected to stiff ac system," in *1999 IEEE Industry Applications Conference*, no. 4, pp. 2180–2187, Phoenix (USA), 1999.
- [3.24] J. M. Guerrero, L. G. de Vicuña, J. Matas, M. Castilla, J. Miret, "A wireless controller to enhance dynamic performance of parallel inverters in distributed generation systems," *IEEE Transactions on Power Electronics*, vol. 19, no. 5, pp. 1205–1213, 2004.
- [3.25] P. Varela, D. Meneses, O. Garcia, J. A. Oliver, P. Alou, J. A. Cobos, "Current mode with RMS voltage and offset control loops for a single-phase aircraft inverter suitable for parallel and 3-phase operation modes," in *2011 IEEE Energy Conversion Congress and Exposition (ECCE)*, pp. 2562–2567, Phoenix (USA), 2011.
- [3.26] Y. Sozer, D. A. Torrey, "Modeling and control of utility interactive inverters," *IEEE Transactions on Power Electronics*, vol. 24, no. 11, pp. 2475–2483, 2009.
- [3.27] E. H. Kim, J. M. Kwon, J. K. Park, B. H. Kwon, "Practical control implementation of a three- to single-phase online UPS," *IEEE Transactions on Industrial Electronics*, vol. 55, no. 8, pp. 2933–2942, 2008.
- [3.28] T. Dragicevic, J. M. Guerrero, J. C. Vasquez, D. Skrlec, "Supervisory Control of an Adaptive-Droop Regulated DC Microgrid with Battery Management Capability," *IEEE Transactions on Power Electronics*, vol. 29, no. 2, pp. 695–706, 2014.
- [3.29] R. Majumber, B. Chaudhuri, A. Ghosh, R. Majumber, G. Ledwich, F. Zare, "Improvement of stability and load sharing in an autonomous microgrid using supplementary droop control loop," *IEEE Transaction on Power Systems*, vol. 25, no. 2, pp. 796–808, 2010.
- [3.30] I. U. Nutkani, P. C. Loh, F. Blandjerg, "Droop scheme with consideration of operating costs," *IEEE Transactions on Power Electronics*, vol. 29, no. 3, pp. 1047–1052, 2014.
- [3.31] H. Kakigano, Y. Miura, T. Ise, "Distribution voltage control for dc microgrids using fuzzy control and gain-scheduling technique," *IEEE Transactions on Power Electronics*, vol. 28, no. 5, pp. 2246–2258, 2013.
- [3.32] X. Lu, K. Sun, J. M. Guerrero, L. Huang, "SoC-based dynamic power sharing method with ac-bus voltage restoration for microgrid applications," in *38th Annual Conference on IEEE Industrial Electronics Society (IECON)*, pp. 5677–5682, Montreal (Canada), 2012.
- [3.33] X. Lu, K. Sun, J. M. Guerrero, J. C. Vasquez, L. Huang, R. Teodorescu, "SoC-based droop method for distributed energy storage in dc microgrid applications," in *2012 IEEE Symposium on Industrial Electronics (ISIE)*, pp. 1640–1645, Hangzhou (China), 2012.
- [3.34] C. K. Sao, P. W. Lehn, "Autonomous load sharing of voltage source converters," *IEEE Transactions on Power Delivery*, vol. 20, no. 2, pp. 1009–1016, 2005.

- [3.35] R. B. Godoy, J. O. P. Pinto, C. A. Canesin, E. A. A. Coelho, A. M. A. C. Pinto, "Differential-evolution-based optimization of the dynamic response for parallel operation of inverters with no controller interconnection," *IEEE Transactions on Industrial Electronics*, vol. 59, no. 7, pp. 2859–2866, 2012.
- [3.36] A. K. Daud, M. S. Ismail, "Design of isolated hybrid systems minimizing costs and pollutant emissions," *Renewable Energy*, vol. 44, pp. 215–224, 2012.
- [3.37] J. Kim, S. Kim, J. Jeon, "Coordinated state-of-charge control strategy for microgrid during islanded operation," in *3rd IEEE Power Electronics for Distributed Generation Systems (PEDG)*, pp. 25–28, Aalborg (Denmark), 2012.
- [3.38] D. E. Olivares, C. A. Canizares, M. Kazerani, "A centralized optimal energy management system for microgrids," in *2011 IEEE Power and Energy Society General Meeting*, San Diego (USA), pp. 24–29, 2011.
- [3.39] A. Urtasun, P. Sanchis, D. Barricarte, L. Marroyo, "Energy management strategy for a battery-diesel stand-alone system with distributed PV generation based on grid frequency modulation," *Renewable Energy*, vol. 66, pp. 325–336, 2014.
- [3.40] D. Wu, J. M. Guerrero, J. C. Vasquez, T. Dragicevic, F. Tang, "Coordinated power control strategy based on primary-frequency-signaling for islanded microgrids," in *2013 IEEE Energy Conversion Congress and Exposition (ECCE)*, pp. 1033–1038, Denver (USA), 2013.
- [3.41] S. Y. Yang, C.W. Zhang, X. Zhang, R. X. Cao, W. X. Shen, "Study on the control strategy for parallel operation of inverters based on adaptive droop method," in *1st IEEE Conference on Industrial Electronics and Applications*, pp. 1–5, Singapore, 2006.
- [3.42] M. Gao, S. Yang, C. Jin, Z. Ren, M. Chen, Z. Qian, "Analysis and experimental validation for power calculation based on p - q theory in single-phase wireless-parallel inverters," in *26th Annual IEEE Applied Power Electronics Conference and Exposition (APEC)*, pp. 620–624, Fort Worth (USA), 2011.
- [3.43] M. Aredes, H. Akagi, E. H. Watanabe, E. V. Salgado, L. F. Encarnacao, "Comparisons between the p - q and p - q - r theories in three-phase four-wire systems," *IEEE Transactions on Power Electronics*, vol. 24, no. 4, pp. 924–933, 2009.
- [3.44] J. L. Afonso, M. J. S. Freitas, J. S. Martins, " p - q theory power components calculations," in *2003 IEEE Symposium on Industrial Electronics*, no. 1, pp. 385–390, Rio de Janeiro (Brazil), 2003.
- [3.45] W. Peng, Y. Baghzouz, "Accurate circuit model for steady-state and dynamic performance of lead-acid AGM batteries," in *2011 Conference and Utility Exhibition on Power and Energy Systems: Issues & Prospects for Asia (ICUE)*, pp. 1–6, Pattaya City (Thailand), 2011.
- [3.46] Y. Tang, W. Yuan, M. Pan, Z. Wan, "Experimental investigation on the dynamic performance of a hybrid PEM fuel cell/battery system for lightweight electric vehicle application," *Applied Energy*, vol. 88, no. 1, pp. 68–76, 2011.
- [3.47] Y. Chen, S. Lin, B. Hong, "Experimental study on a passive fuel cell/battery hybrid power system," *Energies*, vol. 6, no. 12, pp. 6413–6422, 2013.
- [3.48] A. R. Bergen, *Power Systems Analysis*. Englewood Cliffs, NJ: Prentice Hall, 1986.

- [3.49] C. T. Lee, C. C. Chu, P. T. Cheng, "A new droop control method for the autonomous operation of distributed energy resource interface converters," *IEEE Transactions on Power Electronics*, vol. 28, no. 4, pp. 1980–1993, 2013.
- [3.50] T. W. Li, C. Kao, "An accurate power control strategy for power-electronics-interfaced distributed generation units operating in a low-voltage multibus microgrid," *IEEE Transactions on Power Electronics*, vol. 24, no. 12, pp. 2977–2988, 2009.
- [3.51] ISO 13297, 2014.
- [3.52] Guide to the Wiring Regulations. 17th Edition IEE Wiring Regulations, BS: 7671, 2008.
- [3.53] J. He, Y. W. Li, J. M. Guerrero, F. Blaadbjerg, J. C. Vasquez, "An islanding microgrid power sharing approach using enhanced virtual impedance control scheme," *IEEE Transactions on Power Electronics*, vol. 28, no. 11, pp. 5272–5282, 2013.
- [3.54] W. Ghzaïel, M. J. -B. Ghorbal, I. Slama-Belkhdja, J. M. Guerrero, "A novel grid impedance estimation technique based on adaptive virtual resistance control loop applied to distributed generation inverters", in *15th European Conference on Power Electronics and Applications (EPE)*, pp. 1–10, Lille (France), 2013.
- [3.55] J. M. Guerrero, J. Matas, L. G. de Vicuña, M. Castilla, J. Miret, "Wireless-control strategy for parallel operation of distributed-generation inverters," *IEEE Transactions on Industrial Electronics*, vol. 53, no. 5, pp. 1461–1470, 2006.
- [3.56] S. V. Iyer, M. N. Belur, M. C. Chandorkar, "Analysis and mitigation of voltage offsets in multi-inverter microgrids," *IEEE Transactions on Energy Conversion*, vol. 26, no. 1, pp. 354–363, 2011.
- [3.57] M. Xie, Y. Li, K. Cai, P. Wang, X. Sheng, "A novel controller for parallel operation of inverters based on decomposing of output current," in *2005 Industry Applications Conference*, pp. 1671–1676, Kowloon (Hong Kong), 2005.
- [3.58] K. Ng, Y. Huang, C. Moo, Y. Hsieh, "An enhanced coulomb counting method for estimating state-of-charge and state-of-health of lead-acid batteries," in *31st Telecommunications Energy Conference (INTELEC)*, pp. 1–5, Incheon (South Korea), 2009.
- [3.59] T. Markvart, A. Fragaki, J. N. Ross, "PV system sizing using observed time series of solar radiation," *Solar Energy*, vol. 80, no. 1, pp. 46–50, 2006.
- [3.60] K. D. Brabandere, B. Bolsens, J. V. Keybus, A. Woyte, J. Driesen, R. Belmans, "A voltage and frequency droop control method for parallel inverters," *IEEE Transactions on Power Electronics*, vol. 22, no. 4, pp. 1107–1115, 2007.
- [3.61] J. Hu, J. Zhu, D. G. Dorrell, J. M. Guerrero, "Virtual flux droop method – A new control strategy of inverters in microgrids," *IEEE Transactions on Power Electronics*, vol. 29, no. 9, pp. 4704–4711, 2014.
- [3.62] A. Urtasun, P. Sanchis, L. Marroyo, "Limiting the power generated by a photovoltaic system," in *10th Multi-Conference on Systems, Signals & Devices (SSD)*, pp. 1–6, Hammamet (Tunisia), 2013.

- [3.63] Z. M. Dalala, Z. U. Zahid, J.-S. Lai, "New overall control strategy for small-scale WECS in MPPT and stall regions with mode transfer control," *IEEE Transactions on Energy Conversion*, vol. 28, no. 4, pp. 1082–1092, 2013.
- [3.64] Y. Yang, F. Blaabjerg, "Synchronization in single-phase grid-connected photovoltaic systems under grid faults," in *3rd Symposium on Power Electronics for Distributed Generation Systems (PEDG)*, pp. 476–482, Aalborg (Denmark), 2012.
- [3.65] J. Rocabert, A. Luna, F. Blaabjerg, P. Rodriguez, "Control of power converters in AC microgrids," *IEEE Transactions on Power Electronics*, vol. 27, no. 11, pp. 4734–4749, 2012.
- [3.66] S. G. Jorge, J. A. Solsona, C. A. Busada, "Control scheme for a single-phase grid-tied voltage source converter with reduced number of sensors," *IEEE Transactions on Power Electronics*, vol. 29, no. 7, pp. 3758–3765, 2014.
- [3.67] P. Sanchis, L. Marroyo, J. Coloma, "Design methodology for the frequency shift method of islanding prevention and analysis of its detection capability," *Progress in Photovoltaics*, vol. 13, no. 5, pp. 409–428, 2005.
- [3.68] M. Ross, C. Abbey, Y. Brissette, G. Joos, "Photovoltaic inverter characterization testing on a physical distribution system," in *2012 IEEE Power and Energy Society General Meeting*, pp. 1–7, San Diego (USA), 2012.
- [3.69] J. Pascual, P. Sanchis, L. Marroyo, "Implementation and control of a residential electrothermal microgrid based on renewable energies, a hybrid storage system and demand side management," *Energies*, vol. 7, no. 1, pp. 210–237, 2014.
- [3.70] P. O. Kriett, M. Salani, "Optimal control of a residential microgrid," *Energy*, vol. 42, no. 1, pp. 321–330, 2012.
- [3.71] J. M. Guerrero, J. Matas, L. G. de Vicuña, M. Castilla, J. Miret, "Decentralized control for parallel operation of distributed generation inverters using resistive output impedance," *IEEE Transactions on Industrial Electronics*, vol. 54, no. 2, pp. 994–1004, 2007.
- [3.72] A. Urtasun, P. Sanchis, L. Marroyo, "Comparison of linear and small-signal models for inverter-based microgrids," in *2014 Australasian University Power Engineering Conference (AUPEC)*, pp. 1–6, Perth (Australia), 2014.
- [3.73] T. Messo, J. Jokipii, J. Puukko, T. Suntion, "Determining the value of DC-link capacitance to ensure stable operation of a three-phase photovoltaic inverter," *IEEE Transactions on Power Electronics*, vol. 29, no. 2, pp. 665–673, 2014.
- [3.74] S. G. Tesfahunegn, P. J. S. Vie, O. Ulleberg, T. M. Undeland, "A simplified battery charge controller for safety and increased utilization in stand-alone PV applications," in *2011 Conference on Clean Electric Power (ICCEP)*, pp. 137–144, Ischia (Italy), 2011.

CHAPTER 4

CONTROL OF THE DC/DC STAGE IN PV INVERTERS WITH SMALL INPUT CAPACITORS

ABSTRACT

In the case of photovoltaic (PV) systems, an adequate PV voltage regulation is fundamental in order to both maximize and limit the power. For this purpose, a large input capacitor has traditionally been used. However, when reducing that capacitor size, the nonlinearities of the PV array make the performance of the voltage regulation become highly dependent on the operating point. This chapter first analyzes the nonlinear characteristics of the PV generator and clearly states their effect on the control of the DC/DC boost stage of commercial converters by means of a linearization around the operating point. Then, it proposes an adaptive control, which enables the use of a small input capacitor preserving at the same time the performance of the original system with a large capacitor.

A similar analysis is carried out for the control of the two-input buck (TIBuck) converter. This converter possesses a high efficiency and makes it possible to maximize the power of two PV arrays at the same time, improving the overall efficiency under different shading conditions. By means of a small-signal modeling, the control theme of the two PV voltages is formulated and the effect of the nonlinearities is presented.

Although PV systems are generally based on Maximum Power Point Tracking (MPPT), many situations such as stand-alone systems or microgrids increasingly require the PV system to operate below maximum power. This chapter also proposes a control strategy for a DC/DC boost converter that makes it possible to operate in both modes, namely at either maximum or limited power point tracking.

Simulation and experimental validation are provided throughout the chapter.

4.1 INTRODUCTION

PV systems are undergoing continuous expansion and development, mainly in grid-connected but also in isolated applications [4.1]. When connected to the grid, PV arrays generally operate under Maximum Power Point Tracking (MPPT). However, the current trends toward distributed power generation systems based on renewable energies are leading to the introduction of microgrids [4.2], [4.3]. In such systems, it might be necessary to reduce the PV power in order to contribute to grid stability. A technique being able to function below the MPP by tracking a reference power must then be used [4.4]. We will refer to this technique as Limited Power Point Tracking (LPPT). In the same way, in an isolated system, the PV array usually operates under MPPT. Yet, it needs to limit the power and switch to LPPT when the storage element is full and the demand is low [4.5].

Because of the PV generator features, an electronic conversion system is required to be connected to the electric grid. In this chapter, the PV conversion system shown in Fig 4.1 is employed. It consists of a PV generator, an input capacitor (C), a DC/DC converter, a bus capacitor (C_{bus}) and a single-phase inverter.

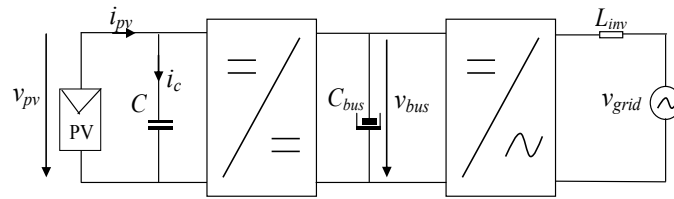


Figure 4.1. PV single-phase conversion system.

There are many MPPT algorithms in the literature [4.6], [4.7]. The most commonly used are perturbation and observation (P&O) [4.2], [4.8], hill-climbing [4.3], [4.9], fractional open-circuit voltage [4.10], and incremental conductance [4.11], [4.12]. Some of these algorithms have already been modified making it possible to operate both in MPPT and LPPT [4.5], [4.13].

The output reference of these algorithms can be the PV voltage [4.13]–[4.17], the PV current [4.18], [4.19], or just the duty cycle of the DC/DC converter [4.5]. However, excluding low power applications, it is well-known that the best option is to control the PV voltage since it changes slowly and it is more stable. Controlling the PV current can result in a voltage drop during the transients and controlling the duty cycle leads to an inappropriate control of PV voltage and current as well as more losses and stresses in the converter [4.14]–[4.16], [4.20], [4.21].

The value of the PV voltage reference is continuously updated by the MPP or LPP tracker. Whilst in MPPT operation the PV voltage is very close to the MPP voltage, in LPPT operation the PV voltage varies from the MPP to the open circuit voltage [4.13]. Thus, a fast and stable regulation in the entire operating range is required for a proper tracking [4.15], [4.16]. However, the nonlinear nature of the PV array can cause the performance of the regulation to change with the operating point. Depending on the conversion structure, the control strategy and the input capacitor size, this nonlinear characteristic can lead to great variations in the dynamics and can even put the stability at risk [4.15], [4.16], [4.22], [4.23].

The variability in the PV voltage control process is caused by the dynamic resistance, which is obtained from the slope of its I-V curve [4.24], [4.25]. This parameter depends on the characteristics of the PV array, and is highly variable with the irradiation, the temperature and especially the PV voltage. As a result, the voltage regulation performance can decrease when operating under MPPT because of the irradiation and temperature change, and it can become even worse when operating under LPPT since the PV voltage also changes.

For buck converters, the influence of the dynamic resistance on the PV voltage control has been quite studied. In [4.16], the authors analyze the single and cascaded feedback loops. In both cases, a proper control is guaranteed in the whole operation range thanks to high cutoff frequencies and a big input capacitor. An in-depth analysis of the cascaded control technique is developed in [4.26] and [4.27]. It is shown that the system can become unstable if a correct regulation and capacitor sizing are not carried out [4.23], [4.26], [4.27].

On the contrary, the effect of the dynamic resistance has been less analyzed in the case of boost converters. In [4.15], the authors regulate the PV voltage by means of the duty cycle, i.e. without inner current loop. These control schemes are usually applied to small PV generators (e.g. 50 W in [4.15]). In these systems, the influence of the dynamic resistance results in a very variable damping factor of the duty cycle to voltage transfer function. However, the undamped natural frequency hardly changes and the system can be easily controlled with a second order controller with no appreciable changes in the regulation performance [4.15], [4.28].

There are other minor proposals to control low-power boost converters. In [4.29], the authors employ a cascaded sliding mode control and a capacitor current sensor in order to both eliminate the dynamic resistance influence and achieve a very fast voltage response, making it possible to reject abrupt irradiance variations. Nevertheless, this strategy requires an additional current sensor in order to measure the input capacitor current.

For higher power boost converters (typically over 1 kW), the PV voltage is usually controlled by means of an inner inductor current loop. The cascaded control avoids current transients and reduces failure rates. In these systems, the influence of the dynamic resistance has not been traditionally taken into account. The current to voltage transfer function has been considered as $1/Cs$, where the PV array is taken as a current source [4.17], [4.30]. Initially, the dynamic resistance effect was hidden by the use of large input capacitors. In recent years, these large electrolytic capacitors are being replaced by smaller polypropylene ones, which are much cheaper and more reliable [4.31], [4.32]. However, this capacitor reduction makes the dynamic resistance not negligible anymore. This renders necessary the analysis of the dynamic resistance effect and the design of new control techniques capable of compensating this effect.

Section 4.2 first presents the PV array small-signal model. Section 4.3 then analyzes the influence of the dynamic resistance for the DC/DC boost stage of a typical single-phase PV converter. It is shown how the dynamic resistance diminishes the performance of the PV voltage regulation. An adaptive control is then proposed in order to obtain a PV voltage regulation with a cutoff frequency and a phase margin that remain almost constant for the whole operating range, in a system with a small input capacitor. The dynamic resistance is estimated from measured variables of the converter, namely the PV voltage and inductor current, and the controller is continuously adapted making use of that estimation.

The converters previously mentioned only perform one MPPT per converter. However, depending on the application, different PV module technologies, orientations and shading conditions can be present, leading to significant power losses [4.33]–[4.35]. In order to reduce the effects of mismatching on the power production of the PV generator, various solutions have been proposed. A review of a number of alternatives is carried in [4.36], where the different actions are divided into three groups: modifying the MPPT algorithm [4.37], changing the electrical connection of the panels into the PV field [4.38], and modifying the power system architecture [4.39], [4.40]. Within the latter group, a frequently adopted solution is the two-stage boost inverter, where the first stage is a boost converter and the second stage is an H-bridge inverter [4.41]–[4.43]. In order to perform two different MPPTs, two DC/DC boost converters can be placed in parallel, as shown in Fig. 4.2(a) [4.44], [4.45]. Although the conversion efficiency is lower when compared to the previous configuration, the overall efficiency is higher for rooftop applications under different shading conditions, orientations or module technologies, thanks to the dual MPPT capability.

As an alternative to two single-input converters, two-input DC/DC converters have been proposed in the literature [4.46]–[4.53]. These converters aim to improve the system performance in terms of conversion efficiency, integration and cost, while, at the

same time, maintain the dual MPPT capability. However, most of the proposed converters still use more than one active switch and several passive components, actually lacking in high power density or high efficiency.

Section 4.4 proposes a new configuration where the first stage is a Two-Input Buck (TIBuck) converter and the second stage is a boost inverter, as shown in Fig. 4.2(b). Similar to the previous cases, this configuration also achieves two MPPTs. However, only one active switch is required for the DC/DC conversion, making the system more cost-effective and reliable. Furthermore, given that the switch and the diode have very low voltage stress, the TIBuck conversion efficiency is very high [4.54].

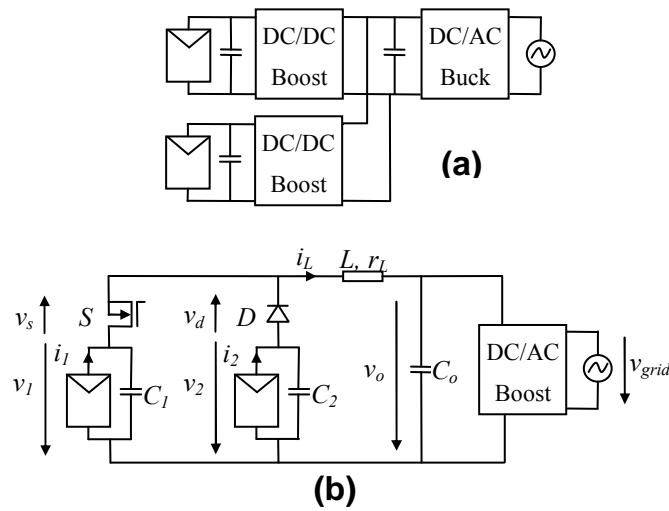


Figure 4.2. Configurations for grid-connected PV systems with dual MPPT capability: (a) Multiple boost converters, (b) Proposed scheme.

The TIBuck converter was first proposed by Sebastian *et al.* in [4.54] to improve AC/DC conversion efficiency. In this first application, the output voltage was the control variable. Section 4.4, however, is concerned about the dual MPPT and thus deals with the two input voltage regulation. The nonlinearity of the two PV arrays is considered, which adds complexity to the analysis of the nonlinear converter [4.15], [4.16], [4.28], [4.41]. Small-signal modeling is carried out in order to apply linear control techniques.

Apart from the cases previously mentioned, there are more situations in which a power reduction is required. In some countries such as Germany and Italy, network operators are already demanding a frequency regulation capability in PV power plants. Thus, the PV power output must be reduced below the MPP when the grid frequency exceeds a certain value. Furthermore, the PV power could exceed the maximum power

output of the electronic converter, which is likely to occur since the peak power of the PV generator is usually higher than the converter maximum power [4.55]. In this situation, the system must also operate under LPPT and thus below the MPP.

Section 4.5 proposes a new method which permits operation in both MPPT and LPPT modes. The strategy obtains high dynamics for the power response and guarantees stability in both modes of operation (MPPT and LPPT), preventing the system from a voltage drop in the PV voltage even for abrupt irradiance changes.

4.2 PV ARRAY SMALL-SIGNAL MODEL

The curve I-V of a PV array can be expressed as [4.16]

$$i_{pv} = I_{ph} - I_0 \cdot \exp \left[\frac{v_{pv} + R_s \cdot i_{pv}}{V_t} - 1 \right] - \frac{v_{pv} + R_s \cdot i_{pv}}{R_p}, \quad (4.1)$$

where I_{ph} and I_0 are the photogenerated and saturation current of the array, R_s is the equivalent series resistance, R_p is the equivalent shunt resistance, and V_t is the thermal voltage, which is defined as

$$V_t = N_s \cdot m \cdot \frac{k \cdot T}{q}, \quad (4.2)$$

where N_s is the cells connected in series, m is the ideality factor of the diode, k is the Boltzmann constant, T is the generator temperature, and q is the electron charge.

To obtain a linear equation for the PV current i_{pv} as a function of the PV voltage v_{pv} and the irradiation g , some parameters are defined. The variation of the current with the temperature is not considered since it changes very slowly, being easily compensated by the regulator. The dynamic resistance of the array R_{pv} , which represents the voltage influence, is calculated using (4.1) as

$$R_{pv} = - \frac{\partial v_{pv}}{\partial i_{pv}} = R_d // R_p + R_s, \quad (4.3)$$

where R_d is defined as

$$R_d = \frac{V_t}{I_0} \cdot \exp \left(- \frac{v_{pv} + R_s \cdot i_{pv}}{V_t} \right). \quad (4.4)$$

Similarly, the PV current coefficient of variation with the irradiation, referred to as K_g , is worked out using (4.1) as

$$K_g = \frac{\partial i_{pv}}{\partial g} = \left(1 - \frac{R_s}{R_{pv}}\right) \cdot \frac{\partial I_{ph}}{\partial g}. \quad (4.5)$$

Thus, the linear model for the operating point with a PV current I'_0 , PV voltage V_0 , irradiation G_0 and generator temperature T_0 is

$$i_{pv} - I'_0 = K_g \cdot (g - G_0) - \frac{v_{pv} - V_0}{R_{pv}}, \quad (4.6)$$

where R_{pv} and K_g are evaluated for (V_0, G_0, T_0) .

Reordering (4.6), one finds

$$i_{pv} = I_{eq} + K_g \cdot g - \frac{v_{pv}}{R_{pv}}, \quad (4.7)$$

where I_{eq} is the equivalent current comprising the constant terms, expressed as follows:

$$I_{eq} = I'_0 - K_g \cdot G_0 + \frac{V_0}{R_{pv}}. \quad (4.8)$$

The nonlinear I-V curve of the array and its linearization around the MPP are shown in Fig. 4.3. The curve reproduces (4.1) for the PV array of Table 4.2 (presented below) and given $G_0=1000 \text{ W/m}^2$ and $T_0=25^\circ\text{C}$. The linearization around the MPP is based on (4.7).

The linear model can also be represented by an electrical circuit. The equivalent circuit, valid at the linearization point, is illustrated in Fig. 4.4.

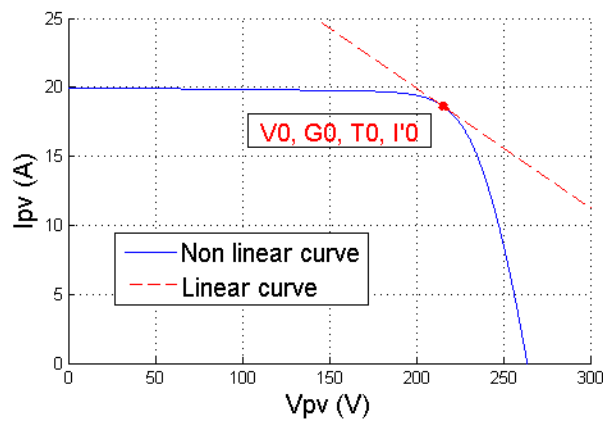


Figure 4.3. Nonlinear I-V curve and linearization at point (V_0, G_0, T_0, I'_0) .

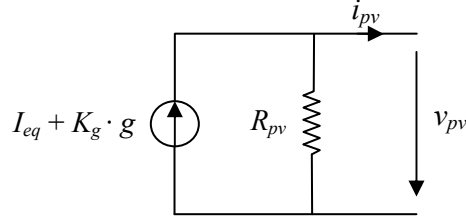


Figure 4.4. Equivalent circuit at the linearization point.

By means of (4.3) and (4.5), both parameters R_{pv} and K_g depend on the PV array (features of the panel and number of panels connected in series and in parallel) and on the operating point. For a certain PV array, they are variable with the irradiation, the temperature and especially with the PV voltage. From (4.3) and (4.4), it can be observed that the dynamic resistance increases as the voltage decreases. Thus, it will be maximum for short-circuit:

$$R_{pv}(v_{pv} = 0, g, T) = R_p + R_s \approx R_p. \quad (4.9)$$

Likewise, it will reach its minimum for open-circuit voltage. In that point, R_p can be neglected and therefore

$$R_{pv}(v_{pv} = V_{oc}, g, T) \approx \frac{V_t}{I_0} \cdot \exp\left(-\frac{V_{oc}}{V_t}\right) + R_s. \quad (4.10)$$

Imposing the open-circuit condition in (4.1), I_{ph} can be approximated as

$$I_{ph} \approx I_0 \cdot \exp\left(\frac{V_{oc}}{V_t}\right). \quad (4.11)$$

From (4.10) and (4.11) the dynamic resistance for V_{oc} is finally worked out as

$$R_{pv}(v_{pv} = V_{oc}, g, T) \approx \frac{V_t}{I_{ph}} + R_s. \quad (4.12)$$

The dynamic resistance is shown in Fig. 4.5 and Fig. 4.6 for the PV array of Table 4.2 (presented below) and different irradiances and array temperatures, respectively. In both figures, R_{pv} is represented as a function of the normalized voltage v_{norm} , which is defined as

$$v_{norm} = \frac{v_{pv} - V_{mpp}}{V_{oc} - V_{mpp}}. \quad (4.13)$$

where V_{mpp} is the voltage at maximum power.

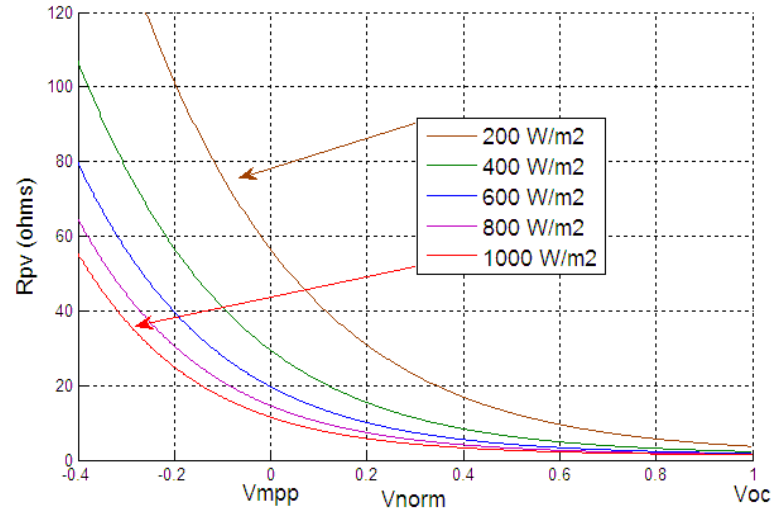


Figure 4.5. Dynamic resistance versus normalized voltage for different irradiances at $T=25^{\circ}\text{C}$.

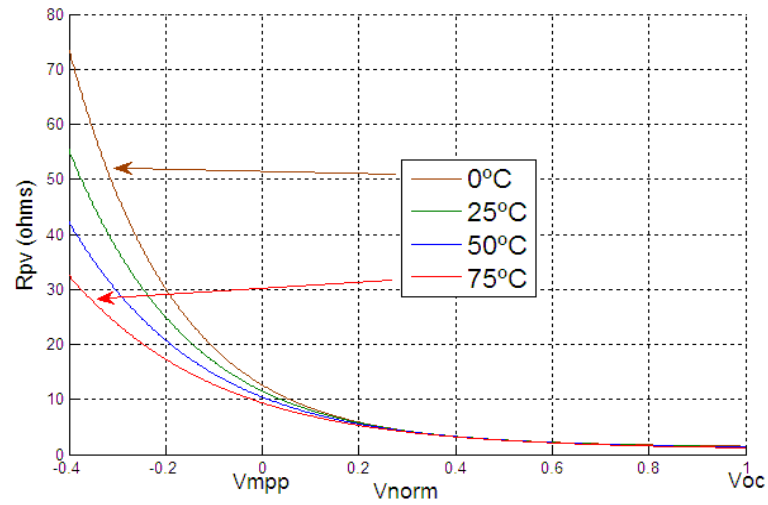


Figure 4.6. Dynamic resistance versus normalized voltage for different temperatures and $g=1000 \text{ W/m}^2$.

This normalized voltage is 1 for $v_{pv}=V_{oc}$, 0 for $v_{pv}=V_{mpp}$, and negative for $v_{pv}<V_{mpp}$. Since the PV voltage is near to V_{mpp} when operating under MPPT and higher than V_{mpp} when operating under LPPT, the dynamic resistance is represented for $v_{norm}>-0.4$. It can be observed in Fig. 4.5 and Fig. 4.6 that R_{pv} decreases for high irradiances, high temperatures and high voltages.

4.3 PV VOLTAGE CONTROL WITH BOOST CONVERTER

Because photovoltaic systems are often of low-voltage, they require a step-up conversion in order to be connected to the electric grid. A two-stage boost inverter, where the first stage is a boost converter and the second stage is an H-bridge inverter, is analyzed in this section. This system is shown in Fig 4.7, consisting of a PV array, an input capacitor (C), a boost converter, a bus capacitor (C_{bus}) and a single-phase inverter.

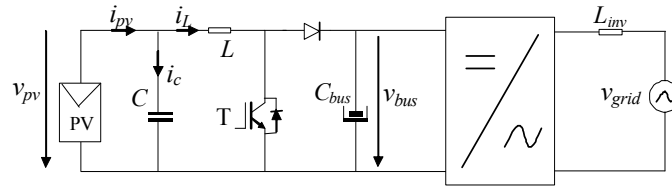


Figure 4.7. PV single-phase conversion system.

In order to control this system, there are two cascaded regulations, one for the inverter, and another for the boost converter. The inverter controls the grid current with the desired power factor and maintains a constant bus voltage. This chapter deals with the cascaded regulation of the boost loop converter, which consists of an outer PV voltage loop and an inner inductor current loop.

4.3.1 Inductor current control

Since it might be necessary to operate in LPPT with low inductor current, the current control must be able to handle both the Continuous Conduction Mode (CCM) and the Discontinuous Conduction Mode (DCM). For this purpose, the current control is based on the technique proposed in [4.56], valid for both conduction modes. As it is shown below, using that strategy, the input impedance has no influence on the current control.

From Fig. 4.7, considering average values for all variables in a commutation period, CCM and Kirchhoff's voltage law leads to

$$v_{pv} - (1-d) \cdot v_{bus} = L \cdot \frac{di_L}{dt}, \quad (4.14)$$

where d is the duty cycle.

Dividing (4.14) by v_{bus} and reorganizing the equation, one finds

$$d - \left(1 - \frac{v_{pv}}{v_{bus}}\right) = d - d_{ccm} = L \cdot \frac{di_L}{dt} \cdot \frac{1}{v_{bus}}, \quad (4.15)$$

where d_{ccm} is defined as

$$d_{ccm} = 1 - \frac{v_{pv}}{v_{bus}}. \quad (4.16)$$

As it can be observed in (4.15) and (4.16), the influence of the PV array on the process is included in d_{ccm} . The value of d_{ccm} can be estimated from the voltages v_{pv} and v_{bus} , which are measured variables. The obtained value, $d_{ccm,ff}$, can be used as feedforward compensation.

Making use of (4.15), (4.16) and this feedforward compensation, the loop for the inductor current regulation in CCM is shown in Fig. 4.8, where C_i represents the controller, S_i the current digital sampler and H_i the inductor current sensing. In these schemes, a bus voltage compensation has also been added by means of the bus voltage measurement, $v_{bus,m}$.

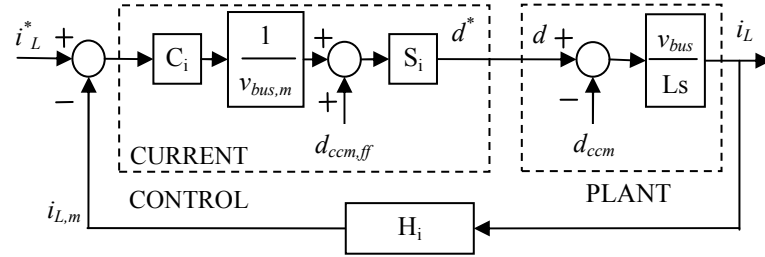


Figure 4.8. Inductor current control loop for CCM.

Being T_{si} the current sample time, the digital sampler S_i can be approximated as [4.57]

$$S_i(s) = \frac{1}{1.5 \cdot T_{si} \cdot s + 1}. \quad (4.17)$$

The inductor current sensing transfer function H_i can be expressed as

$$H_i(s) = \frac{K_i}{\tau_i \cdot s + 1}, \quad (4.18)$$

where τ_i is the time constant of the inductor current sensing and K_i is the scaling constant of the inductor current sensing, which will be taken as 1 in order to simplify the analysis.

Because of the sampler and the retard in the measurements of v_{pv} and v_{bus} , the forwarded duty cycle $d_{ccm,ff}$ does not eliminate the effect of the PV generator for high frequencies. However, it is removed below the sample and sensing frequencies, and thus around the current control cutoff frequency. The process seen by the regulator can therefore be considered as $1/Ls$ for the controller design. A simple PI controller can then be used, obtaining a regulation independent of the dynamic resistance.

For the DCM, a similar analysis is carried out in [4.56], obtaining the same schemes of Fig. 4.8 but with a different equation for the duty cycle d_{dcm} and for its estimation $d_{dcm,ff}$. In this case, only known variables of the system are also required for the estimation.

Since the boost converter can function in both conduction modes, the strategy constantly estimates both duty cycles d_{ccm} and d_{dcm} . The authors prove that when operating in CCM, $d_{ccm} < d_{dcm}$ whereas in DCM, $d_{dcm} < d_{ccm}$. In other words, the lowest duty cycle correspond to the actual mode of conduction. As a result, the technique for both conduction modes uses the same schemes of Fig. 4.8 but choosing the minimum between $d_{ccm,ff}$ and $d_{dcm,ff}$ as feedforward compensation [4.56].

4.3.2 Modeling for the voltage control loop

4.3.2.1 Traditional modeling

From Fig. 4.7 and Kirchhoff's current law

$$i_{pv} = i_c + i_L. \quad (4.19)$$

By replacing the capacitor current in (4.19):

$$i_{pv} = C \cdot \frac{dv_{pv}}{dt} + i_L. \quad (4.20)$$

From (4.20) and by applying the Laplace transformation, the following current to voltage transfer function is obtained:

$$\frac{v_{pv}(s)}{-i_L(s) + i_{pv}(s)} = \frac{1}{C \cdot s}. \quad (4.21)$$

Making use of (4.21), the loop for the PV voltage regulation is shown in Fig. 4.9, where C_v represents the controller, S_v the voltage digital sampler, H_v the PV voltage sensing, G_{icl} the current closed-loop, g the irradiance, and T the array temperature.

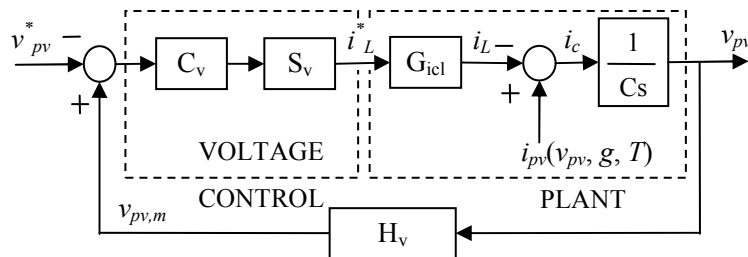


Figure 4.9. Traditional PV voltage control loop.

As it can be observed in the figure, the influence of the PV array on the process is now caused by the PV current i_{pv} . As in the case of the current control by means of the duty cycle (which depends on the PV voltage v_{pv}), a straightforward solution to remove the effect of the dynamic resistance would be to compensate the PV current i_{pv} . However, this current is not usually measured by the converter and an additional sensor would be required. For this reason, the feedforward compensation of i_{pv} is not considered in this work for the PV voltage control.

Being T_{sv} the voltage sample time, the digital sampler S_v can be approximated as [4.57]

$$S_v(s) = \frac{1}{1.5 \cdot T_{sv} \cdot s + 1}. \quad (4.22)$$

The PV voltage sensing transfer function H_v can be expressed as

$$H_v(s) = \frac{K_v}{\tau_v \cdot s + 1}, \quad (4.23)$$

where τ_v is the time constant of the PV voltage sensing and K_v is the scaling constant of the PV voltage sensing, which will be taken as 1 in order to simplify the analysis.

If the inner current and outer voltage loops are totally decoupled, the inner closed-loop could be modeled as 1 [4.17]. Although the loops are decoupled in this work, the inner closed-loop will be modeled as a first order for more precision. Being ω_{ic} the angular cutoff frequency of the current control, the transfer function of the inductor current closed-loop is

$$G_{icl}(s) = \frac{1}{s / \omega_{ic} + 1}. \quad (4.24)$$

Traditionally, the PV current i_{pv} has been considered as a disturbance and therefore independent of the variables that take part in the control. Although the current variation caused by the irradiation and the temperature is decoupled from the regulation, this is not the case for the current variation induced by the PV voltage, which cannot be considered as a disturbance and must be taken into account in the transfer function.

4.3.2.2 Small-signal modeling

The variables v_{pv} , g and i_L can be divided into their steady-state values (capitalized) and their small-signal values (marked with a hat):

$$v_{pv} = V_{pv} + \hat{v}_{pv}, \quad g = G + \hat{g}, \quad i_L = I_L + \hat{i}_L. \quad (4.25)$$

By means of the linear model of the PV array expressed by (4.7), and (4.20), one finds

$$I_{eq} + K_g \cdot g - \frac{v_{pv}}{R_{pv}} = C \cdot \frac{dv_{pv}}{dt} + i_L. \quad (4.26)$$

The linear model is only valid when it is very close to the operating point, that is for the small-signal analysis. Introducing the definitions of (4.25) into (4.26) leads to

$$I_{eq} + K_g \cdot G + K_g \cdot \hat{g} - \frac{V_{pv}}{R_{pv}} - \frac{\hat{v}_{pv}}{R_{pv}} = C \cdot \frac{d\hat{v}_{pv}}{dt} + I_L + \hat{i}_L. \quad (4.27)$$

From (4.27) and by applying the Laplace transformation, the following current to voltage transfer function is obtained as

$$G_v(s) = \frac{\hat{v}_{pv}(s)}{-\hat{i}_L(s) + K_g \cdot \hat{g}(s)} = \frac{1}{C \cdot s + 1/R_{pv}} = \frac{R_{pv}}{C \cdot R_{pv} \cdot s + 1}. \quad (4.28)$$

Using this transfer function, the loop for the PV voltage regulation becomes the one shown in Fig. 4.10. The obtained transfer function accounts for the PV current variation caused by the PV voltage. As a result, it models the behavior of the system more accurately than the traditional approach. In any case, the dynamic resistance is negligible and both transfer functions (4.21) and (4.28) are equivalent when $R_{pv} \cdot C \cdot \omega_{vc} \gg 1$, where ω_{vc} is the angular cutoff frequency of the voltage control. Thus, the traditional model is only valid when operating near short-circuit or with capacitances or voltage cutoff frequencies high enough. However, when the capacitor is reduced and taking into account that in real applications the cutoff frequency will be limited by the microprocessor and the inner current loop, the effect of the large variation range of R_{pv} cannot be neglected.

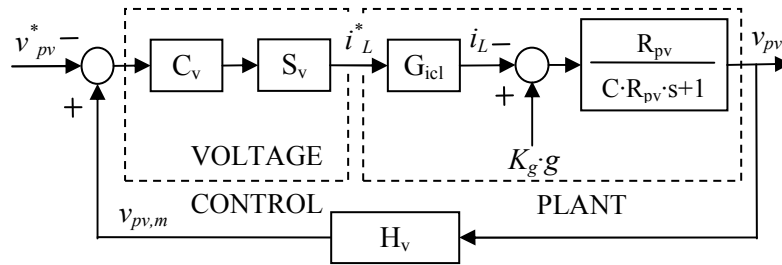


Figure 4.10. PV voltage control loop.

4.3.3 Traditional control

In this section, the variation of the regulation performance is studied for the boost stage of a typical PV converter, whose features are shown in Table 4.1. The specifications of the PV array used for the analysis are shown in Table 4.2.

The current control is carried out by means of the model developed in section 4.3.1 for a 450 Hz cutoff frequency and a 45° phase margin. For the PV voltage regulation, a PI controller is used in the converter, as it is commonly carried out. Its parameters are calculated by means of the traditional modeling, depicted in Fig. 4.9, for a cutoff frequency $f_{vc}=50$ Hz and a phase margin $PM_v=40^\circ$. The behavior of the system is now examined considering the effect of the dynamic resistance, using the modeling shown in Fig. 4.10. As it will be shown below, the dynamic resistance variation will make that the actual cutoff frequency (f_c) and the actual phase margin (PM) differ from their design values (f_{vc} and PM_v).

Nominal power	5000 W
Input capacitor C	40 μ F
Boost inductor L	750 μ H
Commutation frequency f_{com}	16 kHz
PV voltage sample time T_{sv}	250 μ s
Inductor current sample time T_{si}	125 μ s
Time constant of the PV voltage sensing τ_v	74 μ s
Time constant of the inductor current sensing τ_i	74 μ s
Angular cutoff frequency of the current control ω_{ic}	$2\pi \cdot 450$ rad/s
Bus voltage rated value	350 V

Table 4.1. Features of the DC/DC boost stage of a commercial PV converter.

Nominal power	4080 W
MPP voltage V_{mpp}	216 V
MPP current I_{mpp}	18.9 A
Open-circuit voltage V_{oc}	264 V
Short-circuit current I_{sc}	20 A
Equivalent series resistance R_s	0.848 Ω
Equivalent shunt resistance R_p	736 Ω
Cells connected in series in a module N_s	36
Ideality factor m	1

Table 4.2. Specifications of the PV array formed by 4 strings of 12 BP585 modules.

The Bode plots of the compensated system are represented in Fig. 4.11 for three characteristic operating points:

- $v_{pv}=0$: In short-circuit, R_{pv} reaches its maximum value, which is $R_{pv} = R_p = 736 \Omega$ for the analyzed PV array [see (4.9)]. Since $R_{pv} \cdot C \cdot \omega_{vc} \gg 1$, the influence of R_{pv} is negligible and the actual cutoff frequency and phase margin are close to the design ones: $f_c=f_{vc}=50$ Hz and $PM=46^\circ \approx PM_v$.
- $v_{pv}=V_{mpp}$: In the MPP and for the nominal operating conditions ($g=800$ W/m², $T=50^\circ$ C), R_{pv} is equal to 13.18Ω . In this case, the effect of the dynamic resistance is very significant and the regulation becomes much slower and more damped, with $f_c=5$ Hz and $PM>90^\circ$.
- $v_{pv}=V_{oc}$: In open-circuit, R_{pv} reaches its minimum value, which is $R_{pv} = 1.16 \Omega$ [see (4.12)] for the maximum irradiance ($g=1100$ W/m²) and temperature ($T=75^\circ$ C). The effect of R_{pv} is enormous, slowing down the control to an actual cutoff frequency $f_c=0.4$ Hz and with $PM>90^\circ$.

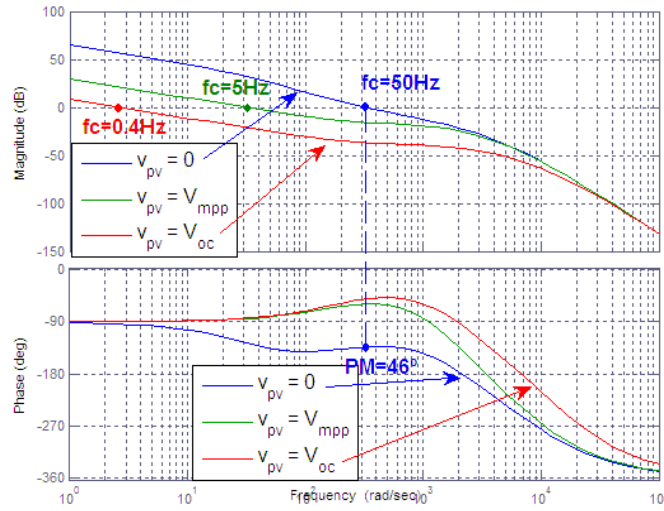


Figure 4.11. Bode plots of the compensated system $C_v \cdot S_v \cdot G_{icl} \cdot G_v \cdot H_v$ ($C=40 \mu$ F).

The effect of the capacitor size on the performance variation for the previously analyzed system is now examined in Fig. 4.12. This figure represents the actual cutoff frequency and phase margin of the voltage control as a function of R_{pv} for three different capacitances (40μ F, 400μ F and 4000μ F). In the three cases, the design cutoff frequency and phase margin are maintained to $f_{vc}=50$ Hz and $PM_v=40^\circ$. The three characteristic operating points are marked with lines. Short-circuit (SC) is the only point where the actual cutoff frequency is equal to the design cutoff frequency (50 Hz) for the three

capacitors. However, the system normally operates between the MPP and the open-circuit (OC). In that range, the performance variation highly depends on the capacitor size. In particular, for $C=40\text{ }\mu\text{F}$ and the considered PV array, the cutoff frequency decreases from 5 Hz at MPP to 0.4 Hz at open-circuit; for $C=400\text{ }\mu\text{F}$, the influence is lower, with the dynamics changing from 43.6 Hz at MPP to 4.4 Hz at open-circuit; and for $C=4000\text{ }\mu\text{F}$, the effect of R_{pv} is now almost negligible, with a variation from 50 Hz to 41.7 Hz. This is the reason why, when using large electrolytic capacitors, it is not necessary to account for dynamic resistance influence on the system modeling. Regarding the stability of the control, the variation range is less critical, since the actual phase margin is always higher than the design one.

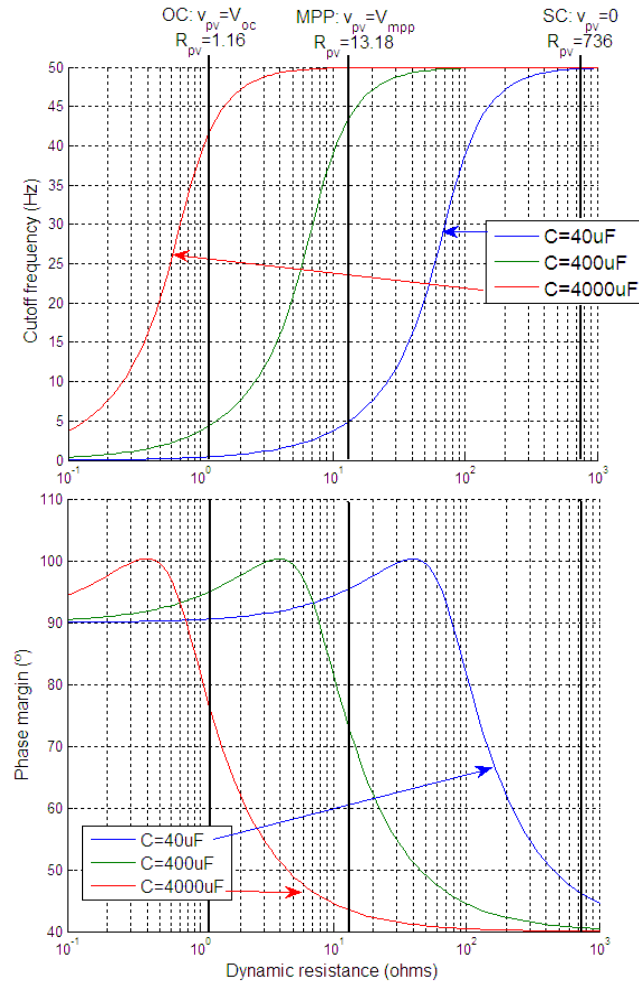


Figure 4.12. Actual cutoff frequency and phase margin of the PV voltage regulation for three different C (40 μF , 400 μF and 4000 μF) and with $f_{vc}=50\text{ Hz}$ and $PM_v=40^\circ$.

The theoretical analysis carried out in this section has been verified by simulation. An accurate model of the PV array and the PV converter was developed using the software PSIM. In Fig. 4.13, the voltage response is represented for an irradiance of 1000 W/m^2 , a temperature of 25°C and using a $40 \mu\text{F}$ capacitor. It consists of downward steps of the PV voltage reference (V_{pv_ref}) from 260 V, close to the open-circuit voltage ($V_{oc}=264 \text{ V}$), to 210 V, below the MPP voltage ($V_{mpp}=216 \text{ V}$). The figure includes the theoretical values of R_{pv} and f_c for each reference voltage level. This dynamic resistance has been worked out by means of (4.3). From the obtained R_{pv} , the actual cutoff frequency has been obtained from Fig. 4.12. In the figure, the real value of the dynamic resistance is also represented. Considering the design cutoff frequency $f_{cv}=50 \text{ Hz}$ and the traditional model of Fig. 4.9, the rise time of the voltage response should be constant and close to 9.5 ms (using $3/\omega_{vc}$). However, as predicted, the rise time is much higher and strongly dependent on voltage level. For example, during the voltage transient from 260 to 250 V, the rise time obtained by simulation is 730 ms. This value indeed agrees with the prediction of the model, that is 853 ms ($f_c=0.56 \text{ Hz}$) for $v_{pv}=260 \text{ V}$ and 672 ms ($f_c=0.71 \text{ Hz}$) for $v_{pv}=250 \text{ V}$. Likewise, it can be verified that there is not overshoot, which means that the phase margin is very high. This also makes sense since the theoretical analysis shown in Fig. 4.12 predicted a phase margin higher than 90° .

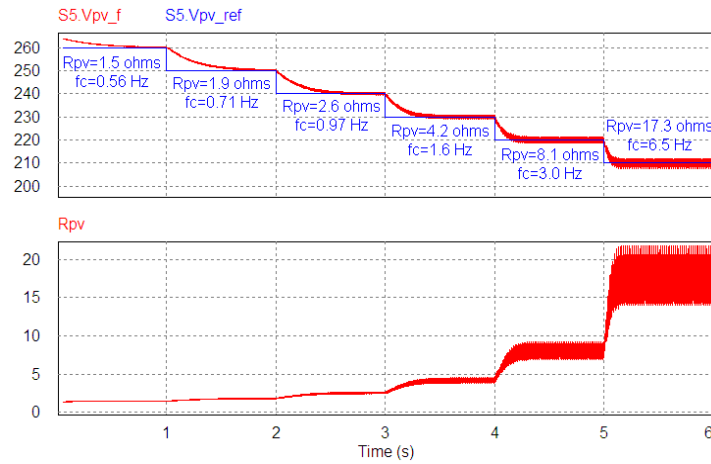


Figure 4.13. Simulation of the PV voltage regulation with the traditional control ($C=40\mu\text{F}$) and with $f_{vc}=50 \text{ Hz}$ and $PM_v=40^\circ$.

It has been shown that, using small capacitors, the regulation becomes very slow for some operating points, which can lead to important problems such as poor behavior of the MPPT/LPPT, resonance phenomena or no rejection of irradiation variations. As a consequence, it is not recommendable to continue with a PI controller. A higher-order controller has also been considered, but the results did not improve.

4.3.4 Proposed control

To solve the problems of the dynamic resistance variation, an adaptive control is proposed in this work. For each voltage sample time (T_{sv}), the control estimates the dynamic resistance and uses this value in order to adapt one parameter of the controller according to the dynamic resistance variation. In this way, the nonlinear system variability is compensated.

4.3.4.1 Dynamic resistance estimation

If a short period is considered, the linear model of the PV array is applicable (4.7). It can be seen that the i_{pv} variation is caused by both v_{pv} and g variations. The irradiance variation is unknown but can have an important effect on the current during a cloud passage. This fact hinders the estimation of the dynamic resistance, which represents the current variation caused by the voltage variation. For this reason, an intrinsic feature of single-phase inverters, particularly its 100 Hz ripple, is used. In real systems, the irradiance component around the 100 Hz is negligible. As a result, the evolution of the 100 Hz ripple of i_{pv} is exclusively provoked by the 100 Hz ripple of v_{pv} . From (4.7), one obtains

$$i_{pv100} = K_g \cdot g_{100} - \frac{v_{pv100}}{R_{pv}} \approx -\frac{v_{pv100}}{R_{pv}}, \quad (4.29)$$

where i_{pv100} , g_{100} and v_{pv100} are, respectively, the PV current, irradiance and PV voltage obtained after applying a type I Chebyshev 100 Hz band-pass filter (100 Hz BPF) to the original signal.

Now, an estimation of the dynamic resistance, $R_{pv,est}$, can be easily found by dividing the RMS value of v_{pv100} (V_{pv100}) by the RMS value of i_{pv100} (I_{pv100}):

$$R_{pv,est} = \frac{V_{pv100}}{I_{pv100}}. \quad (4.30)$$

Generally, the measured current is i_L instead of i_{pv} . However, i_{pv100} can be worked out by means of the 100 Hz ripple of i_L (i_{L100}) and v_{pv100} as follows:

$$i_{pv100} = i_{L100} + C \cdot \frac{v_{pv100}(k) - v_{pv100}(k-1)}{T_{sv}}. \quad (4.31)$$

4.3.4.2 Controller design

The proposed controller is a second order one with two constant parameters K_p and T_n and one variable parameter T_m :

$$C_v(s) = K_p \cdot \frac{T_n \cdot s + 1}{T_n \cdot s} \cdot \frac{T_m \cdot s + 1}{T_m \cdot s}. \quad (4.32)$$

Multiplying the transfer function of the controller by the current to voltage transfer function G_v [see (4.28)], one finds

$$C_v(s) \cdot G_v(s) = K_p \frac{T_n \cdot s + 1}{T_n \cdot s} \frac{1}{C \cdot s} \frac{T_m \cdot s + 1}{T_m} \frac{C \cdot R_{pv}}{C \cdot R_{pv} \cdot s + 1}. \quad (4.33)$$

From (4.33), it is observed that, once the dynamic resistance is known, the variability of the system can be eliminated by means of the controller parameter T_m by doing

$$T_m = C \cdot R_{pv,est}. \quad (4.34)$$

Furthermore, the product $C_v(s) \cdot G_v(s)$ remains now the same as with a PI and the traditional model, and therefore K_p and T_n can be calculated as traditionally. In Fig. 4.14, the proposed control including the R_{pv} estimation is shown.

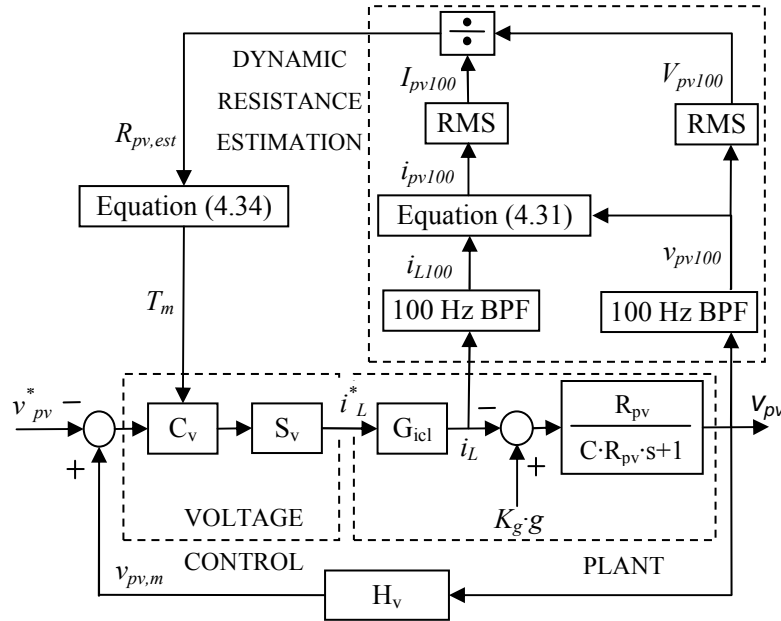


Figure 4.14. Proposed PV voltage control loop.

This control has been validated by simulation with PSIM. The features of the simulated system are identical to the traditional control excluding that now, the proposed control is used. In addition, the design cutoff frequency for the voltage control is $f_{vc}=20$ Hz and the phase margin is $PM_v=55^\circ$. The cutoff frequency is chosen quite lower than 100 Hz in order to avoid interactions with the 100 Hz ripple of the single-phase

converters. Given that the bigger the PV array, the slower the average irradiance variation in the whole PV array, this cutoff frequency is high enough to perform a fast MPPT/LPPT and to reject the irradiance variations [4.58].

The performance of the control is shown in Fig. 4.15 for the same conditions of the test in Fig. 4.13 (note that the time scale is different). The real dynamic resistance and its estimation are also represented in the figure. Given that the design cutoff frequency is 20 Hz, the rise time of the voltage response should be constant and close to 23.9 ms (using $3/\omega_{vc}$). However, during the transient from 260 to 250 V, i.e. near to open-circuit, the rise time is 18.4 ms, whereas from 220 to 210 V, around the MPP, it is 15.1 ms. This deviation of the actual cutoff frequency from the design value is caused by the misestimation of R_{pv} . As it can be observed in the figure, the misestimation only occurs in transients due to a retard in the estimation of $R_{pv,est}$. In any case, when using the proposed control, the rise time is much closer to the design time than in the case of the traditional control, where it was expected to be 9.5 ms but varies from 730 ms near to open-circuit to 108 ms around the MPP (see Fig. 4.13). Furthermore, the rise time obtained with the proposed control is much lower despite having a lower design cutoff frequency (20 Hz versus 50 Hz). Thus, thanks to the proposed control, the MPPT/LPPT controller period can be considerably reduced, which leads to an improvement of its performance. More precisely, on account of the analysis of [4.29] for the stabilization time, the traditional control requires a MPPT/LPPT cycle of about 1 second whereas the proposed control can reduce this time up to about 40 ms.

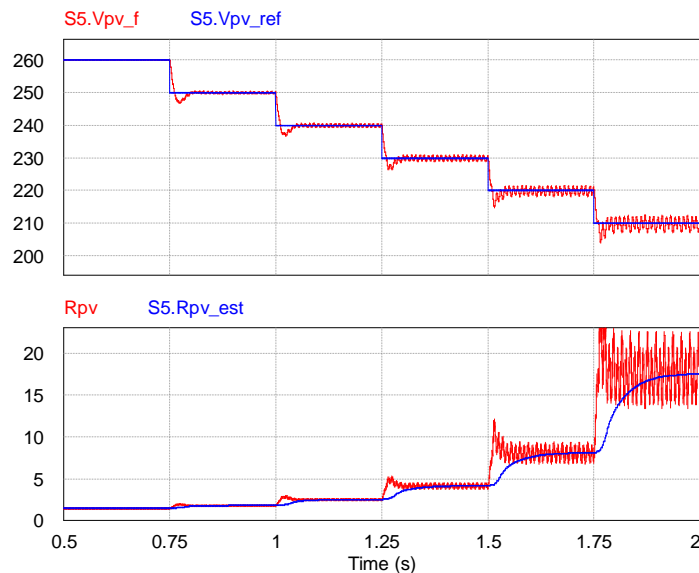


Figure 4.15. Simulation of the PV voltage regulation with the proposed control.

4.3.5 Experimental results

In this section, the modeling is validated and the traditional and proposed control strategies are tested using the commercial single-phase converter which was presented in Table 4.1. Its input is connected to the PV array shown in Table 4.2 and its output is connected to the grid.

Modeling is first validated. From Fig. 4.10, the theoretical current reference to PV voltage transfer function G_v^* can be obtained as follows

$$G_v^*(s) = G_{icl}(s) \cdot G_v(s) = -\frac{1}{s/\omega_{ic} + 1} \cdot \frac{R_{pv}}{R_{pv} \cdot C \cdot s + 1}. \quad (4.35)$$

To validate this model, the voltage control loop is deactivated. For a sunny day, a current reference composed by a constant and a small-signal sinusoidal term is introduced. The constant component is adjusted in order to set the desired v_{pv} operating point, i.e. the desired dynamic resistance. With the sinusoidal term, a frequency range is swept for that operating point. Then, the small-signal PV voltage response is measured, obtaining the gain for each frequency.

The experimental gain diagram of the Bode plot is represented in Fig. 4.16 for one operating point in each of the three different regions of the I-V curve: Constant Current (CC), Maximum Power Point (MPP), and Constant Voltage (CV). The lines represent the theoretical response given by (4.35) and the points represent the experimental values. As it can be observed, the experimental points match the theoretical model carried out in section 4.3.2.

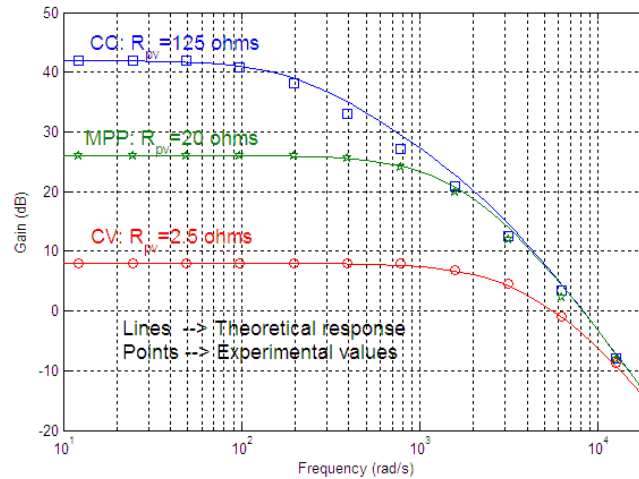


Figure 4.16. Gain of the reference inductor current to PV voltage transfer function G_v^* at three operating points.

In this figure, the effect of the dynamic resistance on the plant can also be observed. In fact, the gain at low frequencies is equal to R_{pv} itself. In addition, it can be observed the influence of the G_v transfer function pole, which is located at a frequency of 200 rad/s in the CC, 1250 rad/s in the MPP, and 10000 rad/s in the CV. The pole due to the current closed-loop is common and equal to 2850 rad/s.

The traditional control is now tested by maintaining the original configuration of the converter; that is, with the design values of $f_{vc}=50$ Hz and $PM_v=40^\circ$ (as in section 4.3.3). The PV voltage and the PV current are depicted in Fig. 4.17 for steps of the voltage reference. At the moment of this test, the conditions were: $g=820$ W/m², $T=51^\circ$ C, and $V_{oc}=227$ V. It can be observed that the regulation speeds up when reducing the voltage since it increases the dynamic resistance. More precisely, the rise time is 660 ms near to the open-circuit, then 470 ms, 310 ms and finally 130 ms around the MPP. Similarly to the simulation results (Fig. 4.13), these rise times validate the slowing down of the control for high values of the PV voltage.

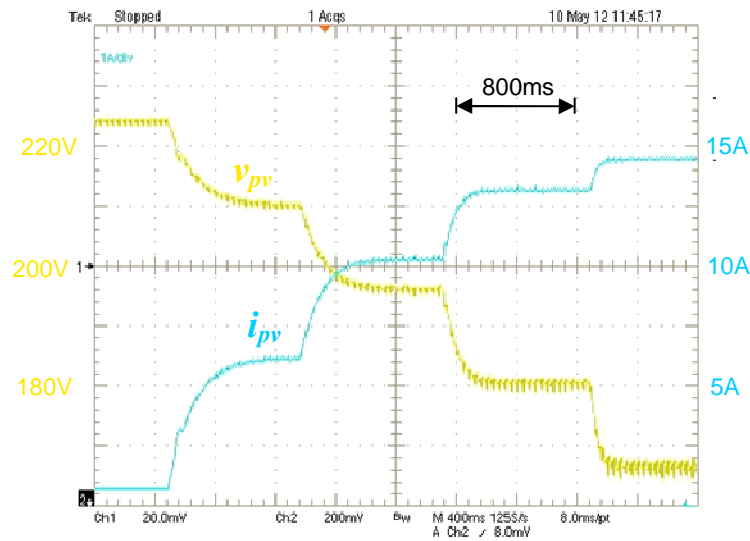


Figure 4.17. Experimental results for the traditional control.

Modifying the converter configuration, the same test was carried out by means of the proposed control, with $f_{vc}=20$ Hz and $PM_v=55^\circ$ (as in section 4.3.4). At that moment, the conditions were: $g=700$ W/m², $T=49^\circ$ C, and $V_{oc}=228$ V. The results are presented in Fig. 4.18, showing that dynamics and overshoot of the regulation remain almost constant independently of R_{pv} . More precisely, the rise time is 20.5 ms near to the open-circuit, then 18.5 ms, 16.8 ms and finally 14.3 ms around the MPP. This figure confirms, in

contrast to the traditional control, that the regulation performance is almost constant independently of the operating point.

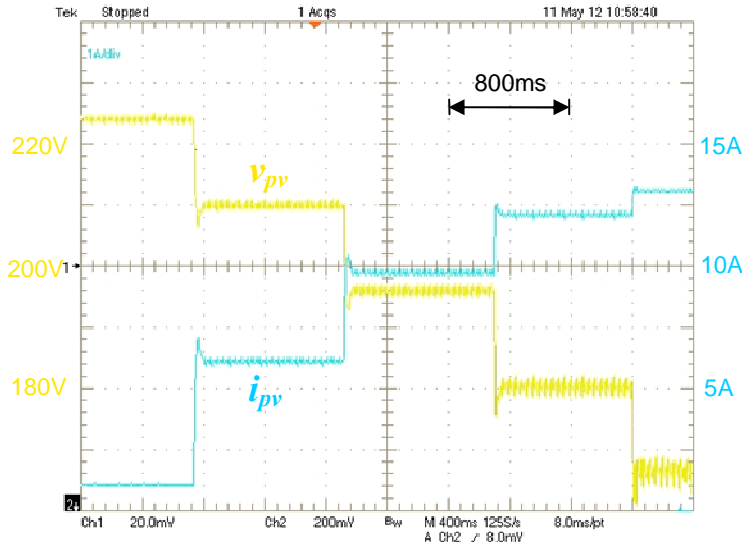


Figure 4.18. Experimental results for the proposed control.

In Fig. 4.19, the 100 Hz ripple of v_{pv} and i_{pv} (v_{pv100} and i_{pv100}), and the estimation of the dynamic resistance are represented. The data are taken from the microprocessor during normal operation, with a sample time of 250 μ s. It can be seen that v_{pv100} and i_{pv100} are accurately obtained. As a result, the dynamic resistance is well estimated even for very low 100 Hz ripple. This small ripple makes it possible to perform a high-efficient MPPT while preventing the components from a lifetime reduction. More precisely, on account of the ripple shown in Fig. 4.15 and Fig. 4.18 at MPP, and considering [4.59], the losses under MPPT are less than 0.1%.

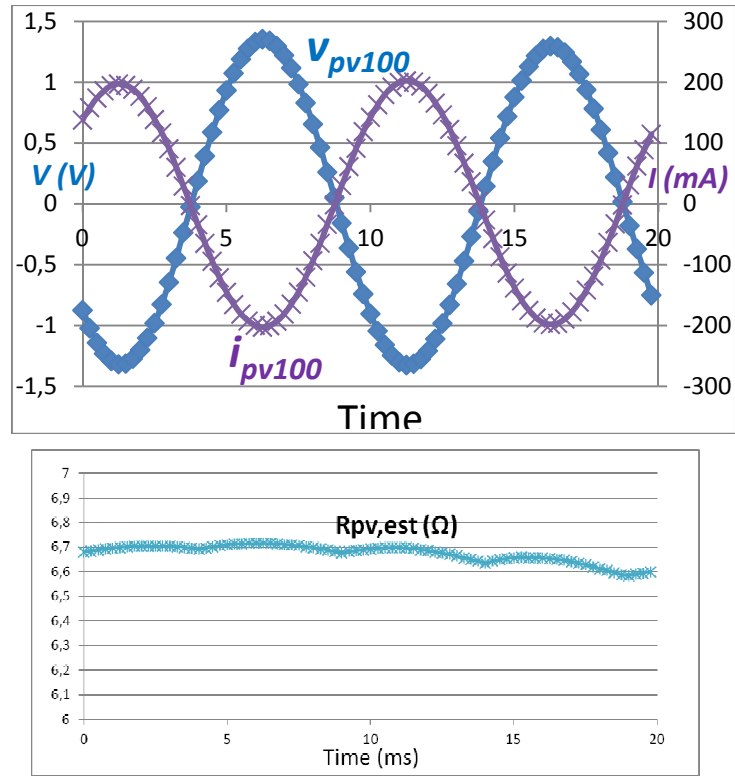


Figure 4.19. Experimental results for the dynamic resistance estimation.

4.4 DUAL PV VOLTAGE CONTROL WITH TIBUCK CONVERTER

4.4.1 Dual MPPT with TIBuck converter

The proposed configuration with the TIBuck converter was shown in Fig. 4.2(b), with i_1 and i_2 being the PV currents, v_1 and v_2 the PV voltages, v_o the output voltage, v_s the switch voltage, v_d the diode voltage, i_L the inductor current, and S the commutation function (0 for off state or 1 for on state). The first stage of this converter is similar to the conventional buck converter, except for the fact that a second input is added. Two capacitors, C_1 and C_2 , are placed each one in parallel with each of the two PV strings to both change the causality from current source to voltage source and reduce the voltage ripple.

The elements used throughout this section are presented in Table 4.3 and 4.4. Table 4.3 shows the features of the TIBuck converter. According to [4.59], the capacitor values have been chosen so that the MPPT losses due to the voltage ripple are lower than

0.2%. The inductor value is obtained in order to avoid discontinuous conduction mode and limit the current ripple. Table 4.4 shows the specifications of the PV arrays. The TiBuck converter makes it possible to interface with different types of PV modules in its two inputs, with the only restriction that v_1 must be higher than v_2 . For this analysis, three polycrystalline modules are considered to be connected in series at input PV1 and two monocrystalline modules, also connected in series, at input PV2.

Rated power	400 W
Input capacitor C_1	32 μ F
Input capacitor C_2	32 μ F
Inductor L	44 μ H
Rated output voltage V_0	40 V
Commutation frequency f_{com}	50 kHz

Table 4.3. Features of the TiBuck converter.

PV1 module model	Sharp NE-080T1J
PV1 array MPP power P_{MPP1}	240 W
PV1 array MPP voltage V_{MPP1}	51.9 V
PV1 array MPP current I_{MPP1}	4.63 A
PV1 array open-circuit voltage V_{oc1}	64.8 V
PV1 array short-circuit current I_{SC1}	5.15 A
PV2 module model	Hurricane HS-80D
PV2 array MPP power P_{MPP2}	160 W
PV2 array MPP voltage V_{MPP2}	36 V
PV2 array MPP current I_{MPP2}	4.5 A
PV2 array open-circuit voltage V_{oc2}	44 V
PV2 array short-circuit current I_{SC2}	4.7 A

Table 4.4. Specifications of the PV arrays.

The control scheme is shown in Fig. 4.20. The MPPT algorithm requires the duty cycle reference d_{ref} as well as the measured variables $v_{1,m}$, $v_{2,m}$, and $i_{L,m}$ as inputs. With this information, and once that the control variables are established, the algorithm provides the reference voltages $v_{1,ref}$ and $v_{2,ref}$ to be controlled. In some situations, the PV power does not have to be maximized and needs to be limited [4.60]. In any case, the analysis carried out here deals with the voltage regulation, and not with the MPPT algorithm or power limitation. It is thus assumed that the reference voltages are known.

The two input voltages can be controlled by the two degrees of freedom, namely the TiBuck switch commutation and the output voltage v_o . From the PV1 voltage error, the

control obtains the switch duty cycle reference, d_{ref} , from which the switch commutations are found after the modulation. From the PV2 voltage error, the other control obtains the output voltage reference, $v_{o,ref}$. In turn, this voltage is then regulated by the inverter. The output voltage control is dynamically restricted to around 20 Hz due to the 100 Hz ripple present in single-phase inverters. As it will be shown later, the slow inner voltage control will hamper the PV2 voltage regulation. On the other hand, the voltage v_o only requires slight variation, resulting in small impact on the boost inverter rated operation.

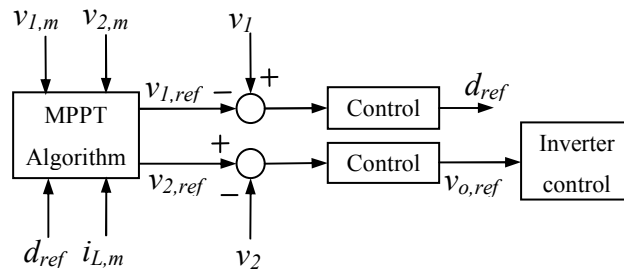


Figure 4.20. Control scheme for dual MPPT with TIBuck converter.

4.4.2 Small-signal modeling

Since the output voltage is controlled by the boost inverter, it will be considered as a controlled voltage source. It is also assumed that the TIBuck converter is operating in continuous conduction mode. In this mode, the switch is conducting and the diode is off for $S=1$, while the switch is off and the diode is conducting for $S=0$. Considering the switch, diode and inductor losses in the model is important for the design of the PV1 voltage control, as it will be shown in section 4.4.3.1. From Kirchhoff's laws applied to the system presented in Fig. 4.2(b), and considering average values, one obtains

$$C_1 \cdot \frac{dv_1}{dt} = i_1 - d \cdot i_L \quad (4.36)$$

$$C_2 \cdot \frac{dv_2}{dt} = i_2 - (1-d) \cdot i_L \quad (4.37)$$

$$L \cdot \frac{di_L}{dt} = d \cdot (v_1 - v_{s,on}) + (1-d) \cdot (v_2 - v_{d,on}) - r_L \cdot i_L - v_o, \quad (4.38)$$

where d is the TIBuck switch duty cycle, $v_{s,on}$ is the switch voltage drop during conduction, and $v_{d,on}$ is the diode voltage drop during conduction.

From (4.36)–(4.38), the steady-state equations can be worked out as

$$I_1 = D \cdot I_L \quad (4.39)$$

$$I_2 = (1 - D) \cdot I_L \quad (4.40)$$

$$V_0 = D \cdot (V_1 - V_{s,on}) + (1 - D) \cdot (V_2 - V_{d,on}) - r_L \cdot I_L, \quad (4.41)$$

where steady-state variables are expressed in capital letters.

The converter model represented by (4.36)–(4.38) is nonlinear. In order to use linear control techniques, small-signal analysis is applied to those equations, resulting in

$$C_1 \cdot \frac{d\hat{v}_1}{dt} = \hat{i}_1 - D \cdot \hat{i}_L - I_L \cdot \hat{d} \quad (4.42)$$

$$C_2 \cdot \frac{d\hat{v}_2}{dt} = \hat{i}_2 - (1 - D) \cdot \hat{i}_L + I_L \cdot \hat{d} \quad (4.43)$$

$$L \cdot \frac{d\hat{i}_L}{dt} = D \cdot (\hat{v}_1 - \hat{v}_{s,on}) + (1 - D) \cdot (\hat{v}_2 - \hat{v}_{d,on}) - r_L \cdot \hat{i}_L + (V_1 - V_2 - V_{s,on} + V_{d,on}) \cdot \hat{d} - \hat{v}_0, \quad (4.44)$$

where small-signal variables are marked with a circumflex and the operating point is defined by (4.39)–(4.41).

The voltage drop during conduction across the switch and diode can be approximated by a constant voltage source in series with a resistor, namely r_s for the switch and r_d for the diode. As a result, the switch and diode small-signal model can be expressed as

$$\hat{v}_{s,on} = r_s \cdot \hat{i}_L \quad (4.45)$$

$$\hat{v}_{d,on} = r_d \cdot \hat{i}_L. \quad (4.46)$$

PV currents i_1 and i_2 depend on the PV voltage, the irradiation and the array temperature through nonlinear expressions. Since the temperature variation is very slow, their small-signal effect can be neglected. The small-signal model for the PV arrays can then be expressed as follows (see section 4.2):

$$\hat{i}_1 = K_{g1} \cdot \hat{g}_1 - \frac{\hat{v}_1}{R_1} \quad (4.47)$$

$$\hat{i}_2 = K_{g2} \cdot \hat{g}_2 - \frac{\hat{v}_2}{R_2}, \quad (4.48)$$

where g_1 and g_2 are the small-signal irradiances, K_{g1} and K_{g2} are the coefficients of the PV current variation with the irradiation, and R_1 and R_2 are the dynamic resistances of the arrays. The dynamic resistance is related to the slope of the I - V curve and represents the PV array nonlinear behavior. In the constant current region, it reaches high values, while in the constant voltage region, it has low values.

Introducing (4.45)–(4.48) into (4.42)–(4.44), reordering and applying Laplace transforms leads to

$$s \cdot X = A \cdot X + B \cdot U, \quad (4.49)$$

where

$$X = [\hat{v}_1 \quad \hat{v}_2 \quad \hat{i}_L]^T \quad (4.50)$$

$$U = [\hat{g}_1 \quad \hat{g}_2 \quad \hat{d} \quad \hat{v}_o]^T \quad (4.51)$$

$$A = \begin{bmatrix} -1/R_1 C_1 & 0 & -D/C_1 \\ 0 & -1/R_2 C_2 & -(1-D)/C_2 \\ D/L & (1-D)/L & -r_{eq}/L \end{bmatrix} \quad (4.52)$$

$$B = \begin{bmatrix} K_{g1}/C_1 & 0 & -I_L/C_1 & 0 \\ 0 & K_{g2}/C_2 & I_L/C_2 & 0 \\ 0 & 0 & V_{eq}/L & -1/L \end{bmatrix} \quad (4.53)$$

$$r_{eq} = D \cdot r_s + (1-D) \cdot r_d + r_L \quad (4.54)$$

$$V_{eq} = (V_1 - V_{S,on}) - (V_2 - V_{D,on}). \quad (4.55)$$

4.4.3 Voltage regulation

4.4.3.1 Plant for the PV1 voltage regulation

The PV1 voltage is regulated by means of the TIBuck switch duty cycle through a single feedback loop. The loop for the PV1 voltage regulation is shown in Fig. 4.22, where C_{v1} represents the controller, S_{v1} the digital sampler, G_{v1-d} the duty cycle to PV1 voltage transfer function, and H_{v1} the PV1 voltage sensing.

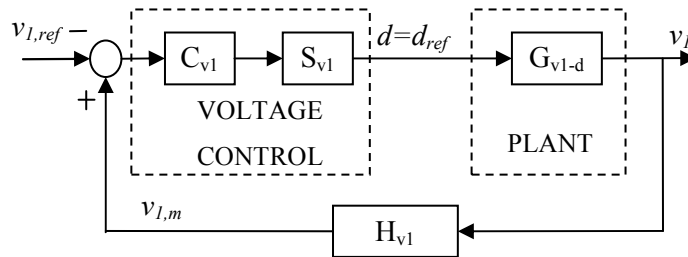


Figure 4.22. PV1 voltage control loop.

In order to design the controller, the system plant must be worked out. Transfer function G_{v1-d} can be obtained from (4.49)–(4.53), and its expression is as follows:

$$G_{v1-d} = \frac{\hat{v}_1}{\hat{d}} = -\frac{a_2 \cdot s^2 + a_1 \cdot s + a_0}{b_3 \cdot s^3 + b_2 \cdot s^2 + b_1 \cdot s + b_0}, \quad (4.56)$$

where

$$a_2 = I_L \cdot L \cdot C_2 \quad (4.57)$$

$$a_1 = I_L \cdot L / R_2 + I_L \cdot r_{eq} \cdot C_2 + D \cdot V_{eq} \cdot C_2 \quad (4.58)$$

$$a_0 = I_L \cdot r_{eq} / R_2 + I_L \cdot (1-D) + D \cdot V_{eq} / R_2 \quad (4.59)$$

$$b_3 = L \cdot C_1 \cdot C_2 \quad (4.60)$$

$$b_2 = L \cdot (C_1 / R_2 + C_2 / R_1) + r_{eq} \cdot C_1 \cdot C_2 \quad (4.61)$$

$$b_1 = L / (R_1 \cdot R_2) + r_{eq} (C_1 / R_2 + C_2 / R_1) + (1-D)^2 C_1 + D^2 C_2 \quad (4.62)$$

$$b_0 = r_{eq} / (R_1 \cdot R_2) + (1-D)^2 / R_1 + D^2 / R_2. \quad (4.63)$$

As it can be observed in (4.56)–(4.63), the plant zeros and poles are variable depending on the operating point because the converter and the PV arrays are nonlinear. As it has been proved in some papers, the variability of the dynamic resistance diminishes the voltage regulation performance and can compromise the stability for some operating points [4.15], [4.16], [4.28], [4.41]. For the proposed configuration, the analysis becomes even more delicate because not only one but two different dynamic resistances take part in the control.

The effect of the two dynamic resistances, R_1 and R_2 , will be analyzed here. In order to ensure stability, the dynamic resistance variation within the whole operating range must be taken into account. For MPP, dynamic resistance can be readily obtained as $R_{MPP} = V_{MPP} / I_{MPP}$, which leads to $R_{MPP1} = 11.2 \Omega$ and $R_{MPP2} = 8 \Omega$ in this case [4.12]. During the system startup or PV power limitation, the system operates in the constant voltage region. At open-circuit voltage, the dynamic resistance has its smallest value, which can be roughly estimated as $R_{min} = R_{MPP} / 10$. On the other hand, transients can make the system operate at the constant current region, where the dynamic resistance increases very quickly. The value $R_{max} = \infty$ can be used in this case. The operating range $R_{MPP} / 10 < R < \infty$ must therefore be considered. More details about the dynamic resistance variation range can be consulted in section 4.2.

Fig. 4.23 shows the bode plot of the transfer function $-G_{v1-d}$ for the nine possible combinations of R_{min1} , R_{MPP1} , R_{max1} with R_{min2} , R_{MPP2} , R_{max2} . The large influence of the dynamic resistances on the plant can be observed, especially for low frequencies. Two

conjugate poles appear between 14000–19000 rad/s (about 2200–3000 Hz), being less damped for high dynamic resistance values. Besides, these poles highly depend on the switch, diode and inductor losses, which should not therefore be neglected for the analysis. Then, from a certain frequency, all curves tend to join together and the dynamic resistance effect disappears.

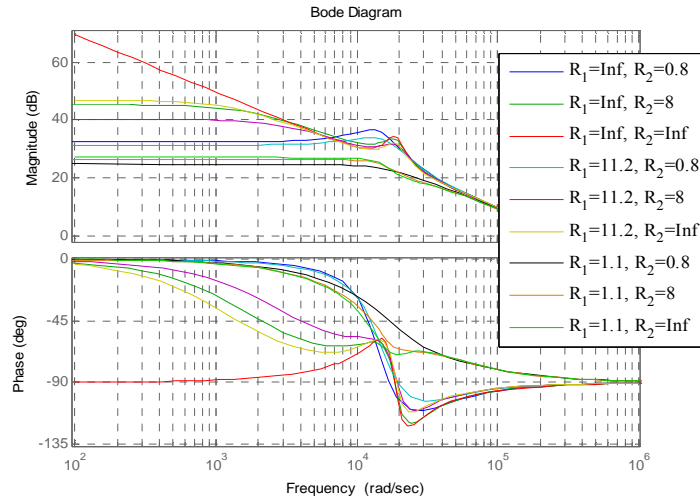


Figure 4.23. Bode plot of $-G_{v1-d}$ for different R_1 and R_2 values.

4.4.3.2 Controller design for the PV1 voltage regulation

According to Fig. 4.23, the frequency from which the dynamic resistance effect is no longer present is too high for practical purposes. This frequency could be reduced by increasing the capacitor and inductor values, making it possible to achieve high dynamics as well as prevent the dynamic resistance effect. However, a considerable increase is required in the passive components, which makes this solution not worth the effort.

Instead, a crossover frequency f_c below the resonance frequency f_r is chosen. For the controller design, the resistance values $R_1=R_{max1}$ and $R_2=R_{max2}$ are considered since the plant bode plot with these values is more problematic concerning stability. In fact, the resonance peak is higher and the phase is lower than for other resistance combinations (see Fig. 4.23). In order to prevent the resonance peak from cutting the 0 dB axis and ensure a certain Gain Margin (GM), the crossover frequency cannot be close to the resonance one. It is therefore selected as $f_c=500$ Hz, while $f_r=3000$ Hz. A pole at $\omega_p=2\pi\cdot600$ rad/s is added to the conventional PI controller in order to further enhance the gain margin, and the Phase Margin (PM) is imposed to 40° . The controller C_{v1} is thus a type II amplifier, which has three parameters, K_p , T_n and ω_p , and can be expressed as

$$C_{v1} = K_p \frac{T_n \cdot s + 1}{T_n \cdot s} \cdot \frac{\omega_p}{\omega_p + s} \quad (4.64)$$

The bode plot of the compensated system is shown in Fig. 4.24 for three different dynamic resistance combinations. Transfer functions S_{v1} and H_{v1} are modeled as first order low-pass filters with time constants $\tau_s = 1.5 \cdot T_s = 30 \mu s$ and $\tau_v = 26.5 \mu s$, respectively, where T_s is the sample time (see Fig. 4.22). Since the regulator is designed for $R_1 = R_{max1}$ and $R_2 = R_{max2}$, it can be observed that the control behaves as desired, that is $f_c = 500$ Hz and $PM = 40^\circ$. Besides, thanks to the controller pole at $\omega_p = 2\pi \cdot 600$ rad/s, the gain margin is high enough, $GM = 18$ dB. However, when the system operates with dynamic resistances different from the design values, the voltage response differs. When both PV arrays are operating at MPP, i.e. $R_1 = R_{MPP1}$ and $R_2 = R_{MPP2}$, it can be seen in the figure how the response becomes slower and more damped, with $f_c = 350$ Hz and $PM = 103^\circ$. On the other hand, when both PV arrays at open-circuit, $R_1 = R_{min1}$ and $R_2 = R_{min2}$, and the effect of the dynamic resistances becomes enormous, slowing down the response to $f_c = 12$ Hz, and with $PM = 102^\circ$.

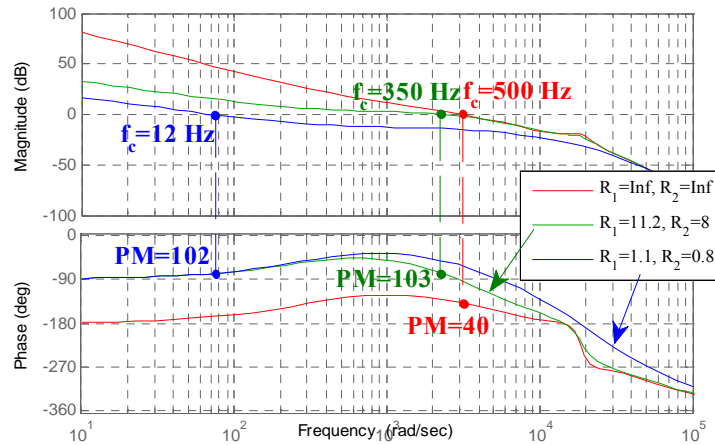


Figure 4.24. Bode plot of the compensated system $-C_{v1} \cdot S_{v1} \cdot G_{v1} \cdot d \cdot H_{v1}$.

Fig. 4.25 shows the effect of the dynamic resistances on the voltage response in more detail. The crossover frequency and the phase margin are represented as a function of R_1 for three different R_2 values ($R_{min2} = 0.8 \Omega$, $R_{MPP2} = 8 \Omega$ and $R_{max2} = \infty$). It can be clearly observed that, as the dynamic resistances get lower than the maximum values, the phase margin increases. As a consequence, the system is stable for every operating point. Concerning the dynamics, the response slows down when the resistances decrease. However, the voltage response is very quick for every operating point except for the points very close to open-circuit voltage.

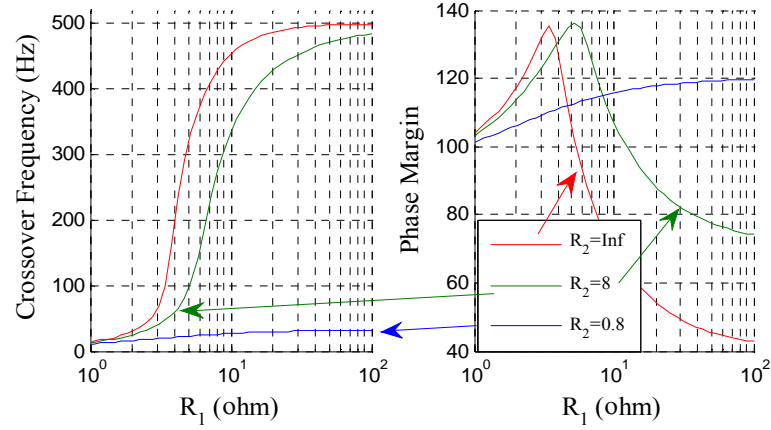


Figure 4.25. Crossover frequency and phase margin as a function of R_1 for three different R_2 ($R_{\min 2}=0.8 \Omega$, $R_{MPP2}=8 \Omega$ and $R_{\max 2}=\infty$), for PV1 voltage regulation.

4.4.3.3 PV2 voltage regulation

The PV2 voltage is regulated through a double feedback loop. The outer loop obtains the output voltage reference $v_{0,ref}$, which is controlled by the boost inverter in the inner loop. The loop for the PV2 voltage regulation is shown in Fig. 4.26, where C_{v2} represents the controller, S_{v2} the digital sampler, $G_{v0,cl}$ the output voltage closed-loop, G_{v2-v0} the output voltage to PV2 voltage transfer function, and H_{v2} the PV2 voltage sensing.

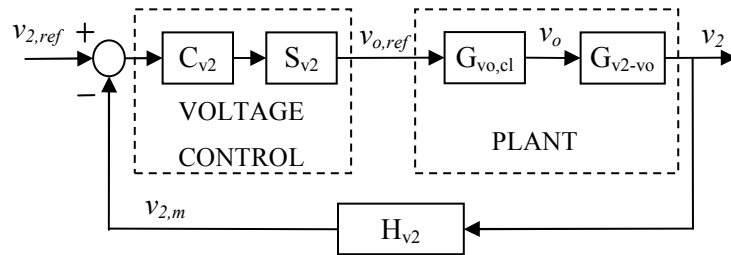


Figure 4.26. PV2 voltage control loop.

Due to the presence of the 100 Hz ripple in single-phase inverters, the inner loop crossover frequency is 20 Hz. This supposes a dynamic limitation for the PV2 regulation, which is taken into account by means of the closed-loop transfer function $G_{v0,cl}$. In order to obtain the plant transfer function G_{v2-v0} , it can be considered that the PV1 voltage regulation is instantaneous in relation to the PV2 voltage regulation, which makes it possible to remove R_1 from the plant. In doing so, G_{v2-v0} can be obtained from the model of section 4.4.2 as

$$G_{v2-v0} = \frac{K}{s^2 / \omega_n^2 + 2 \cdot \xi \cdot s / \omega_n + 1}, \quad (4.65)$$

where

$$K = \left[r_{eq} / R_2 + D \cdot V_{eq} / (R_2 \cdot I_L) + (1 - D) \right]^{-1} \quad (4.66)$$

$$\omega_n = 1 / \sqrt{K \cdot L \cdot C_2} \quad (4.67)$$

$$\xi = 1 / 2 \cdot \sqrt{K / (L \cdot C_2)} \cdot (L / R_2 + r_{eq} \cdot C_2 + D \cdot V_{eq} \cdot C_2 / I_L). \quad (4.68)$$

From (4.65), the plant G_{v2-v0} possesses two poles. Since ξ is always higher than zero, both poles are in the left half-plane. Furthermore, because ω_n is much higher than the frequencies of concern for the PV2 voltage regulation, G_{v2-v0} can be approximated as a constant value, that is

$$G_{v2-v0} \approx K. \quad (4.69)$$

The controller C_{v2} is an integral controller, $C_{v2} = K_i / s$, where K_i is the integral gain, and is designed to obtain a crossover frequency equal to 10 Hz for $R_2 \rightarrow \infty$. However, similarly to the PV1 voltage control, the PV2 voltage regulation performance change as R_2 decreases. Fig. 4.27 shows how the crossover frequency and phase margin vary as a function of this resistance. It can be clearly observed that, as the dynamic resistance gets lower than the maximum values, the phase margin increases. As a consequence, the response is stable for every operating point. Concerning the dynamics, the response slows down when the resistance decreases. However, the crossover frequency variation is less important than for the PV1 voltage regulation, and the PV2 voltage response is fast enough for every operating point.

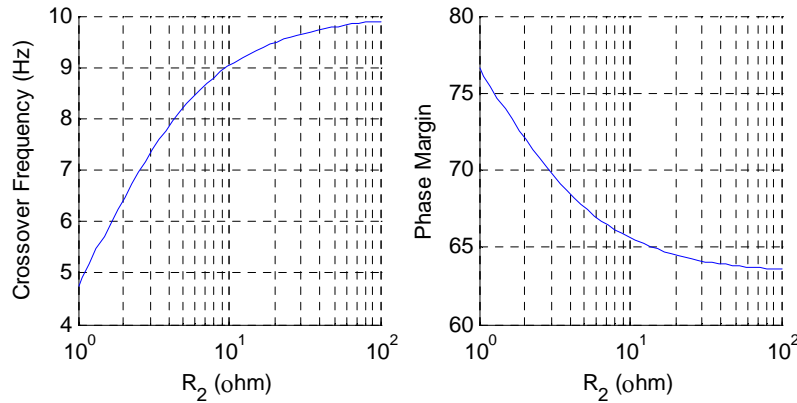


Figure 4.27. Crossover frequency and phase margin as a function of R_2 for the PV2 voltage regulation.

4.4.4 Simulation results

The TiBuck converter, presented in Fig. 4.2(b) and Table 4.3, and the two PV arrays, shown in Table 4.4, were modeled using the software PSIM.

The PV1 voltage regulation, which scheme was shown in Fig. 4.21, was first validated. For this purpose, the TiBuck output is modeled as a constant voltage source with $V_o=40$ V. In Fig. 4.28, the voltage response is represented for an irradiance of 1000 W/m^2 and an array temperature of 25°C . It consists in 4 V downward steps of the PV1 voltage reference from 64 V, close to the open-circuit voltage ($V_{oc1}=64.8$ V), to 48 V, below the MPP voltage ($V_{MPP1}= 51.9$ V). Voltages v_1 , $v_{1,ref}$, v_2 , and v_o are shown in the figure. It can be observed how PV1 voltage response becomes faster and less damped as PV1 voltage decreases, due to the dynamic resistance R_1 increase. In any case, the rise time and overshoot are adequate for every operating point.

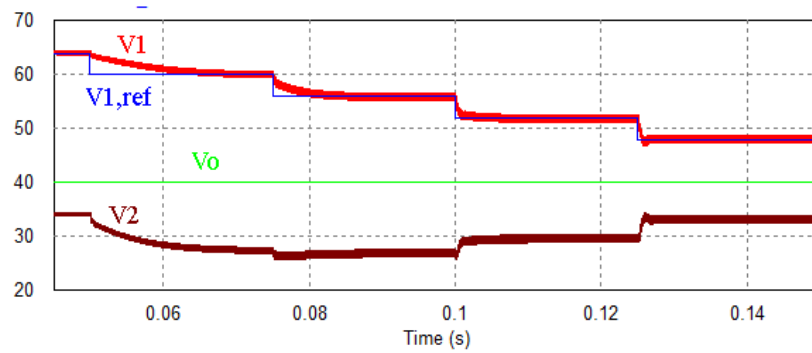


Figure 4.28. Simulation of the PV1 voltage control.

The regulation of the two PV voltages at the same time was validated in a second simulation. In this case, the output capacitor C_o and the boost inverter are replaced by a controlled voltage source, whose value is obtained as $v_o=G_{vo,cl} \cdot v_{o,ref}$. In order to regulate PV1 and PV2 voltages, the controls of Fig. 4.21 and Fig. 4.26 were applied. In Fig. 4.29, the voltage response is represented for an irradiance of 1000 W/m^2 and an array temperature of 25°C . For PV1 voltage, the same downward steps as in Fig. 4.28 are applied (note that the time scale is different). For PV2 voltage, 2.5 V reference downward steps are set from 43.5 V, close to the open-circuit voltage ($V_{oc2}=44$ V), to 33.5 V, below the MPP voltage ($V_{MPP2}= 36$ V). The steps are applied at the same time to both voltages, as it would be done by the MPPT algorithm. Voltages v_1 , $v_{1,ref}$, v_2 , $v_{2,ref}$, v_o , and $v_{o,ref}$ are shown in the figure. As it can be observed, the response becomes faster for both voltages when the dynamic resistances R_1 and R_2 increase, as it was predicted. The figure also shows that the PV2 voltage response is affected by the $v_{1,ref}$ change, which is a disturbance for

the control, while the PV1 voltage response is hardly affected by the $v_{2,ref}$ and consequent v_o changes. In any case, a correct regulation of both PV voltages is obtained, which makes the control suitable to maximize the PV power of two PV arrays at the same time.

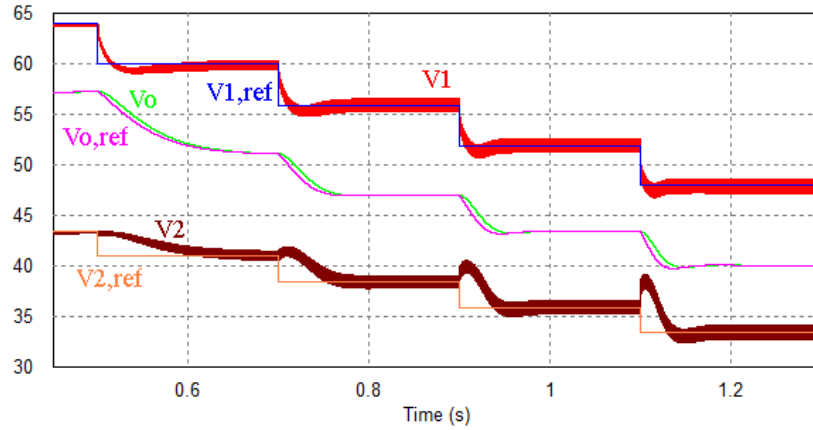


Figure 4.29. Simulation of the PV1 and PV2 voltage controls.

4.4.5 Experimental results

The small-signal model and the voltage regulations are validated in this section by means of experimental results. For this purpose, a prototype of the TIBuck converter, presented in Fig. 2(b) and Table 4.3, was built. During the tests, its first input was attached to three series-connected polycrystalline modules while its second input was attached to two series-connected monocrystalline modules, whose features were shown in Table 4.4. The TIBuck output was connected to both an electrolytic capacitor and the electronic DC load LD300 (TTi), what made it possible to emulate the inverter control. The system control was implemented by using a dSPACE DS1104 R&D controller board with ControlDesk and Matlab/Simulink software packages. The experimental setup is shown in Fig. 4.30, where the PV modules were facing north with a tilt angle of 24 degrees, optimum orientation for grid-connected PV systems in Sydney (Australia).

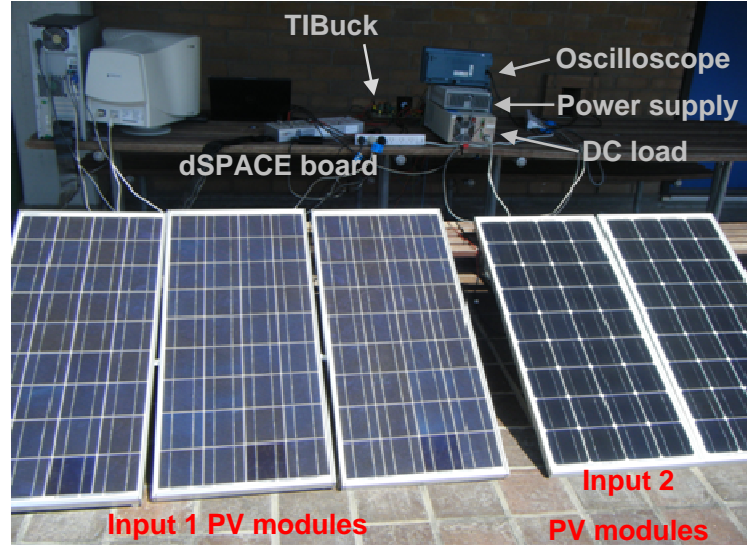


Figure 4.30. Experimental setup.

The transfer function for the control of the PV1 voltage by means of the duty cycle, G_{v1-d} , whose theoretical expression was given in (4.56), was experimentally obtained. For a sunny day, a small-signal duty cycle was introduced around $D=0.5$, leading to $I_1=I_2$ [see (4.39) and (4.40)]. The DC output voltage V_o was adjusted in order to set the desired operating point, i.e. Constant Current (CC) region, Maximum Power Point (MPP) and Constant Voltage (CV) region. For each operating point, a frequency range is swept and the small-signal response is measured. High resolution oscilloscope PicoScope 4424 served to obtain the data, measuring the duty cycle d , PV voltages v_1 and v_2 , and PV current i_1 . From d and v_1 , the magnitude (dB) and phase for the bode plot were obtained. Then, from v_1 and i_1 , the operating dynamic resistance R_1 was calculated. The dynamic resistance R_2 was obtained in the same way but by means of an estimation of the PV current i_2 . By using (4.42) and (4.43), the small-signal value of i_2 can be estimated from measured variables as

$$\hat{i}_2 = \hat{i}_1 + C_2 \cdot s \cdot \hat{v}_2 - C_1 \cdot s \cdot \hat{v}_1 - (I_L / D) \cdot \hat{d} . \quad (4.70)$$

The experimental and theoretical bode plots of G_{v1-d} are represented in Fig. 4.31 for three different operating points: CC region ($R_1=38 \Omega$, $R_2=20 \Omega$), MPP ($R_1=11 \Omega$, $R_2=5 \Omega$) and CV region ($R_1=3 \Omega$, $R_2=2.4 \Omega$). The lines represent the theoretical response and the points represent the experimental values. As it can be observed, the experimental points match the model developed in section 4.4.3.1.

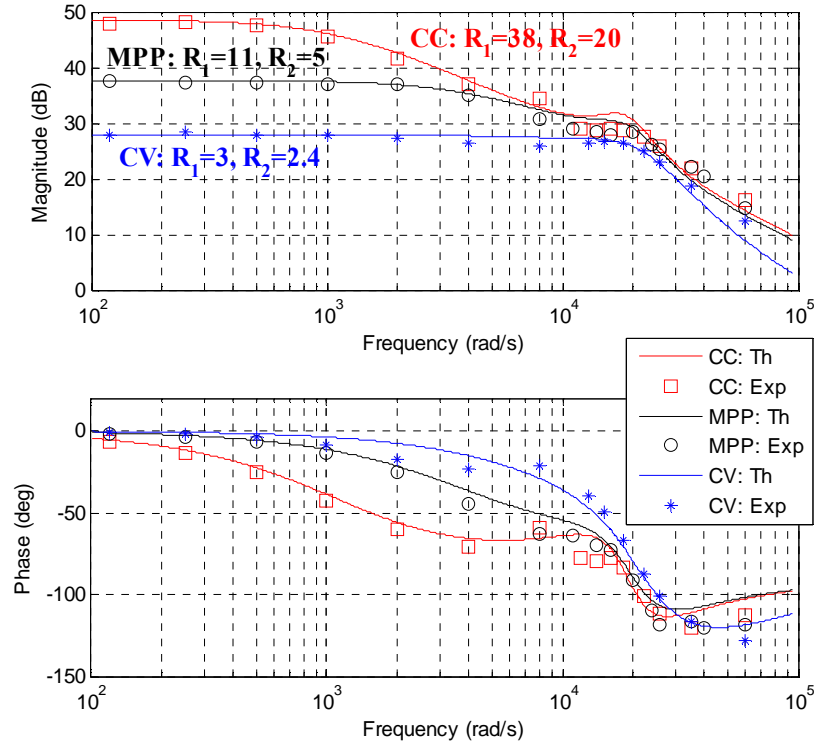


Figure 4.31. Experimental and theoretical bode plots of $-G_{v1-d}$.

Once the model was validated, the PV1 voltage regulation was tested. PV1 voltage, PV2 voltage, output voltage and PV1 current are depicted in Fig. 4.32 for steps of the PV1 voltage reference. At the moment of this test, the conditions for the PV1 array were $V_{oc1}=59.2$ V and $V_{MPP1}=45.7$ V, while V_0 was maintained equal to 35 V so that the PV2 array operated in the CC region with high R_2 values. It can be observed that the PV1 voltage regulation speeds up when reducing the PV1 voltage due to the R_1 increase, as predicted by the theoretical analysis (see Fig. 4.25) and by the simulation results (see Fig. 4.28). In any case, this figure corroborates that the PV1 voltage response is fast enough as well as stable for the whole operating range of R_1 together with high values of R_2 (note that high resistance values are more problematic concerning stability).

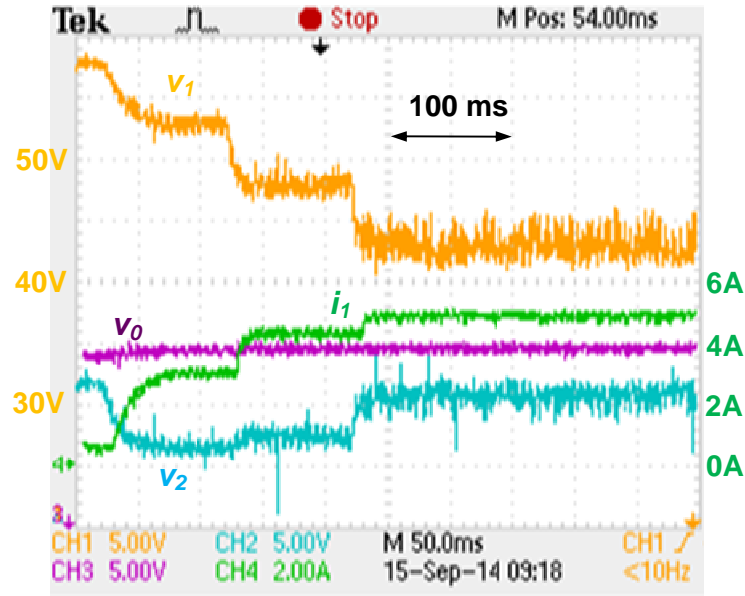


Figure 4.32. Experimental results for the PV1 voltage control.

The regulation of the two PV voltages at the same time was validated in another test. In this case, the DC load controlled the output voltage according to an external reference $v_o = G_{v_o, cl} \cdot v_{o, ref}$, where $v_{o, ref}$ comes from the C_{v2} controller (see Fig. 4.26). PV1 voltage, PV2 voltage, output voltage and PV1 current are depicted in Fig. 4.33 for steps of the PV1 and PV2 voltage reference, which are applied at the same time, as it would be done by the MPPT algorithm. At the moment of this test, the conditions were $V_{oc1} = 59.8$ V and $V_{MPP1} = 46.3$ V for the PV1 array, and $V_{oc2} = 38.6$ V and $V_{MPP2} = 31.0$ V for the PV2 array. As it can be observed in the figure, both v_1 and v_2 responses become faster as the dynamic resistances increase. The figure also shows how the PV2 voltage regulation is affected by the changes in the PV1 voltage reference whereas the PV1 voltage regulation is not perturbed by the PV2 voltage control. These results are thus in agreement with the previous analysis and demonstrate that the proposed control is suitable to maximize the photovoltaic power of two PV arrays at the same time.

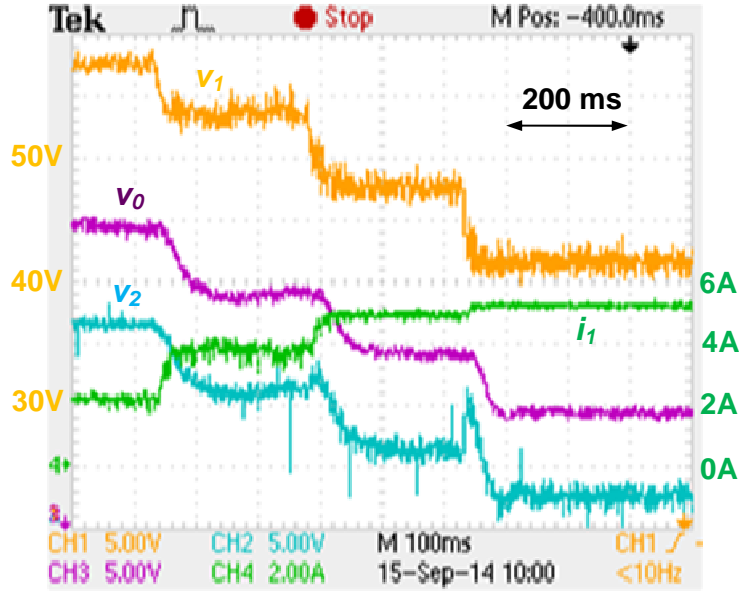


Figure 4.33. Experimental results for the PV1 and PV2 voltage controls.

4.5 PV POWER LIMITATION

Although photovoltaic systems are generally based on Maximum Power Point Tracking (MPPT), many situations such as stand-alone systems or microgrids increasingly require the PV system to operate below maximum power. This section presents a control strategy for the DC/DC boost converter shown in Fig. 4.7 which makes it possible to maximize but also to reduce the PV power.

4.5.1 Proposed control strategy

The boost converter uses an inner control loop in order to control the inductor current i_L and set it to its command i_L^* . The core of the strategy is based on the way in which this reference is obtained, as explained in this section.

4.5.1.1 MPPT operation

In normal conditions, the system operates under Maximum Power Point Tracking (MPPT). The control schematics are shown in Fig 4.34. The MPPT algorithm calculates the voltage reference v_{pv}^* , which is introduced to the outer PV voltage loop. This voltage

reference is compared with the measured PV voltage, $v_{pv,m}$, and then, a PI regulator calculates the MPP current command, $i_{L,mpp}^*$. The outer PV voltage loop is designed much slower than that of the inductor current, making it possible to decouple both loops. In this mode of operation, the power corresponds to the MPP power, P_{mpp} , and the voltage to the MPP voltage, v_{mpp} .

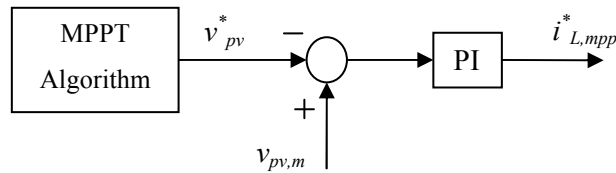


Figure 4.34. Control schematics for MPPT operation.

4.5.1.2 LPPT operation

The system operates under Limited Power Point Tracking (LPPT) primarily in two situations. The first one concerns system stability. Both for on-grid and off-grid applications, the power must be reduced if the total generation is higher than the total demand and there is no possibility of storing the excess. The second situation occurs when the electronic converter is unable to output all the power generated by the PV array. In both cases, a power reference P_{lpp}^* is given, which will be controlled by the LPPT strategy. This limit power reference is thus equal to the converter nominal power in normal operation and goes lower if a more restrictive reduction needs to be carried out.

The control schematics for the LPPT are shown in Fig. 4.35. The power reference P_{lpp}^* is divided by the measured voltage, obtaining the LPP current command, $i_{L,lpp}^*$. This control is very simple but quick, since the power and current dynamics are very similar.

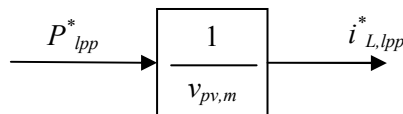


Figure 4.35. Control schematics for LPPT operation.

Now let us check how this power regulation works. For the subsequent analysis it must be considered that, on the one hand, the boost converter imposes the reference power according to the control of Fig. 4.35 and, on the other hand, the PV array delivers a power which depends on PV voltage and irradiance (temperature is constant in the analysis). Thus, the difference between these powers will cause a variation of the PV voltage in the input capacitor. In Fig. 4.36, the P-V curve of a PV array at 45°C is represented for three different irradiances, 1000, 600 and 400 W/m². At the start, the

irradiance is 1000 W/m^2 and the system is following a power reference of 5000 W . Thus, it is situated at point 1, with a PV voltage of 224.1 V and a PV current of 22.31 A . Then, for whatever reason, P_{lpp}^* switches to 3000 W and the power absorbed by the boost converter follows that reference almost immediately. Initially, the PV voltage does not change and thus the PV power remains 5000 W . As result, the input capacitor absorbs the power difference, which leads to a voltage increase and to a PV power reduction until both power curves cut at point 2 of Fig. 4.36, with a PV power of 3000 W , a PV voltage of 248.5 V and a PV current of 12.07 A .

Later on, the irradiance drops to 600 W/m^2 but the power reference is maintained at 3000 W . The PV array is still capable of delivering that power since $P_{mpp} > P_{lpp}^*$. Due to the irradiance variation, the PV power drops to 1860 W , which causes the PV voltage to decrease and the PV power to rise until point 3 of Fig. 4.36 is reached, with a PV voltage of 229.7 V and a PV current of 13.06 A .

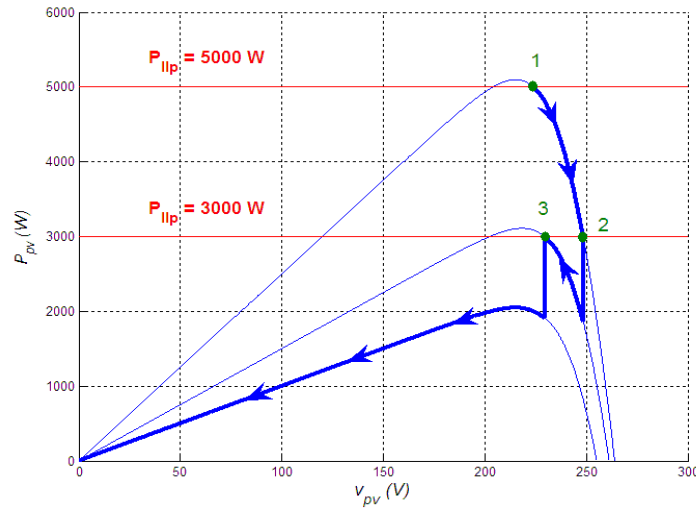


Figure 4.36. Instability during LPPT operation.

At this moment, the irradiance drops to 400 W/m^2 and thus, the PV power drops to 1913 W . Since the PV power has become lower than the power reference P_{lpp}^* , the PV voltage decreases. However, given that P_{mpp} is now lower than P_{lpp}^* , the PV array is unable to deliver the reference power and the PV voltage falls below v_{mpp} . As a result, from Fig. 4.35, a higher current is demanded, which does not improve the situation but accelerates the power reduction towards the short-circuit.

As observed with this example, a PV voltage drop takes place when a power higher than the MPP power is demanded and therefore there is a need to guarantee that $v_{pv} > v_{mpp}$. Obviously, if the power reference exceeds the MPP power, then the system

cannot remain in LPPT and must switch to MPPT. The problem is that the MPP power is not known since the irradiance will probably have changed during the LPPT operation. For this reason, a technique that is able to assure stability by switching from one mode of conduction to the other is developed below.

4.5.1.3 MPPT and LPPT operation

Fig. 4.37 represents the schematics used during the system operation, which includes the schematics developed for MPPT (see Fig. 4.34) and LPPT (see Fig. 4.35). Both current references, $i_{L,mp}^*$ and $i_{L,lp}^*$ are calculated, and the algorithm selects the lowest one. Thus, the selected current determines the mode of operation. On the one hand, the LPPT loop is continuously running, obtaining the current reference $i_{L,lp}^*$ from the limit reference power. On the other hand, the unchanged MPPT loop (i.e. as in Fig. 4.34) only runs if MPPT is the actual mode of conduction ($i_{L,mp}^* < i_{L,lp}^*$). If, on the contrary, LPPT is the actual mode of conduction ($i_{L,mp}^* > i_{L,lp}^*$), then two modifications are made to the MPPT loop. Firstly, the MPPT algorithm is cancelled and the PV voltage reference is frozen to the last value, $v_{mpp,fr}$. Secondly, the reference $i_{L,mp}^*$ is limited to I_{max} , which is $i_{L,lp}^*$ plus a constant I_0 . This saturation with anti windup is imposed in order to enable a quick response and to avoid a voltage drop during the switch from LPPT to MPPT, as will be shown below with an example. The value of the constant I_0 together with the input capacitor size and the PV voltage loop rapidity determine the voltage drop in this change of mode of operation. Constant I_0 must then be sized considering the input capacitor size and the voltage control cutoff frequency. In order to prevent a voltage drop, it is important to set a low I_0 value when working with a small input capacitor.

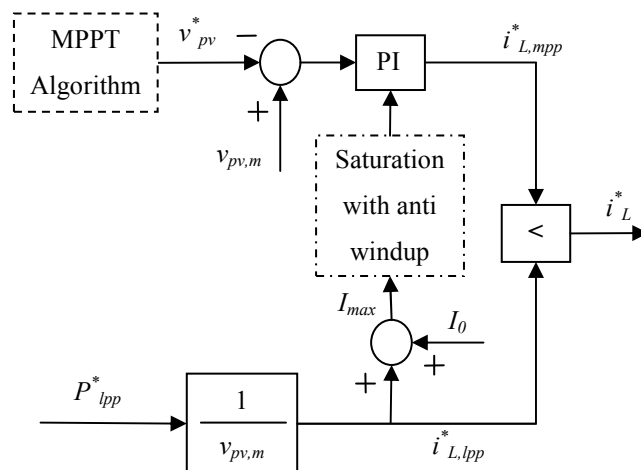


Figure 4.37. Control strategy for MPPT and LPPT operation.

Let us check how this regulation works with a similar example to the one represented in Fig. 4.36. In Fig. 4.38, the P-V curve of a PV array at 45°C is shown for three irradiance values, 1000, 600 and 400 W/m². At the start, the irradiance is 1000 W/m² and $P_{mpp} < P_{lpp}^* = P_{nom} = 5200$ W, where P_{nom} is the converter nominal power. Since $P_{mpp} < P_{lpp}^*$, the reference current $i_{L,lpp}^*$ obtained from Fig. 4.37 is higher than $i_{L,mpp}^*$. Thus, the system is operating under MPPT at point 1, with an MPP power of 5098 W, a PV voltage of 215.3 V and a PV current of 23.68 A. The system will remain in MPPT until the current condition is changed, which can only occur by means of an irradiance variation ($i_{L,mpp}^*$ would change) or a power reference variation ($i_{L,lpp}^*$ would change).

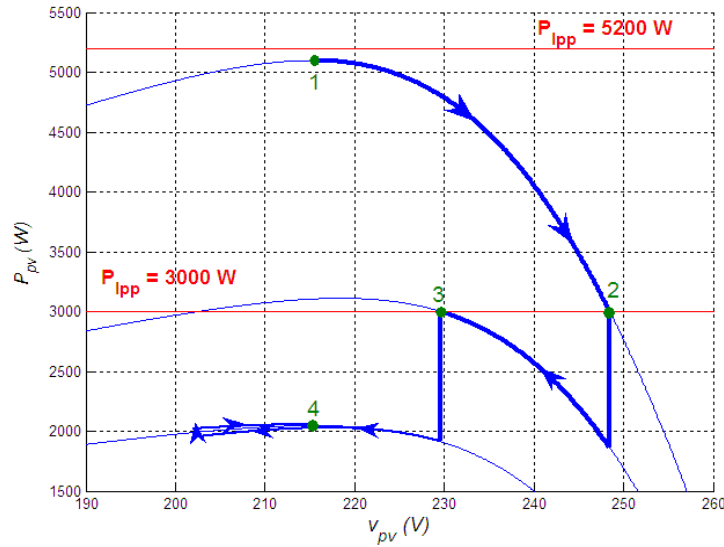


Figure 4.38. MPPT and LPPT operation.

Then, the power reference switches to 3000 W. From Fig. 4.37, $i_{L,lpp}^*$ becomes 13.93 A, lower than $i_{L,mpp}^*$ (23.68 A). Thus, i_L^* is now selected as $i_{L,lpp}^*$, changing the mode of operation to LPPT. Due to the change in the mode of operation, firstly the I_{max} saturation is activated and secondly, the MPPT algorithm is cancelled and the PV voltage reference v_{pv}^* is frozen to the last MPP value, that is $v_{mpp,fr} = 215.3$ V. The current i_L quickly follows its reference, causing the boost converter to demand 3000 W. This fact leads to a PV voltage increase and a PV power reduction until the intersection of both power curves, reaching point 2 of Fig. 4.38, with a PV power of 3000 W, a PV voltage of 248.5 V and a PV current of 12.07 A. Since the voltage is higher than the reference $v_{mpp,fr}$, the controller (see Fig. 4.37) increases its output $i_{L,mpp}^*$ up to the saturation I_{max} . As I_{max} is higher than $i_{L,lpp}^*$, $i_{L,mpp}^*$ is also higher than $i_{L,lpp}^*$ and the system remains in LPPT under these conditions.

Then, the irradiance drops to 600 W/m^2 . Since P_{mpp} is still higher than P_{lpp}^* , the system continues to operate under LPPT, delivering a power of 3000 W . The PV voltage decreases and the PV current increases until reaching point 3 of Fig. 4.38, with a PV voltage of 229.7 V and a PV current of 13.06 A . Given that the PV voltage $v_{pv,m}$ is still higher than $v_{mpp,fr}$, $i_{L,mpp}^*$ remains saturated to I_{max} and there is no change in the mode of operation. In fact, the reference $i_{L,mpp}^*$ will only decrease below I_{max} if there is a voltage drop below the frozen MPP voltage $v_{mpp,fr}$.

If at this moment, being in point 3, the irradiance drops to 400 W/m^2 , the PV power drops to 1913 W . Since the power reference P_{lpp}^* is higher than the PV power, the PV voltage decreases. However, since a power higher than P_{mpp} is now being demanded, the PV array is unable to deliver it and the PV voltage and the PV power fall below the MPP values (left side of the P-V curve). This fact activates the PI regulator: when the voltage goes below $v_{mpp,fr}$, the controller reduces its output $i_{L,mpp}^*$ (see Fig. 4.37). The voltage continues to decrease, $i_{L,lpp}^*$ to increase and $i_{L,mpp}^*$ to decrease until $i_{L,mpp}^*$ reaches a value lower than $i_{L,lpp}^*$. At that point, the mode of operation switches to MPPT, and the MPPT algorithm searches for the new maximum power point. Since $i_{L,mpp}^*$ was saturated to I_{max} , the reaction delay and the voltage drop (represented in Fig. 4.38) highly depend on the constant I_o . Finally, the system operates at point 4 of Fig. 4.38, with an MPP power of 3111 W , a PV voltage of 217.2 V and a PV current of 14.32 A .

With this example, it has been verified that this regulation makes it possible to operate in both MPPT and LPPT and that the mode of operation changes whenever necessary, assuring a small voltage drop in the input capacitor.

4.5.2 Simulation results

The change from one mode of operation to the other represents the most critical situation for the system stability. There are four critical situations depending on the change (from MPPT to LPPT or vice versa) and the cause of this change (P_{lpp}^* or P_{mpp} variation). In this section, these four cases are explained and the simulation results are presented. Using these examples, the correct performance of the proposed control represented in Fig. 4.37 is verified.

For the simulation, the PSIM software is used. The model comprises a PV array followed by an input capacitor C , a boost converter and a voltage source V_{bus} , similarly to the model of Fig. 4.7. The PV array specifications are given in Table 4.5 and boost converter features are provided in Table 4.6. The dynamics of the PV voltage regulation is variable as a result of the PV array nonlinear characteristics, as presented in section 4.3 and in [4.41]. The temperature of the PV array is 45°C in all simulations.

Nominal power	5700 W
MPP voltage V_{mpp}	241 V
MPP current I_{mpp}	23.6 A
Open-circuit voltage V_{oc}	294 V
Short-circuit current I_{sc}	25 A

Table 4.5. PV array specifications at STC.

Nominal power P_{nom}	5200 W
Input capacitance C	40 μ F
Boost inductance L	750 μ H
Commutation frequency	16 kHz
Cutoff frequency of the PV voltage control under nominal operating conditions	10 Hz
Cutoff frequency of the inductor current control	450 Hz
Current constant I_0	1 A
Bus voltage V_{bus}	350 V

Table 4.6. Boost converter features.

4.5.2.1 Switch from MPPT to LPPT: P_{lpp}^* reduction

The simulation results are shown in Fig. 4.39. In the first graph, the PV current i_{pv} and the LPP and MPP inductor current references ($i_{L,lpp}^*$ and $i_{L,mpp}^*$) are shown; in the second, the PV voltage v_{pv} ; and in the third, the PV power P_{pv} and the PV power reference P_{lpp}^* (P_{pv}^* in the figure). Initially, the power reference is 4000 W and the irradiance is 600 W/m², which corresponds to an MPP power of 3111 W. Thus, $i_{L,mpp}^* < i_{L,lpp}^*$ and the system is operating under MPPT with a PV voltage of 217.2 V and a PV current of 14.32 A, equal to $i_{L,mpp}^*$. Then, at second 0.6, the power reference is instantaneously reduced to 2000 W. As a result, $i_{L,lpp}^*$ becomes 9.21 A, lower than $i_{L,mpp}^*$, and the LPPT is therefore activated. The current and the power are established very quickly, in less than 10 ms. Once the LPPT mode has started, the PV voltage reference is frozen to $v_{mpp,fr} = 217.2$ V. Since the PV voltage is higher, the PI controller tends to increase the MPP current reference. However, it actually remains saturated at I_{max} , slightly over the LPP current reference.

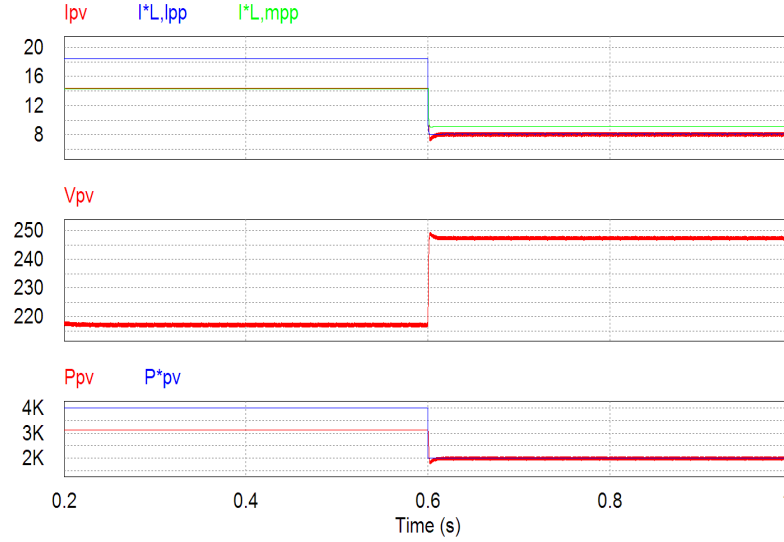


Figure 4.39. Switch from MPPT to LPPT caused by a P^*_{lp} reduction.

4.5.2.2 Switch from MPPT to LPPT: P_{mpp} increase

The simulation results are shown in Fig. 4.40, depicting the same variables represented in Fig. 4.39. The initial conditions are also the same as for the last case: $P^*_{lp} = 4000$ W, irradiance of 600 W/m² ($P_{mpp} = 3111$ W), $v_{pv} = 217.2$ V, $i_{pv} = 14.32$ A, $i^*_{L,mpp} < i^*_{L,lp}$ and MPPT operation. Then, from second 0.4 to 0.8, the irradiance varies linearly from 600 to 1000 W/m² (P_{mpp} from 3111 W to 5098 W). In a real system, this irradiance variation of 1000 W/m² per second corresponds to a very abrupt one [4.58]. At first, the MPPT tracks the maximum power, although there is a voltage variation caused by the effect of the irradiance disturbance on the PV voltage control. The voltage controller increases the reference $i^*_{L,mpp}$ and thus the current i_{pv} . However, when the MPP power exceeds the power reference (just before second 0.6), $i^*_{L,mpp}$ becomes higher than $i^*_{L,lp}$. As a result, the system switches to LPPT. The LPPT control sets the power to the command of 4000 W by increasing the PV voltage and decreasing the current until the irradiance becomes constant at second 0.8. Meanwhile, since the voltage reference has been frozen to 217.2 V, $i^*_{L,mpp}$ increases until current saturation I_{max} .

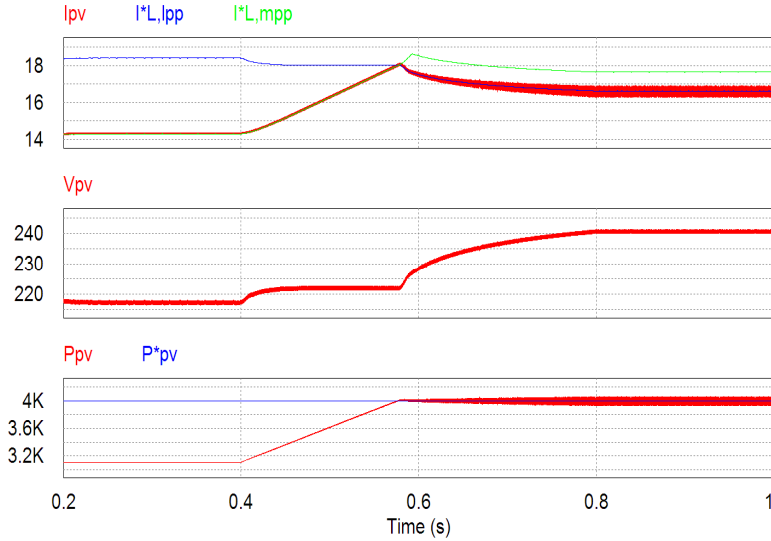


Figure 4.40. Switch from MPPT to LPPT caused by a P_{mpp} increase.

4.5.2.3 Switch from LPPT to MPPT: P^*_{lp} increase

Fig. 4.41 depicts the simulation results for the same variables as indicated previously. Initially, the power reference is 3000 W and the irradiance is 800 W/m², which is equivalent to an MPP power of 4129 W. Thus, the system is operating under LPPT with $P_{pv} = 3000$ W, $v_{pv} = 244.7$ V, $i_{pv} = i^*_{L,lp} = 12.26$ A and $i^*_{L,mpp} = i^*_{L,lp} + I_0 = 13.26$ A. Then, at second 0.6, the power reference P^*_{lp} is instantaneously increased to 5000 W, which exceeds the MPP power. In order to follow P^*_{lp} , the current reference $i^*_{L,lp}$ rises to 20.43 A, over the current reference $i^*_{L,mpp}$. This fact causes a soft mode of operation change to MPPT, which prevents a voltage drop. Then, the voltage is at first controlled towards the last MPP voltage $v_{mpp,fr} = 217.7$ V until the voltage reference is updated by the MPPT algorithm.

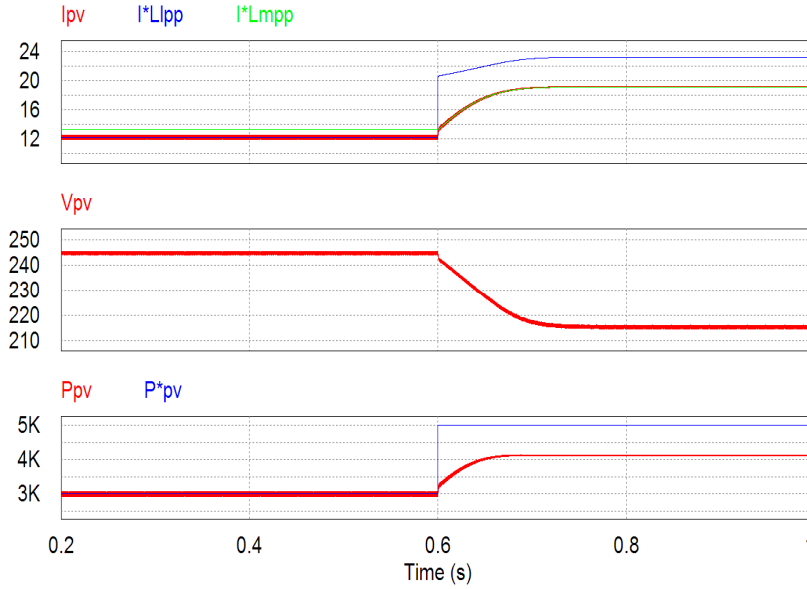


Figure 4.41. Switch from LPPT to MPPT caused by a P^*_{lpp} increase.

4.5.2.4 Switch from LPPT to MPPT: P_{mpp} reduction

The simulation results are shown in Fig. 4.42 for the same variables as for previous figures. The initial conditions are also the same as the last case: $P_{pv} = P^*_{lpp} = 3000$ W, irradiance of 800 W/m² ($P_{mpp}=4129$ W), $v_{pv}=244.7$ V, $i_{pv}=i^*_{L,lpp}=12.26$ A, $i^*_{L,mpp} = i^*_{L,lpp} + I_0 = 13.26$ A and LPPT operation. Then, from second 0.4 to 0.8, the irradiance varies linearly from 800 to 400 W/m² (P_{mpp} from 4129 W to 2047 W), which corresponds to a sudden irradiance variation of 1000 W/m² per second. At first, the LPPT maintains the power equal to 3000 W. In order to maintain that power with the irradiance variation, the voltage is reduced and the current increased. In this case, reference $i^*_{L,mpp}$ remains greater than $i^*_{L,lpp}$ since the PV voltage is still higher than the last MPP voltage $v_{mpp,fr} = 215.5$ V. However, as soon as the MPP power drops below the power reference (just after second 0.6), the power reference cannot be delivered. Then, the voltage falls below $v_{mpp,fr}$, leading to a reduction of $i^*_{L,mpp}$ and an increase of $i^*_{L,lpp}$. The voltage drop continues until $i^*_{L,mpp}$ becomes lower than $i^*_{L,lpp}$, the point at which the voltage control is enabled and the system switches to MPPT mode. This case is the most critical but, as it has been observed with the example, the PI controller saturation limits the voltage drop by means of constant I_0 .

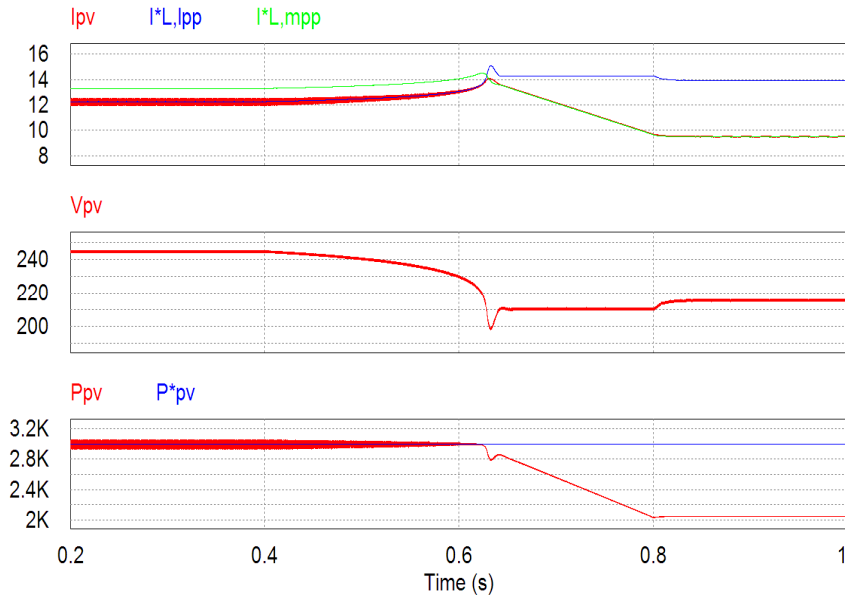


Figure 4.42. Switch from LPPT to MPPT caused by a P_{mpp} reduction.

4.6 CONCLUSIONS

In PV systems, the PV voltage regulation depends on the dynamic resistance, which changes with the characteristics of the PV array and is highly variable with the irradiation, the temperature and especially the PV voltage. In traditional control loops for the DC/DC boost stage of PV converters with large input capacitor, the effect of the dynamic resistance variation on the dynamic response of the compensated system is negligible. However, in the last years, the input capacitor of the commercial converters has been reduced in order to cut costs, which has brought the performance of the voltage regulation highly dependent on the operating point.

By means of a linearization of the PV array, it is exposed how the dynamic resistance reduces the performance of the regulation to a high extent when a small capacitor is used. In order to avoid that variability, an adaptive control is proposed. The dynamic resistance is firstly estimated from measured variables of the converter, namely the PV voltage and the inductor current. Then, the controller is continuously adapted making use of the estimation. The resistance is accurately calculated by means of the voltage and current 100 Hz ripple present in single-phase inverters. This avoids misestimations caused by abrupt irradiance variations.

The traditional control and the proposed control are tested using a commercial converter with a small 40 μF input capacitor, and a 4 kW PV array. The experimental results validate the theoretical analysis, show the problems of the traditional control, and demonstrate the higher performance of the proposed control and the correct estimation of the dynamic resistance.

As for the previous configuration composed by a DC/DC boost converter and an H-bridge inverter, a similar analysis is also carried for a TIBuck converter and a boost inverter. This configuration is an interesting solution for low-voltage grid-connected PV systems thanks to its high efficiency and two-MPPT capability with only one extra switch. However, the presence of two nonlinear PV arrays together with the nonlinear converter makes the voltage control design a delicate task.

A control scheme for regulating the two input voltages is first presented. Then, a system small-signal modeling which accounts for the nonlinear characteristics of the converter and the two PV arrays is derived. Thanks to the derived model, the two controllers are designed and the effect of the dynamic resistances on the control performance is evaluated. It is shown that the dynamic response becomes slower and more damped as the operating point moves towards the constant voltage region, and that stability is ensured for every situation. Simulation and experimental results validate the analysis and show that the proposed voltage regulation is adequate to perform MPPT of two arrays at the same time.

While the previous work deals with the voltage regulation, the power limitation is also tackled in chapter 4. The last section of this chapter presents a control strategy for a PV array connected to a DC/DC boost converter which makes it possible to operate in both modes, namely at either maximum or limited power point tracking. The strategy obtains high dynamics for the power response. It also assures stability in both modes of operation when switching from one mode to the other. Simulation results are carried out for a 5.7 kW PV array and a 5.2 kW boost converter at the most critical situations. The results validate the proposed control and show that a voltage drop is prevented even for the most adverse conditions.

4.7 REFERENCES

- [4.1] J. Campillo, S. Foster, "Global solar photovoltaic industry analysis with focus on the chinese market," Mälardalen University, Mälardalen, Sweden, Student Thesis, 2008.
- [4.2] A. K. Abdelsalam, A. M. Massoud, S. Ahmed, P. N. Enjeti, "High-performance adaptive perturb and observe MPPT technique for photovoltaic-based microgrids," *IEEE Transactions on Power Electronics*, vol. 26, no. 4, pp. 1010–1021, 2011.

- [4.3] B. N. Alajmi, K. H. Ahmed, S. J. Finney, B. W. Williams, "Fuzzy-logic-control approach of a modified hill-climbing method for maximum power point in microgrid standalone photovoltaic system," *IEEE Transactions on Power Electronics*, vol. 26, no. 4, pp. 1022–1030, 2011.
- [4.4] H. F. Wedde, S. Lehnhoff, E. Handschin, O. Krause, "Establishing large-scale renewable reserve capacity through distributed multi-agent support," in *5th IEEE Conference on Industrial Informatics*, vol. 2, pp. 1157–1163, Vienna (Austria), 2007.
- [4.5] L. D. Watson, J. W. Kimball, "Frequency regulation of a microgrid using solar power," in *26th IEEE Applied Power Electronics Conference and Exposition (APEC)*, pp. 321–326, Fort Worth (USA), 2011.
- [4.6] T. Esum, P. L. Chapman, "Comparison of photovoltaic array maximum power point tracking techniques," *IEEE Transactions on Energy Conversion*, vol. 22, no. 2, pp. 439–449, 2006.
- [4.7] S. Jain, V. Agarwal, "Comparison of the performance of maximum power point tracking schemes applied to single-stage grid-connected photovoltaic systems," *IET Electric Power Applications*, vol. 1, no. 5, pp. 753–762, 2007.
- [4.8] N. Femia, G. Petrone, G. Spagnuolo, M. Vitelli, "Optimization of perturb and observe maximum power point tracking method," *IEEE Transactions on Power Electronics*, vol. 20, no. 4, pp. 963–973, 2005.
- [4.9] W. Xiao, W. G. Dunfort, "A modified adaptive hill climbing MPPT method for photovoltaic power systems," in *IEEE 35th Annual Power Electronics Specialists Conference (PESC)*, vol. 3, pp. 1957–1963, Aachen (Germany), 2004.
- [4.10] K. Kohayashi, H. Matsuo, Y. Sekine, "A novel optimum operating point tracker of the solar cell power supply system," in *IEEE 35th Annual Power Electronics Specialists Conference (PESC)*, vol. 3, pp. 2147–2151, Aachen (Germany), 2004.
- [4.11] Q. Mei, M. Shan, L. Liu, J. M. Guerrero, "A novel improved variable step-size incremental-resistance MPPT method for PV systems," *IEEE Transactions on Industrial Electronics*, vol. 58, no. 6, pp. 2427–2434, 2011.
- [4.12] A. Safari, S. Mekhilef, "Simulation and hardware implementation of incremental conductance MPPT with direct control method using Cuk converter," *IEEE Transactions on Industrial Electronics*, vol. 58, no. 4, pp. 1154–1161, 2011.
- [4.13] V. A. K. Pappu, B. Chowdhury, R. Bhatt, "Implementing frequency regulation capability in a solar photovoltaic power plant," in *2010 North American Power Symposium (NAPS)*, pp. 1–6, Arlington (USA), 2010.
- [4.14] T. Suntio, J. Leppäaho, J. Huusari, L. Nusiainen, "Issues on solar-generator interfacing with current-fed MPP-tracking converters," *IEEE Transactions on Power Electronics*, vol. 25, no. 9, pp. 2409–2419, 2010.
- [4.15] W. Xiao, W. G. Dunford, P. R. Palmer, A. Capel, "Regulation of photovoltaic voltage," *IEEE Transactions on Industrial Electronics*, vol. 54, no. 3, pp. 1365–1374, 2007.
- [4.16] M.G. Villalva, T.G. de Siqueira, E. Ruppert, "Voltage regulation of photovoltaic arrays: small-signal analysis and control design," *IET Power Electronics*, vol. 3, no. 6, pp. 869–880, 2010.

- [4.17] R. Kadri, J. Gaubert, G. Champenois, "An improved maximum power point tracking for photovoltaic grid-connected inverter based on voltage-oriented control," *IEEE Transactions on Industrial Electronics*, vol. 58, no. 1, pp. 66–75, 2011.
- [4.18] T. Esum, J. W. Kimball, P.T. Krein, P.L. Chapman, P. Midya, "Dynamic maximum power point tracking of photovoltaic arrays using ripple correlation control," *IEEE Transaction on Power Electronics*, vol. 21, no. 5, pp. 1282–1291, 2006.
- [4.19] T. Suntio, J. Leppäaho, J. Huusari, "Issues on solar-generator-interfacing with voltage-fed converter," in *35th Annual Conference of IEEE Industrial Electronics (IECON)*, pp. 595–600, Porto (Portugal), 2009.
- [4.20] P. A. Sobeira, M. G. Villalva, P. G. Barbosa, H. A. C. Braga, J. R. Gazoli, E. Ruppert, A. A. Ferreira, "Comparative analysis of current and voltage-controlled photovoltaic maximum power point tracking," in *2011 Brazilian Power Electronics Conference (COBEP)*, pp. 858–863, Praiaamar (Brazil), 2011.
- [4.21] M. G. Villalva, J. R. Gazoli, E. R. Filho, "Analysis and simulation of the P&O MPPT algorithm using a linearized PV array model," in *35th Annual Conference of IEEE Industrial Electronics (IECON)*, pp. 231–236, Porto (Portugal), 2009.
- [4.22] M. G. Villalva E. R. Filho, "Dynamic analysis of the input-controlled buck converter fed by a photovoltaic array," *Sba Controle & Automação*, vol. 19, no. 4, 2008.
- [4.23] J. Puukko, L. Nousiainen, T. Suntio, "Effect of minimizing input capacitance in VSI-based renewable energy source converters," in *IEEE 33rd Telecommunications Energy Conference (INTELEC)*, pp. 1–9, Amsterdam (Netherlands), 2011.
- [4.24] J. Thongprona, K. Kirtikara, C. Jivacate, "A method for the determination of dynamic resistance of photovoltaic modules under illumination," *Solar Energy Materials and Solar Cells*, vol. 90, pp. 3078–3084, 2006.
- [4.25] A. Mäki, S. Valkealahti, T. Suntio, "Dynamic terminal characteristics of a photovoltaic generator," in *14th Power Electronics and Motion Control Conference (EPE/PEMC)*, pp. T12-76–T12-80, Ohrid (Macedonia), 2010.
- [4.26] L. Nousiainen, J. Puukko, T. Suntio, "Appearance of a RHP-zero in VSI-based photovoltaic converter control dynamics," in *IEEE 33rd Telecommunications Energy Conference (INTELEC)*, pp. 1–8, Amsterdam (Netherlands), 2011.
- [4.27] L. Nousiainen, J. Puukko, T. Suntio, "Simple VSI-based single-phase inverter: Dynamical effect of photovoltaic generator and multiplier-based grid synchronization," in *2011 IET Conference on Renewable Power Generation (RPG)*, pp. 1–6, Edinburgh (UK), 2011.
- [4.28] L. Nousiainen, J. Puukko, A. Mäki, T. Messo, J. Huusari, J. Jokipii, J. Viinamäki, D. T. Lobera, S. Valkealahti, T. Suntio, "Photovoltaic generator as an input source for power electronic converters," *IEEE Transactions on Power Electronics*, vol. 28, no. 6, pp. 3028–3028, 2013.
- [4.29] E. Bianconi, J. Calvente, R. Giral, E. Mamarelis, G. Petrone, C. A. Ramos-Paja, G. Spagnuolo, M. Vitelli, "A fast current-based MPPT technique employing sliding mode control," *IEEE Transactions on Power Electronics*, vol. 60, no. 3, pp. 1168–1178, 2013.

- [4.30] J. L. Agorreta, L. Reinaldos, R. González, M. Borrega, J. Balda, L. Marroyo, "Fuzzy switching technique applied to PWM boost converter operating in mixed conduction mode for PV systems," *IEEE Transactions on Industrial Electronics*, vol. 56, no. 11, pp. 4363–4373, 2009.
- [4.31] G. Petrone, G. Spagnuolo, R. Teodorescu, M. Veerachary, M. Vitelli, "Reliability issues in photovoltaic power processing systems," *IEEE Transactions on Industrial Electronics*, vol. 55, no. 7, pp. 2569–2580, 2008.
- [4.32] S. V. Dhople, A. Davoudi, A. D. Domínguez-García, P. L. Chapman, "A unified approach to reliability assessment of multiphase DC-DC converters in photovoltaic energy conversion systems," *IEEE Transactions on Power Electronics*, vol. 27, no. 2, pp. 739–751, 2012.
- [4.33] Y.-J. Wang, P.-C. Hsu, "Analytical modeling of partial shading and different orientation of photovoltaic modules," *IET Renewable Power Generation*, vol. 4, no. 3, pp. 272–282, 2010.
- [4.34] A. Maki, S. Valkealahti, "Power losses in long string and parallel-connected short strings of series-connected silicon-based photovoltaic modules due to partial shading conditions," *IEEE Transactions on Energy Conversion*, vol. 27, no. 1, pp. 173–183, 2012.
- [4.35] M. Z. S. El-Dein, M. Kazerani, M. M. A. Salama, "An optimal total cross tied interconnection for reducing mismatch losses in photovoltaic arrays," *IEEE Transactions on Sustainable Energy*, vol. 4, no. 1, pp. 99–107, 2013.
- [4.36] J. D. Bastidas-Rodríguez, E. Franco, G. Petrone, C. A. Ramos-Paja, G. Spagnuolo, "Maximum power point tracking architectures for photovoltaic systems in mismatching conditions: a review," *IET Power Electronics*, vol. 7, no. 6, pp. 1396–1413, 2014.
- [4.37] H. Patel, V. Agarwal, "Maximum power point tracking scheme for PV systems operating under partially shaded conditions," *IEEE Transactions on Industrial Electronics*, vol. 55, no. 4, pp. 1689–1698, 2008.
- [4.38] G. Velasco-Quesada, F. Guinjoan-Gispert, R. Pique-Lopez, M. Roman-Lumbreras, A. Conesa-Roca, "Electrical PV array reconfiguration strategy for energy extraction improvement in grid-connected PV systems," *IEEE Transactions on Industrial Electronics*, vol. 56, no. 11, pp. 4319–4331, 2009.
- [4.39] N. Femia, G. Lisi, G. Petrone, G. Spagnuolo, and M. Vitelli, "Distributed maximum power point tracking of photovoltaic arrays: novel approach and system analysis," *IEEE Transactions on Industrial Electronics*, vol. 55, no. 7, pp. 2610–2621, 2008.
- [4.40] P. Tsao, S. Sarhan, I. Jorio, "Distributed max power point tracking for photovoltaic arrays," in *34th IEEE Photovoltaic Specialists Conference (PVSC)*, pp. 2293–2298, Philadelphia (USA), 2009.
- [4.41] A. Urtasun, P. Sanchis, L. Marroyo, "Adaptive voltage control of the dc/dc boost stage in PV converters with small input capacitors," *IEEE Transactions on Power Electronics*, vol. 28, no. 11, pp. 5038–5048, 2013.
- [4.42] E. Bianconi, J. Calvente, R. Giral, E. Mamarelis, G. Petrone, C. A. Ramos-Paja, G. Spagnuolo, M. Vitelli, "A fast current-based mppt technique employing sliding mode control," *IEEE Transactions on Power Electronics*, vol. 60, no. 3, pp. 1168–1178, 2013.

- [4.43] J. L. Agorreta, L. Reinaldos, R. Gonzalez, M. Borrega, J. Balda, L. Marroyo, "Fuzzy switching technique applied to PWM boost converter operating in mixed conduction mode for PV systems," *IEEE Transactions on Industrial Electronics*, vol. 56, no. 11, pp. 4363–4373, 2009.
- [4.44] M. J. V. Vazquez, J. M. A. Marquez, F. S. Manzano, "A methodology for optimizing stand-alone PV-system size using parallel-connected DC/DC converters," *IEEE Transactions on Industrial Electronics*, vol. 55, no. 7, pp. 2664–2673, 2008.
- [4.45] S. V. Dhople, J. L. Ehlmann, A. Davoudi, P. L. Chapman, "Multiple-input boost converter to minimize power losses due to partial shading in photovoltaic modules," in *2010 IEEE Energy Conversion Congress and Exposition (ECCE)*, pp. 2633–2636, Atlanta (USA), 2010.
- [4.46] Y. M. Chen, Y. C. Liu, S. H. Lin, "Double-input PWM DC-DC converter for high-/low- voltage sources," *IEEE Transactions on Industrial Electronics*, vol. 53, no. 5, pp. 1538–1544, 2006.
- [4.47] C.-T. Pan, C.-F. Chuang, C.-C. Chu, "A novel transformerless interleaved high step-down conversion ratio DC-DC converter with low switch voltage stress," *IEEE Transactions on Industrial Electronics*, vol. 61, no. 10, pp. 5290–5299, 2014.
- [4.48] Y.-C. Liu, Y.-M. Chen, "A systematic approach to synthesizing multi-input DC-DC converters," *IEEE Transactions on Power Electronics*, vol. 24, no. 1, pp. 116–127, 2009.
- [4.49] X. Sun, Y. Zhou, W. Wang, B. Wang, Z. Zhang, "Alternative source port tolerant series-connected double-input DC-DC converter," *IEEE Transactions on Power Electronics*, early access.
- [4.50] R.-J. Wai, C.-Y. Lin, B.-H. Chen, "High-efficiency DC-DC converter with two input power sources," *IEEE Transactions on Power Electronics*, vol. 27, no. 4, pp. 1862–1875, 2012.
- [4.51] L. D. Salazar, J. R. Urra, "A novel three ports power conditioner for renewable electricity generators," in *37th Annual Conference on IEEE Industrial Electronics Society (IECON)*, pp. 1131–1136, Melbourne (Australia), 2011.
- [4.52] A. Khaligh, J. Cao, Y.-J. Lee, "A multiple-input DC-DC converter topology," *IEEE Transactions on Power Electronics*, vol. 24, no. 3, pp. 862–868, 2009.
- [4.53] R.-J. Wai, L.-S. Hong, "High-efficiency dual-input converter with high-voltage gain and internal charge function," *IET Power Electronics*, vol. 7, no. 2, pp. 299–315, 2014.
- [4.54] J. Sebastian, P. Villegas, F. Nuno, M. Hernando, "High-efficiency and wide-bandwidth performance obtainable from a two-input buck converter," *IEEE Transactions on Power Electronics*, vol. 13, no. 4, pp. 706–717, 1998.
- [4.55] G. Velasco, F. Guinjoan, R. Pique, A. Conesa, J.J. Negroni, "Inverter power sizing considerations in grid-connected PV systems," in *2007 European Conference on Power Electronics and Applications*, pp. 1–10, Aalborg (Denmark), 2007.
- [4.56] K. Gussemé, D. M. Syte, A. P. M. Bossche, J. A. Melkebeek, "Digitally controlled boost power-factor-correction converters operating in both continuous and discontinuous conduction mode," *IEEE Transactions on Industrial Electronics*, vol. 52, no. 1, pp. 88–97, 2005.

- [4.57] K. Jalili, S. Bernet, "Design of LCL filters of active-front-end two-level voltage-source converters," *IEEE Transactions on Industrial Electronics*, vol. 56, no. 5, pp. 1674–1689, 2009.
- [4.58] J. Marcos, L. Marroyo, E. Lorenzo, D. Alvira, E. Izco, "Power output fluctuations in large scale PV plants: One year observations with one second resolution and a derived analytic model," *Progress in Photovoltaics*, vol. 19, no. 2, pp. 218–227, 2011.
- [4.59] C. R. Sullivan, J. J. Awerbuch, A. M. Latham, "Decrease in photovoltaic power output from ripple: simple general calculation and the effect of partial shading," *IEEE Transactions on Power Electronics*, vol. 2, no. 2, pp. 740–747, 2013.
- [4.60] A. Urtaun, P. Sanchis, L. Marroyo, "Limiting the power generated by a photovoltaic system," in *10th Multi-Conference on Systems, Signals & Devices (SSD)*, pp. 1–6, Hammamet (Tunisia), 2013.

CHAPTER 5

SENSORLESS MPPT CONTROL OF SMALL WIND TURBINES: MODELING AND ROBUSTNESS ANALYSIS

ABSTRACT

The Permanent Magnet Synchronous Generator (PMSG) with diode bridge is frequently used in small Wind Energy Conversion Systems (WECS) thanks to its reliability and low cost. In order to achieve Maximum Power Point Tracking (MPPT) with no mechanical sensors, it is possible to impose the relationship between the DC voltage and the DC current at the optimum operating points. However, this relationship is difficult to calculate theoretically since the whole system is involved. This chapter develops an accurate model of the whole WECS, thereby making it possible to relate the electrical variables to the mechanical ones. With this model, it is possible to calculate the optimum curve $I_L^(V_{dc})$ from commonly-known system parameters and to control the system from the DC side. Experimental results validate the theoretical analysis and show that maximum power is captured for actual wind speed profiles.*

However, the proposed strategy requires having knowledge of the system parameters, which can be inaccurately known and vary in real applications. As a result, the optimum curve is not often precisely obtained, leading to power losses. This chapter thus evaluates to what extent the power is reduced due to parameter errors. It is shown how the power can be drastically decreased due to some parameter variation whereas it is not affected by others such as the resistance, which can then be neglected in order to simplify the model. Simulation results for an actual wind profile validate the theoretical analysis.

5.1 INTRODUCTION

Among all renewable resources, wind is one of the most accessible. Thanks to technological advances, costs of wind-based systems are continuously being reduced (4 cents/kWh), making them competitive against other energy sources [5.1]. As a result, the global wind power capacity is rapidly increasing. During 2012, almost 45 GW began operation and from the end of 2007 through 2012, annual growth rates of cumulative wind power capacity averaged 25% [5.2].

Regarding small turbines, more than 21,000 units and 64 MW were installed in 2011 [5.3]. For small wind generation (less than 100 kW), a Permanent Magnet Synchronous Generator (PMSG) is preferred because of its reliability, high efficiency and low cost. Two configurations are currently in major use with this machine [5.4], [5.5], as shown in Fig. 5.1.

In the first configuration (Fig. 5.1(a)), the PMSG is driven by an active rectifier, followed by the DC bus capacitor. A vector control is carried out, where the generator torque is controlled by means of the quadrature current i_q and the losses are minimized by the direct current i_d [5.6]. This enables improved control and higher efficiency [5.4], [5.6].

In the second alternative (Fig. 5.1(b)), the PMSG is followed by a diode bridge, a boost converter (which could also be either a buck or buck-boost converter) and the DC bus capacitor. Since reactive power is not indispensable for the PMSG operation, this direct connection to a diode bridge is possible. The torque can be controlled by means of the voltage or current at the diode bridge output [5.7], [5.8]. With this configuration, the PMSG efficiency is lower and more harmonics are generated. However, robustness, simplicity of control and conversion efficiency, all of which are essential features in small wind turbines, are substantially improved and costs are lowered [5.5].

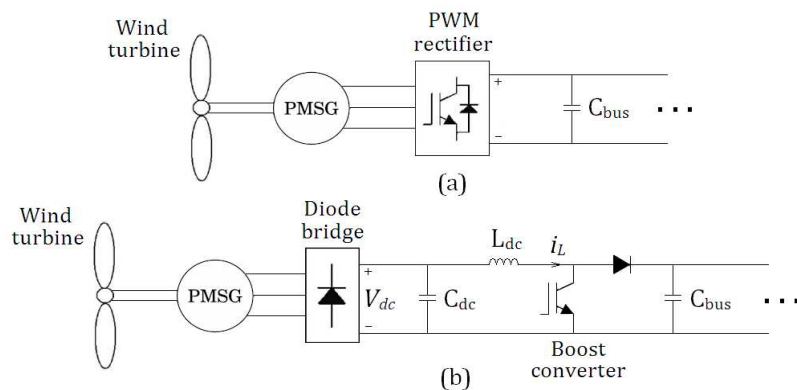


Figure 5.1. Wind turbine system: active/passive rectifier.

Without measuring the wind speed, two different methods for Maximum Power Point Tracking (MPPT) are usual for this second configuration. If the characteristics of the system are unknown, the perturbation and observation (P&O) strategy might be used [5.7], [5.9]–[5.12]. The problem with this strategy is that larger power variations are often caused by wind changes, which can be misinterpreted by the MPPT strategy. This can drive the system off, resulting in a poor MPPT [5.13]–[5.14].

The second strategy makes the system operate based on a pre-obtained system curve. Normally, the optimum curve $P^*(\omega)$ is used [5.15]–[5.16]. The problem of this optimum curve is that a shaft speed sensor is required. This is also the case if the curve $V_{dc}^*(\omega)$ is used [5.17].

Some authors have pointed out that the MPPT can be achieved using only the DC variables. As a result, alternative optimum curves have been proposed in other works, such as $V_{dc}^*(P_{dc})$ [5.18], [5.19] and $I_L^*(V_{dc})$ [5.1], having similar characteristics and not requiring a mechanical speed sensor. However, since the whole system is involved, these curves are more complicated to calculate theoretically. Consequently, they are calculated using an interpolation based on optimum points obtained by sweeping, either experimentally [5.1], [5.19], or by simulation [5.18], the complete output power curves for different wind speeds.

In order to avoid sweeping the power curve, a model of the WECS relating the electrical variables to the mechanical ones must be used. However, there is no model of the whole system in the literature. Although its different subsystems have been analyzed separately, they have never been considered as a whole. Regarding the “PMSG + diode bridge” subsystem, many models have been developed without considering the losses [5.20], [5.21]. However, in small wind applications, the power and speed are low and the line can be very long. As a result, the copper losses cannot be neglected and these models lead to major errors in the power curves [5.13].

This chapter first presents a theoretical analysis of the whole system, which makes it possible to relate the DC electrical variables to the mechanical ones of the turbine. Firstly, a more accurate model of the PMSG with diode bridge which accounts for the generator and line losses is developed. Then, based on this model, a model for the whole system is obtained. This study is very useful to understand the system operation. Furthermore, it makes it possible to obtain an accurate optimum curve $I_L^*(V_{dc})$ from known system parameters, thereby avoiding the need for experimental tests or simulations. Based on this curve, the system is easily controlled from the DC side and the MPPT is optimized for the entire operating range.

However, the system parameters, which are required for the optimum curve calculation, are supposed to be perfectly known. In real applications, the parameters

have errors and can be variable with temperature or aging. Thus, the MPPT performance will not be as expected and maximum power will not be tracked. Some authors have made a robustness analysis, trying to solve this problem [5.22], [5.23]. However, a comprehensive and in-depth study must be carried out.

In this context, this chapter also evaluates the influence of the system parameters on the power captured by the MPPT control. Using the equations and modeling methodology previously developed in this chapter, the MPPT efficiency is independently evaluated for the different parameters. Then, it is shown how the power is significantly reduced for two negative but realistic scenarios of parameter variation. Finally, the influence of the resistance is also assessed. Although the resistance makes change the power curves, it is proved that it can be neglected for the optimum curve calculation with no power reduction, which makes this calculation much easier.

5.2 MODELING OF THE WIND ENERGY CONVERSION SYSTEM

5.2.1 Interaction between subsystems

The WECS studied in this work is shown in Fig. 5.2. The behavior of this system can be defined by the wind speed v_w and three internal variables: the mechanical speed ω_m , the diode bridge output voltage V_{dc} and the inductor current I_L . Three subsystems will be distinguished, where the behavior of each subsystem is defined by two of these variables:

- The wind turbine (v_w and ω_m).
- The PMSG with diode bridge (ω_m and V_{dc}).
- The boost converter (V_{dc} and I_L).

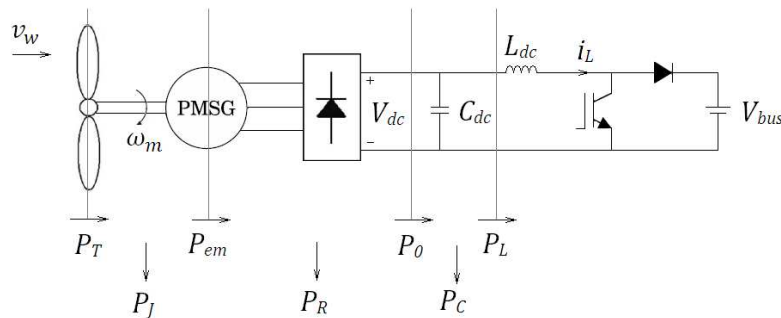


Figure 5.2. Global system and power balance.

With regard to Fig. 5.2, the power $P_T(v_w, \omega_m)$ represents the power captured by the wind turbine once the friction losses have been deducted. Part of this power is absorbed by the PMSG, and the remainder changes the shaft speed (P_J). The power entering the PMSG is its electromagnetic power $P_{em}(\omega_m, V_{dc})$. Neglecting the magnetic losses of the machine and the diode losses of the bridge, the electromagnetic power $P_{em}(\omega_m, V_{dc})$ is divided into the resistive losses caused by the PMSG and the line, $P_R(\omega_m, V_{dc})$, and the diode bridge output power, $P_0(\omega_m, V_{dc})$. Finally, most of the $P_0(\omega_m, V_{dc})$ enters the boost converter, $P_L(V_{dc}, I_L)$, and the remainder goes to change the C_{dc} capacitor voltage (P_C).

This power balance only accounts for the slowest dynamics, namely the mechanical inertia and the C_{dc} capacitor. It is expressed as

$$P_T(v_w, \omega_m) - P_{em}(\omega_m, V_{dc}) = J\omega_m \frac{d\omega_m}{dt} \quad (5.1)$$

$$P_{em}(\omega_m, V_{dc}) - P_R(\omega_m, V_{dc}) = P_0(\omega_m, V_{dc}) \quad (5.2)$$

$$P_0(\omega_m, V_{dc}) - P_L(V_{dc}, I_L) = C_{dc}V_{dc} \frac{dV_{dc}}{dt}, \quad (5.3)$$

where J is the total inertia moment of both the wind turbine and the PMSG.

In steady-state operation, (5.1) and (5.3) become

$$P_T(v_w, \omega_m) = P_{em}(\omega_m, V_{dc}) \quad (5.4)$$

$$P_0(\omega_m, V_{dc}) = P_L(V_{dc}, I_L). \quad (5.5)$$

The model of the PMSG connected to a diode bridge will first be studied in section 5.2.2. With this model, accurate expressions for the electromagnetic power $P_{em}(\omega_m, V_{dc})$ and the diode bridge output power $P_0(\omega_m, V_{dc})$ will be obtained. This will make it possible to consider the “PMSG + diode bridge” configuration as a single subsystem, with the input and output powers being calculated as a function of the mechanical speed ω_m and the output voltage V_{dc} .

Then, in section 5.3.1, the wind turbine will be integrated into the “PMSG + diode bridge”. For this purpose, the power $P_{em}(\omega_m, V_{dc})$ and the power captured by the turbine $P_T(v_w, \omega_m)$ will be related making use of (5.1) in dynamic operation or (5.4) in steady-state operation.

Finally, in section 5.3.2, the boost converter will be incorporated in order to obtain the global model. With this aim, the power $P_0(\omega_m, V_{dc})$ and the power that enters the boost converter $P_L(V_{dc}, I_L)$ will be related making use of (5.3) in dynamic operation or (5.5) in steady-state operation.

The modeling developed throughout this chapter is applied to an actual wind turbine installed at the campus of the Public University of Navarra in Pamplona, Spain. The features of the wind turbine are compiled in Table 5.1 and the specifications of the PMSG and the line are compiled in Table 5.2.

Nominal power	4200 W
Wind speed for turn on	3.5 m/s
Wind speed for nominal power	12 m/s
Optimum power coefficient	0.316
Optimum tip speed ratio	8.63
Diameter of the rotor	4 m
Inertia	5 kg·m ²
Height of the nacelle	23 m

Table 5.1. Features of the wind turbine placed in the campus of the Public University of Navarre (Pamplona, Spain).

Nominal speed	600 rpm
Line voltage constant	475 V/krpm
Nominal current	11.6 A
Number of pole pairs	15 pairs
Stator equivalent resistance	0.6 Ω
Stator equivalent inductance	4.9 mH
Line resistance	0.2 Ω
Line inductance	0.3 mH

Table 5.2. Specifications of the PMSG and the line.

5.2.2 PMSG with diode bridge

5.2.2.1 System description

The equivalent circuit of a PMSG connected to a diode bridge at steady-state operation is shown in Fig. 5.3, where R and L include the resistance and inductance of the PMSG, the line, and the possible transformer; e_a , e_b and e_c are the induced electromotive forces; i_a , i_b and i_c are the phase currents; i_{dc} is the diode bridge output current; and V_{dc} is the diode bridge output voltage.

The electrical system, represented by Fig. 5.3, is related to the mechanical system by

$$e_a = \sqrt{2}E \sin(\theta) \quad (5.6)$$

$$e_b = \sqrt{2}E \sin(\theta - 2\pi/3) \quad (5.7)$$

$$e_c = \sqrt{2}E \sin(\theta + 2\pi/3) \quad (5.8)$$

$$E = k \cdot \omega \quad (5.9)$$

$$\theta = \omega \cdot t \quad (5.10)$$

$$\omega = p \cdot \omega_m, \quad (5.11)$$

where E is the RMS value of the induced electromotive force, θ is the electrical angle, k is the PMSG voltage constant, ω is the electrical speed, p is the number of pole pairs, and ω_m is the mechanical speed.

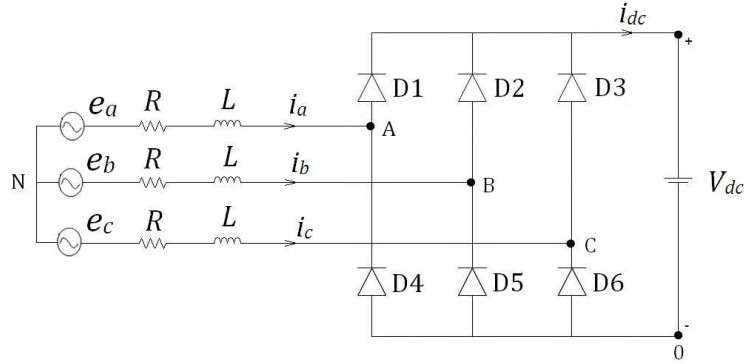


Figure 5.3. Equivalent circuit of a PMSG connected to a diode bridge at steady-state.

Operating at steady-state and given that the C_{dc} capacitor and the system inertia are high enough to neglect the ripple, the voltage V_{dc} and the speeds ω and ω_m can be considered as constant. Depending on the value of ω_m and V_{dc} , the phase current will be either continuous or discontinuous, resulting in different expressions for powers. Since the system is balanced, only phase A is henceforth studied.

5.2.2.2 Continuous conduction mode

For high voltage E or low voltage V_{dc} the current is continuous (the exact relationship for the boundary will be obtained in section 5.2.2.4). Thus, each diode conducts for π radians: D1 while the current of phase A is positive and D4 while it is negative.

The voltage v_{AN} can be defined as a function of the conducting diodes:

$$v_{AN} = (2u_1 - u_2 - u_3) \cdot V_{dc} / 3, \quad (5.12)$$

where u_1 , u_2 and u_3 are the connection functions of D1, D2 and D3, respectively (1 while conducting and 0 while being switched off).

Fig. 5.4 shows voltages e_a and v_{AN} and currents i_a , i_b , i_c and i_{dc} . Considering the sign of the currents and (5.12), the current i_a and the voltage v_{AN} are in phase. Furthermore, since the diode bridge does not exchange reactive power, the PMSG must provide its own reactive power, resulting in the lag angle φ between e_a and i_a shown in Fig. 5.4. According to the commutations, six intervals are defined in a period. In the subsequent paragraphs, the expressions for the current and the output and input powers are determined.

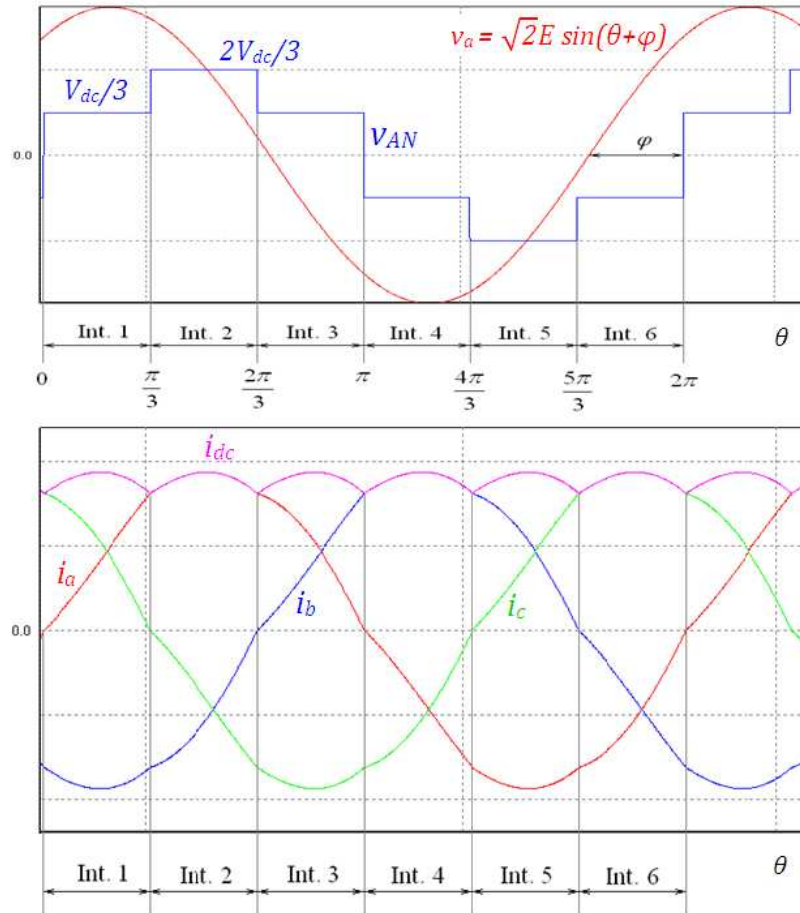


Figure 5.4. Waveforms for continuous conduction mode.

The current i_a can be deduced from a simple RL circuit with two voltage sources, namely voltages e_a and v_{AN} , as shown in Fig. 5.5. To simplify the notation throughout the chapter, the magnitude, phase and quality factor of the impedance as well as other parameters are introduced:

$$Z = \sqrt{R^2 + (\omega L)^2}, \quad \varphi_z = \tan^{-1}(\omega L / R), \quad Q = \omega L / R \quad (5.13)$$

$$e1 = \exp\left(-\frac{1}{Q} \frac{\pi}{3}\right), \quad e2 = \exp\left(-\frac{1}{Q} \frac{2\pi}{3}\right), \quad e3 = \exp\left(-\frac{1}{Q} \pi\right) \quad (5.14)$$

$$e_{aux} = \frac{1 + e1 - e2 - e3}{1 + e3} \quad (5.15)$$

$$b = \sin(\varphi - \varphi_z) \quad (5.16)$$

$$c = \cos(\varphi - \varphi_z). \quad (5.17)$$

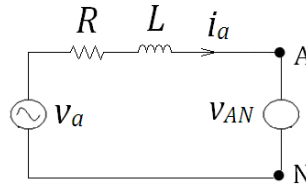


Figure 5.5. Equivalent circuit for current calculation.

The differential equation for the current i_a is expressed as follows:

$$\omega L \frac{di_a}{d\theta} + R \cdot i_a = e_a - v_{AN}, \quad i_a(\theta = 0) = 0. \quad (5.18)$$

The resolution of this equation is developed in the appendix, section 5.7.1. Then, thanks to the condition $i_a(\theta=\pi)=0$, the angle φ is calculated, as also shown in that section. As a result, i_a is defined at any time as a function of the shaft speed ω_m and the capacitor voltage V_{dc} at steady-state operation.

Given that the active component of the fundamental harmonic of the phase current I_{ad} is the only one to contribute to the active power, P_{em} can be calculated as

$$P_{em} = 3 \cdot E \cdot I_{ad}. \quad (5.19)$$

Using the Fourier analysis:

$$I_{ad} = \frac{1}{\sqrt{2}} \cdot \frac{2}{\pi} \cdot \int_0^\pi i_a(\theta) \sin(\theta + \phi) d\theta. \quad (5.20)$$

By means of (5.19), (5.20) and the expression for the current i_a , an expression for the electromagnetic power $P_{em}(\omega_m, V_{dc})$ in CCM is obtained as a function of the shaft speed ω_m and the capacitor voltage V_{dc} :

$$P_{em} = \frac{6E^2}{\pi Z} \left[\frac{\pi}{2} \cdot \frac{R}{Z} - \frac{b \cdot Q \cdot (1 + e3)}{Q^2 + 1} \cdot (Q \cdot \cos \phi + \sin \phi) \right] + \quad (5.21)$$

$$- \frac{\sqrt{2}E \cdot V_{dc}}{\pi R} \left[3 \cos \phi + \frac{Q \cdot (-2 + e1 - e2 - e3)}{Q^2 + 1} \cdot (Q \cdot \cos \phi + \sin \phi) \right]$$

The current i_a coincides with the output current i_{dc} in interval 2, where D1 is conducting and D2 and D3 are switched off (see Fig. 5.4). The ripple of i_{dc} has a 6ω angular frequency. Thus, the output power P_0 is given by:

$$P_0 = V_{dc} \cdot I_{dc} = V_{dc} \cdot \frac{3}{\pi} \cdot \int_{\frac{\pi}{3}}^{\frac{2\pi}{3}} i_a(\theta) d\theta. \quad (5.22)$$

where I_{dc} is the average value of i_{dc} .

Using (5.22) and the expression for the current i_a , an expression for the diode bridge output power $P_0(\omega_m, V_{dc})$ in CCM is obtained as a function of the shaft speed ω_m and the capacitor voltage V_{dc} :

$$P_0 = \frac{3\sqrt{2}E}{\pi Z} \cdot V_{dc} \cdot [c - b \cdot Q \cdot (e1 - e2)] - \frac{V_{dc}^2}{\pi R} \cdot \left[\frac{2\pi}{3} - Q \cdot (1 - e2) \right]. \quad (5.23)$$

5.2.2.3 Discontinuous conduction mode

For low voltage E or high voltage V_{dc} the current is discontinuous (the exact relationship for the boundary will be obtained in section 5.2.2.3). There is a retard angle α for each diode during which the expression (5.12) is no longer valid. Instead, the fact that the current is zero in one of the phases can be taken into account to calculate the voltage v_{AN} . Because of the discontinuous conduction, and contrary to the three intervals defined in CCM, six intervals are identified in a semi-period. The evolution of v_{AN} and the six intervals are shown in Fig. 5.6. The voltage e_a and currents i_a , i_b , i_c and i_{dc} are also illustrated.

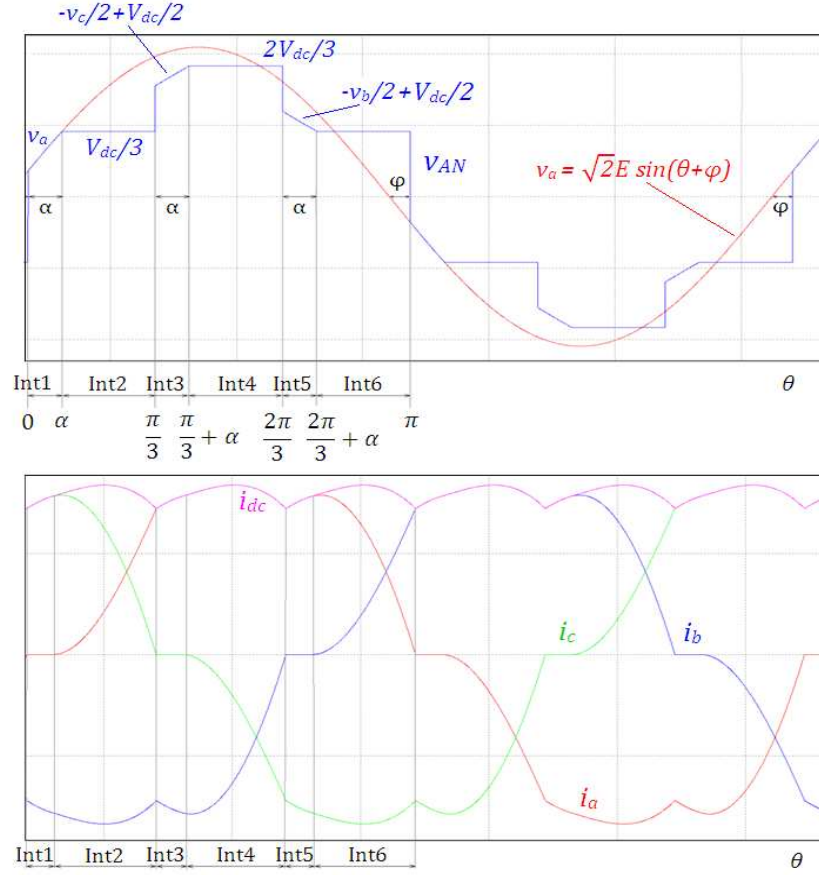


Figure 5.6. Waveforms for discontinuous conduction mode.

During interval 1:

$$e_a = v_{AN}, \quad v_{B0} = 0, \quad v_{C0} = V_{dc} \quad (5.24)$$

$$v_{A0} = \frac{3e_a + v_{B0} + v_{C0}}{2} = \frac{3e_a + V_{dc}}{2} \quad (5.25)$$

$$v_{AN} = e_a, \quad v_{BN} = -e_a/2 - V_{dc}/2, \quad v_{CN} = -e_a/2 + V_{dc}/2. \quad (5.26)$$

The same considerations are taken for intervals 3 and 5. In this way, the expression for v_{AN} is finally obtained (Fig. 5.6), but the complete calculation is not shown for reasons of space. Then, the expressions for the current and output and input powers are determined in the same way as for the CCM. Although three cases of DCM can be distinguished [5.20], only the case which is closer to the CCM is analyzed for the purposes of this work.

As in the continuous conduction mode (Fig. 5.5), the current i_a can be obtained from an RL circuit. To simplify the notation, some parameters are also defined in this case:

$$e\alpha = \exp(-\alpha/Q) \quad (5.27)$$

$$a = \sin(\alpha + \phi - \phi_z), \quad d = \cos(\alpha + \phi - \phi_z). \quad (5.28)$$

The differential equation for the current i_a in DCM is (5.18), the same as in CCM. However, the voltage v_{AN} is different, as was shown in Fig. 5.6. The resolution of this equation is developed in the appendix, in section 5.7.2. Then, thanks to the condition $i_a(\theta=\pi)=0$ and $e_a(\theta=\alpha)=V_{dc}/3$, the angles ϕ and α are calculated, as also shown in that section. Hence, i_a is defined at any time as a function of the shaft speed ω_m and the capacitor voltage V_{dc} at steady-state operation.

As in CCM, the electromagnetic power P_{em} can be obtained by means of (5.19) and (5.20). Considering the expression for the current i_a , an expression for the electromagnetic power $P_{em}(\omega_m, V_{dc})$ in DCM is obtained as a function of the shaft speed ω_m and the capacitor voltage V_{dc} :

$$\begin{aligned} P_{em} = & \frac{3E^2}{\pi Z} \left\{ \left(\pi - \frac{3\alpha}{2} \right) \frac{R}{Z} - \frac{3}{4} \sin(2\phi - \phi_z) + \frac{3}{4} \sin(2\phi + 2\alpha - \phi_z) + \right. \\ & + \frac{Q}{Q^2 + 1} \left[\left(b + a \frac{e1}{e\alpha} - b \cdot e1 - a \frac{e2}{e\alpha} + b \cdot e2 - 2a \frac{e3}{e\alpha} \right) \cdot (Q \cos \phi + \sin \phi) + \right. \\ & \left. \left. - 3a (Q \cos(\phi + \alpha) + \sin(\phi + \alpha)) \right] \right\} + \frac{\sqrt{2}E}{2\pi R} V_{dc} \{ -3 \cos \phi - 3 \cos(\phi + \alpha) + \\ & + \frac{Q}{Q^2 + 1} \left[\left(1 - \frac{e1}{e\alpha} - e1 + \frac{e2}{e\alpha} + e2 + 2 \frac{e3}{e\alpha} \right) \cdot (Q \cos \phi + \sin \phi) + \right. \\ & \left. \left. + 3 (Q \cos(\phi + \alpha) + \sin(\phi + \alpha)) \right] \right\} \end{aligned} \quad (5.29)$$

Making use of (5.22), the output power P_o can be obtained. Considering the expression for the current i_a , an expression for the diode bridge output power $P_o(\omega_m, V_{dc})$ in DCM is obtained as a function of the speed ω_m and the voltage V_{dc} :

$$\begin{aligned} P_o = & \frac{3\sqrt{2}E}{2\pi Z} Q \cdot V_{dc} \left(\frac{c+d}{Q} - a + b - a \frac{e1}{e\alpha} - b \cdot e1 + 2a \frac{e2}{e\alpha} \right) + \\ & + \frac{V_{dc}^2}{2\pi R} Q \cdot \left(\frac{\alpha - 4\pi/3}{Q} + 2 + \frac{e1}{e\alpha} - e1 - 2 \frac{e2}{e\alpha} \right) \end{aligned} \quad (5.30)$$

5.2.2.4 Boundary between modes of conduction

The expressions for the powers $P_{em}(\omega_m, V_{dc})$ and $P_o(\omega_m, V_{dc})$ have been obtained for CCM and DCM. Now, in order to choose the corresponding expression, the mode of conduction must be known. For this purpose, an expression for the boundary between modes of conduction is obtained below.

As the angle φ in Fig. 5.4 gets smaller, the voltage e_a at $\theta=0$ decreases. The value of e_a below which the diode D1 does not start conducting at $\theta=0$ represents the beginning of the discontinuous conduction mode. This value is given by

$$e_a(\theta=0) = \sqrt{2}E \sin \varphi = V_{dc} / 3. \quad (5.31)$$

With (5.31) and the expression of $\varphi(\omega, V_{dc})$ obtained in CCM after applying the condition $i_a(\theta=\pi)=0$ and shown in section 5.7.1, a relationship between V_{dc} and ω can be determined for the boundary between CCM and DCM as

$$V_{dc} = 3\sqrt{2}E \frac{\omega L \cdot R}{Z \sqrt{R^2 (1 + eaux)^2 + (\omega L)^2 eaux^2}}. \quad (5.32)$$

where E , Z and $eaux$ depend on ω . This curve is practically linear, which was expected since the electromotive force E is proportional to ω .

The boundary between the DCM and the non-conduction mode (NCM) is defined by the following well-known relationship:

$$V_{dc} = \sqrt{6} \cdot E. \quad (5.33)$$

The three conduction modes and the boundaries are represented in Fig. 7.

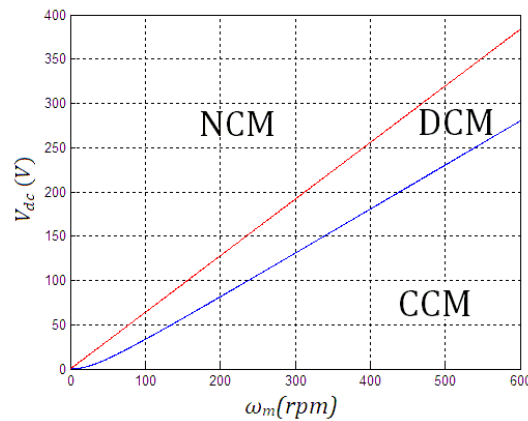


Figure 5.7. Boundaries between conduction modes.

5.2.2.5 Power curves

The equations obtained show that, in the configuration PMSG with diode bridge, electromagnetic and output powers (P_{em} and P_o) depend on the mechanical speed ω_m and the output voltage V_{dc} , both in CCM and in DCM. From these equations, powers P_o and P_{em} are first illustrated as a function of the voltage V_{dc} for constant speed ($\omega_{nom}/2$ and ω_{nom}) and then as a function of the speed ω_m for constant voltage (125 and 250V) in Fig. 5.8. The results have been validated by simulation using the software Simulink.

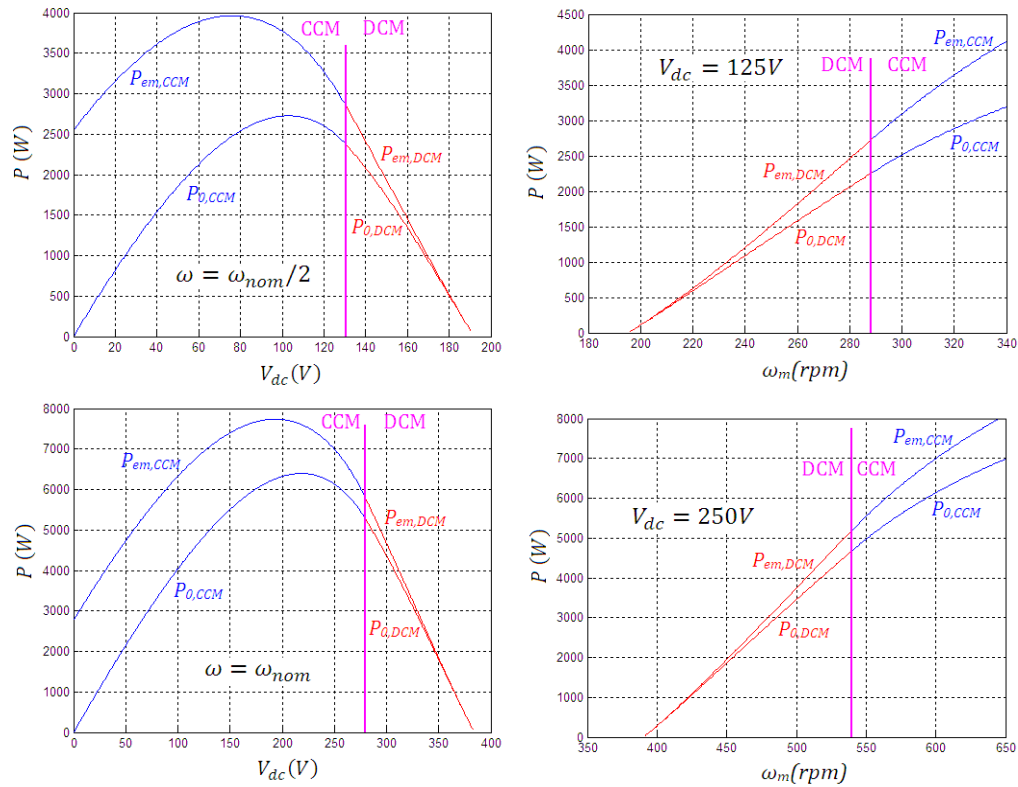


Figure 5.8. Power curves for the PMSG with diode bridge for CCM and DCM.

The curves at constant speed show how the power can be imposed by means of the voltage V_{dc} . This voltage is the degree of freedom since it can be set by controlling the inductor current (see Fig. 5.2). Thus, electromagnetic power P_{em} can be easily controlled in the PMSG with diode bridge. Working with high voltages results in a higher efficiency since currents and consequently losses are lower. In fact, this configuration cannot operate at the left part of the curve because the current exceeds the nominal current.

The curves at constant voltage for the PMSG with diode bridge will be used to analyze the interaction with the wind turbine. The intersection of the P_{em} curve with the turbine power curve will determine the point of steady-state operation and can be modified by means of V_{dc} .

In any case, when connecting a diode bridge to a PMSG, it must be considered that output power is limited since reactive power is not provided. Taking into account only the fundamental component, and operating at nominal speed ω_{nom} and nominal current I_{nom} , the relationship between active and reactive powers at the output of the PMSG is represented in the curve in Fig. 5.9. Then, if a diode bridge is added, maximum power of the PMSG is diminished. The power reduction ΔP_{max} depends on the reactive power absorbed by the inductance, as the following expression shows:

$$\Delta P_{max} = S_E - \sqrt{S_E^2 - (3 \cdot p \cdot \omega_{nom} \cdot L \cdot I_{nom}^2)^2} \quad (5.34)$$

$$S_E = 3 \cdot p \cdot k \cdot \omega_{nom} \cdot I_{nom} \quad (5.35)$$

Considering all the harmonics of the current, maximum power is reduced more than in (5.34) or Fig. 5.9 because of the higher losses in the equivalent resistance R .

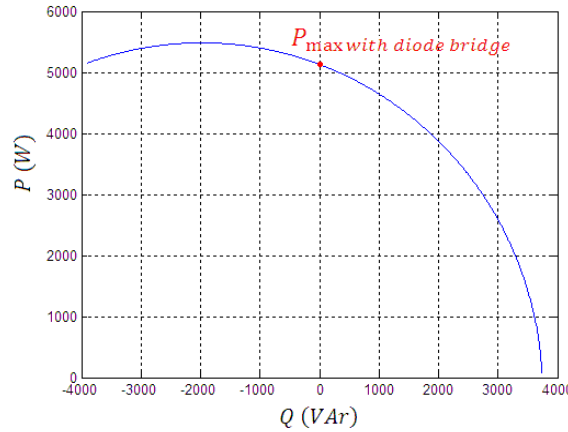


Figure 5.9. Power limit for a PMSG.

5.2.3 Experimental results

In this section, the model of PMSG with diode bridge is tested. The analysis is based on the wind turbine installed at the campus of the Public University of Navarra (Pamplona, Spain), with the features shown in Table 5.1. This wind turbine is emulated by means of a variable-speed drive (VSD) with a permanent magnet synchronous motor

(PMSG) and an inertia of $5 \text{ kg}\cdot\text{m}^2$ coupled with the mechanical shaft. The specifications of the PMSG which is connected to the shaft and of the line are provided in Table 5.2. The total equivalent resistance R is 0.8Ω and the total equivalent inductance L is 5.2 mH . The real wind turbine and the wind turbine emulator, which have the same power and very similar parameters, are shown in Fig. 5.10. The capacitance of C_{dc} is 2 mF .



Figure 5.10. Wind turbine and wind turbine emulator.

The theoretical curves for the output power P_o at constant speed and voltage are compared with the obtained experimental points. The results are shown in Fig. 5.11. It can be seen that the experimental results are very close to the theoretical curves, which validates the model of the PMSG with diode bridge previously described.

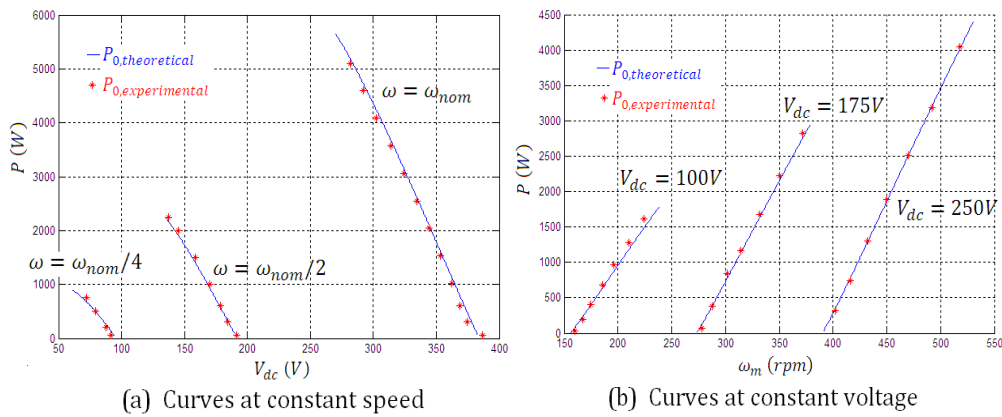


Figure 5.11. Theoretical and experimental power curves for the PMSG with diode bridge.

5.3 MPPT CONTROL

5.3.1 Integration of the wind turbine

The power captured by a wind turbine using a fixed pitch depends on the wind and turbine speeds through the following well-known expression (although the friction losses will be considered later on, they are not taken into account here in order to make the analysis clearer):

$$P_T = \frac{1}{2} \rho \cdot S \cdot v_w^3 \cdot C_P(\lambda), \quad (5.36)$$

where ρ is the air density, S is the wind turbine rotor swept area and C_P is the power coefficient. In turn, the power coefficient is a function of tip speed ratio, λ , and represents the wind turbine characteristics. The tip speed ratio is given by

$$\lambda = \frac{R_T \cdot \omega_m}{v_w}, \quad (5.37)$$

where R_T is the radius of the rotor.

At a certain wind speed, from (5.36), there is a λ_{opt} which maximizes the power coefficient C_{Popt} and, consequently, the power captured by the turbine P_{Topt} . Using (5.37), the required turbine speed ω_{mopt} becomes proportional to the wind speed:

$$\omega_{mopt} = \frac{\lambda_{opt}}{R_T} v_w. \quad (5.38)$$

By introducing (5.38) in (5.36), the power P_{Topt} can be expressed as a function of ω_m :

$$P_{Topt} = \frac{1}{2} \rho \cdot S \cdot C_{Popt} \cdot v_w^3 = \frac{1}{2} \rho \cdot \pi \cdot R_T^5 \cdot \frac{C_{Popt}}{\lambda_{opt}^3} \cdot \omega_m^3. \quad (5.39)$$

This curve P_{Topt} represents the power absorbed by the turbine when operating at MPP and thus at the optimum speed ω_{mopt} .

To analyze the interaction between the wind turbine and the PMSG with diode bridge, the expressions for the power captured by the wind turbine $P_T(v_w, \omega_m)$ and the input power to the PMSG $P_{em}(\omega_m, V_{dc})$ must be used. On account of (5.1), the difference between these powers will cause a variation of the speed ω_m until both powers are equal at a certain speed. Although the model of the PMSG with diode bridge has been developed for steady-state operation, expression (5.1) can still be used for the transient response since the variation of the speed and voltage is much slower than the rising of the currents.

In order to show the interaction graphically, curves of P_T at a constant wind speed (8m/s, 10m/s, 12m/s) and curves of P_{em} at a constant voltage (150V, 218V, 300V) are represented in Fig. 5.12 as a function of the shaft speed ω_m . In this figure, the optimum curve $P_{Topt}(\omega_m)$ (5.39) is also plotted.

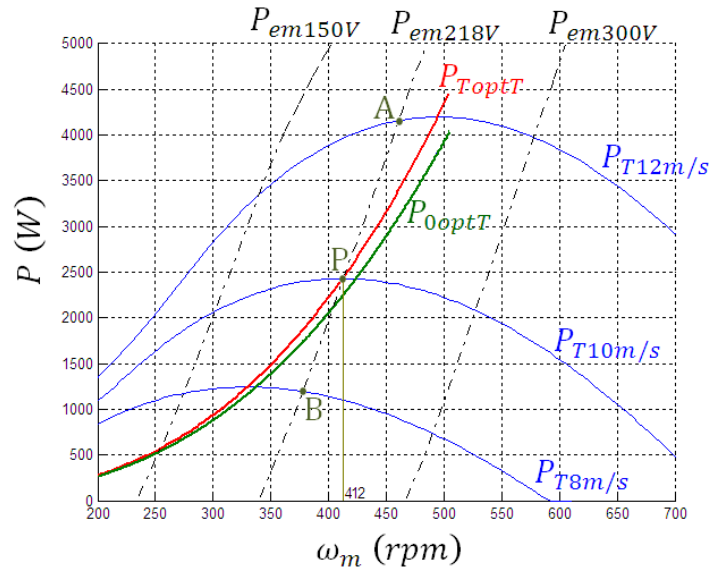


Figure 5.12. Power curves for the interaction between the wind turbine and the subsystem PMSG with diode bridge.

Let us consider, for example, a system that operates at a constant voltage at the diode bridge output, $V_{dc}=218V$. Then, the point at steady-state operation will be the intersection of the curve P_{em} at the constant voltage 218V and the curve P_T at the actual wind speed, that is point A for $v_w=12m/s$, point P for $v_w=10m/s$ and point B for $v_w=8m/s$. In that situation, the maximum power will only be absorbed when $v_w=10m/s$ but not for any other wind speed, resulting in a loss of energy.

Thus, in order to harvest the optimum power for any wind speed, the voltage V_{dc} must be adjusted in such a way that the curve $P_{em}(\omega_m, V_{dc})$ coincides with the curve P_{Topt} at all times. In other words,

$$P_{em}(\omega_m, V_{dc}) = P_{Topt}(\omega_m). \quad (5.40)$$

From (5.40) and using the expression (5.39) for $P_{Topt}(\omega_m)$ and the expressions (5.21) in CCM or (5.29) in DCM for $P_{em}(\omega_m, V_{dc})$, the voltage V_{dcopt} that provides maximum power for the turbine can be determined by iteration as a function of the shaft speed ω_m . The curve obtained is represented in Fig. 5.13.

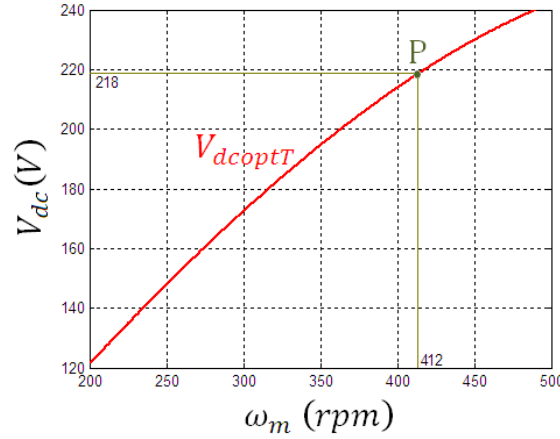


Figure 5.13. Optimum curve V_{dc}^{optT} versus ω_m .

Hence, the curve $V_{dc}^{opt}(\omega_m)$, which makes it possible to implement one of the MPPT techniques, has been theoretically determined. In that strategy the rotor speed is measured and the voltage reference V_{dc}^* is calculated from that speed according to the curve $V_{dc}^{opt}(\omega_m)$. In so doing, the electromagnetic power would follow the curve $P_{Topt}(\omega_m)$ for any rotor speed. Then, if the actual rotational speed is under the optimum speed, the power demanded by the PMSG drops below the wind turbine power and the system accelerates; if the actual rotational speed is over the optimum speed, then the power demanded goes above the wind turbine power and the system brakes (see Fig. 5.12). In both cases, the power evolves until it reaches maximum power. However, a mechanical sensor is required. In order to do without this sensor, the analysis must continue beyond the mechanical interaction.

To control the system from the DC side, it is necessary to obtain the power P_0 that must be imposed at the output in order to guarantee that the power P_{em} is P_{Topt} . This curve is called P_{0opt} and is defined as the turbine power P_{Topt} minus the resistive losses. It can be easily determined using the expression for $P_0(V_{dc}, \omega_m)$ in CCM, (5.23), or in DCM, (5.30), evaluated by means of the curve $V_{dc}^{opt}(\omega_m)$ shown in Fig. 5.13. The curve P_{0optT} is represented as a function of the rotor speed ω_m in Fig. 5.12.

5.3.2 Behavior of the whole system

Finally, the boost converter will be integrated into the whole system. Since the inductor current I_L is controlled, the boost converter functions as a current source. Consequently, the power that enters the converter is

$$P_L = V_{dc} \cdot I_L. \quad (5.41)$$

To analyze the interaction between the boost converter and the rest of the system, the expressions for the power absorbed by the boost converter $P_L(V_{dc}I_L)$ and for the diode bridge output power $P_o(\omega_m V_{dc})$ must be used. On account of (5.3), the difference between these powers will cause a variation of the voltage V_{dc} until both powers are equal at a certain voltage.

In order to show the interaction graphically, curves of P_o at a constant rotor speed (320rpm, 412rpm, 500rpm) and curves of P_L at a constant current (5A, 10.3A, 15A) are represented in Fig. 5.14 as a function of voltage V_{dc} . Since V_{dc} is the common variable, the power P_{0opt} must also be obtained as a function of this voltage. This curve can easily be determined by evaluating $P_o(V_{dc}\omega_m)$ (expression (5.23) in CCM or (5.30) in DCM) at the optimum points, which are defined by the optimum curve $V_{dcopt}(\omega_m)$ shown in Fig. 5.13. In so doing, $P_{0opt}(V_{dc})$ can now be included in Fig. 5.14.

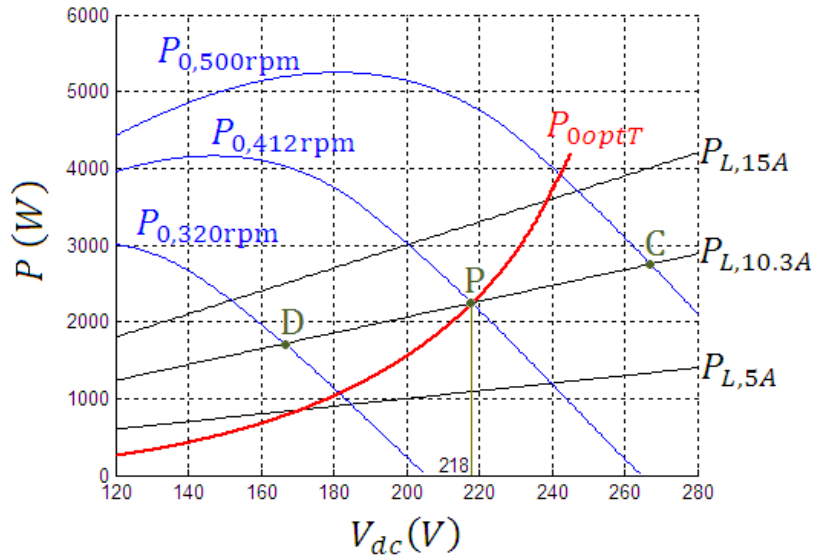


Figure 5.14. Power curves for the interaction between the boost converter and the PMSG with diode bridge.

Let us set for example a constant current at the output of the diode bridge $I_L=10.3A$. Then, the point at steady-state operation will be the intersection of the curve P_L at the constant current 10.3A and the curve P_o for the rotor speed at that moment, that is point C for $\omega_m=500rpm$, point P for $\omega_m=412rpm$ and point D for $\omega_m=320rpm$. In that situation, the diode bridge output power P_o will be the optimum power P_{0opt} only when $\omega_m=412rpm$ but not for any other rotor speed. Likewise, the voltage will be V_{dcopt} and therefore the electromagnetic power will be P_{Topt} only when $\omega_m=412rpm$ but not for any other rotor speed.

Thus, in order to follow those optimum curves for any rotor speed, the current I_L must be controlled in such a way that the curve $P_L(V_{dc}, I_L)$ coincides with the curve P_{0opt} at all times. In other words,

$$P_L(V_{dc}, I_L) = P_{0opt}(V_{dc}). \quad (5.42)$$

By means of (5.41) and (5.42), the current I_{Lopt} can be determined as a function of the voltage V_{dc} :

$$I_{Lopt} = \frac{P_{0opt}(V_{dc})}{V_{dc}}. \quad (5.43)$$

The curve obtained is represented in Fig. 5.15.

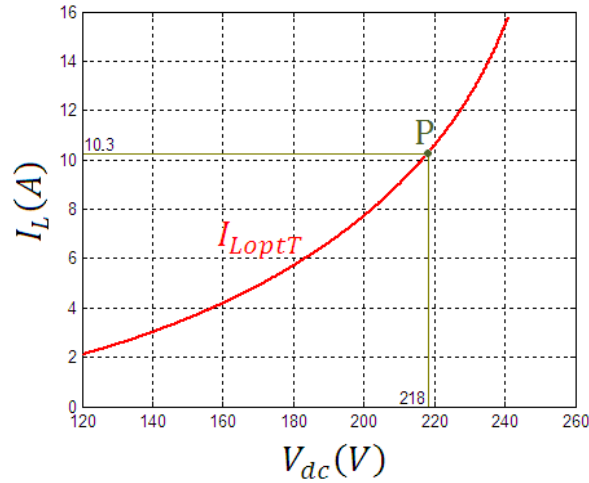


Figure 5.15. Optimum curve I_{Lopt} versus V_{dc} .

The complete process to determine the curve $I_{Lopt}(V_{dc})$ is summarized in Fig. 5.16. The optimum curve $P_{Topt}(\omega_m)$, which is provided by the manufacturer, and the specifications of the PMSG and the line (voltage constant V/rpm , number of pole pairs p , equivalent resistor R and equivalent inductance L) are required for the calculation. By means of (5.40), and considering the turbine curve and the expressions for the $P_{em}(\omega_m, V_{dc})$ in CCM (5.21) or DCM (5.29), the relationship between the voltage V_{dc} and the speed ω_m at the optimum operating points is determined. Then, the latter is used to evaluate $P_0(\omega_m, V_{dc})$ (expression (5.23) in CCM and (5.30) in DCM) and to obtain the optimum curve $P_{0opt}(V_{dc})$ as a function of V_{dc} . Finally, with (5.43), the curve $I_{Lopt}(V_{dc})$ is calculated.

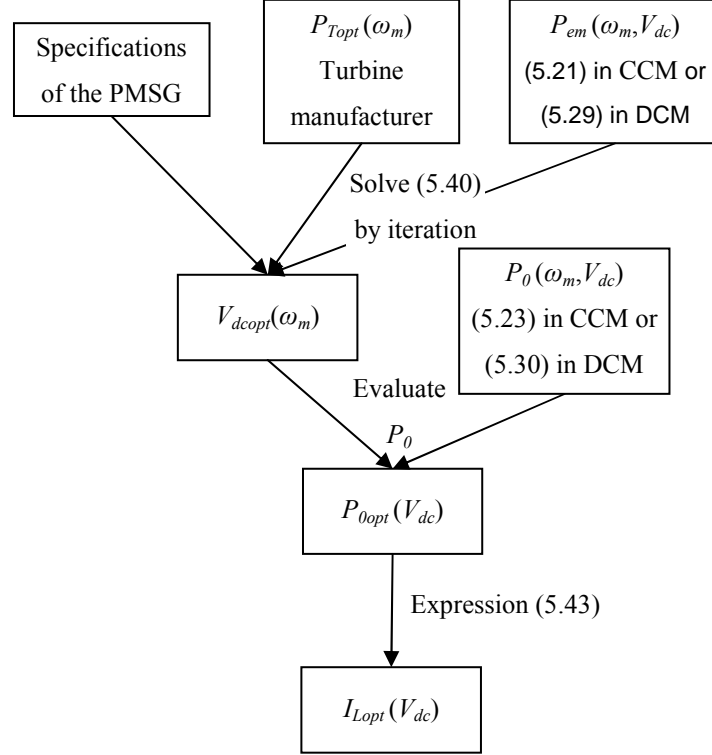


Figure 5.16. Determination of the optimum curve I_{Lopt} .

The curve I_{Lopt} is static and needs to be determined only once. Then, it can be stored in a lookup table to obtain the current reference I_L^* from the measured voltage V_{dc} during operation.

In so doing, the system evolves to the optimum point for any wind speed. Indeed, imposing the inductor current I_{Lopt} as a function of the measured voltage V_{dc} causes the power P_L to be P_{0opt} for any voltage. Then, if the actual voltage is under the optimum voltage for a given rotor speed, the power demanded by the boost converter drops below the diode bridge output power and the voltage increases; on the contrary, if the actual voltage is over the optimum voltage, then the power demanded goes above the output power and the voltage decreases (see Fig. 5.14). In both cases, the diode bridge output power P_0 changes until it reaches curve P_{0opt} . Since the voltage varies at a faster rate than the rotor speed, the diode bridge output power P_0 always gets equal to P_{0opt} . As a result, voltage V_{dc} follows V_{dcopt} for any rotor speed (see Fig. 5.13) and the electromagnetic power P_{em} is P_{Topt} at all times (see Fig. 5.12). This implies that the rotor speed follows the optimum speed, leading to the MPPT for any wind speed.

5.3.3 Experimental results

Once the model was validated in section 5.2.3, the MPPT control is implemented for the same system (see Fig. 5.10). The inductor current reference I_L^* is obtained as a function of the measured voltage V_{dc} from a lookup table which stores the curve $I_{Lopt}(V_{dc})$ of Fig. 5.15. This current is controlled by means of the strategy explained in [5.24], which is valid and robust for continuous and discontinuous inductor current. The block diagram of the MPPT control is shown in Fig. 5.17. In order to emulate the wind turbine, the torque reference for the VSD is calculated by a DSP as a function of the measured shaft and wind speeds according to the turbine power curves shown in Fig. 5.12. The wind profile, presented in Fig. 18(a), was obtained from two anemometers located in the wind turbine tower, providing one value per second.

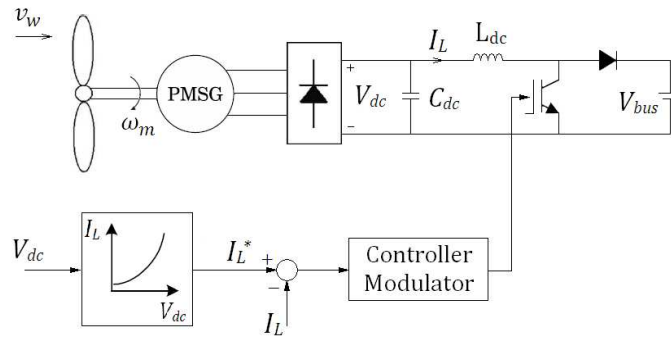


Figure 5.17. Block diagram of the MPPT control.

In Fig. 18(b), the optimum and actual speeds are shown. Although there is an expected delay caused by the inertia, it can be seen how the actual speed follows the optimum speed. Since this delay is limited as a result of the MPPT control, maximum power is achieved during the whole experiment, as shown in Fig. 16(c). More precisely, 50.81 Wh of the 51.14 Wh available are extracted by the turbine in the 90 second duration of the experiment, representing an MPPT efficiency of 99.36%. Other experiments have been carried out, with efficiencies varying between 99.0 and 99.5%. Furthermore, in Fig. 16(d), it can be observed how the voltage V_{dc} evolves as a function of the actual speed ω_m , actually following the optimum curve $V_{dcopt}(\omega_m)$ (see Figure 5.14). Likewise, the inductor current I_L evolves as a function of the voltage V_{dc} as imposed by the MPPT strategy. Thus, since I_L evolves as a function of V_{dc} and V_{dc} evolves as a function of ω_m , the dynamics of all the variables are determined by the inertia, which has two positive effects. Firstly, the output power is filtered and does not follow the wind speed variation even though maximum power is extracted. Secondly and more importantly for small wind turbines, the control is very robust since the system evolves naturally.

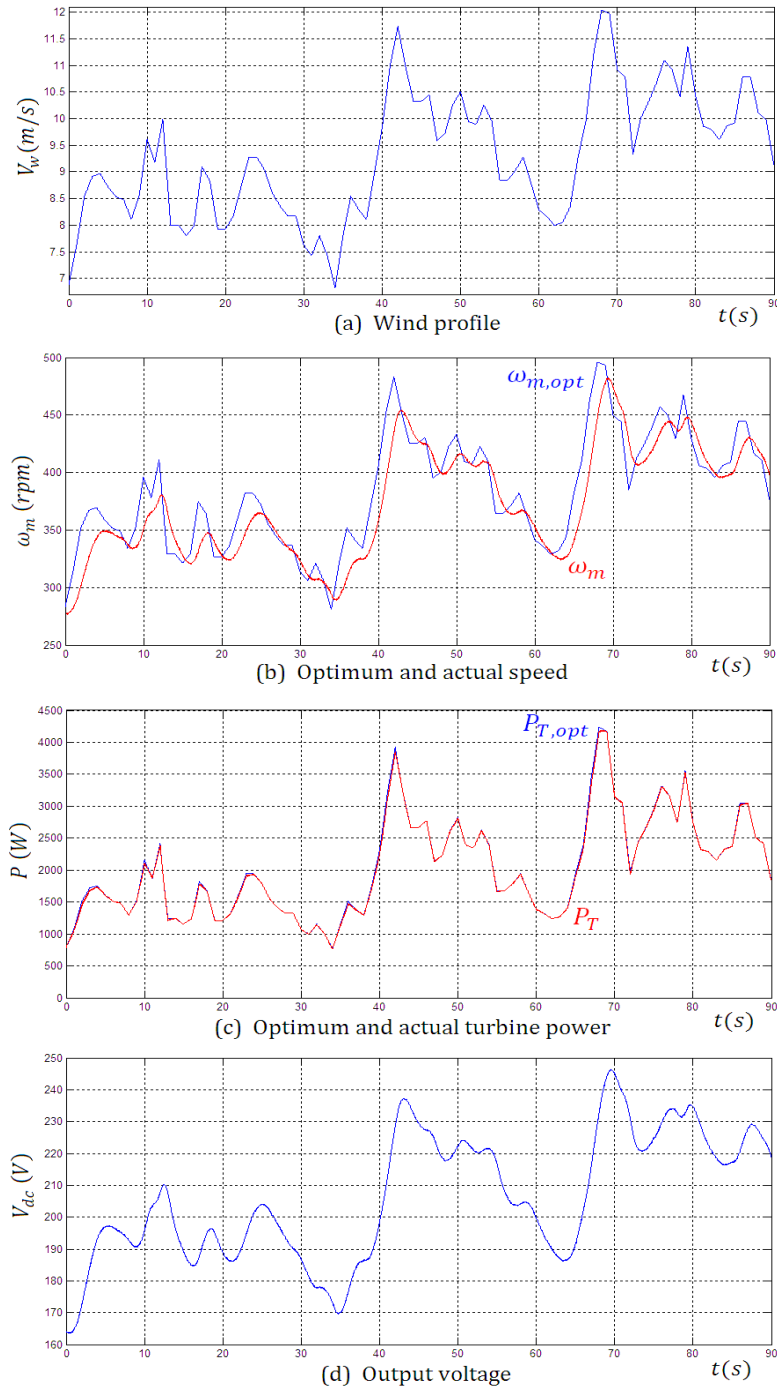


Figure 5.18. Experimental results with a real wind profile.

5.4 ROBUSTNESS ANALYSIS AND LOSSLESS APPROACH

5.4.1 Robustness analysis

The MPPT technique previously described will be employed in this section. For the calculation of the optimum curve the system parameters are required. These parameters include the features of the PMSG and the line (PMSG voltage constant k , resistance of the PMSG and the line R , and inductance of the PMSG and the line L) and the features of the wind turbine optimum curve $P_{Topt}(\omega_m)$ (C_{popt} and λ_{opt}).

If the real system parameters were equal to the parameters used for the optimum curve calculation, to be called k_{calc} , R_{calc} , L_{calc} , $(\lambda_{opt})_{calc}$ and $(C_{popt})_{calc}$, the MPPT efficiency would be 100% at steady-state. However, in a real system, parameters are not usually accurately known and can be variable with many factors such as temperature and aging. Accordingly, the parameters considered differ from its real values and the calculated optimum curve $I_{Lcalc}(V_{dc})$ is not equal to the actual optimum curve $I_{Lopt}(V_{dc})$. As a result, turbine speed is different to optimum speed ω_{mopt} for a certain wind speed and the power captured by the turbine is lower than the optimum power P_{Topt} .

Accounting for the characteristics of the different elements, the following variation range will be considered for the system parameters:

- Voltage constant of the PMSG k is generally well given by the manufacturer but can vary due to saturation: $\pm 10\%$ range is considered.
- Equivalent resistance R and inductance L of the PMSG and the line can be imprecisely known and change with the temperature: $\pm 30\%$ range.
- Optimum curve $P_{Topt}(\omega_m)$ can also be inaccurately provided by the manufacturer. $\pm 20\%$ range will be considered for λ_{opt} and C_{popt} .

With the model previously developed in this chapter [5.25], the power reduction can be predicted. In section 5.4.1.1, the MPPT efficiency for each parameter variation will be independently studied. Then, in section 5.4.1.2, the two worst scenarios will be described. Finally, in section 5.4.1.3, the MPPT efficiency for a model with $R=0$ will be analyzed.

5.4.1.1 Single parameter variation

If the optimum power coefficient given by the manufacturer $(C_{Popt})_{calc}$ is a 20% higher than its real value, that is $(C_{Popt})_{calc}=1.2 \cdot C_{Popt}$, curve $I_{Lcp+}(V_{dc})$, represented in Fig. 5.20, will be worked as the optimum curve but in reality differs from the actual optimum curve $I_{Lopt}(V_{dc})$. By means of the model previously presented, and using now the real parameter C_{Popt} , $I_{Lcp+}(V_{dc})$ can be translated to $P_{TCp+}(\omega_m)$, shown in Fig. 5.19, which is different to the actual optimum curve $P_{Topt}(\omega_m)$. This means that the intersection of the curve $P_{TCp+}(\omega_m)$ with the turbine power curve $P_T(v_w, \omega_m)$ will not lead to the maximum power for any wind speed. For example, for a wind speed $v_{wB}=10$ m/s, $P_{TB}=2411$ W, whereas the maximum power is $P_{TA}=2429$ W, which yields to a MPPT efficiency $\eta_B=99.26\%$ (see point B in the figures). The MPPT efficiency at steady-state $\eta_{cp+}(v_w)$ is shown in Fig. 5.21 for every wind speed. Now, if the optimum power coefficient given by the manufacturer $(C_{Popt})_{calc}$ is a 20% lower than its real value, that is $(C_{Popt})_{calc}=C_{Popt}/1.2$, the power is also reduced. The power curve $P_{TCp-}(\omega_m)$, inductor current curve $I_{Lcp-}(V_{dc})$ and the efficiency curve $\eta_{cp-}(v_w)$ are shown in Fig. 5.19, Fig. 5.20 and Fig. 5.21, respectively. It can be observed that C_{Popt} variation effect is low since the MPPT efficiency is higher than 99.2% for the whole operating range.

The same analysis has been independently carried out for all the parameters. For the optimum tip speed ratio λ_{opt} , the corresponding power curves $P_{T\lambda+}(\omega_m)$ and $P_{T\lambda-}(\omega_m)$, inductor current curves $I_{L\lambda+}(V_{dc})$ and $I_{L\lambda-}(V_{dc})$ and efficiency curves $\eta_{\lambda+}(v_w)$ and $\eta_{\lambda-}(v_w)$, are represented in Fig. 5.19, Fig. 5.20 and Fig. 5.24, respectively.

With regard to the electrical parameters, the power curves $P_{Tk+}(\omega_m)$, $P_{Tk-}(\omega_m)$, $P_{TL+}(\omega_m)$, $P_{TL-}(\omega_m)$, $P_{TR+}(\omega_m)$ and $P_{TR-}(\omega_m)$ are depicted in Fig. 5.22 and the inductor current curves $I_{Lk+}(V_{dc})$, $I_{Lk-}(V_{dc})$, $I_{LL+}(V_{dc})$, $I_{LL-}(V_{dc})$, $I_{LR+}(V_{dc})$ and $I_{LR-}(V_{dc})$ are depicted in Fig. 5.23. The MPPT efficiency curves $\eta_{k+}(v_w)$ and $\eta_{k-}(v_w)$ are represented in Fig. 5.24 and $\eta_{L+}(v_w)$, $\eta_{L-}(v_w)$, $\eta_{R+}(v_w)$ and $\eta_{R-}(v_w)$ are shown in Fig. 5.21.

From the MPPT efficiency at steady-state for all the parameters (see Fig. 5.21 and Fig. 5.24), it can be observed that λ_{opt} is the most influential, followed by k , C_p , L and finally R . The effect of C_p , L and R is not important for the considered range, the parameter k starts to be significant and the effect of parameter λ_{opt} is important. Since more energy is captured at high wind speeds, it must be noted that these operating points are more significant.

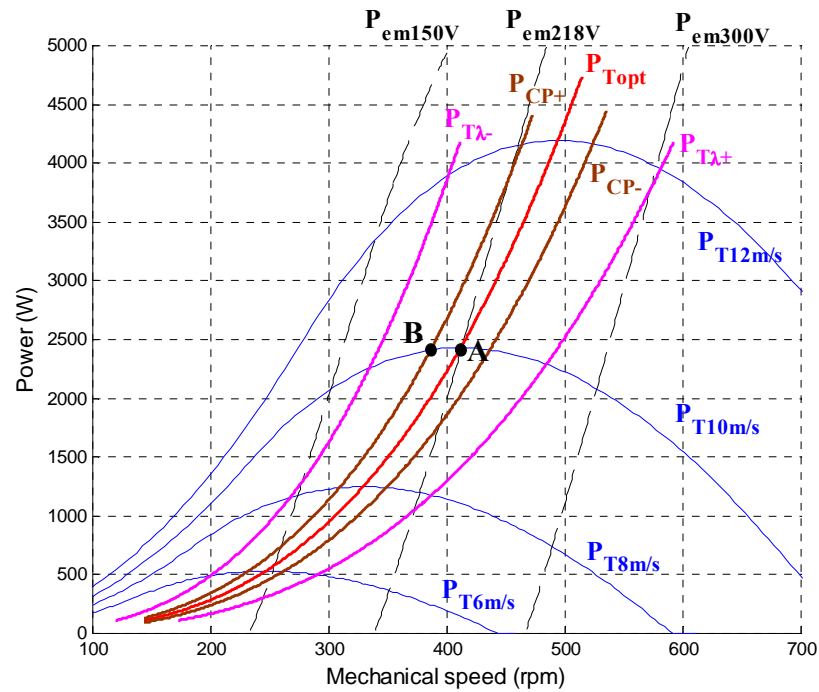


Figure 5.19. Wind turbine curves, electromagnetic power curves and calculated optimum power curves $P_{T\lambda}$ and P_{TCP} versus ω_m .

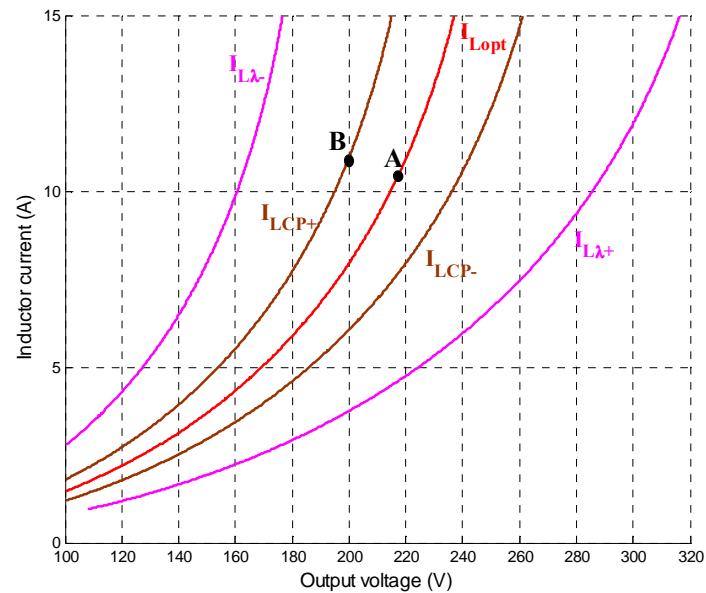


Figure 5.20. Calculated optimum current curves $I_{L\lambda}$ and I_{LCP} versus V_{dc} .

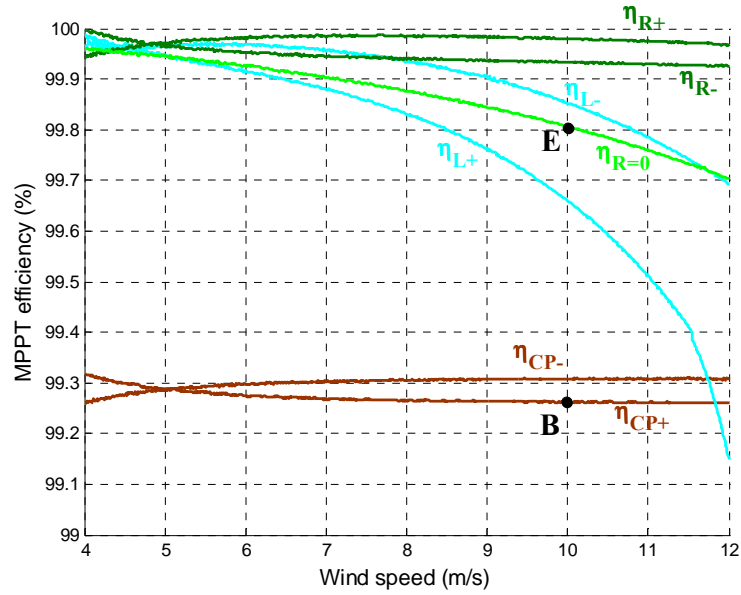


Figure 5.21. MPPT efficiency at steady-state η_R , $\eta_{R=0}$, η_L and η_{CP} versus v_w .

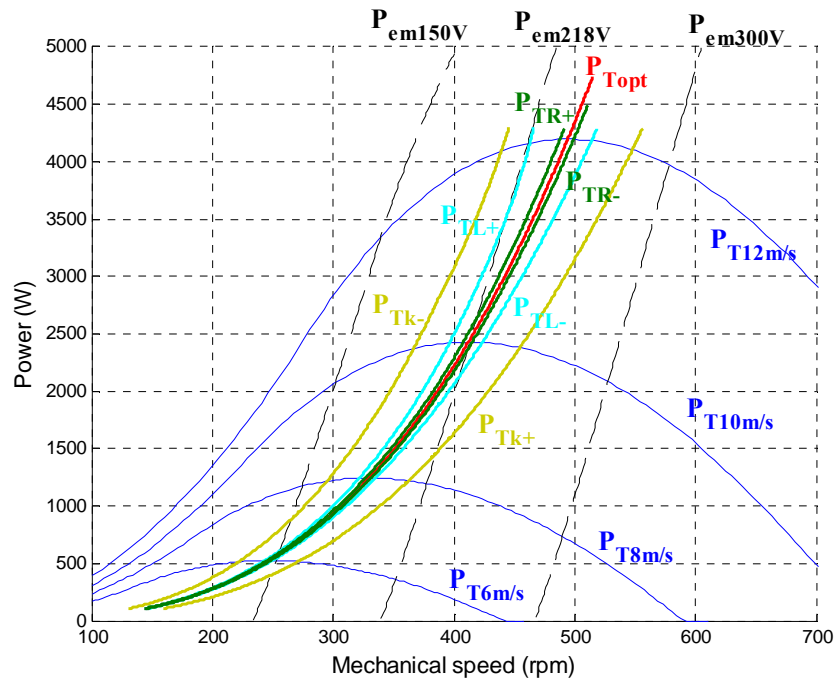


Figure 5.22. Wind turbine curves, electromagnetic power curves and calculated optimum power curves P_{Tk} , P_{TL} and P_{TR} versus ω_m .

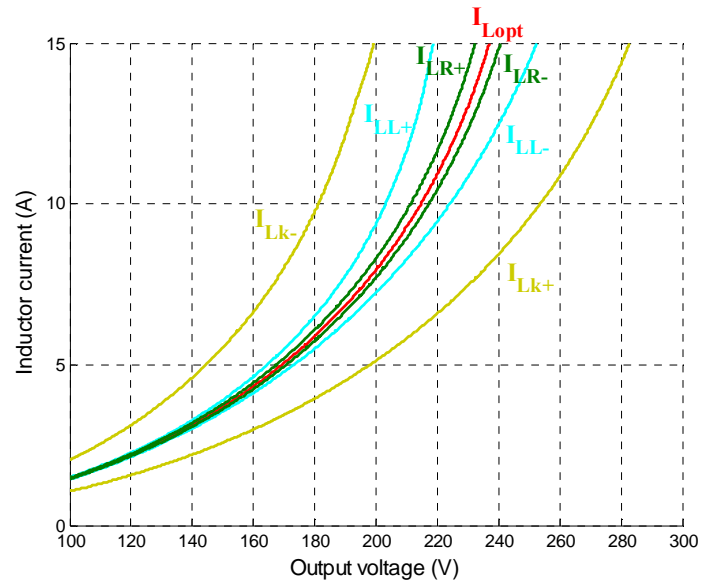


Figure 5.23. Calculated optimum current curves I_{Lk} , I_{LL} and I_{LR} versus V_{dc} .

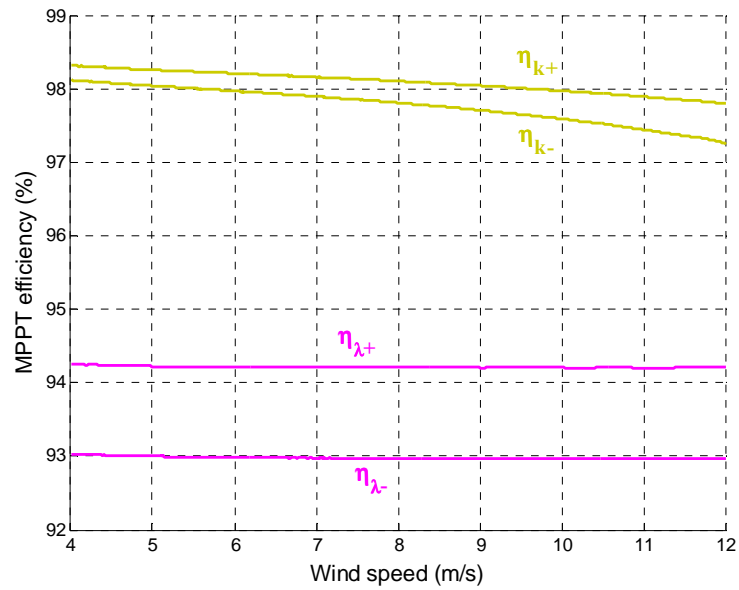


Figure 5.24. MPPT efficiency at steady-state η_λ and η_k versus v_w .

5.4.1.2 Worst scenarios

It was shown for C_{popt} (see Fig. 5.19), that when $(C_{popt})_{calc} > C_{popt}$, the system operates at a speed lower than the optimum speed. On the contrary, when $(C_{popt})_{calc} < C_{popt}$, the system operates at higher speed. After evaluating the effect of each parameter variation, the two worst scenarios can be analyzed. The first one, denoted by ω_{max} , consists of a combination of parameter variation in such a way that all parameters contribute towards an operating point with a speed higher than the real optimum speed. Accounting for the considered variation range and the effect of each parameter, the worst scenario ω_{max} is found for: $k_{calc} = 1.1 \cdot k$, $R_{calc} = R/1.3$, $L_{calc} = L/1.3$, $(\lambda_{opt})_{calc} = 1.2 \cdot \lambda_{opt}$ and $(C_{popt})_{calc} = C_{popt}/1.2$. In this case, the calculated optimum curve is $I_{L\omega_{max}}(V_{dc})$, shown in Fig. 5.26, which leads to a captured power $P_{T\omega_{max}}(\omega_m)$, represented in Fig. 5.25. The MPPT efficiency $\eta_{\omega_{max}}(v_w)$ is significantly reduced, as it can be observed in Fig. 5.27. Point D, also shown in the figures, corresponds to the real operating point for $v_{wD}=10$ m/s. On the other hand, the worst scenario ω_{min} is found for: $k_{calc} = k/1.1$, $R_{calc} = 1.3 \cdot R$, $L_{calc} = 1.3 \cdot L$, $(\lambda_{opt})_{calc} = \lambda_{opt}/1.2$ and $(C_{popt})_{calc} = 1.2 \cdot C_{popt}$. The calculated optimum curve $I_{L\omega_{min}}(V_{dc})$ is plotted in Fig. 5.26 and the captured power $P_{T\omega_{min}}(\omega_m)$ is depicted in Fig. 5.25. The MPPT efficiency $\eta_{\omega_{min}}(v_w)$, shown in Fig. 5.27, is drastically reduced. Point C, also represented in the figures, corresponds to the real operating point for $v_{wC}=10$ m/s.

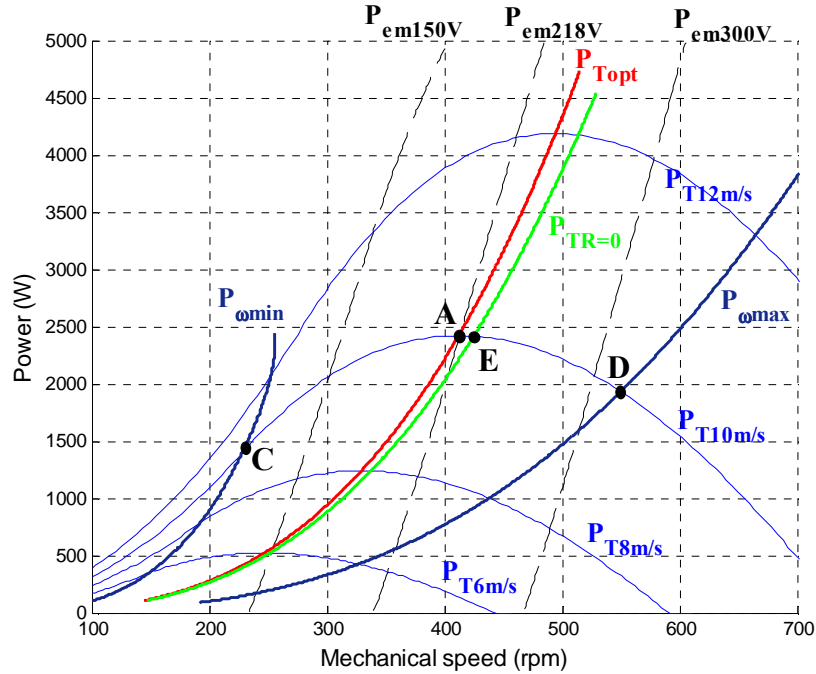


Figure 5.25. Block diagram of the MPPT control.

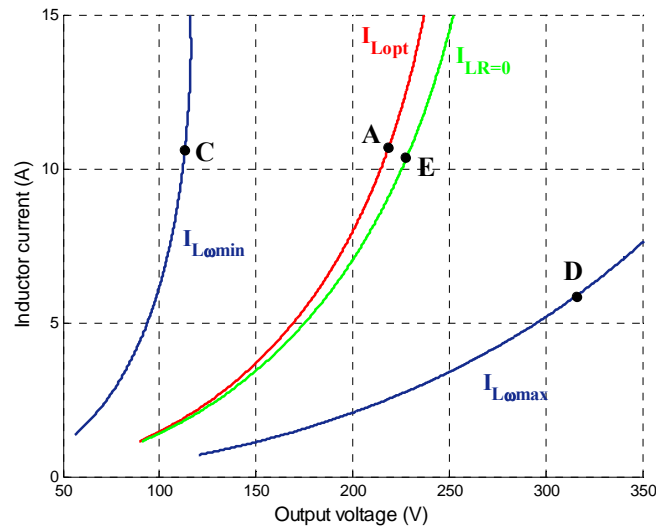


Figure 5.26. Block diagram of the MPPT control.

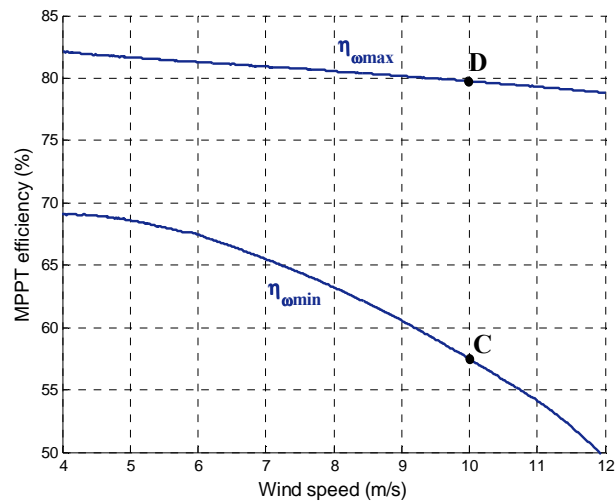


Figure 5.27. Block diagram of the MPPT control.

In addition, maximum values must be taken into account. For the worst situation ω_{max} , rotor speed ω_m and output voltage V_{dc} can exceed the nominal values. In our example, for nominal wind speed $v_w=12$ m/s, rotor speed becomes 664 rpm and output voltage becomes 368 V while optimum values are 495 rpm and 240 V. For the worst situation ω_{min} , it is inductor current I_L that can exceed nominal current. This is not the case in this example, but attention must be paid. Furthermore, the system operates with low voltages and high currents, which reduces the overall efficiency.

5.4.1.3 Influence of the resistance

It has been shown (see Fig. 5.21), that the resistance's effect is very small. More precisely, the power reduction for the variation range considered is lower than 0.1%.

For this reason, the same robustness analysis has been carried out neglecting the losses, that is for $R_{calc}=0$. The corresponding power curve $P_{TR=0}(\omega_m)$, inductor current curve $I_{LR=0}(V_{dc})$ and efficiency curve $\eta_{R=0}(v_w)$ are represented in Fig. 5.25, Fig. 5.26 and Fig. 5.21, respectively. Point E, pointed out in the figures, corresponds to the real operating point for $v_{we}=10$ m/s.

From the MPPT efficiency $\eta_{R=0}(v_w)$, it can be observed that the effect of considering $R=0$ is very small. In fact, the MPPT efficiency is higher than 99.7% for every operating point. As a result, the resistance can be neglected for the optimum curve calculation, which strongly simplifies the modeling. It is worth mentioning that the variation of other parameters will reduce the captured power in a very similar manner to the precedent analysis. The modeling of the subsystem PMSG with diode bridge with $R=0$ is developed in the next section following the methodology of section 5.2.2.

5.4.2 System modeling for the lossless approach

In order to obtain the PMSG with diode bridge power equations, the equivalent circuit of Fig. 5.3 is used. Since the losses are neglected, R is taken as 0 for the analysis. Equations (5.6)–(5.11) make it possible to relate the electrical and mechanical subsystems, and steady-state is also considered in this case.

5.4.2.1 Continuous conduction mode

For high voltage E or low voltage V_{dc} the current is continuous (the exact relationship for the boundary will be obtained in section 5.4.2.3). Thus, each diode conducts for π radians: D1 while the current of phase A is positive and D4 while it is negative. Fig. 5.4 shows voltages e_a and v_{AN} , currents i_a , i_b , i_c and i_{dc} and the lag angle φ between e_a and i_a . According to the commutations, six intervals (I1–I6) are defined in a period.

The current i_a can be obtained from the following differential equation:

$$\omega L \frac{di_a}{d\theta} = e_a - v_{AN}, \quad i_a(\theta = 0) = 0 \quad (5.44)$$

$$I1: i_a(\theta) = \frac{\sqrt{2}k}{L} [\cos\varphi - \cos(\theta + \varphi)] - \frac{V_{dc}}{3\omega L} \cdot \theta \quad (5.45)$$

$$I2: i_a(\theta) = \frac{\sqrt{2}k}{L} [\cos \varphi - \cos(\theta + \varphi)] - \frac{V_{dc}}{3\omega L} \left(2\theta - \frac{\pi}{3} \right) \quad (5.46)$$

$$I3: i_a(\theta) = \frac{\sqrt{2}k}{L} [\cos \varphi - \cos(\theta + \varphi)] - \frac{V_{dc}}{3\omega L} \left(\theta + \frac{\pi}{3} \right). \quad (5.47)$$

Then, thanks to the condition $i_a(\theta=\pi)=0$ (see Fig. 5.4) and (5.47), the angle φ can be calculated as

$$\varphi = \cos^{-1} \left(\frac{\sqrt{2}\pi \cdot V_{dc}}{9E} \right). \quad (5.48)$$

On account of expressions (5.45)–(5.48), i_a is now defined at any time as a function of the shaft speed ω_m and the capacitor voltage V_{dc} at steady-state operation.

Since the losses are neglected for the modeling, the PMSG electromagnetic power P_{em} is equal to the power at the diode bridge output P_o . In order to work this power out, (5.22) can also be used here. Using (5.22) and the expression for the current i_a (5.46), an expression for the diode bridge output power $P_o(\omega_m, V_{dc})$ in CCM is obtained as a function of the shaft speed ω_m and the capacitor voltage V_{dc} :

$$P_o = \frac{3\sqrt{2}k \cdot V_{dc}}{\pi L} \sin \varphi = \frac{V_{dc}}{3\pi\omega L} \sqrt{162E^2 - 4\pi^2 V_{dc}^2}. \quad (5.49)$$

5.4.2.2 Discontinuous conduction mode

For low voltage E or high voltage V_{dc} the current is discontinuous (the exact relationship for the boundary will be obtained in section 5.4.2.3). There is a retard angle α for each diode during which the current is zero in one of the phases. Because of the discontinuous conduction, and contrary to the three intervals defined in CCM, six intervals (I1-I6) are identified in a semi-period. The evolution of v_{AN} and the six intervals are shown in Fig. 5.6. The voltage e_a and currents i_a , i_b , i_c and i_{dc} are also illustrated. Although three cases of DCM can be distinguished [5.20], only the case which is closer to the CCM is analyzed for the purposes of this work.

The current i_a in DCM can also be obtained from (5.44) but taking into account that v_{AN} in DCM is different to v_{AN} in CCM (compare Fig. 5.4 and Fig. 5.6):

$$I1: i_a(\theta) = 0 \quad (5.50)$$

$$I2: i_a(\theta) = \frac{\sqrt{2}k}{L} [\cos(\alpha + \varphi) - \cos(\theta + \varphi)] - \frac{V_{dc}}{3\omega L} (\theta - \alpha) \quad (5.51)$$

$$I3: i_a(\theta) = \frac{\sqrt{2}k}{2L} \left[2 \cos(\alpha + \varphi) - \cos \varphi - \sqrt{3} \cos\left(\theta + \varphi + \frac{\pi}{6}\right) \right] - \frac{V_{dc}}{6\omega L} \left(3\theta - 2\alpha - \frac{\pi}{3} \right) \quad (5.52)$$

$$I4: i_a(\theta) = \frac{\sqrt{2}k}{2L} \left[3 \cos(\alpha + \varphi) - \cos \varphi - 2 \cos(\theta + \varphi) \right] - \frac{V_{dc}}{3\omega L} \left(2\theta - \frac{3\alpha}{2} - \frac{\pi}{3} \right) \quad (5.53)$$

$$I5: i_a(\theta) = \frac{\sqrt{2}k}{2L} \left[3 \cos(\alpha + \varphi) - \sqrt{3} \cos\left(\theta + \varphi - \frac{\pi}{6}\right) \right] - \frac{V_{dc}}{2\omega L} (\theta - \alpha) \quad (5.54)$$

$$I6: i_a(\theta) = \frac{\sqrt{2}k}{L} \left[\cos(\alpha + \varphi) - \cos(\theta + \varphi) \right] - \frac{V_{dc}}{3\omega L} \left(\theta - \alpha + \frac{\pi}{3} \right). \quad (5.55)$$

Then, thanks to the conditions $e_a(\theta=\alpha)=V_{dc}/3$ and $i_a(\theta=\pi)=0$, the angles φ and α can be calculated. Defining $\beta=\alpha+\varphi$, the first condition yields to

$$\beta = \alpha + \varphi = \sin^{-1} \left(\frac{V_{dc}}{3\sqrt{2}E} \right). \quad (5.56)$$

From the second condition, (5.55) and (5.56),

$$\frac{\sqrt{2}k}{L} \cos \varphi - \frac{V_{dc}}{3\omega L} \varphi + \frac{\sqrt{2}k}{L} \cos \beta - \frac{V_{dc}}{3\omega L} \left(\frac{4\pi}{3} - \beta \right) = 0. \quad (5.57)$$

The Newton-Raphson method is used to determine φ from (5.57), and (5.56) is used to determine α . Hence, on account of (5.50)–(5.57), the expressions of phase current i_a is defined at any time as a function of the shaft speed ω_m and the capacitor voltage V_{dc} at steady-state operation.

Making use of (5.22), the output power P_o can be obtained. Considering the expression for the current i_a , an expression for the diode bridge output power $P_o(\omega_m, V_{dc})$ in DCM is obtained as a function of the speed ω_m and the voltage V_{dc} :

$$P_o = \frac{3\sqrt{2}k \cdot V_{dc}}{2\pi L} \left[\sin \varphi + \sin(\alpha + \varphi) + (\pi - \varphi) \cos(\alpha + \varphi) \right] - \frac{\sqrt{2}k \cdot V_{dc}}{2L} \cos \varphi - \frac{V_{dc}^2}{\omega L} \left(\frac{2\pi}{9} - \frac{\alpha}{2} - \frac{\alpha^2}{4\pi} \right) \quad (5.58)$$

5.4.2.3 Boundary between modes of conduction

The expressions for the power $P_o(\omega_m, V_{dc})$ have been obtained for CCM and DCM. Now, in order to choose the corresponding expression, the mode of conduction must be known. For this purpose, an expression for the boundary between modes of conduction is obtained below.

As the angle φ in Fig. 5.4 gets smaller, the voltage e_a at $\theta=0$ decreases. The value of e_a below which the diode D1 does not start conducting at $\theta=0$ represents the beginning of the discontinuous conduction mode. This value is given by

$$e_a(\theta=0) = \sqrt{2}E \sin \varphi = V_{dc} / 3. \quad (5.59)$$

With (5.48) and (5.56), a relationship between V_{dc} and E can be determined for the boundary between CCM and DCM as

$$V_{dc} = \frac{9\sqrt{2}}{\sqrt{4\pi^2 + 9}} E. \quad (5.60)$$

The boundary between the DCM and the non-conduction mode (NCM) is defined by the following well-known relationship:

$$V_{dc} = \sqrt{6}E. \quad (5.61)$$

5.4.3 Simulation results

The global system of Fig. 5.2, features shown in Table 5.1 and Table 5.2, has been modeled using the software PSIM. The boost converter is replaced by a voltage controlled current source where the current is obtained according to the calculated optimum curve $I_{Lcalc}(V_{dc})$. A real wind profile is applied to four different calculated curves previously described: $I_{Lopt}(V_{dc})$, $I_{L\omega max}(V_{dc})$, $I_{L\omega min}(V_{dc})$ and $I_{LR=0}(V_{dc})$. For the calculation of $I_{Lopt}(V_{dc})$ and $I_{LR=0}(V_{dc})$, all the parameters are perfectly known (apart from R , which is considered as 0 for $I_{LR=0}(V_{dc})$), whilst for the calculation of $I_{L\omega max}(V_{dc})$ and $I_{L\omega min}(V_{dc})$, realistic errors are considered for the parameter estimation. The results are shown in Fig. 5.28 for the wind speed (m/s), the different rotor speeds (rpm) and captured powers (W). The variables ω_{mopt_dyn} and P_{Topt_dyn} represent the actual optimum point, which could only be followed if there was no inertia. It can be observed how rotor speeds ω_{mopt} , and $\omega_{mR=0}$ follow optimum speed ω_{mopt_dyn} with a small delay whereas rotor speeds $\omega_{m\omega max}$ and $\omega_{m\omega min}$ are always over and below optimum speed, respectively. As a result, captured power P_{Topt} and $P_{TR=0}$ are very similar to optimum power P_{Topt_dyn} while $P_{T\omega max}$ and $P_{T\omega min}$ are below optimum power. More precisely, from the 45.95 Wh which could have been obtained from second 10 to 120, a 99.15% was captured with $I_{Lopt}(V_{dc})$ curve, a 99.04% with $I_{LR=0}(V_{dc})$ curve, a 79.96% with $I_{L\omega max}(V_{dc})$ curve, and a 58.08% with $I_{L\omega min}(V_{dc})$ curve. These results confirm the predicted analysis: the resistance can be neglected for the optimum curve calculation and the performance of the MPPT can be drastically reduced due to errors in the parameters.

The MPPT efficiencies for the curves $I_{Lopt}(V_{dc})$ and $I_{LR=0}(V_{dc})$ are similar and very high, which confirms that the resistance can be neglected for the modeling. However, low MPPT efficiencies are obtained for the curves $I_{L\omega max}(V_{dc})$ and $I_{L\omega min}(V_{dc})$. This means that, for the conventional curve-based MPPT method, an additional control should be added to compensate for the errors in case that accuracy in the parameters cannot be guaranteed.

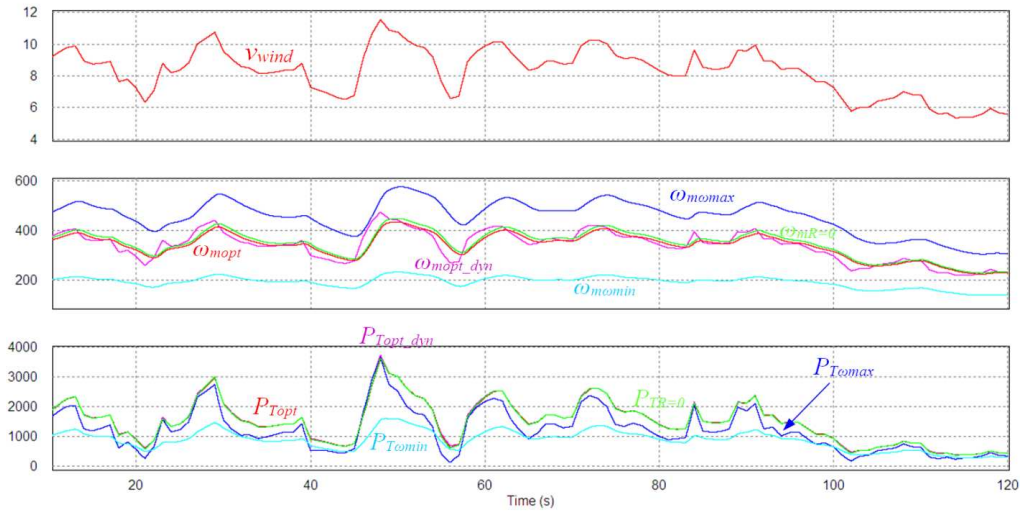


Figure 5.28. Simulation results.

5.5 CONCLUSIONS

This chapter first develops an accurate and complete model of a small WECS which uses a PMSG with diode bridge. This study makes it possible to relate the electrical variables to the mechanical ones. In this way, the optimum curve $I_{Lopt}(V_{dc})$ is obtained, which makes it possible to control the WECS from the DC side. Thanks to the equations of the model, the optimum curve can be calculated from commonly known system parameters, thereby avoiding the need for experimental tests or simulations. The control is very simple because only the measurements of the V_{dc} voltage and of the I_L current are required. It imposes the relationship $I_{Lopt}(V_{dc})$ at any moment in time and, consequently, the system evolves to the optimum power for any wind speed. Firstly, the model is validated by experimental results. Then, the MPPT control is tested using a wind turbine emulator and a real wind speed profile. The results show that more than 99% of the energy available is extracted by the turbine and validate both the model accuracy and the control performance.

Then, using the same model, a robustness analysis of the proposed MPPT control is carried out. By means of two realistic scenarios of parameter variation, it is shown how the captured power can be significantly reduced. Thus, an additional control to compensate for the estimation errors is necessary in case that accuracy in the parameters cannot be guaranteed. On the other hand, it is proved that the resistance has no influence on the MPPT efficiency and can then be neglected, leading to a much simpler model. The power curves for the PMSG with diode bridge with $R=0$ have then been provided. Simulation results for an actual wind profile corroborate the theoretical analysis for all scenarios.

5.6 APPENDICES

5.6.1 Calculation of the current i_a for CCM

Current i_a can be deduced from a simple RL circuit with two voltage sources, namely voltages e_a and v_{AN} . To simplify, the superposition principle is used as shown in Fig 5.29. Hence, the current can be expressed as a function of currents i_1 and i_2 as

$$i_a = i_1 - i_2. \quad (5.62)$$

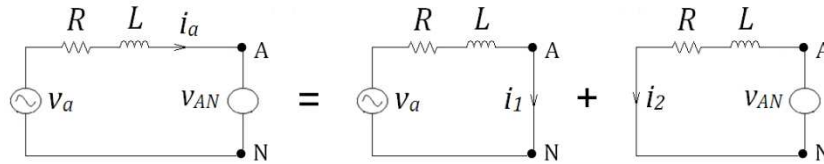


Figure 5.29. Equivalent circuit for current calculation using the superposition principle.

Because of symmetry, the current is determined for $0 < \theta < \pi$, corresponding to intervals 1, 2 and 3 of Fig. 5.4. The current initial value is set and the angle φ will be calculated thanks to the following conditions:

$$i_a(\theta = 0) = 0 \quad (5.63)$$

$$i_a(\theta = \pi) = 0. \quad (5.64)$$

From (5.62) and (5.63), the initial values of i_1 and i_2 are equal and have an unknown value of i_0 . The differential equations and their solutions are expressed as follows:

$$\omega L \frac{di_1}{d\theta} + Ri_1 = \sqrt{2}E \sin(\theta + \varphi), \quad i_1(\theta = 0) = i_0 \quad (5.65)$$

$$i_1(\theta) = \frac{\sqrt{2}E}{Z} \left[\sin(\theta + \varphi - \varphi_z) - b \cdot e^{-\frac{\theta}{Q}} \right] + i_0 \cdot e^{-\frac{\theta}{Q}} \quad (5.66)$$

$$\omega L \frac{di_2}{d\theta} + Ri_2 = v_{AN}, \quad i_2(\theta = 0) = i_0 \quad (5.67)$$

$$\text{Int 1: } i_2(\theta) = \frac{V_{dc}}{3R} \left(1 - e^{-\frac{\theta}{Q}} \right) + i_0 \cdot e^{-\frac{\theta}{Q}} \quad (5.68)$$

$$\text{Int 2: } i_2(\theta) = \frac{V_{dc}}{3R} \left[2 + (-1 - e1) \cdot e^{-\frac{\theta - \pi/3}{Q}} \right] + i_0 \cdot e^{-\frac{\theta}{Q}} \quad (5.69)$$

$$\text{Int 3: } i_2(\theta) = \frac{V_{dc}}{3R} \left[1 + (1 - e1 - e2) \cdot e^{-\frac{\theta - 2\pi/3}{Q}} \right] + i_0 \cdot e^{-\frac{\theta}{Q}}. \quad (5.70)$$

From (5.62), it can be observed in (5.66), and (5.68)–(5.70) that the initial condition i_0 is cancelled out when calculating the current i_a . Thus, in order to simplify the notation, this initial value is considered to be zero henceforth.

From (5.62) and (5.64),

$$i_1(\theta = \pi) = i_2(\theta = \pi). \quad (5.71)$$

Then considering expressions (5.16), (5.66) and (5.70) to evaluate (5.71), the lag angle φ is determined as

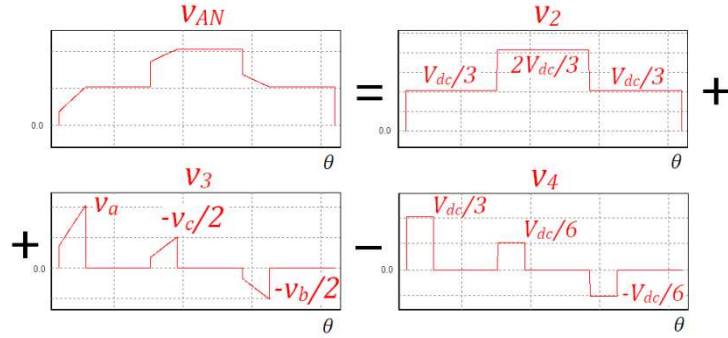
$$\varphi = \varphi_z - \sin^{-1} \left(\frac{V_{dc}}{3\sqrt{2}E} \cdot \frac{Z}{R} \cdot e_{aux} \right). \quad (5.72)$$

The previous expressions define the phase current i_a at any time as a function of the shaft speed ω_m and the capacitor voltage V_{dc} at steady-state operation.

5.6.2 Calculation of the current i_a for DCM

As in the continuous conduction mode (Fig. 5.29), the current can be obtained from an RL circuit by applying the superposition principle. However, in this case, the voltage v_{AN} is split into three components (v_2 , v_3 and v_4).

The three components of v_{AN} are shown in Fig. 5.30, where v_2 is the voltage v_{AN} in the continuous conduction mode, v_3 is composed by the pieces of sinusoidal waves of the intervals 1, 3 and 5, and v_4 by the remaining waves (see also Fig. 5.6).

Figure 5.30. Splitting of v_{AN} in DCM.

In this way, the voltage applied to the RL circuit can be split into four different components:

$$e_a - v_{AN} = e_a - (v_2 + v_3 - v_4) = e_a - v_2 - v_3 + v_4. \quad (5.73)$$

The current of the phase A can then be calculated as

$$i_a = i_1 - i_2 - i_3 + i_4, \quad (5.74)$$

where currents i_1 and i_2 are due to e_a and v_2 respectively, and their expressions have been calculated for the CCM (although angle φ is not the same); currents i_3 and i_4 are due to v_3 and v_4 respectively, and are determined below. As in CCM, the initial conditions for the currents i_1 , i_2 , i_3 and i_4 can be set to zero without changing the final expression of i_a .

The differential equation for i_3 and its solution are:

$$\omega L \frac{di_3}{d\theta} + Ri_3 = v_3, \quad i_3(\theta=0) = 0 \quad (5.75)$$

$$\text{Int 1: } i_3(\theta) = \frac{\sqrt{2}E}{Z} \left[\sin(\theta + \varphi - \varphi_z) - b \cdot e^{-\frac{\theta}{Q}} \right] \quad (5.76)$$

$$\text{Int 2: } i_3(\theta) = \frac{\sqrt{2}E}{Z} (a - b \cdot e\alpha) \cdot e^{-\frac{\theta - \alpha}{Q}} \quad (5.77)$$

$$\text{Int 3: } i_3(\theta) = \frac{\sqrt{2}E}{2Z} \left[\sin\left(\theta - \frac{\pi}{3} + \varphi - \varphi_z\right) + \left(-b + 2a \frac{e1}{e\alpha} - 2b \cdot e1\right) \right] \quad (5.78)$$

$$\text{Int 4: } i_3(\theta) = \frac{\sqrt{2}E}{2Z} (a - b \cdot e\alpha + 2a \cdot e1 - 2b \cdot e1 \cdot e\alpha) \cdot e^{-\frac{\theta - \pi/3 - \alpha}{Q}} \quad (5.79)$$

$$\text{Int 5: } i_3(\theta) = \frac{\sqrt{2}E}{2Z} \left[-\sin\left(\theta - \frac{2\pi}{3} + \phi - \phi_z\right) + \left(b + a \frac{e1}{e\alpha} - b \cdot e1 + 2a \frac{e2}{e\alpha} - 2b \cdot e2\right) e^{\frac{\theta - 2\pi/3}{Q}} \right] \quad (5.80)$$

$$\text{Int 6: } i_3(\theta) = \frac{\sqrt{2}E}{2Z} (-a + b \cdot e\alpha + a \cdot e1 - b \cdot e1 \cdot e\alpha + 2a \cdot e2 - 2b \cdot e2 \cdot e\alpha) e^{\frac{\theta - 2\pi/3 - \alpha}{Q}}. \quad (5.81)$$

In the same way, for i_4 :

$$\omega L \frac{di_4}{d\theta} + Ri_4 = v_4, \quad i_4(\theta = 0) = 0 \quad (5.82)$$

$$\text{Int 1: } i_4(\theta) = \frac{V_{dc}}{3R} \left(1 - e^{\frac{\theta}{Q}} \right) \quad (5.83)$$

$$\text{Int 2: } i_4(\theta) = \frac{V_{dc}}{3R} (1 - e\alpha) e^{\frac{\theta - \alpha}{Q}} \quad (5.84)$$

$$\text{Int 3: } i_4(\theta) = \frac{V_{dc}}{6R} \left[1 + \left(-1 + 2 \frac{e1}{e\alpha} - 2e1 \right) e^{\frac{\theta - \pi/3}{Q}} \right] \quad (5.85)$$

$$\text{Int 4: } i_4(\theta) = \frac{V_{dc}}{6R} (1 - e\alpha + 2e1 - 2e1 \cdot e\alpha) e^{\frac{\theta - \pi/3 - \alpha}{Q}} \quad (5.86)$$

$$\text{Int 5: } i_4(\theta) = \frac{V_{dc}}{6R} \left[-1 + \left(1 + \frac{e1}{e\alpha} - e1 + 2 \frac{e2}{e\alpha} - 2e2 \right) e^{\frac{\theta - 2\pi/3}{Q}} \right] \quad (5.87)$$

$$\text{Int 6: } i_4(\theta) = \frac{V_{dc}}{6R} (-1 + e\alpha + e1 - e1 \cdot e\alpha + 2e2 - 2e2 \cdot e\alpha) e^{\frac{\theta - 2\pi/3 - \alpha}{Q}}. \quad (5.88)$$

Furthermore, the two angles α and φ are related by the following equation (see Fig. 5.6):

$$e_a(\theta = \alpha) = \sqrt{2}E \sin(\varphi + \alpha) = V_{dc}/3. \quad (5.89)$$

And thus,

$$\varphi = \sin^{-1} \left(\frac{V_{dc}}{3\sqrt{2}E} \right) - \alpha. \quad (5.90)$$

Then, (5.64) must also be considered to calculate α and φ . The Newton-Raphson method is used to determine α from (5.64), and (5.90) is used to determine φ . Hence, the expressions of phase current i_a is defined at any time as a function of the shaft speed ω_m and the capacitor voltage V_{dc} at steady-state operation.

5.7 REFERENCES

- [5.1] S. Song, S. Kang, N. Hahm, "Implementation and control of grid connected AC-DC-AC power converter for variable speed wind energy conversion system," in *18th Annual Applied Power Electronics Conference and Exposition (APEC)*, vol. 1, pp. 154–158, Miami Beach (USA), 2003.
- [5.2] REN21 Renewable Energy Policy Network for the 21st Century, "Renewables global status report 2013".
- [5.3] AWEA American Wind Energy Association, "AWEA U.S. small wind turbine market report year ending 2011".
- [5.4] N. A. Orlando, M. Liserre, V. G. Monopoli, R. A. Mastromauro, A. Dell'Aquila, "Comparison of power converter topologies for permanent magnet small wind turbine system," in *2008 IEEE Symposium on Industrial Electronics (ISIE)*, pp. 2359–2364, Cambridge (UK), 2008.
- [5.5] J. A. Baroudi, V. Dinavahi, A. M. Knight, "A review of power converter topologies for wind generators," *Renewable Energy*, vol. 32, no. 14, pp. 2369–2385, 2007.
- [5.6] T. Senjyu, S. Tamaki, E. Muhandu, N. Urasaki, H. Kinjo, T. Funabashi, H. Fujita, H. Sekine, "Wind velocity and rotor position sensorless maximum power point tracking control for wind generation system," *Renewable Energy*, vol. 31, no. 11, pp. 1764–1775, 2006.
- [5.7] R. Esmaili, L. Xu, D.K. Nichols, "A new control method of permanent magnet generator for maximum power tracking in wind turbine application," in *2005 IEEE Power Engineering Society General Meeting*, vol. 3, pp. 2090–2095, San Francisco (USA), 2005.
- [5.8] S. Hao, G. Hunter, V. Ramsden, D. Patterson, "Control system design for a 20kW wind turbine generator with a boost converter and battery bank load," in *IEEE 32nd Annual Power Electronics Specialists Conference (PESC)*, vol. 4, pp. 2203–2206, Vancouver (Canada), 2001.
- [5.9] M. Kesraoui, N. Korichi, A. Belkadi, "Maximum power point tracker of wind energy conversion system," *Renewable Energy*, vol. 36, no. 10, pp. 2655–2662, 2010.
- [5.10] H. Wang, C. Nayar, J. Su, M. Ding, "Control and interfacing of a grid-connected small-scale wind turbine generator," *IEEE Transactions on Energy Conversion*, vol. 26, no. 2, pp. 428–434, 2011.
- [5.11] N. Yamamura, M. Ishida, T. Hori, "A simple wind power generating system with permanent magnet type synchronous generator," in *1999 Conference on Power Electronics and Drive Systems (PEDS)*, vol. 2, pp. 849–854, Hong Kong 1999.
- [5.12] E. Koutroulis, K. Kalaitzakis, "Design of a maximum power tracking system for wind-energy-conversion applications," *IEEE Transactions on Industrial Electronics*, vol. 53, no. 2, pp. 486–494, 2006.
- [5.13] S. M. R. Kazmi, H. Goto, H. J. Guo, O. Ichinokura, "A novel algorithm for fast and efficient speed sensorless maximum power point tracking in wind energy conversion systems," *IEEE Transactions on Industrial Electronics*, vol. 58, no. 1, pp. 29–36, 2011.
- [5.14] M. Narayana, G. A. Putrus, M. Jovanovic, P. S. Leung, S. McDonald, "Generic maximum power point tracking controller for small-scale wind turbines," *Renewable Energy*, vol. 44, pp. 72–79, 2012.

- [5.15] M. E. Haque, M. Negnevitsky, K. M. Muttaqi, "A novel control strategy for a variable-speed wind turbine with a permanent-magnet synchronous generator," *IEEE Transactions on Industry Applications*, vol. 46, no. 1, pp. 331–339, 2010.
- [5.16] V. Lazarov, D. Roye, D. Spirov, Z. Zarkov, "New control strategy for variable speed wind turbine with DC-DC converters," in *14th Power Electronics and Motion Control Conference (EPE/PEMC)*, pp. T12-120–T12-124, Ohrid (Macedonia) 2010.
- [5.17] S. M. Dehghan, M. Mohamadian, A. Y. Varjani, "A new variable-speed wind energy conversion system using permanent-magnet synchronous generator and Z-source inverter," *IEEE Transactions on Energy Conversion*, vol. 24, no. 3, pp. 714–724, 2009.
- [5.18] K. Tan, S. Islam, "Optimum control strategies in energy conversion of PMSG wind turbine system without mechanical sensors," *IEEE Transactions on Energy Conversion*, vol. 19, no. 2, pp. 392–399, 2004.
- [5.19] I. Serban, C. Marinescu, "A sensorless control method for variable-speed small wind turbines," *Renewable Energy*, vol. 43, pp. 256–266, 2012.
- [5.20] P. Pejovic, J. W. Kolar, "An analysis of three-phase rectifiers with constant voltage loads," in *5th European Conference on Circuits and Systems for Communications (ECCSC)*, Belgrade (Serbia) pp. 119–126, 2010.
- [5.21] V. Caliskan, D. J. Perreault, T. M. Jahns, J. G. Kassakian, "Analysis of three-phase rectifiers with constant-voltage loads," *IEEE Transactions on Circuits and Systems I: Fundamental Theory and Applications*, vol. 50, no. 9, 1220–1225, 2003.
- [5.22] M. Rizo, A. Rodríguez, E. Bueno, F.J. Rodríguez, "Robustness analysis of wind turbines based on PMSG with sensorless vector control," in *36th Annual Conference on IEEE Industrial Electronics Society*, pp. 3103–3108, Glendale (USA), 2010.
- [5.23] J. Chen, J. Chen, C. Gong, "New overall power control strategy for variable-speed fixed-pitch wind turbines within the whole wind velocity range," *IEEE Transaction on Industrial Electronics*, vol. 60, no. 7, pp. 2652–2660, 2013.
- [5.24] K. Gussemé, D. M. Van de Sype, A. P. M. Van den Bossche, J. A. Melkebeek, "Digitally controlled boost power-factor-correction converters operating in both continuous and discontinuous conduction mode," *IEEE Transactions on Industrial Electronics*, vol. 52, no. 1, pp. 88–97, 2005.
- [5.25] A. Urtasun, P. Sanchis, I. San Martín, J. López, L. Marroyo, "Modeling of small wind turbines based on PMSG with diode bridge for sensorless maximum power tracking," *Renewable energy*, vol. 55, pp. 138–149, 2013.

CHAPTER 6

CONCLUSIONS

ABSTRACT

For AC microgrids under stand-alone operation, the elimination of the communication cables is favorable in terms of cost and reliability. By using the grid frequency and voltage as communication signals, a correct frequency and voltage regulation, as well as energy management have been achieved in this thesis both for centralized-storage and distributed-storage systems. The control of the distributed generators within the microgrid has also been studied in the thesis. It has been shown that the non-linear characteristics of the PV generators must be considered for a proper control design. The effect of the dynamic resistance on the control has been analyzed and design guidelines to cope with the problem have been provided for both the boost and TIBuck converters. Concerning small wind turbines, it has been shown that the curve-based MPPT control is adequate when the parameters are accurately known and a correct model is used. However, the captured power can be significantly reduced if the parameters are misestimated, which renders necessary the use of an additional control.

This thesis has given rise to a number of publications in international journals, and conferences and is the result of the participation in public and private R&D projects. Some future research lines are proposed for the management of AC microgrids, the control of different PV converters, and the MPPT control and power limitation of small wind turbines.

6.1 FINAL CONCLUSIONS

Electrical microgrids are currently one of the most promising technical approaches to reach a high level of renewable energy penetration into the electrical grid. In order to make possible the introduction of microgrids, it is of great importance to improve their reliability and reducing their cost. Searching for new control methods represents a perfect means for this purpose since the control can reduce the number of required elements and at the same time the rate of failure, all with no additional cost.

In AC microgrids under stand-alone operation, the use of the grid frequency and RMS voltage as a communication signal makes it possible to prevent the use of communication cables between the different inverters or with a central supervisor. This is favorable since the complexity of the system is reduced, thereby reducing costs. The reliability is also improved because one source of failure disappears. Furthermore, since all elements become able of independent operation, the failure of one of them does not affect the correct operation of the others.

In order to transmit the information through the electrical lines, the grid frequency and RMS voltage are continuously changed during operation. The frequency is related to real power management whereas the voltage has to do with the control of reactive power. As a result, these variables do not remain equal to their rated values but vary around them. However, this does not represent a problem since small frequency and voltage modifications are enough to guarantee a correct system operation. On the other hand, the control with no communication cables becomes more complicated because all inverters must operate based on local variables, but the improvement in costs and reliability makes that this solution is well worth the effort.

Two types of AC microgrid can be considered, depending on whether the storage system and controllable generators are centralized or distributed. The control of the centralized case is simpler since the supervisor is also centralized and has information about the storage units and the controllable generators. This system has been analyzed in chapter 2 for battery storage together with a diesel generator. The grid voltage generation is easily achieved in this system. When the diesel generator is connected, it operates under voltage-control mode and the battery inverter operates under current-control mode. On the other hand, if the diesel generator is not connected, the battery inverter becomes responsible of regulating the grid voltage.

The energy management is also simpler in the centralized-storage system. When the battery SOC is within limits, the diesel generator is not connected and the battery offsets the difference between generation and consumption. Whenever either the battery voltage or the absorbing current is over its rated value, the battery inverter increases the frequency. This is detected by the distributed generators, which continuously reduce

their power to control the battery voltage or current. On the other hand, when the battery SOC is low, the diesel generator is connected and the battery is charged.

The control of a system with distributed battery storage has been developed in chapter 3. The generation of the grid voltage is jointly carried out by the battery inverters thanks to droop methods. By introducing frequency, RMS voltage and harmonic voltage droops, it is possible to share the real power, reactive power and harmonic currents in relation to the inverter ratings.

In order to carry out the energy management in this system, conventional droop methods are modified so that the real power becomes unbalanced when required. When the battery SOC is within limits, a SOC-based droop control makes it possible to maintain the same SOC level for all batteries and, at the same time, to optimize the power response performance. On the other hand, when the batteries are fully charged or discharged, the strategy allows for the regulation of one or more battery voltages or currents, as required. When needed, the frequency is also modified in order to reduce the generation power, regulate the non-critical loads or make an emergency stop.

Apart from preventing the use of communication cables, the control strategies developed for both centralized and distributed storage systems possess other benefits. Firstly, the batteries are correctly managed and the diesel generator only operates when required, thus increasing their expected life. Secondly, the renewable generators operate under MPPT as long as possible and continuously reduce their power when MPPT is not possible. Furthermore, the diesel generator operates at its rated power as far as possible. These factors guarantee high system efficiency.

The effort placed in the system modeling has certainly had an important role in the success of the proposed control strategies. It has been proved that linear models are suitable for modeling the voltage and frequency regulation in droop-based microgrids because they are much simpler than small-signal methods and have similar accuracy. However, small-signal models are required for assessing the management strategy characteristics due to the battery non-linearities. In any case, the control parameters must be carefully designed in order to ensure good performances in terms of dynamic response and stability. Guidelines have been provided to select the most important control elements, which include the droop coefficients, the battery current and voltage controllers, and the measurement and filtering of the real power, reactive power and grid frequency.

Distributed generators are the reason behind the establishment of microgrids and efforts must therefore be made to improve their performance. The main renewable energy sources, due to their potential and current development, are PV generators and wind turbines. In AC microgrids, these systems are usually interfaced by a first-stage

conversion structure, and then followed by the inverter. The first stage controls the renewable source so that its power is either maximized or limited, according to the energy management strategy. At the same, this first-stage converter provides a constant and stable DC value for the second-stage inverter. The control of the first-stage conversion structure has been analyzed in chapter 4 for PV generators and in chapter 5 for small wind turbines.

In low- and medium-power photovoltaic systems, a DC/DC boost converter is usually attached to the PV generator since a PV voltage step-up conversion is required in order to be connected to the inverter. Although these systems are generally based on MPPT, a PV power limitation is demanded by the energy management strategy when the batteries are fully charged. In this situation, the inductor current is controlled so that the power reference is tracked, achieving fast power dynamics. On the other hand, when the reference power cannot be delivered anymore, the voltage control is activated in order to prevent a PV voltage drop and ensure stability. Then, MPPT is performed again until otherwise required.

In this system, an adequate PV voltage regulation is thus fundamental in order to maximize the power and guarantee stability during the transition from MPPT to power limitation. However, when using small input capacitors, the nonlinearities of the PV array make the performance of the voltage regulation become highly dependent on the operating point. A double-feedback control loop is recommended for medium-power DC/DC boost converters, and is therefore analyzed in this work. In this case, a small-signal modelling showed that the voltage regulation performance is as designed in the constant current region. However, the control slows down when the operating point moves towards the maximum power point and it becomes very slow in the constant voltage region. Concerning stability, the phase margin is always higher than designed and the control is thus stable for every operating point. In order to avoid the dynamic response variability, an adaptive control can be used. The PV dynamic resistance is firstly estimated from measured variables of the converter, namely the PV voltage and the inductor current, and then, the controller is continuously adapted making use of the estimation.

The DC/DC boost converter can only use MPP tracker. However, depending on the application, different PV module technologies, orientations and shading conditions can exist, which would lead to significant power losses. In order to perform two independent MPPTs with no extra switches, a two-input buck (TIBuck) converter can be employed. In this case, the nonlinearity of the two PV arrays must be considered, which adds complexity to the analysis of the nonlinear converter. However, a correct regulation of the two PV arrays can be achieved with linear controllers, confirming the TIBuck converter as an interesting solution to perform MPPT of two PV arrays at the same time.

With regard to small wind turbines, the configuration formed by a permanent magnet synchronous generator, a three-phase diode bridge and a DC/DC boost converter is frequently used as the first-stage conversion structure. For the sake of cost efficiency and reliability, it is desirable to prevent wind and turbine speed measurements, which require mechanical sensors. Instead, sensorless MPPT can be achieved by imposing the relationship between the DC voltage and current under optimum operation. In order to obtain the optimum curve, an accurate model of the whole wind energy conversion system is required. Although this model is complex, it is totally justified since it avoids carrying out experimental tests of each wind turbine and ensures a high MPPT efficiency.

However, this method requires having knowledge of the system parameters, which can be inaccurately known in small wind turbines. In fact, the captured power can be significantly reduced for negative but realistic scenarios of parameter misestimations. Thus, an additional control to compensate for the estimation errors is necessary in case that accuracy in the parameters cannot be guaranteed. On the other hand, the resistance has no influence on the MPPT efficiency and can then be neglected for the optimum curve calculation, which leads to a much simpler model.

6.2 CONTRIBUTIONS

In this section, the main contributions of this thesis are presented.

Contributions to international journals

- A. Urtasun, D. D.-C. Lu, "Control of a single-switch two-input buck converter for MPPT of two PV strings," submitted.
- A. Urtasun, P. Sanchis, L. Marroyo, "State-of-charge-based droop control for stand-alone AC supply systems with distributed energy storage," submitted.
- A. Urtasun, E. L. Barrios, P. Sanchis, L. Marroyo, "Frequency-based energy management strategy for stand-alone systems with distributed battery storage," *IEEE Transactions on Power Electronics*, 2015, in press.
- A. Urtasun, P. Sanchis, L. Marroyo, "Small Wind Turbines Sensorless MPPT: Robustness Analysis and Lossless Approach," *IEEE Transactions on Industry Applications*, 2014, in press.
- A. Urtasun, P. Sanchis, D. Barricarte, L. Marroyo, "Energy management strategy for a battery-diesel stand-alone system with distributed PV generation based on grid frequency modulation," *Renewable Energy*, vol. 66, pp. 325–336, 2014.

- A. Urtasun, P. Sanchis, L. Marroyo, "Adaptive voltage control of the dc/dc boost stage in PV converters with small input capacitor," *IEEE Transactions on Power Electronics*, vol. 28, no. 11, pp. 5038–5048, 2013.
- A. Urtasun, P. Sanchis, I. San Martin, J. Lopez, L. Marroyo, "Modeling of small wind turbines based on PMSG with diode bridge for sensorless maximum power tracking," *Renewable Energy*, vol. 55, pp. 138–149, 2013.

Contribution to international conferences

- A. Urtasun, D. D.-C. Lu, "Control of a single-switch two-input buck converter for MPPT of two PV strings," in *2014 Australasian University Power Engineering Conference (AUPEC)*, pp. 1–6, Perth (Australia), 2014.
- A. Urtasun, P. Sanchis, L. Marroyo, "Comparison of linear and small-signal models for inverter-based microgrids," in *2014 Australasian University Power Engineering Conference (AUPEC)*, pp. 1–6, Perth (Australia), 2014.
- A. Urtasun, P. Sanchis, L. Marroyo, "RMS voltage control with harmonic compensation for parallel-connected inverters feeding non-linear loads," in *2014 IEEE Symposium on Circuits and Systems (ISCAS)*, pp. 1179–1182, Melbourne (Australia), 2014.
- A. Urtasun, P. Sanchis, L. Marroyo, "Small wind turbines sensorless MPPT: robustness analysis and lossless approach," in *2013 IEEE Energy Conversion Congress and Exposition (ECCE)*, pp. 2420–2427, Denver (USA), 2013.
- A. Urtasun, P. Sanchis, L. Marroyo, "Limiting the power generated by a photovoltaic system," in *10th International Multiconference on Signal, Systems & Devices (SSD)*, pp. 1–6, Hammamet (Tunisia), 2013.

Participation in public R&D projects

- R&D national plan project, "Power-electronics architectures for distributed generation: hybrid microgrids," DPI2009-14713-C03-01, Spanish Ministry of Economy and Competitiveness, Public University of Navarre (UPNA), 2010–2013.
- R&D national plan project, "Sustainable mobility, hydrogen technologies and renewable supply: energy," DPI2010-21671-C02-01, Spanish Ministry of Economy and Competitiveness, Public University of Navarre (UPNA), 2011–2014.
- R&D national plan project, "Technologies for the grid integration of renewable energies: power electronics, storage, energy management and interaction," DPI2013-42853-R, Spanish Ministry of Economy and Competitiveness, Public University of Navarre (UPNA), 2014–2016.

Participation in private R&D projects

- Contract between the Public University of Navarra (UPNA) and the National Center of Renewable Energies (CENER): “Design, development and implementation of microgrids in Navarre,” OTRI code 2012-024-132, 2013–2015.
- Contract between the Public University of Navarra (UPNA) and Ingeteam Power Technology: “Investigation and development of new conversion converters for photovoltaic systems,” OTRI code 2012-024-121, 2012–2014.

6.3 FUTURE WORK**6.3.1 Management of AC microgrids**

The management of AC microgrids under stand-alone operation has been analyzed in chapter 2 for centralized battery storage and in chapter 3 for distributed battery storage. For these systems, three different research lines, which would expand or complement the current thesis, are proposed as future work.

The first point is related to the real power management and the control of the battery current or voltage, which is carried in section 2.3 for centralized battery storage and in section 3.7 for distributed battery storage. In both cases, a battery small-signal model was used in order to design the controllers. The employed model is very simple and only takes into account the internal resistance and the first order dynamics of the battery, but is reported to be appropriate for this system. That model was integrated in the overall system model, making it possible to design the system parameters and to predict the real power response. Although the control was successfully carried out, some deviation from the predicted behavior was observed in the experimental tests in some operating points. According to its characteristics, this deviation seems to be caused by the strong variation of the battery parameters as a function of the operating point, namely the battery SOC, voltage and temperature. In order to cope with this issue, a more complete small-signal model for the battery response should be used. The model should make it possible to obtain the battery parameters for a certain battery as well as to predict their variation within the operating points of concern.

Another aspect which can be studied as a continuation of this thesis is related to grid voltage and reactive power management. In the AC microgrids presented in the thesis, the RES inverters participate in the frequency regulation by reducing their real power when the grid frequency is high. However, even though it is technically feasible, they never provide or absorb reactive power and do not therefore contribute to the voltage regulation. Similarly to grid regulations which are increasingly demanding reactive

power support to renewable-energy systems, reactive power can be supplied by the RES inverters in AC microgrids. The reactive power management strategy could be implemented in these inverters as a reactive power – voltage droop, where the curve slope and limits must be carefully designed in order to guarantee stability. As a result, instead of using the battery inverters as the only reactive power controllers, this strategy provides distributed reactive power control, which is favorable for the system in terms of efficiency and voltage regulation all over the microgrid. On the other hand, the strategy should also deal with the situations in which the RES inverters apparent power is exceeded, dictating how the real and/or reactive power should be reduced.

Finally, although the stand-alone operation of AC microgrids has been analyzed in this thesis, these systems also operate connected to the electrical grid. The grid-connected operation of AC microgrids and the transition between modes bring along many research opportunities. Some potential future lines include transition from stand-alone to grid-connected operation and vice versa, frequency and voltage regulation, real and reactive power management, and hierarchical control of microgrids.

6.3.2 Control of the photovoltaic system

The control of the PV system has been studied in chapter 4, focusing on the interaction between the DC/DC converter and the PV generator. In order to expand that work, four different research topics are proposed.

The influence of the PV generator on the control of both the DC/DC boost and TIBuck converters has been assessed in this thesis through the PV dynamic resistance, whose variation represents the PV non-linear characteristics. As a direct extension, the influence of this resistance on the voltage control and power limitation of other converters can be carried out. The H-bridge inverter and DC/DC buck converter are frequently used as PV interface and should thus be the first ones to be analyzed. Based on the analyses, general conclusions could be obtained about what the effect of the PV non-linear behavior is, and when the dynamic resistance can be neglected.

The second aspect which can be studied is related to the TIBuck converter operation. In this thesis, the TIBuck converter operation and control have been analyzed in continuous conduction mode. In that mode, very low voltage stress in the switches and high efficiency are achieved. However, the converter can also operate in two other modes of conduction which have not been analyzed: discontinuous conduction mode and Discontinuous Voltage Mode (DVM). The latter appears when the two input voltages are very close to each other. In this situation, these voltages can reach the same value while the active switch is conducting, making the diode start conducting too. This situation is interesting since the voltage stress is even lower than in CCM, the inductor current ripple

is reduced, and the efficiency can thus be improved. In order to achieve this situation, the same number of PV panels can be placed in series at both inputs. Due to mismatched conditions, input 1 can be forced to have a slightly higher open-circuit voltage than input 2. Furthermore, the panels connected to input 2 should be located where shades or higher temperatures are expected, because they cause a MPP voltage reduction. As a result, the condition $V_{MPP1} > V_{MPP2}$ will always be achieved and the converter will operate in DVM during normal operation and may change to CCM when shades or high temperatures are present in the PV2 array. Concerning the control in DVM, the plant for the PV1 voltage regulation becomes less damped than in CCM, and attention must be paid to designing a control suitable for both modes of conduction.

Another research opportunity has to do with the extension of the TIBuck converter. Following the same philosophy, this converter can be extended to form a multiple-input buck converter, as shown in Fig. 6.1. This converter maintains the same favorable performance in terms of conversion efficiency, integration, cost and voltage stress in the semiconductors. Furthermore, when connected to an inverter, it makes it possible to perform n MPPT algorithms with $n-1$ active switches. On the other hand, the restrictions are that the voltage v_n must be lower than all other PV voltages, and that the active switches must block negative currents. The latter can be easily achieved by using an IGBT transistor or by adding a diode in series with the MOSFET transistor, but the first solution is preferred for efficiency. Concerning the control of the multiple PV voltages, it seems to be appropriate for each active switch to regulate its corresponding PV voltage, being able to achieve fast dynamic response. For its part, the voltage of the n^{th} PV array would be controlled by means of the output voltage, similarly to the TIBuck converter.

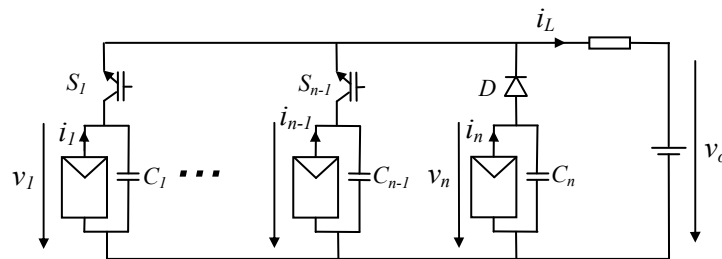


Figure 6.1. Multiple-input buck converter.

Finally, the analysis of other two-input converters can be carried out. As an example, a two-input converter can be formed by adding a second input source to a boost converter or to a buck/boost converter, as shown in Fig. 6.2. The Two-Input Boost (TIBoost) converter also makes it possible to perform two MPPT algorithms when the output voltage can be modified, and a step-up voltage conversion is achieved. However,

the voltage stress in the semiconductors is higher than for the boost or buck/boost converters and it imposes the restriction that the PV1 current must be always higher than the PV2 current.

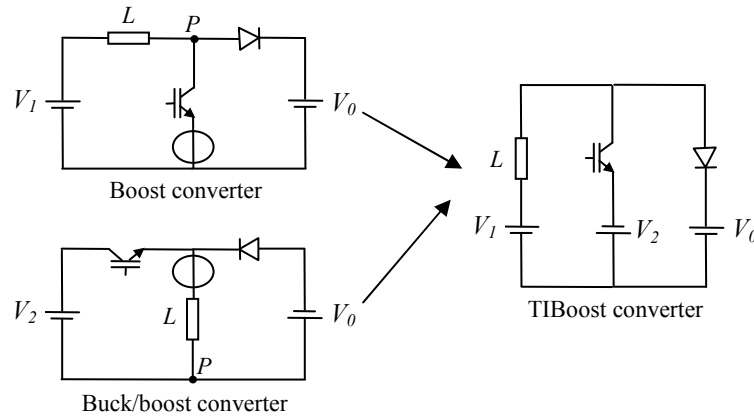


Figure 6.2. Two-input boost converter.

6.3.3 Control of small wind turbines

The MPPT control of small wind turbines has been studied in chapter 5. Two different aspects can be further investigated in line with the realized analysis.

It has been shown that the curve-based MPPT control is effective when the system parameters are accurately known but can lead to power losses if the parameters are misestimated. This is often the case in small wind turbines, where the curve-based MPPT should thus be improved. On the other hand, Perturbation and Observation (P&O) MPPT algorithms do not require any knowledge about the system parameters. However, larger power variations, which are often caused by wind changes, can be misinterpreted by the MPPT strategy. Since wind speed is usually very variable for small wind turbines, this strategy can also result in important power losses. As an alternative, a combined MPPT technique can be developed. This strategy can be based in a preobtained optimum curve, which is then updated in operation so that the parameter errors are compensated.

The second topic is related to power limitation for small wind turbines. Similarly to the PV system, the power limitation should be carried out when the frequency is higher than a certain value, making it possible to control the battery current, voltage or state-of-charge. The power limitation can be implemented by controlling the DC/DC converter, preventing a modification of the inverter operation. The stored energy in a wind turbine is high due to the mechanical inertia, which renders necessary the use of a braking resistor for systems from a certain rated power.

NOMENCLATURE AND ACRONYMS

Symbols

Symbol	Description	Units
A	Plant matrix for the small-signal model with stiff AC grid	Various
a	Overload coefficient (chapter 3)	–
a, b, c, d	Defined parameters (chapter 5)	–
B	Plant matrix for the small-signal model with load influence	Various
C	Battery rated capacity in Wh (chapters 2 and 3)	Wh
C	PV input capacitor (chapter 4)	F
C_{Ah}	Battery rated capacity in Ah	Ah
C_{bat}	Capacitor for the battery small-signal model	F
C_{bus}	Bus capacitor	F
C_{dc}	Diode bridge output capacitor	F
C_P	Wind turbine power coefficient	–
d	Duty cycle	–
d_{ccm}	Duty cycle during CCM	–
d_{dcm}	Duty cycle during DCM	–
E	RMS inverter output voltage (chapter 3)	V
E	RMS induced electromotive force (chapter 5)	V
e	Inverter output voltage (chapter 3)	V
e	Induced electromotive force (chapter 5)	V
$e1, e2, e3$	Defined parameters	–
E_0	RMS nominal inverter output voltage	V
$eaux, ea$	Defined parameters	–

E_{dc}	Inverter DC output voltage	V
E_i	Initial controller output (RMS inverter output voltage)	V
f	Grid frequency (chapter 2)	Hz
f	Frequency generated by the inverter (chapter 3)	Hz
f_0	Nominal grid frequency	Hz
f_{bat}	Frequency generated by the battery inverter (chapter 2)	Hz
f_c	Cutoff frequency for the PV voltage control	Hz
f_{ci}	Cutoff frequency for the current control	Hz
f_{com}	Commutation frequency	Hz
f_{cP}	Cutoff frequency for the real power control	Hz
f_{cQ}	Cutoff frequency for the reactive power control	Hz
f_{cP}	Cutoff frequency for the real power control	Hz
f_{cV}	Cutoff frequency for the RMS voltage control	Hz
f_{cv}	Cutoff frequency for the voltage control	Hz
f_{error}	Error in the frequency generated by the inverter	Hz
f_{pv}	Frequency measured by the PV inverter	Hz
f_r	Resonance frequency	Hz
f_{vc}	Design cutoff frequency for the PV voltage control	Hz
g	Irradiation in the PV array	W/m ²
GM	Gain margin for the PV voltage control	dB
I	RMS inverter current	A
i	Inverter current (delivered) (chapter 3)	A
i	PMSG stator current (chapter 5)	A
I_0	Current constant for the PV power limitation	A
I_0	PV array saturation current (only in section 4.2)	A
i_0	Initial current	A
I_{ad}	Active component of the PMSG stator current fundamental harmonic	A
i_{bat}	Battery current (absorbed in chapter 2, delivered in chapter 3)	A
$i_{bat,Imax}$	Maximum battery current due to battery restriction (absorbed)	A

$i_{bat,Smax}$	Maximum battery current due to inverter restriction (absorbed)	A
i_c	Capacitor current	A
I_d	Small-signal current coefficient for the real power	A
i_d	PMSG stator current in the d axis	A
I_{dc}	Inverter DC current (chapter 3)	A
I_{dc}	Average value of the diode bridge output current (chapter 5)	A
i_{dc}	Diode bridge output current	A
$I_{dc,T}$	DC current absorbed by the loads	A
i_{diesel}	Diesel generator current	A
I_{eq}	Equivalent current for the PV linear model	A
i_{gen}	Total PV inverter current	A
i_{inv}	Battery inverter current (absorbed)	A
I_L	Inductor current (chapter 5)	A
i_L	Inductor current	A
i_{load}	Total load current	A
$i_{L,lpp}$	LPP current reference	A
$i_{L,mpp}$	MPP current reference	A
I_{mpp}	Current at the maximum power point	A
I_{ph}	PV array photogenerated current	A
i_{pv}	PV current	A
I_q	Small-signal current coefficient for the reactive power	A
i_q	PMSG stator current in the q axis	A
I_{SC}	Short-circuit current	A
i_T	Net current (to be provided by the VSIs)	A
i_α	Inverter current	A
i_β	Inverter current delayed $\pi/2$	A
J	Total inertia (wind turbine and PMSG)	kg·m ²
K	Gain of the G_{v2-v0} transfer function	–
k	Constant for the harmonic compensation (chapter 3)	VA·H
k	Boltzmann constant (chapter 4)	J/K
k	PMSG voltage constant (chapter 5)	V/rpm

K_g	Coefficient of the PV current variation with the irradiation	$A \cdot m^2/W$
K_i	Controller integral gain	s^{-1}
K_P	Controller gain constant	Various
K_{pi}	Gain constant of the current controller	Various
K_{pv}	Gain constant of the voltage controller	Various
L	Inverter output inductance (line and output filter). It is considered equal to L_f for short lines (chapter 3)	H
L	Boost/TIBuck converter inductor (chapter 4)	H
L	Inductance of the PMSG, line and possible transformer (chapter 5)	H
L_{dc}	Boost converter inductor	H
L_f	Inverter output filter inductance	H
L_{harm}	Harmonic inductance	H
L_{inv}	PV inverter output filter inductance	H
L_v	Inverter virtual inductance	H
m	Diode ideality factor of the PV array	–
M	Number of photovoltaic inverters	–
M_0	Droop coefficient for SOC=1 for the slope changing method	Hz
M_p	Droop coefficient of the per-unit real power	Hz
m_P	Droop coefficient of the real power	Hz/W
M_q	Droop coefficient of the per-unit reactive power	V
m_Q	Droop coefficient of the reactive power	V/VAr
M_S	SOC coefficient	Hz
N	Number of voltage source inverters	–
n	SOC exponent for the slope changing method	–
N_S	PV cells connected in series	–
P	Inverter real power	W
p	Inverter per-unit real power (chapter 3)	pu
p	Instantaneous power (only in section 3.2)	W
p	Number of PMSG pole pairs (chapter 5)	–
P_0	Diode bridge output power	W
$P_{available}$	Extra power available in the diesel generator	W

P_{bat}	Battery inverter real power (absorbed)	W
p_{bat}	Battery real power (delivered)	W
P_C	Power absorbed by the capacitor C_{dc}	W
P_{diesel}	Diesel generator real power	W
P_{em}	PMSG electromagnetic power	W
P_J	Power absorbed by the inertia J	W
P_L	Power entering the boost inverter	W
P_{load}	Load real power	W
P_{lpp}	Reference PV power	W
PM_i	Phase margin for the current control	°
PM_p	Phase margin for the real power control	°
P_{mpp}	Power at the maximum power point	W
$P_{mpp,fr}$	Frozen MPP power	W
$P_{mpp,tot}$	Total frozen MPP power	W
PM	Phase margin for the PV voltage control	°
PM_Q	Phase margin for the reactive power control	°
PM_V	Phase margin for the RMS voltage control	°
PM_v	Phase margin for the voltage control (chapter 2)	°
PM_v	Design phase margin for the PV voltage control (chapter 4)	°
P_{pv}	Photovoltaic real power	W
P_R	Power losses in the PMSG, line and possible transformer	W
P_{RES}	RES real power	W
P_T	Net real power (to be provided by the VSIs) (chapter 3)	W
P_T	Power captured by the wind turbine (chapter 5)	W
P_{WT}	Wind turbine real power	W
$p_{\alpha\beta}$	Inverter real power using dq theory	W
Q	Inverter reactive power (chapter 3)	VA _r
Q	Z-impedance quality factor (chapter 5)	–
q	Inverter per-unit reactive power (chapter 3)	pu
q	Electron charge (chapter 4)	C
Q_{bat}	Battery inverter reactive power (absorbed)	VA _r

Q_{diesel}	Diesel generator reactive power	VAr
Q_{load}	Load reactive power	VAr
Q_{pv}	Photovoltaic inverter reactive power	VAr
Q_T	Net reactive power (to be provided by the VSIs)	VAr
$q_{\alpha\beta}$	Inverter reactive power using dq theory	VAr
R	Inverter output resistance (line and output filter) (chapter 3)	Ω
R	PV dynamic resistance (chapter 4)	Ω
R	Resistance of the PMSG, line and possible transformer (chapter 5)	Ω
R_C	Resistance for the battery small-signal model	Ω
R_d	Equivalent PV diode resistance	Ω
R_{dc}	Droop resistance	Ω
R_T	Turbine rotor radius	m
r_{dc}	Per-unit droop resistance	pu
r_{eq}	Equivalent resistance for the small-signal model	Ω
R_L	Load resistance	Ω
R_l	Line resistance	Ω
r_L	Inductor resistance	Ω
R_p	PV array shunt resistance	Ω
R_{pv}	PV dynamic resistance	Ω
$R_{pv,est}$	PV dynamic resistance estimation	Ω
R_S	Resistance for the battery small-signal model	Ω
R_s	PV array series resistance	Ω
S	Wind turbine swept area	m ²
s	Laplace operator	rad/s
s	Per-unit inverter apparent power (only in section 3.4)	pu
S_{bat}	Battery inverter apparent power (chapter 2)	VA
S_{bat}	Battery inverter rated power (chapter 3)	VA
$S_{bat,nom}$	Battery inverter rated power (chapter 2)	VA
$S_{bat,tot}$	Rated power of all battery inverters	VA
S_{diesel}	Diesel generator apparent power	VA
$S_{diesel,nom}$	Diesel generator rated power	VA

S_{load}	Load apparent power	VA
$S_{load,nom}$	Load rated power	VA
SOC	Battery state of charge	–
SOC_0	Constant for the curve shifting method	–
SOC_i	Initial battery state of charge	–
SOC_{off}	Battery SOC for diesel generator disconnection	–
SOC_{on}	Battery SOC for diesel generator connection	–
S_{pv}	PV inverter rated power	VA
$S_{pv,nom}$	Total PV inverter rated power	VA
T	PV array temperature	K or °C
t	Time	s
T_d	Delay time	s
T_m, T_n	Controller time constants	s
T_{ni}	Time constant of the current controller	s
T_{nv}	Time constant of the voltage controller	s
T_s	Sample time	s
T_{si}	Current loop sample time	s
T_{sv}	Voltage loop sample time	s
$u_{1,2,3}$	Connection functions of diodes D1, D2, D3	–
V	RMS grid voltage	V
v	Grid voltage (chapter 3)	V
v	PV voltage (chapter 4)	V
V_0	RMS nominal grid voltage	V
$v_{A0,B0,C0}$	Voltage between points A-0, B-0, C-0	V
$v_{AN,BN,CN}$	Voltage between points A-N, B-N, C-N	V
v_{bat}	Battery voltage	V
$V_{bat,abs}$	Battery absorption voltage	V
$V_{bat,fl}$	Battery float voltage	V
$V_{bat,nom}$	Battery rated voltage	V
V_{bus}	DC bus voltage (chapter 5)	V
v_{bus}	DC bus voltage	V
v_d	Diode voltage	V
V_{dc}	DC grid voltage (chapter 3)	V

V_{dc}	Diode bridge output voltage (chapter 5)	V
v_{diesel}	Diesel generator voltage	V
$v_{d,on}$	Diode voltage drop during conduction	V
V_{eq}	Equivalent voltage for the small-signal model	V
v_{grid}	Grid voltage	V
v_{norm}	Normalized PV voltage	V
V_{mpp}	Voltage at the maximum power point	V
v_{mpp}	Voltage at the maximum power point (for the control)	V
$v_{mpp,fr}$	Frozen MPP voltage	V
V_0	Rated output voltage	V
v_o	Output voltage	V
V_{oc}	PV open-circuit voltage	V
v_{pv}	Photovoltaic voltage	V
v_s	Transistor voltage	V
$v_{s,on}$	Transistor voltage drop during conduction	V
V_t	PV array thermal voltage	V
v_w	Wind speed	m/s
v_α	Grid voltage	V
v_β	Grid voltage delayed $\pi/2$	V
X	Inverter output reactance (line and output filter)	Ω
X_d	Equivalent droop reactance	Ω
X_l	Line reactance	Ω
Z	Inverter output impedance (line and output filter) (chapter 3)	Ω
Z	Impedance of the PMSG, line and possible transformer (chapter 5)	Ω
Z_l	Line impedance	Ω
α	Conduction delay angle in DCM	rad
β	Sum of α and φ	rad
δ	Power angle (angle between e and v)	rad
δf	Shifting frequency	Hz
δf_c	Charge shifting frequency	Hz
$\delta f_{c,i}$	Charge shifting frequency for the current control	Hz

$\delta f_{c,v}$	Charge shifting frequency for the voltage control	Hz
δf_d	Discharge shifting frequency	Hz
$\delta f_{d,i}$	Discharge shifting frequency for the current control	Hz
$\delta f_{d,v}$	Discharge shifting frequency for the voltage control	Hz
Δf	Frequency deviation in relation to the nominal value	Hz
Δf_{error}	Total error in the frequency generated by the inverters	Hz
Δf_i	Frequency deviation for the current control	Hz
Δf_v	Frequency deviation for the voltage control	Hz
Δf_{stop}	Shutdown frequency deviation	Hz
ΔP_{max_Afer}	Real power error due to errors in the generated frequency	W
η	MPPT efficiency	%
η_{bat}	Battery efficiency	%
θ	Electrical angle of the PMSG	rad
θ_i	Angle between inverter grid voltage and AC bus voltage (only in section 3.4)	rad
θ_i	Initial angle position of the inverter output voltage	rad
θ_v	Angle position of the grid voltage	rad
λ	System pole (chapter 3)	rad/s
λ	Tip speed ratio of the wind turbine (chapter 5)	–
ξ	Damping factor	–
ρ	Air density	kg/m ³
τ_f	Time constant of the frequency measurement	s
τ_i	Time constant of the current measurement	s
τ_P	Time constant of the real power measurement	s
τ_Q	Time constant of the reactive power measurement	s
τ_s	Time constant of the sampling	s
$\tau_{SOC,sl}$	SOC response time constant for the slope changing method	s
$\tau_{SOC,sh}$	SOC response time constant for the curve shifting method	s
τ_V	Time constant of the RMS voltage measurement	s
τ_v	Time constant of the voltage measurement	s

φ	Angle between voltage and current	$^{\circ}$
φ_z	Impedance phase of the PMSG, line and possible transformer	rad
ω	Fundamental angular frequency (chapter 3)	rad/s
ω	PMSG electrical speed	rad/s
ω_0	Nominal angular frequency	rad/s
ω_{ic}	Angular cutoff frequency of the current control	rad/s
ω_m	PMSG and wind turbine mechanical speed	rad/s
ω_n	Angular natural frequency	rad/s
ω_p	Angular cutoff frequency of the controller pole	rad/s
ω_{vc}	Angular cutoff frequency of the PV voltage control	rad/s

Transfer functions

Symbol	Description
B	Power delay due to the DC bus voltage control
$C_{c,i}$	Current controller for charging mode
$C_{c,v}$	Voltage controller for charging mode
$C_{d,i}$	Current controller for discharging mode
$C_{d,v}$	Voltage controller for discharging mode
C_i	Current controller
C_v	Voltage controller
C_{Vdc}	DC voltage controller
D_{CON}	Related to the conventional droop control
den_D	Characteristic equation for the difference response
den_S	Characteristic equation for the sum response
den_{SOC}	Characteristic equation for the SOC response
den_P	Characteristic equation for the real power response
den_{PQV}	Characteristic equation for the coupled response
den_Q	Characteristic equation for the reactive power response
den_V	Characteristic equation for the RMS voltage response

D_{PL}	Related to the difference response plant
G_{bat}	Battery current to voltage transfer function (chapter 2)
G_{bat}	Battery power to voltage transfer function (chapter 3)
G_f	Frequency deviation to power reference transfer function
G_{icl}	Inductor current closed-loop
G_v	Inductor current to PV voltage transfer function
$G_{v0,cl}$	Output voltage closed-loop
G_{v1-d}	Duty cycle to PV1 voltage transfer function
G_{v2-v0}	Output voltage to PV2 voltage transfer function
G_v^*	Inductor current reference to PV voltage transfer function
H_f	Frequency measurement
H_i	Current measurement
H_P	Real power measurement
H_Q	Reactive power measurement
H_V	RMS voltage measurement
H_v	Voltage measurement
I	Laplace integrator ($2\pi/s$)
PI	Proportional-integral controller
S_{BAT}	Related to the energy management control
S_i	Current digital sampler
S_{RES}	Related to the sum response plant
S_v	Voltage digital sampler

Subscripts and superscripts

Symbol	Description
$1, 2, \dots$	Refers to different units or different harmonics
100	Refers to the 100 Hz component
a, b, c	Refers to the phase in a three-phase system
c	Refers to battery charging mode
$calc$	Refers to the parameters used for the optimum curve calculation

<i>d</i>	Refers to battery discharging mode
<i>ff</i>	Refers to a feedforward compensation
<i>fund</i>	Refers to the fundamental component
<i>harm</i>	Refers to the harmonic components
<i>i</i>	Refers to a certain inverter
<i>opt</i>	Refers to an optimum value (at maximum power operation)
<i>m</i>	Refers to a measured variable or to a certain harmonic
<i>max</i>	Refers to a maximum value
<i>min</i>	Refers to a minimum value
<i>ref</i>	Refers to a reference variable
<i>R=0</i>	Refers to the lossless approach
<i>ω_{max}</i>	Refers to the high speed scenario
<i>ω_{min}</i>	Refers to the low speed scenario
<i>+</i>	Refers to a parameter overestimation
<i>–</i>	Refers to a parameter underestimation
<i>^</i>	Refers to a small-signal variable
<i>*</i>	Refers to a reference variable

Acronyms

AC	Alternating current
BPF	Band-pass filter
CC	Constant current
CCM	Continuous conduction mode
CPL	Constant power load
CPS	Constant power source
CSI	Current-source inverter
CV	Constant voltage
DC	Direct current
DCM	Discontinuous conduction mode
DG	Distributed generator

ESS	Energy storage system
GM	Gain margin
LOLP	Loss of load probability
LPF	Low-pass filter
LPPT	Limited power point tracking
MPPT	Maximum power point tracking
NCM	Non-conduction mode
OC	Open-circuit
PCC	Point of common coupling
PI	Proportional-integral
PLL	Phase locked loop
PM	Phase margin
PMSG	Permanent magnet synchronous generator
PV	Photovoltaic
P&LPF	Product and low pass filter
P&O	Perturbation and observation
SC	Short-circuit
RES	Renewable energy source
RMS	Root mean square
R&D	Research and development
SOC	State of charge
THD	Total harmonic distortion
VSI	Voltage-source inverter
WECS	Wind energy conversion system
WT	Wind turbine